

Design and development for the Rearsection of the KATRIN experiment

Zur Erlangung des akademischen Grades eines
DOKTORS DER NATURWISSENSCHAFTEN

von der Fakultät für Physik
des Karlsruher Instituts für Technologie
genehmigte

DISSERTATION

von

Dipl.-Phys. Martin Babutzka

ausgearbeitet am Institut für experimentelle Kernphysik und dem
Tritiumlabor Karlsruhe

Erstgutachter: Prof. Dr. Guido Drexlin
Institut für experimentelle Kernphysik (KIT)

Zweitgutachter: Prof. Dr. Thomas Müller
Institut für experimentelle Kernphysik (KIT)

Tag der mündlichen Prüfung: 28.11.2014

Declaration of authorship

I declare that I have developed and written the enclosed thesis completely by myself, and have not used sources or means without declaration in the text.

Erklärung der Selbstständigkeit

Hiermit versichere ich, die vorliegende Arbeit selbstständig angefertigt, alle dem Wortlaut oder Sinn nach entnommenen Inhalte anderer Werke an den entsprechenden Stellen unter Angabe der Quellen kenntlich gemacht und keine weiteren Hilfsmittel verwendet zu haben.

Karlsruhe, February 11, 2015

.....

(Martin Babutzka)

Some of the cited sources are not available in published form but details of interest may be requested via electronic mail to martin.babutzka@online.de.

Contents

Introduction and objectives of the thesis	1
1. Neutrino physics	3
1.1. Basic properties of neutrinos	3
1.2. Neutrino sources	4
1.2.1. Atmospheric neutrinos	4
1.2.2. Relic neutrinos	4
1.2.3. Neutrinos produced in particle accelerators	4
1.2.4. Solar neutrinos	5
1.2.5. Neutrinos from Beta decays	5
1.3. Neutrino oscillations	6
1.3.1. The solar neutrino problem	6
1.3.2. Neutrino oscillations	7
1.4. Methods to measure the neutrino mass	9
1.4.1. Neutrinoless double beta decay	9
1.4.2. Cosmological methods	11
1.4.3. Kinematic methods	12
1.5. Impact of the neutrino mass	14
2. The KATRIN experiment and the Rearsection	17
2.1. Components of KATRIN	18
2.1.1. Tritium source	18
2.1.2. Transport and pumping sections	19
2.1.3. Energy filtering spectrometers	20
2.1.4. Main detector	22
2.1.5. Rearsection	22
2.2. Monitoring methods for the KATRIN tritium source	22
2.2.1. Composition of the gas mixture	23
2.2.2. Monitoring the WGTS activity	24
2.2.3. Measurement and stability of the gas density	26
2.3. Physics objectives of the Rearsection	27
2.3.1. Reference potential for the WGTS plasma	28
2.3.2. Monitoring of the source activity with beta-induced X-ray spectroscopy	29
2.3.3. Calibration methods using an electron source	30
3. Mechanical design of the Rearsection	33
3.1. Vacuum system	33
3.1.1. Design of the vacuum and pumping system	36
3.1.2. Magnetic shielding for the turbomolecular pumps	39
3.1.3. Sensors and controlling	47
3.2. Tritium safe second containment	51
3.2.1. Second containment implementation at the Rearsection	52

3.3.	Interfaces to neighbor systems	54
3.3.1.	Interfaces to the DPS1-R	55
3.3.2.	Interfaces to the tritium infrastructure	56
4.	Rearsection electron gun and electromagnetic transport	59
4.1.	Design of the electron gun	59
4.1.1.	Principles of photoelectron sources	59
4.1.2.	Acceleration electrodes design	60
4.1.3.	High voltage calculations at the electron gun	61
4.1.4.	Optics and UV light source	65
4.2.	Electromagnetic transport section simulation	69
4.2.1.	Adiabatic transport	70
4.2.2.	Simulations with axially symmetric fields	70
4.2.3.	Test of the dipole coils	74
4.2.4.	Evaluation of the dipole electrodes	77
4.2.5.	Adiabaticity of the post-acceleration electrodes	81
4.2.6.	Optimizations at the transport section	84
4.3.	Implementation of the electron gun to the simulation	88
4.3.1.	Results for the combined system	91
4.3.2.	E-gun calibration procedures	100
4.4.	Piezoelectric motor performance test	101
4.4.1.	Experimental setup	102
4.4.2.	Motor performance evaluation	105
4.5.	The electron gun beam tracker	108
4.5.1.	Design of the electron gun beam tracker	109
4.5.2.	Implementation with an electron gun	113
4.5.3.	Detection measurements	114
4.5.4.	Calibration measurements	117
5.	Rear Wall and WGTS activity monitoring	123
5.1.	Design of the Rear Wall	124
5.1.1.	Work function and the source potential	124
5.1.2.	Flux tube transport to the Rear Wall	128
5.1.3.	Technical implementation of the Rear Wall	131
5.2.	Work function measurements using a Kelvin Probe	134
5.2.1.	Kelvin probe working principle	134
5.2.2.	Scanning Kelvin probe setup	137
5.2.3.	Measurements of prototypes	138
5.2.4.	Conclusions for the qualification strategy	144
5.3.	Work function measurements with the photoelectric effect	145
5.3.1.	Measurement setup	146
5.3.2.	Measurements using a photo-spectroscopic filter	149
5.3.3.	Measurements with an electrostatic filter	153
5.3.4.	Conclusions for qualification	156
5.4.	Tritium adsorption on the Rear Wall	158
5.4.1.	Theory of tritium adsorption on gold	159
5.4.2.	Test for tritium adsorption using a quartz crystal microbalance . . .	162
5.5.	Implementation of the beta-induced X-ray spectroscopy system	170
	Conclusion	177
	Bibliography	181

Appendix	191
A. E-gun beam tracker - circuitry documentation	191
B. UV light source calibration	193
Acknowledgements	195

List of Figures

1.1.	Feynman diagram of the beta decay	5
1.2.	The Super-Kamiokande neutrino observatory	7
1.3.	Schema for a two-state neutrino oscillation	9
1.4.	Mass parabola of isobar nuclei	10
1.5.	Feynman diagram of the neutrinoless double beta decay	10
1.6.	Energy spectrum of the tritium beta decay electrons	13
1.7.	Mass hierarchies of neutrino mass states	14
1.8.	Contributions to the energy density of the universe	15
2.1.	Beamline setup of the KATRIN experiment	18
2.2.	Operating principle of a MAC-E-Filter	21
2.3.	Overview of control and monitoring methods at the source and transport section	23
2.4.	Impact of the column density on the systematic uncertainty	24
2.5.	Transmission and response function	27
2.6.	Schema of the Rearsection	28
3.1.	Side cut view of the full system	34
3.2.	Vacuum system of the Rearsection	36
3.3.	Schema for vacuum pressure estimation	38
3.4.	Magnetic field at the turbomolecular pump position	40
3.5.	Magnetic shielding calculations with FEMM	41
3.6.	Magnetic heating of a turbomolecular pump	42
3.7.	Magnetic field compatibility test stand	43
3.8.	Magnetic shielding calculations with OperaFEA	44
3.9.	Magnetic field at the E-gun TMP position	44
3.10.	Magnetic field at the Edwards scroll pump	46
3.11.	Pressure sensors tested for magnetic field compatibility	47
3.12.	Cold cathode pressure sensor readout value in dependency of the magnetic field	48
3.13.	Cold cathode pressure sensor readout value in dependency of the magnetic field	48
3.14.	Baratron pressure indicator value in dependency of the applied magnetic field	49
3.15.	Baratron pressure indicator value in dependency of the applied magnetic field	49
3.16.	Vacuum schema of the Rearsection primary system	51
3.17.	Second containments of the Rearsection	53
3.18.	Rearsection placed in building 452	54
3.19.	DPS1-R/WGTS end cap	55
3.20.	Second containment adapter	56
4.1.	High voltage electrode configuration at the E-gun	62
4.2.	Representation of Pashen's law	63

4.3. Model for the FEM field calculation	63
4.4. Electric field check at the main electrode	64
4.5. Electric field check of the high voltage supply lines	65
4.6. Electric field check at the high voltage feed-through	66
4.7. Picture of the EQ-99X	67
4.8. Deep UV light sources considered for the Rearsection E-gun	68
4.9. Ultraviolet light path at the photoelectric electron gun	69
4.10. Solenoid setup as used for the electromagnetic simulations	71
4.11. Solenoid field strength in the Rearsection	72
4.12. Magnetic field of the normally conducting solenoids	73
4.13. Adiabaticity of the solenoid transport field	74
4.14. Magnetic field of the dipole coils	76
4.15. Shift of a field line by the magnetic dipoles	77
4.16. Displacement effects by the magnetic dipoles	78
4.17. Electric field of the dipole electrodes	79
4.18. Importance of the dipole electrode design	80
4.19. Removal of reflected electrons by the dipole electrodes	82
4.20. Removal of incoming tritium ions by the dipoles electrodes	82
4.21. Electric potential within the post-acceleration electrodes	84
4.22. Electron post-acceleration	85
4.23. Comparison of electric field strengths at the dipole and post-acceleration electrodes	86
4.24. Electron polar angle in dependence of the path through the transport section	87
4.25. Electron magnetic moment in dependence of the path through the transport section	88
4.26. Energy distribution of the photo-emission electrons	90
4.27. Absolute electric potential between the E-gun plates	91
4.28. Electron path starting from the electron gun with a plate tilt angle of zero degree	92
4.29. Kinetic energy of an electron passing through the E-gun electrodes	93
4.30. Electron maximum polar angle behavior at E-gun simulations	93
4.31. Electron path with E-gun at maximum polar angle	94
4.32. Absolute electric and magnetic forces at the E-gun	95
4.33. Electron gun configurations to generate electrons with maximum polar angle	96
4.34. Angular distribution of a full Rearsection electron gun simulation at zero degree plate tilt angle	97
4.35. Energy distribution of a full Rearsection electron gun simulation at zero degree plate tilt angle	97
4.36. Angular distribution of a full Rearsection electron gun simulation for maxi- mum electron polar angle	99
4.37. Energy distribution of a full Rearsection electron gun simulation for maxi- mum electron polar angle	99
4.38. Simplified visualization of the piezoelectric effect	103
4.39. CAD picture of the piezoelectric motor Attocube ANPx101eXT20	104
4.40. Schema of the Attocube motor test experimental setup	104
4.41. Piezo-motor driving operations in vacuum	107
4.42. Piezo-motor driving operations in tritium atmosphere	108
4.43. Picture of the piezoelectric motor after the measurements	109
4.44. Pictures of the prototype for the electron gun beam tracker	113
4.45. Dark measurement of the detector signal	114
4.46. Signal events with the beam tracker detector	116
4.47. Beam tracker signal dependence on the focus coil current	117

4.48.	Beam tracker signal dependence on the electron energy	119
4.49.	Electron beam sweep over a detector quadrant	120
4.50.	Beam crossover with two opposed quadrants	121
5.1.	Influence of the Rear Wall potential on the WGTS	127
5.2.	CAD drawing of the Rear Wall domain including the magnetic flux tube . .	129
5.3.	Flux tube intersection with the Rear Wall	130
5.4.	Solenoid magnetic field at the Rear Wall	132
5.5.	Technical design of the Rear Wall mount	135
5.6.	Necessary steps for a Kelvin probe measurement	136
5.7.	Picture of the overall Kelvin Probe setup	137
5.8.	Picture of the Kelvin probe measurement platform	138
5.9.	Kelvin probe scan of the gold coated silicon wafer	139
5.10.	Kelvin probe scan of the gold grown on corundum	140
5.11.	Kelvin probe scan of the gold coated Beryllium window	141
5.12.	Height profile of the beryllium window	142
5.13.	Humidity in the Kelvin probe enclosure	143
5.14.	Long-term stability of the reference sample	144
5.15.	Impact of electric fields on the effective surface work function	146
5.16.	Picture of the pierce electrode installed on a flange	147
5.17.	Optical setup for the monitor spectrometer measurements	148
5.18.	Picture of the full measurement setup at the monitor spectrometer	148
5.19.	Wavelength scan of the gold galvanized copper sample	150
5.20.	Fit of a complementary error function to a monitor spectrometer voltage scan	153
5.21.	Dependence of the photo-electron energy distribution broadness on the pho- ton energy	155
5.22.	UV light cone for Rear Wall illumination	157
5.23.	Theoretical initial adsorption process	161
5.24.	Theoretical desorption process	162
5.25.	Energy schema for adsorption/desorption of hydrogen on gold	163
5.26.	Schema of the QCMB experimental setup	165
5.27.	Temperature dependence of AT-cut quartz crystals	166
5.28.	Picture of the quartz crystal installed to the CF flange	166
5.29.	Temperature dependence of the QCMB	168
5.30.	Pressure dependence of the QCMB	168
5.31.	Long term drifts of the QCMB in vacuum	169
5.32.	Long term drifts of the QCMB in tritium	170
5.33.	Exemplary BIXS spectrum	171
5.34.	Design of the BIXS detector systems at the Rearsection	173
5.35.	Monitoring cone of one BIXS detector	174
A.1.	Board layout of the E-gun beam tracker	191
A.2.	Circuit layout of the E-gun beam tracker	192

List of Tables

2.1. Electron gun measurements modes	32
3.1. Magnetic field limits for Leybold MAG W600 Turbopump	45
4.1. Magnet configurations for the simulation	75
4.2. Electrodes configuration for the simulation	85
4.3. Electron gun fixed fiber positions	98
4.4. Performance of the piezo-motor	106
4.5. Effect of the focus coil current	118
4.6. Maximum measured signal at different electron energies	119
5.1. Photo-spectroscopic work function evaluation	151
5.2. MAC-E-filter measurements of photoelectrons	156
B.1. Calibration of the filtered UV light source	193

Introduction and objectives of the thesis

After the experimental discovery of the neutrinos in the year 1953[1], many experiments followed up to measure the properties of the elementary particles. Typically, only high precision, low background experiments can retrieve new information about neutrino properties. This is caused by the small cross-sections of neutrino interactions because these particles couple neither to the strong nor the electromagnetic force. One of the most considerable questions concerns the rest mass of the neutrinos. With the evidence of the neutrino flavor oscillations has been proven that neutrinos have a non-vanishing rest mass - more specifically at least 2 out of 3 neutrino mass eigenstates must be non-zero. So far experiments with the goal of a direct measurement of any neutrino mass could only define upper limits. The smallest upper limit for the rest mass of the electron anti-neutrino is $m(\bar{\nu}_e) < 2.05 \text{ eV}/c^2$ (95 C.L.) as it resulted from a data re-evaluation of the Troitsk neutrino mass experiment [2].

The Karlsruhe Tritium Neutrino Experiment (KATRIN) is going to measure the energy spectrum of the tritium β -decay with an unmatched precision [3]. The electron spectroscopy is the basis of a model independent method to determine the neutrino mass using only the energy-momentum conservation and without the need for any assumptions on the neutrino properties. The goal of the KATRIN experiment is to measure the rest mass of the electron anti-neutrino with a discovery potential down to $350 \text{ meV}/c^2$ at 5σ significance or place an upper limit at $200 \text{ meV}/c^2$ with 90 % confidence level. This measurement requires an electron spectrometer with high energy resolution and a high luminosity tritium source. While the large activity in the source is necessary to achieve a small statistical error, uncertainties in the tritium source are also responsible for a large contribution to the systematic error. A group of instruments defined as the Calibration and Monitoring Systems (CMS) have the task to detect and record changes in the tritium source. Only one of these dedicated systems is capable of controlling or monitoring multiple source parameters in one component: The so called "Rearsection" which is installed at the rear end¹ of the gaseous tritium source.

The most fundamental purpose of the Rearsection (RS) is to properly close the ultra-high vacuum (UHV) system of the windowless gaseous tritium source (WGTS) towards the rear side. Because of the windowless implementation of the source, it is inherent that tritium can stream into the RS. Therefore, the requirements on the vacuum encasement exceed the usual standards and the Rearsection must also fulfill all requirements for a tritium safe enclosure [4]. The Rearsection character of termination does not only apply from the vacuum concern but also as electrical termination: By decays and ionization in the high luminosity tritium source a cold plasma is generated. The plasma motion is confined in motion by the strong magnetic field generated by superconducting magnets of the WGTS. As a result, the motion towards either spectrometer or Rearsection is dominating. The charged particles moving in rear direction are absorbed or neutralized at

¹As front direction of the KATRIN experiment is considered where pumping systems, the electron spectrometer and the electron detector are following up the tritium source

the gold-coated “Rear Wall” of the RS. Together with the large mobility also the electric conductivity of the plasma from Rearsection into the to the WGTS is significant. The surface properties of the Rear Wall can become important for the electrostatic potential within large parts of the WGTS. An important research objective is therefore to measure and qualify the surface of Rear Wall candidates. Furthermore, the photons generated at the Rear Wall via the inverse photoelectric effect are used for a high precision monitoring of the source activity. Further downstream follows the electromagnetic transport section and the photoelectric electron gun (E-gun) of the Rearsection. This electron gun will be a versatile calibration tool for KATRIN because it can provide an adjustable electron beam to imitate the tritium β -electrons. To enable a precise source calibration the E-gun must be able to sharply select the kinetic energy of the electrons as well as the angle of the electrons towards the magnetic field lines (polar angle). The electromagnetic design of electron gun and the transport section have been optimized to meet the challenging requirements. Dedicated experiments were necessary to test instrumentation which shall be installed in the vacuum system to control or monitor the E-gun beam behavior.

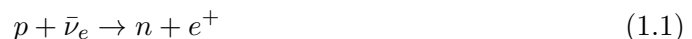
The chapters in this thesis are not organized by the scientific approach (theoretical, experimental, simulations, . . .) but by their instrumental meaning for the Rearsection. This is reasonable because the investigations on the different Rearsection instruments are only weakly linked to each other or even completely independent. Chapter 1 summarizes the most important neutrino properties and previous experiments for the KATRIN experiment. The focus of chapter 2 is on the KATRIN experiment itself. The main components and the different methods to control and monitor the tritium source are explained. For the Rearsection the physics objectives are listed in detail while the following chapters show how these requirements shall be achieved. The mechanical design of the Rearsection like the support structure, the vacuum system and the tritium-safe encasement are discussed in chapter 3. It also evaluates the vacuum instrumentation that will be used such as pressure sensors, valves and pumps. Chapter 4 comprises the developments for the electron gun and the electromagnetic design. The focus is on the detailed simulations and the necessary optimizations. The construction is the task of our collaboration partners at the University of California Santa Barbara (UCSB). The test experiments related to the electron gun that were conducted at KIT are also described in the chapter. Finally, chapter 5 is concentrated on the Rear Wall and corresponding instrumentation. The main focus of the chapter are the different measurements to qualify prototypes for the potential usage as KATRIN Rear Wall. The thesis concludes with a report on the main achievements and on current status and outlook about the Rearsection development.

1. Neutrino physics

1.1. Basic properties of neutrinos

Neutrinos are Spin-1/2 fermions and exist in the 3 different flavors as electron neutrino ν_e , muon neutrino ν_μ and tau neutrino ν_τ . They contribute to the well-known lepton group as part of the standard model of particle physics [5]. Neutrinos interact neither via the strong nor the electromagnetic force so any method of proving their existence must proceed via charged (W^+/W^-) or neutral (Z^0) currents in the weak interaction. Due to the extremely small interaction cross-sections of the weak force it is very difficult to experimentally detect neutrinos and measure their properties. For this reason the existence of neutrinos had already been postulated in the year 1930 by Wolfgang Pauli [6], but it needed 25 more years to accomplish the experimental proof. The postulation of an up to then unknown particle has been necessary because of an apparent contradiction between the theoretical considerations of the kinematics of the beta decay and experimental results.

The first experimental detection of neutrinos succeeded in 1953 by the physicists Clyde Cowan and Fred Reines with the “Poltergeist” experiment [1]. It was carried out close to a nuclear reactor core because the fission processes produce neutron-enriched nuclides, which provides an intense neutrino source by their β -decays. A water tank containing dissolved cadmium chloride (CdCl_2) served as neutrino detector. Anti-neutrinos can react with protons (e.g. from hydrogen) to produce a free neutron and a positron. This process is called inverse β -decay:



The positron quickly loses energy in collisions and eventually annihilates with a shell electron. Thereby two γ -particles with an energy of 511 keV each are created. The free neutron becomes thermalized on the time scale of microseconds by collisions with water molecules. Before the free neutron decays, it is captured by a Cd nucleus. The cadmium nucleus is excited after this process and returns to its ground state via the emission of γ -quanta. This was the decisive signature in the Poltergeist experiment: Two events of multiple γ -quanta separated by a few microseconds. The signals were detected by scintillation counters which surround the water tank.

The cross-section for the reaction of neutrinos in the Poltergeist experiment has been determined to the very small value of $\sigma = 6.3 \cdot 10^{-44} \text{ cm}^2$ [7]. Therefore, neutrino detectors

in general - just as at the project Poltergeist - need a large sensitive detector volume or a high neutrino intensity to obtain a significant reaction rate.

1.2. Neutrino sources

1.2.1. Atmospheric neutrinos

High energetic cosmic particles (mainly protons) collide with nuclei of air molecules when entering the earth atmosphere. In this process primary pions, other mesons, neutrons and protons are created which end up in broad showers after multiple decay and collision events. Additionally, for every single decaying muon, a neutrino and an anti-neutrino are created. This is the main source of the so called atmospheric neutrinos [8].

Besides these atmospheric neutrinos the muons play an important role in most neutrino experiments because they may contribute to the background. To mitigate this background most neutrino experiments are realized in underground laboratories and use muon-vetos to separate muon events from neutrino events.

1.2.2. Relic neutrinos

Relic neutrinos are remnant particles from the beginning of the universe: By the expansion of space-time the universe cools down after the big bang. Until a temperature equivalent of 1 MeV the following reaction of production and annihilation of electrons, gammas and neutrinos is in equilibrium:

$$\nu + \bar{\nu} \leftrightarrow e^+ + e^- \leftrightarrow \gamma + \gamma \quad (1.2)$$

Below this temperature the neutrinos decouple. Today these neutrinos exist as relic background and are assumed to be isotropically and homogeneously distributed in the universe [9]. The neutrino temperature has been reduced by the expansion of the universe to approximately 1.95 Kelvin (combination of the results of [10] and [9]) and the neutrino density is 339 cm^{-3} [9]. Because of the very low energy and very small cross-sections of the relic neutrinos their experimental proof is still outstanding.

As hot dark matter (HDM) relic neutrinos play an important role in cosmology for the structure formation in the early universe [9]. Furthermore, depending on their rest mass, these neutrinos contribute either a negligible or significant part of the total energy density in the universe.

1.2.3. Neutrinos produced in particle accelerators

Neutrino streams of high intensity can be created specifically in particle accelerators. The production is possible for instance when high-energy protons hit a static target. Emerging pions and kaons produce muon-neutrinos and furthermore muons, which again produce further neutrinos on decay. The underlying processes are the artificial equivalents to the reaction that produce atmospheric neutrinos. But neutrinos from particle accelerators can be produced with a much sharper energy resolution and short term intensity. Additionally, there are experimental advantages since the exact position of the neutrino source as well as the exact point in time of neutrino production are known.

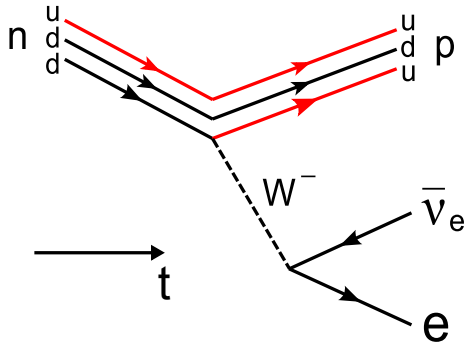


Figure 1.1: Feynman diagram of the β^- -decay - The down quark of a neutron changes to an up quark by emitting an electron and an electron anti-neutrino. The process is mediated by a virtual W^- boson for the weak interaction.

1.2.4. Solar neutrinos

The sun is a very intense neutrino source in our solar system. In the exothermic fusion reactions from hydrogen to helium in the core of the sun (hydrogen burning) in the process



2 electron neutrinos are created for each helium nucleus. From this reaction a neutrino flux intensity of

$$\Phi_e = 6.6 \cdot 10^{10} \nu_e / (\text{cm}^2\text{s}) \quad (1.4)$$

[11] reaches the earth from the sun. These neutrinos provide information about the status and processes in the sun's core since they are mostly able to pass through the sun without scattering or interaction (in contrast to photons). A very important insight arose from the comparison of the measured neutrino flux to the one expected from the standard solar model (SSM). The discrepancies become known as the "solar neutrino problem" and could only be resolved satisfactorily with the theory of neutrino oscillations (described in more detail in section 1.3).

1.2.5. Neutrinos from Beta decays

A β -decay is possible in a nucleus when a change of the effective nuclear charge Z by one, while the nucleon number remains unchanged, results in an energetically preferable state. The largest binding energy for an atomic nucleus with the nucleon number A shall be at the proton number Z_0 and the neutron number $N_0 = A - Z_0$. The case of a neutron excess with $N > N_0$ leads to a β^- -decay in which a neutron of the nucleus is converted into a proton, an electron and an electron anti-neutrino (compare figure 1.1):



Conversely the β^+ -decay occurs in case of proton excess ($Z > Z_0$) and converts a proton into a neutron, a positron and an electron neutrino:



Both decays are only possible when allowed by energy conservation, meaning the mass difference Q between mother and daughter nucleus is larger than the rest mass of the two created leptons. The excess energy of the nuclear reaction is mainly distributed among the leptons - the nucleus only takes the recoil momentum. Hence the neutrino not only ensures the lepton number conservation but also enables a continuous energy distribution for the created charged leptons up to a maximum kinetic energy of $E = Q - m_e c^2 - m_\nu c^2$. This kinetic energy distribution has been already measured at the beginning of the 20th century. Without neutrinos the β -decay would be a two-body problem and the decay products would have discrete, fixed energies. Wolfgang Pauli postulated the neutrino

in order to resolve this contradiction, while preserving energy, momentum and angular momentum conservation [6].

The beta decay is an important neutrino source in science. The radioactive isotopes are created either in natural processes like by cosmic radiation or synthetically as in nuclear reactors. Also in the sun, nuclei which are beta-radioactive are produced in some fusion processes. These nuclei contribute to the neutrino radiation from the sun besides the hydrogen burning.

1.3. Neutrino oscillations

1.3.1. The solar neutrino problem

Using the standard solar model (SSM) it is possible to calculate the fusion activity in the sun by its luminosity. From the fusion activity and the fusion reactions the expected neutrino flux arriving at earth can be determined. The Homestake-Experiment has been measuring the solar neutrino flux with the radiochemical chlorine-argon-method since approximately 1970 [12]. Hereby electron neutrinos can be captured by ^{37}Cl nuclei:



The accumulated argon can be separated and the quantitative amount can be determined via the radioactivity of ^{37}Ar . The rate of neutrino events measured in this experiment was significantly smaller than expected in the framework of the SSM (the “solar neutrino problem”). Further radiochemical experiments with ^{71}Ga (GALLEX [13], SAGE [14]) to measure the solar neutrino flux at lower energy thresholds confirmed this deficit.

Neutrinos interactions can excite charged particles within matter to high kinetic energies, e.g. by exchange of a Z^0 boson with a shell electron. Neutrino detectors like Super-Kamiokande or SNO can detect neutrinos via the Cherenkov light of the excited charged particles. At Super-Kamiokande there are 50 kt of ultra-clean water monitored by approximately 12000 photo multipliers [15] and at SNO it is 1 kt of heavy water (D_2O) monitored by 9600 photo multipliers [16] searching for neutrino events. These experiments are able to detect neutrinos in real time and partially resolve the direction from where the neutrinos came. The disadvantage compared to radiochemical experiments is a higher energy threshold for the neutrinos. With the directional reconstruction it was possible to prove that the registered neutrinos actually originate from the sun. These two experiments also confirmed the deficit of electron neutrinos.

At the newer experiments Super-Kamiokande and SNO it is also possible to detect muon and tau neutrinos. These neutrinos can, exactly like ν_e , interact with shell electrons via charged or neutral weak currents. In the first case at Super-Kamiokande a muon is created which produces a Cherenkov light cone that is distinguishable from a light cone produced by an electron (compare figure 1.2). In contrast, at the SNO experiment the interaction of neutrinos with the deuterium nuclei in the heavy water is dominant. The relative rates of the different neutrino flavors can be extracted if all possible reaction processes and their cross sections and detector signatures are considered. By this distinction of different flavors and the directional reconstruction it was possible to show that the expected neutrino flux from the SSM can be confirmed if the measured rates of muon and electron neutrinos are combined. Since ν_μ are not created in fusion processes in the sun they must be produced by some conversion process from the ν_e .

Furthermore, a similar discrepancy could be measured with the atmospheric neutrinos: A disappearance of muon neutrinos if they traversed the earth between creation and detection. Since this effect cannot be explained quantitatively by absorption, also muon

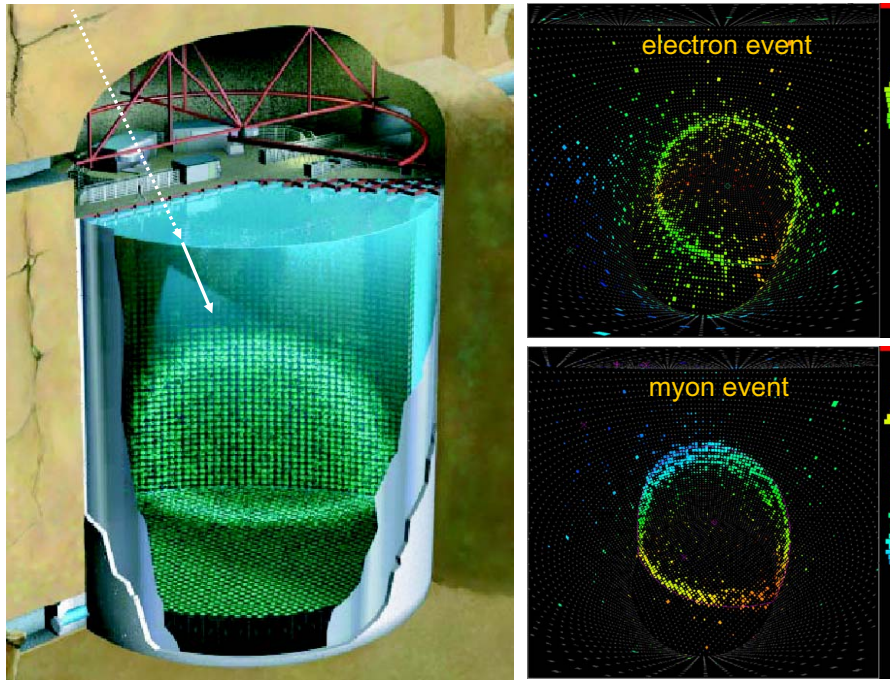


Figure 1.2.: The Super-Kamiokande neutrino observatory - On the left a schema of the neutrino detection principle based on Cherenkov light is shown. On the right side differences of the measured light cones caused by electron events or muon events are visualized. Electron events result in more diffuse rings because of their smaller rest mass and larger scattering probability (from [17])

neutrinos must follow a conversion process on their path. Appearance and disappearance effects of different neutrino flavors could also be reproduced with artificial neutrino sources like nuclear power plants (e.g. the KamLAND experiment [18]) or particle accelerators (e.g. the MINOS experiment [19]). All these effects can be explained by the theory of neutrino oscillations which will be described in the next section.

1.3.2. Neutrino oscillations

Neutrino oscillations describe the effect of periodic changes of the probability that a neutrino can be measured in a certain flavor. Such a time dependent change in the flavor state can be understood on the quantum-mechanical level if the weak eigenstates ν_e, ν_μ, ν_τ differ from the mass eigenstates ν_1, ν_2, ν_3 of the neutrinos. The time dependence is linked to the rest mass via the time evolution operator of quantum mechanics which depends on the energy and therefore on the rest mass of the propagating particle.

Analogous to the CKM matrix¹ which describes the mixing of weak and mass eigenstates of quarks, the mixing of weak and mass eigenstates of neutrinos can be described by the Maki-Nakagawa-Sakata matrix (MNS matrix). The MNS matrix is a unitary 3×3 matrix defined as follows [20]:

$$\begin{pmatrix} \nu_e \\ \nu_\mu \\ \nu_\tau \end{pmatrix} = \begin{pmatrix} U_{e1} & U_{e2} & U_{e3} \\ U_{\mu1} & U_{\mu2} & U_{\mu3} \\ U_{\tau1} & U_{\tau2} & U_{\tau3} \end{pmatrix} \begin{pmatrix} \nu_1 \\ \nu_2 \\ \nu_3 \end{pmatrix} \quad (1.8)$$

By utilizing the unitarity of the matrix it is possible to write the matrix in a physically

¹Cabibbo-Kobayashi-Maskawa matrix

meaningful, reduced representation with only 6 free parameters. In the factorized mode it is given by:

$$U = \begin{pmatrix} 1 & 0 & 0 \\ 0 & \cos \theta_{23} & \sin \theta_{23} \\ 0 & -\sin \theta_{23} & \cos \theta_{23} \end{pmatrix} \times \begin{pmatrix} \cos \theta_{13} & 0 & \sin \theta_{13} e^{i\delta} \\ 0 & 1 & 0 \\ -\sin \theta_{13} e^{-i\delta} & 0 & \cos \theta_{13} \end{pmatrix} \\ \times \begin{pmatrix} \cos \theta_{12} & -\sin \theta_{12} & 0 \\ \sin \theta_{12} & \cos \theta_{12} & 0 \\ 0 & 0 & 1 \end{pmatrix} \times \begin{pmatrix} 1 & 0 & 0 \\ 0 & e^{-i\phi_2/2} & 0 \\ 0 & 0 & e^{-i\phi_3/2} \end{pmatrix}$$

The neutrino mixing is defined by the 3 mixing angles θ_{12} , θ_{23} and θ_{13} equivalently to the CKM matrix. A potential CP violation can be given by the phase δ which equals zero if CP symmetry is conserved. In the case neutrinos are Majorana particles (compare section 1.4.1) this property can be defined via the phases ϕ_2 and ϕ_3 .

Due to the fact that all known neutrino generating processes proceed via the weak interaction all created neutrinos start in a weak eigenstate. This corresponds to a mixture of mass eigenstates which propagate independently on their way to a detector. At the detector the neutrino interacts weakly again - so the wave function collapses. The transition probability for a neutrino which is created with the flavor α and interacts at the detector as a flavor β neutrino can be approximated (using the assumption that the kinetic energy is much higher than the energy corresponding to the rest mass) to:

$$P_{\nu_\alpha \rightarrow \nu_\beta}(l, t) = \left| \sum_k U_{\alpha k}^* e^{ip_k l - iE_k t} U_{\beta k} \right|^2 \quad (1.9)$$

Here, p_k is the momentum and E_k the energy of the corresponding mass eigenstates, l is the path length and t the time between neutrino production and detection. Continuing the calculation leads to the result that the oscillation probabilities in fact only depend on the mass square differences $\Delta m_{kj}^2 = m_k^2 - m_j^2$ and not on the absolute masses.

With the simplifying assumption of a two state system (only ν_1 , ν_2 and ν_e , ν_μ) with $\theta = \theta_{12}$ and $\Delta m^2 = m_{\nu_1}^2 - m_{\nu_2}^2$ the transition probability can be given explicitly as

$$P_{\nu_\alpha \rightarrow \nu_\beta} = \sin^2(2\Theta) \sin^2 \left(\frac{\Delta m^2 l}{4E} \right) \quad (1.10)$$

with the neutrino energy E and the path length l . Figure 1.3 visualizes how the probabilities for the two flavor eigenstates depend on the path length l in oscillation lengths $L = 4\pi E/\Delta m^2$ and the mixture angle Θ .

Below the combined results from different experiments, which measured neutrino oscillation parameters, are given. Thereby the CP violating phases are unknown yet and the mass differences are redundant: $\Delta m_{13}^2 = \Delta m_{12}^2 - \Delta m_{23}^2$.

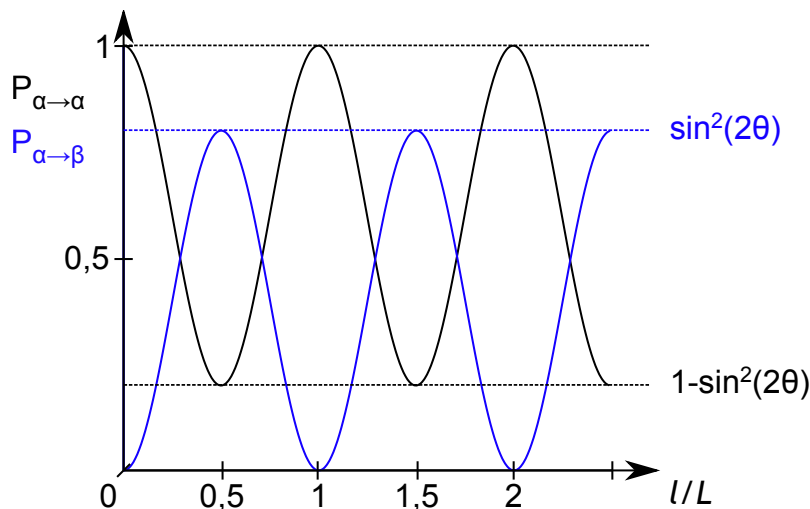


Figure 1.3.: Schema for a two-state neutrino oscillation - This example shows the transition probabilities for a two-flavor system in dependence of the traveled distance. Extrema of the mixed states are defined by the mixing angle Θ .

$$\begin{aligned}
 \sin^2(2\theta_{12}) &= 0.846 \pm 0.021 \quad [20] \\
 \sin^2(2\theta_{13}) &= 0.106 \pm 0.030 \pm 0.025 \quad [21] \\
 \sin^2(2\theta_{23}) &> 0.999 + 0.001 - 0.018 \quad \text{normal mass hierarchy}^2 \quad [20] \\
 \sin^2(2\theta_{23}) &> 1.000 + 0.000 - 0.017 \quad \text{inverted mass hierarchy} \quad [20] \\
 \Delta m_{21}^2 &= (7.53 \pm 0.18) \cdot 10^{-5} \text{ eV}^2/c^4 \quad [20] \\
 |\Delta m_{32}^2| &= (2.44 \pm 0.06) \cdot 10^{-3} \text{ eV}^2/c^4 \quad \text{normal mass hierarchy} \quad [20] \\
 |\Delta m_{32}^2| &= (2.52 \pm 0.07) \cdot 10^{-3} \text{ eV}^2/c^4 \quad \text{inverted mass hierarchy} \quad [20]
 \end{aligned}$$

One of the most important implications of the evidence of neutrino oscillations is that at least two of the three neutrino mass eigenstates must differ from zero and, with consideration to the mixing, also the masses attributed to the flavor states ν_e , ν_μ , ν_τ must be non vanishing. This insight is, just as the non-conservation of the neutrino flavor, not yet part of the standard model of particle physics because to assign masses to neutrinos mechanisms beyond the standard model are required (for example mechanisms as described in [22], [23], [24] or [25]). Since neutrino oscillations naturally only allow the measurement of differences of squared masses, the determination of the absolute neutrino mass scale requires a different method. These methods will be presented in the next section.

1.4. Methods to measure the neutrino mass

1.4.1. Neutrinoless double beta decay

With consecutive beta decay nuclei change the atomic number Z while keeping the nuclear number A constant until the maximum binding energy, or the minimum nuclear mass, is reached. The semi-empirical Bethe-Weizsäcker formula which describes the binding energy in dependence of A and Z also includes a pairing term. This term incorporates the energetic advantage if the amount of protons and neutrons are both even. For nuclei with an odd atomic number the pairing term vanishes and the nuclei has the characteristic mass parabola centered around the optimal nuclear number Z_0 . The other nuclei alternate

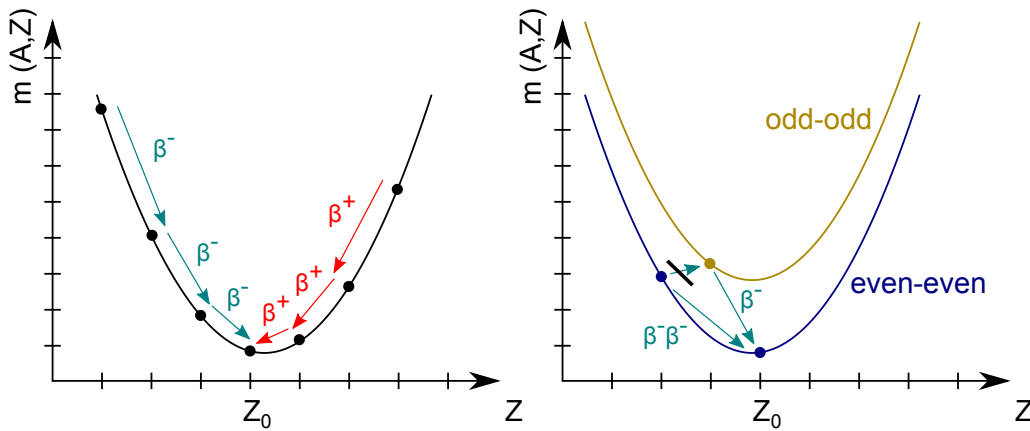
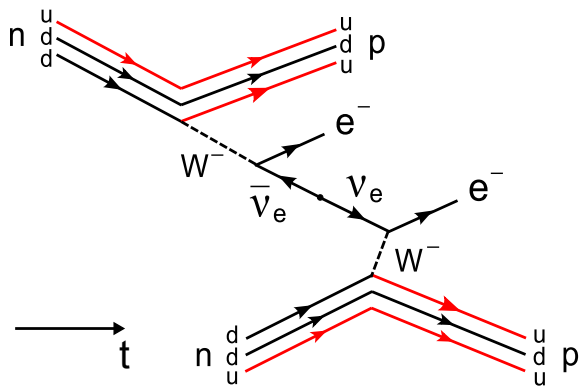


Figure 1.4.: Mass parabola of isobar nuclei - The symmetry contribution to the Bethe-Weizsäcker formula can lead to metastable states. These nuclei can only reach a more stable state by a double beta decay.

Figure 1.5: Feynman diagram of the neutrinoless double-beta decay - In this process the emitted electron anti-neutrino transforms into an electron neutrino and induces a further (neutrinoless) beta decay.



with each beta decay between even and odd nuclei numbers. The difference between the energetically preferable even nuclei and the less stable odd nuclei can be represented with two shifted mass parabolas. By this effect metastable states with $Z \neq Z_0$ are possible if a beta decay from an even nucleus to an odd nucleus is forbidden by energy conservation (compare figure 1.4). For some isotopes in this metastable state the double beta decay $2n \rightarrow 2p + 2e^- + 2\bar{\nu}_e$ can still occur but is suppressed as process of higher order. The energy distribution of the produced electrons is, just as for the single beta decay forms, a continuous spectrum up to the end point energy E_0 . The end point energy is close to the maximum energy available to the process by the mass difference between the mother and daughter nucleus.

There is a further theoretical decay process from this meta stable state which is called the “neutrinoless double beta decay” (compare Feynman diagram 1.5). This process requires neutrinos to be Majorana particles, which means that a neutrino and the anti-neutrino of one flavor are, except for their spin, the same particle. Furthermore, the $0\nu\beta\beta$ decay requires the inversion of the helicity³. An inversion of helicity is possible for non-vanishing neutrino masses since the neutrino velocity v_ν is then always smaller than the speed of light c . By a Lorentz transformation in an inertial system with a speed of $v_{IS} > v_\nu$ the momentum vector of the neutrino is reversed. At the same time the spin vector remains conserved, hence the sign of the helicity changes. This relativistic approach is a simplified explanation for a suppression of the neutrinoless double beta decay by a factor of $(1 - v_\nu/c)$. By this factor the decay rate becomes dependent on the kinetic energy and the rest mass of the neutrinos.

³Helicity is the projection of the particle spin on its momentum: $H = \vec{S} \cdot \vec{p}/|\vec{p}|$

In the decay process an emitted electron anti neutrino $\bar{\nu}_e$ is captured as electron neutrino ν_e by another neutron of the same nucleus. Consequently, only two electrons are emitted from the nucleus which are mono-energetic, each with the reaction energy Q , due to the reduction in degrees of freedom.

$$2n \rightarrow 2p + 2e^- \quad (1.11)$$

From the measured rate of $0\nu\beta\beta$ events it is possible to derive the effective Majorana neutrino mass $\langle m_{0\nu\beta\beta} \rangle = |\sum_i U_{ei}^2 m_i|$ [26]. Due to the CP-violating and the Majorana phases it is possible that the Majorana mass differs from the absolute electron neutrino mass. The expected rate $R_{0\nu\beta\beta}$ also depends on the phase space factor $F^{0\nu}$ and the transition matrix element $M^{0\nu}$ and is described by:

$$R_{0\nu\beta\beta} = F^{0\nu} |M^{0\nu}| \left(\frac{\langle m_{\beta\beta} \rangle}{m_e} \right)^2 \quad (1.12)$$

The main difficulty of this method is the prerequisite that neutrinos are Majorana particles, which up to now is an open question. Furthermore, the effective Majorana mass can be significantly smaller than the corresponding mass eigenstates since terms that add up to $|m_{0\nu\beta\beta}|$ can also be negative due to the Majorana phases. The very low signal event rates are overlaid by background from muons, neutrons and ambient radioactivity. For the measurements appropriate isotopes, which undergo double beta decay, are selected and most commonly used as decay source and detector (scintillation-, bolometer- or semiconductor-based detection) at the same time. Recent experiments searching for the neutrinoless double beta-decay ([27, 28, 29, 30]) have set lower limits for the decay half time but did not find significant evidence for the decay. This leads to an upper limit on the Majorana electron neutrino mass $m_{0\nu\beta\beta}$ in the range of $0.2 \text{ eV}/c^2$ to $0.4 \text{ eV}/c^2$ [27].

1.4.2. Cosmological methods

The determination of the neutrino mass by cosmological methods is done by the fit of theoretical cosmological models to experimental data. Relic neutrinos act as hot dark matter (HDM) and its mass density has an impact on the structure formation in the early universe. In this method there is no distinction between the different neutrino flavors, consequently only information about the sum of the neutrino masses can be gathered. The massive and free-streaming neutrinos can smear out developing fine structures during the formation of galaxy clusters. Data to evaluate the development of large scale structures is provided by the following observations:

- **Cosmic microwave background (CMB)** Fluctuations in the energy density distribution of the early universe can be calculated from the anisotropy data of the CMB provided by precise measurements of the satellites COBE [31], WMAP [32, 32] and PLANCK [33]. Due to the expansion of the universe these density fluctuations deliver the structure information on the largest length scales ($> 100 \text{ Mpc}$). Furthermore, the density of relic neutrinos can be calculated from the measured density of CMB photons. The number density of relic neutrinos is an essential parameter for the neutrino mass density in the total energy density Ω of the universe.
- **Large scale structures (LSS)** With the redshift measurement of far distant galaxies or other bright cosmic objects (e.g. quasars) by surveys like SDSS and 2dFGRS one can gain structure information on length scales from few Mpc up to 100 Mpc.
- **Lyman-alpha forest (Ly- α)** The Lyman-alpha forest is a result of multiple absorption of the Lyman-alpha-line by hydrogen “clouds” between the light emitting object and the detection on earth. The absorption line at $f_{\text{Ly}-\alpha} = 2.47 \cdot 10^{15} \text{ Hz}$

[34] becomes red-shifted multiple times depending on the distance of the absorbing object. By these measurements it is possible to investigate the density distribution on length scales from 0.1 to 1 Mpc but with higher uncertainties compared to the other methods.

The sum of neutrino masses can be estimated by a fit of the cosmological Λ CDM-model parameters to available experimental data. The sum over the masses of all neutrino flavors is only one of many fit parameters in the calculation. By combining multiple data sources, gathered with the methods described above, very stringent upper limits for the neutrino masses have been determined: $\sum m_\nu < 0.17$ eV (95% C.L.) [35] or $\sum m_\nu < 0.4$ eV (99% C.L.) [36].

The drawback of this method are that multiple, strongly correlated fit parameters have to be adjusted at the same time. Consequently, the trueness and completeness of the results heavily depend on the validity of the cosmological model. So far the results deliver no lower limit for $\sum m_\nu$ so there is no indication for a non-vanishing neutrino mass yet. A model independent determination of the neutrino mass scale would be of high importance for the development of cosmological models since the structure formation in the universe is very sensitive to the absolute neutrino mass. Therefore, it is ultimately necessary to determine the neutrino mass with a method which requires fewer assumptions on physical models. Independent measurements will help to validate or falsify cosmological models.

1.4.3. Kinematic methods

In comparison to the previously described methods, kinematic methods provide the possibility to measure the neutrino mass in a model independent way, only relying on the relativistic energy and momentum conservation. The method is based on a very precise energy measurement of a specific decay. Concerning the mass of the electron neutrino, stringent limits are known from precise spectral measurements of radioactive β -decays. The experimental challenge is to measure the very small impact of the electron neutrino rest mass on the energy balance of the particles in the process. This impact is only significant if the kinetic energy of the neutrino is not significantly larger than its rest energy. Since a direct spectroscopic measurement of a neutrino itself is not possible, the energy spectrum of the electrons close to the electron energy endpoint E_0 has to be measured with high precision. From Fermi's golden rule it is possible to derive the momentum spectrum of the electrons to

$$N(p_e)dp_e = \frac{2\pi}{\hbar} \cdot |M_{fi}|^2 \cdot \frac{dn_e \cdot dn_\nu}{dE} \quad (1.13)$$

with the transition matrix element M_{fi} , which only weakly depends on the energy and the density of states $dn_e dn_\nu / dE$ in the phase space interval which causes the energy dependence of the spectrum [3]. After the calculation of phase space density and transition matrix element one obtains the theoretical energy spectrum

$$\frac{dN_e}{dE}(E) = C \cdot F(Z, E) \cdot p \cdot (E + m_e c^2) \cdot (E_0 - E) \cdot \sqrt{(E_0 - E)^2 - m(\nu_e)^2 c^4} \quad (1.14)$$

with the kinetic electron energy E which is limited to the range $(0, E_0 - m(\nu_e)c^2)$ [3]. The function further depends on the electron momentum p , the endpoint energy E_0 and the electron mass m_e . The observable of the experiment is the mass square of the electron neutrino $m(\nu_e)^2 = \sum_i |U_{ei}|^2 \cdot m_i^2$ instead of the electron neutrino mass itself. The Fermi function $F(Z, E)$ accounts for the Coulomb interaction between the daughter nucleus and the outgoing β -electron. Since the decay is a process of the weak interaction the constant C depends on the Cabibbo-angle Θ_C , the Fermi coupling constant G_f and the nuclear matrix element M and is given by

$$C = \frac{G_F^2 \cos^2 \theta_C}{2\pi^3 \hbar^7 c^5} |M|^2 \quad (1.15)$$

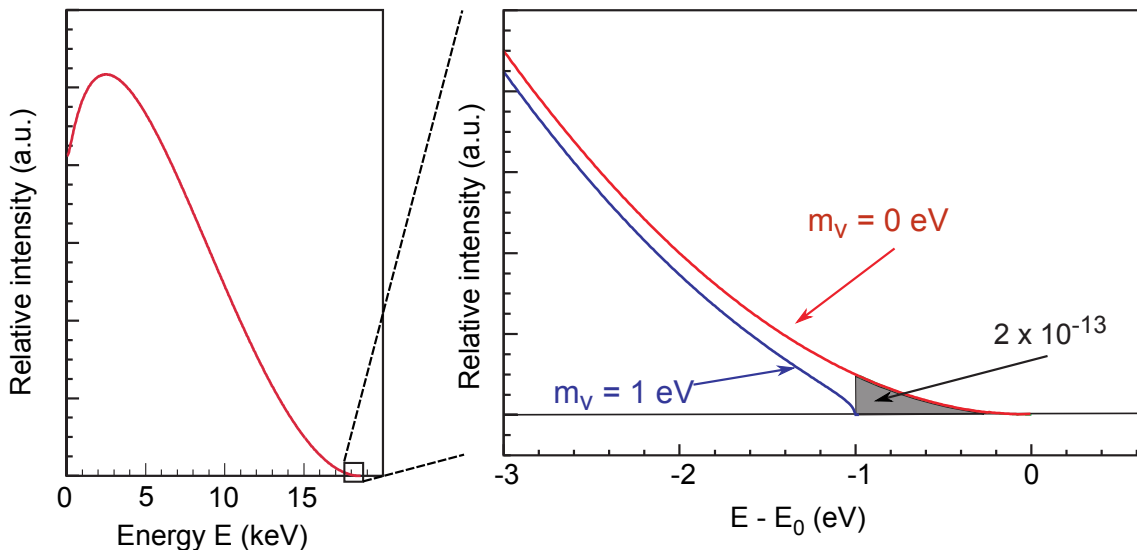


Figure 1.6.: Energy spectrum of the tritium beta decay electrons - On the left side is the relative intensity distribution in dependence of the β -electron energy. On the right side is a close-up view of the end point region for two exemplary neutrino masses: $m_{\nu_e} = 0 \text{ eV}/c^2$ and $m_{\nu_e} = 1 \text{ eV}/c^2$ (adapted from [3]).

As mentioned above only events with electrons close to the endpoint energy E_0 are useful for the measurement of the neutrino mass. But the rate of such events is proportional to $1/E_0^3$, therefore the usage of a radioactive isotope with low endpoint energy is favorable.

One concept are calorimetric measurements in which the complete energy of the decays (except for the neutrinos) are measured as thermal signal. In this case the radioactive source is also the detector and it is running at cryogenic temperatures. This has been carried out with a radioactive isotope of rhenium, ^{187}Re , which has the lowest known endpoint energy of all β -decaying isotopes with $E_0 = 2.47 \text{ keV}$. On the other hand, the overall decay rate is extremely small due to the half life of $O(10^{10} \text{ a})$. Previous experiments based on calorimeters with an energy resolution of $\Delta E = 20 - 30 \text{ eV}$ resulted in an upper limit of $m(\nu_e) < 15 \text{ eV}$ for the electron neutrino mass [37].

The yet most stringent upper limits for the electron neutrino mass by kinematic methods have been found by measurements of the tritium β -spectrum with electrostatic spectrometers. The endpoint energy of tritium is the second lowest of all known β -decaying isotopes with about 18.6 keV [3]. The electrons which are isotropically emitted by the decay



must be collimated and guided adiabatically by magnetic fields to the spectrometer. All previous, possible energy gains or losses have to be considered. Among these are:

- Doppler effect
- Inelastic scattering with gas molecules
- Electrostatic potentials
- Synchrotron radiation of the electrons
- Excited states at the tritium molecules in case of a gaseous source or
- Solid state excitations (e.g. phonons) in case of a non-gaseous source

All these energy changes before the electrons are analyzed by the spectrometer contribute to statistical or systematic errors of the neutrino mass. An advantage of tritium is that

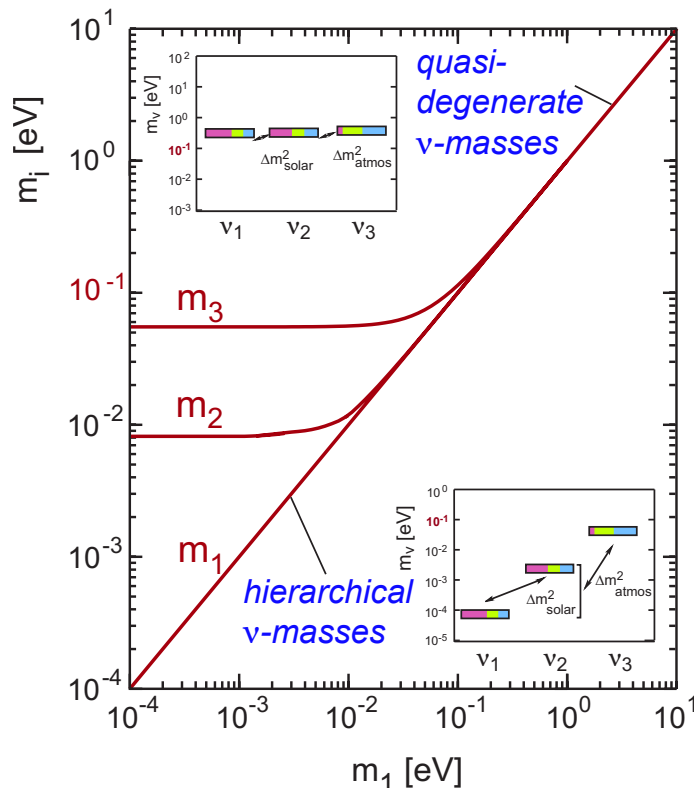


Figure 1.7.: Mass hierarchies of neutrino mass states - The diagram shows the distribution of neutrino mass eigenvalues in dependency of m_1 : If m_1 is large the mass differences are negligible and the mass eigenvalues are quasi-degenerate. If m_1 is relatively small the eigenvalues are hierarchical in an order which is not completely known yet (from [3]).

the β -decay is super-allowed, therefore the nuclear matrix element is energy independent and large with $|M|^2 = 5.55$. Because of the low atomic number and only one shell electron it is possible to calculate the molecular final states and the Coulomb interaction between nucleus and emitted electron comparably straightforward. With a half life of $T_{1/2} = 12.3$ a tritium permits designing a source which is long term stable and has a high activity as well. This high source activity is essential for the measurement, as the fraction of events close to the endpoint energy is very small (compare figure 1.6).

Once the electrons are emitted and guided it is the task of the spectrometer to measure their kinetic energy with high precision. This is complicated by the isotropic emission of the β -electrons. The KATRIN experiment uses an electrostatic retardation filter with magnetic adiabatic collimation (“MAC-E-Filter”) which is explained in detail in section 2.1.3. The required retardation voltage of approximately 18.6 keV is technically feasible. With this measurement principle, which was described above in a generalized way, the most accurate upper limit for the neutrino mass of $m(\nu_e) < 2$ eV [20] has been found by experiments in Mainz and Troitsk.

1.5. Impact of the neutrino mass

A model independent measurement of the absolute neutrino mass is of great importance both for elementary particle physics and for the development & evaluation of cosmological models. Especially when considering the fact that neutrinos are handled as being massless in the standard model but a non vanishing mass is required to explain the neutrino oscillations.

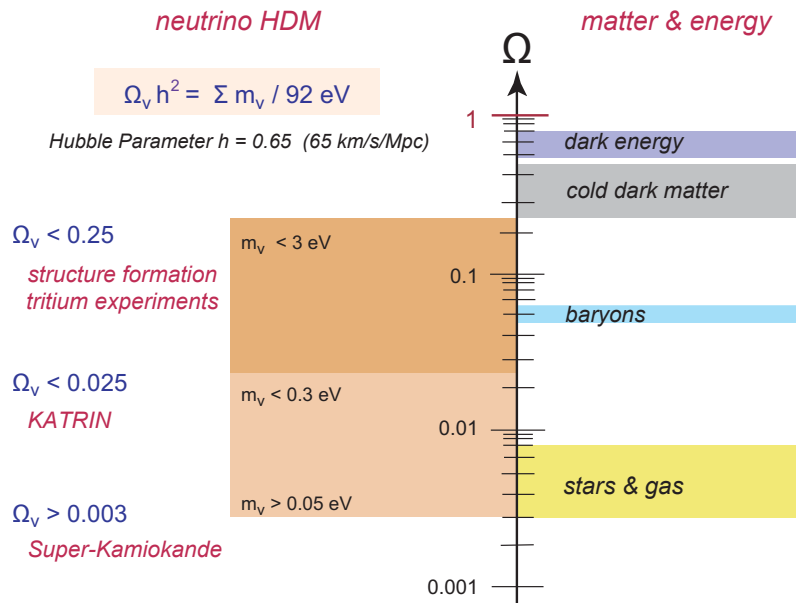


Figure 1.8.: Contributions to the energy density of the universe - The importance of the mass contribution by neutrinos is dependent on the unknown neutrino rest mass. With the known neutrino density and the experimentally determined lower and upper limits it is possible to estimate the total contribution to the energy density (from [38]).

The differences of squared neutrino masses, extracted from neutrino oscillation measurements, provide no information about the absolute neutrino masses and the mass hierarchy. Depending on the scale of the absolute masses the mass differences can truly be a hierarchal mass distribution (e.g., $m_3 > m_2 > m_1$) or a pseudo-degenerate mass ($m_3 \approx m_2 \approx m_1$) distribution.

The masses of the elementary particle in the standard model are described with their coupling to the Higgs field. To explain the very small neutrino masses would require the coupling to the Higgs field to be at least 6 orders of magnitude smaller than for the other elementary particles [22]. This can not be explained in the scope of the Standard Model, hence new theoretical mechanisms have been developed for neutrinos to acquire their rest mass. Among these mechanisms there is the Seesaw I mechanism which requires a heavy right-handed Majorana neutrino or the Seesaw II mechanism in which the neutrinos directly couple to a Higgs triplet.

For the verifiability of these or other models it is important whether the neutrino masses are hierarchal or pseudo degenerate. If the KATRIN experiment successfully determines a value for the electron anti-neutrino mass the neutrino mass scale is degenerate. Furthermore, with a defined value for $m(\nu_e)$ it might be possible to determine further parameters of the neutrino masses, like the CP violating phase or the Majorana phases.

As described in section 1.4.2 it is possible to use observations and measurements of cosmology in combination with cosmological models to infer limits on the neutrino mass. But the necessary calculation of the Λ CDM model require to fit multiple parameters at once. This means a reliable value for the absolute neutrino mass scale would enable a better fit with higher accuracy for the other parameters. If an independent experiment were to measure a neutrino mass with a direct method which can not be reconciled with the cosmological models in a consistent way, new cosmological models would have to be developed. For instance there are possibilities for good fits with the existing data and a non-vanishing neutrino mass under the assumption of a coupling between dark energy and dark matter [39].

2. The KATRIN experiment and the Rearsection

The Karlsruhe TRItium Neutrino experiment (KATRIN experiment) aims for the measurement of the electron anti-neutrino mass by the kinematic investigation of the tritium β -decay. The experiment with a length of approximately 70 m is currently under construction at the KIT¹ campus north. Locating the experiment at KIT allows using expertise and infrastructure of to the Tritium Laboratory Karlsruhe (TLK) which is licensed store and handle tritium amounts up to 40 g. The discovery potential of the experiment depends on the neutrino mass itself: For example, for a mass $m(\nu_e) = 0.4 \text{ eV}/c^2$ a significance of 6.5σ is expected [3]. In case no signal of a non-vanishing neutrino mass is found it is still possible to derive an upper limit of $200 \text{ meV}/c^2$ (90 % C.L.) for the mass of the electron anti-neutrino. In comparison to the experiments in Mainz or Troitsk the sensitivity is improved by a factor of 10 which requires an overall improvement in accuracy by a factor of 100 on the measurement variable $m(\nu_e)^2$.

The windowless gaseous tritium source (WGTS) is supplied with a source gas mixture with a tritium purity of $\epsilon_T \approx 95\%$. The β -electrons emitted in the source are guided by fields from superconducting magnets in a cyclotron motion to the spectrometer. On this way turbomolecular pumps in the WGTS and in the differential pumping section DPS remove the largest part of the gas. The pumped gas then is processed by the tritium inner loop system and after processing and purification it is again injected into the source. The cryogenic pumping section (CPS) further reduces the remaining tritium density on the way to the spectrometer. The β -electrons are analyzed in the pre- and main spectrometer where an electrostatic potential allows only those electrons to pass which have a sufficiently high kinetic energy. Electrons that are able to pass the spectrometers hit the main detector which registers and counts the incoming electrons. On the back side of the source the Rearsection is connected - an instrument which provides multiple control and monitoring features for the source section.

The transport of the electrons through all components takes place by virtue of magnetic fields which are mainly produced by superconducting magnets. The magnetic flux tube is given by

$$\Phi = \int B \cdot dA \quad (2.1)$$

¹Karlsruhe Institute of Technology

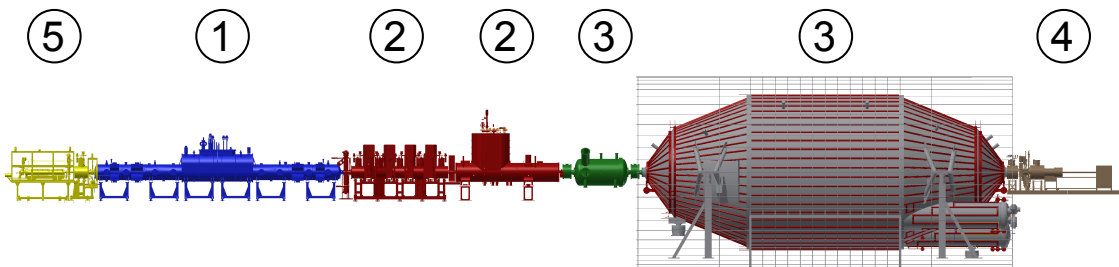


Figure 2.1.: Beamline setup of the KATRIN experiment with the windowless gaseous tritium source WGTS (1), the pumping sections DPS2 and CPS (2), the pre- and main spectrometer (3), the main detector (4) and the Rearsection (5).

and is conserved throughout the whole experiment. Therefore, it is simple to calculate the area of the electron flux tube A at any given magnetic flux density B . In the WGTS the largest provided flux tube is $\Phi_{\text{tot}} = 229 \text{ Tcm}^2$ while only the “inner” flux tube with $\Phi = 191 \text{ Tcm}^2$ is actually transported, analyzed and finally imaged onto the detector.

To transport the electrons over the distance of the KATRIN experiment a very good vacuum is required. In the whole experiment high vacuum (HV) with pressures $p < 10^{-6}$ mbar will be achieved except for the tritium source itself and the source facing sides of the Rearsection and the DPS [40]. At the spectrometers the experiment design targets for extreme high vacuum (XHV) with pressures of $p < 10^{-11}$ mbar by the combination of different highly efficient pumping techniques [40]. In the following section the source and transport (STS) components, the spectrometers and the main detector section will be described in more detail. Further information to the experiment is available in the KATRIN design report [3].

2.1. Components of KATRIN

2.1.1. Tritium source

The β -decay electrons are mainly emitted within the windowless gaseous tritium source (WGTS). The tritium is injected at the center of the 10 m long pipe which has an inner diameter of 90 mm. There is no possibility to insert a window or any gas barrier at the end of the source since it would lead to an unacceptably high electron absorption or energy loss. Due to this lack of any physical barrier between source and spectrometer, the tritium molecules must be removed by pumps. Otherwise, they can stream into the electrostatic spectrometers, decay there and produce background at the main detector. Therefore, the gas amount injected in the center of the source is reduced at both ends of the WGTS by the differential pumping sections DPS1-F (front) and DPS1-R (rear). In the direction of the spectrometers the tritium partial pressure is further reduced by the pumping sections DPS2-F and CPS (compare section 2.1.2). The source is supplied with a constant inlet pressure p_{in} and evacuated at a stable pumping speed. This should result in an equilibrium with a gas density distribution which is nearly uniform over the cross-section of the WGTS pipe but drops rapidly from the mid to the ends of the source. For the description of the source strength it is useful to introduce the column density $\rho d = N/A$ which equals the number of gas molecules per cross-section area.

The temperature stabilization of the WGTS is realized using a two-phase mixture of liquid and gaseous neon. Depending on the pressure of this two-phase mixture the source temperature can be set between 27 and 30 Kelvin for tritium operation. At a temperature of 27 K and a gas inlet pressure of $p_{\text{in}} = 3.4 \cdot 10^{-5}$ mbar the column density equilibrates at the reference value of $\rho d = 5 \cdot 10^{17} \text{ cm}^{-2}$. Any further increase of the column density

would still increase the source activity but this advantage is mainly compensated by the scattering probability which increases as well. The impact of the column density on the overall experiment is discussed in detail in section 2.2.

The magnetic flux density inside the WGTS solenoids peaks at 3.6 T which results in a total flux tube of $\Phi_{\text{total}} = 229 \text{ Tcm}^2$ under consideration of the source tube diameter of 90 mm. For data analysis only the inner flux tube of $\Phi = 191 \text{ Tcm}^2$ is used - this corresponds to an area of $A_S = 53 \text{ cm}^2$ at the magnetic flux density of 3.6 T. With a tritium purity of $\epsilon_T = 95 \%$ the total number of tritium molecules is given as

$$N(\text{T}_2) = \epsilon_T \cdot \rho d \cdot A_S \quad (2.2)$$

Since each tritium molecule contains two tritium atoms with a half life of $t_{1/2}({}^3\text{H}) = 12.3$ years, this set-up results in a source activity of approximately 10^{11} decays per second. Unconsidered or undetected variations of the scattering probability and the source intensity result in systematic errors and slightly change the statistic errors. Due to this effect the column density, the source activity and the tritium isotope purity are measured and monitored with various methods (compare section 2.2).

2.1.2. Transport and pumping sections

The tritium flow is further reduced by the second differential pumping section DPS2 and the cryogenic pumping section CPS. The combined pumping power of the TMPs in DPS1-F and DPS2 achieve a reduction by a factor of 10^7 . The CPS reduces the tritium flow by further 7 orders of magnitude. So starting with a gas inlet rate of the order of $1 \text{ mbar} \cdot \text{l/s}$ the tritium flow is reduced to the order of $10^{-14} \text{ mbar} \cdot \text{l/s}$ at the spectrometers. By this the rate of tritium related background is cut down to below 1 mHz. Each of the two dedicated pumping sections contain 4 bents of the flux tube in order to prevent neutral gas molecules reaching the spectrometer section on a direct path.

The DPS2 uses 4 high performance turbomolecular pumps with an overall pumping speed of more than 2000 l/s for H_2 . The superconducting magnets of this section create magnetic fields up to a strength of 5.6 T which leads to a minimal flux tube diameter of 7 cm. The DPS2 is also the component to remove another possible background: Positively charged ions can be produced in the whole source and transport section by decay or ionization. As charged particles they are guided by the magnetic fields and as positively charged particles they are even accelerated in the spectrometers and can lead to background by interaction with rest gas molecules. To prevent this the ions are kept back in the DPS2 by a small electrostatic barrier and removed by electrostatic dipole fields using the $\vec{E} \times \vec{B}$ drift. Furthermore, the ions composition is monitored by Fourier transformation of the spectrum created in an ion cyclotron resonance trap.

In the cryogenic pumping section the gas molecules are not mechanically pumped but bound by adsorption. The most inner wall of the CPS is cooled with liquid helium down to 4.5 K - this leads to a high sticking probability for impinging gas molecules. The efficiency of this sorption pump is further increased by argon snow which is frozen to the wall surfaces. Every 60 days after the end of a typical KATRIN run the cryosorption pump is regenerated by removal of adsorbed gas, flushing, bake-out and the application of a new layer of argon frost. Additionally, the CPS can be instrumented with radioactive calibration sources. At a maintenance port on the spectrometer-side of the CPS a steerable detector shall be attached. This detector scans the flux tube for variations in activity and monitors the long term activity of the source.

2.1.3. Energy filtering spectrometers

The purpose of the spectrometer is to measure the kinetic energy of the electrons with high resolution. Due to the isotropic emission of the β -electrons in the source the electron angle θ towards the z-axis/beam axis is uniformly distributed from 0° to 90° . The overwhelming majority of electrons therefore possesses a non-vanishing transversal momentum. The corresponding transversal energy E_T can not be measured by an electrostatic potential as long the particles move in a cyclotron motion. In order to measure electrons with an arbitrary angle θ the KATRIN experiment uses a spectrometer with magnetic adiabatic collimation and a superimposed electrostatic retardation potential (MAC-E-Filter).

To understand the working principle of a MAC-E-Filter it is illustrative to consider the impact of changes in the magnetic field strength on the β -electrons which follow the magnetic field lines on a cyclotron motion. If the change in the magnetic field during one cyclotron turn is sufficiently small the angular momentum of the cyclotron motion is conserved. As a consequence the magnetic moment, the quotient of transversal kinetic energy and magnetic flux density is conserved as well:

$$\mu = \frac{E_T}{B} = \text{const.} \quad (2.3)$$

This conservation of the magnetic momentum is an indicator of the adiabaticity of the electron motion. The details of the conservation of electron parameters in electromagnetic fields and how it is possible to quantify and verify the adiabaticity of the electron motion is described in section 4.2.1. For the understanding of the MAC-E-Filter working principle it is important to recognize that the combined conservation of energy and magnetic moment results in a transformation of transversal to longitudinal energy when the magnetic field is reduced along the electron path. At the KATRIN spectrometer the smallest magnetic field is reached in the so called analyzing plane which is situated approximately at the center plane of the MAC-E-Filter. Since the magnetic field is not exactly zero the transformation of transversal into longitudinal energy is not complete and a small amount of transversal energy remains. The energy analysis is ensured by an electrostatic field which is superpositioned to the magnetic field. At a given high voltage U applied to the spectrometer all electrons with a longitudinal energy of $E_L > eU$ are able to pass the spectrometer. As a consequence, a MAC-E-Filter always measures an integrated spectrum. After passing the analyzing plane, the electrons are accelerated again by the same potential U . Furthermore, with the rising magnetic field the reverse transformation from longitudinal to transversal energy occurs and the original angular and energy distribution is restored. The energy resolution of a MAC-E-Filter ΔE is given by the minimal magnetic field strength in the spectrometer B_{\min} , the maximal magnetic field outside of the spectrometer B_{\max} and the electron energy E by the following relation:

$$\frac{\Delta E}{E} = \frac{B_{\min}}{B_{\max}} \quad (2.4)$$

Besides the source with $B_S = 3.6$ T and the analyzing plane with $B_A = 0.3$ mT the magnetic field reaches a maximum strength of $B_{\max} = 6$ T at the pinch magnet. From this the energy resolution of the main spectrometer for 18.6 keV electrons can be calculated to

$$\Delta E = 0.93 \text{ eV} \quad (2.5)$$

During the transition of magnetic fields from B_S to B_{\max} a part of the longitudinal kinetic energy is transformed to transversal energy - similar to the downstream of the MAC-E-Filter. If the starting angle of the electron is too large, it is possible that the direction

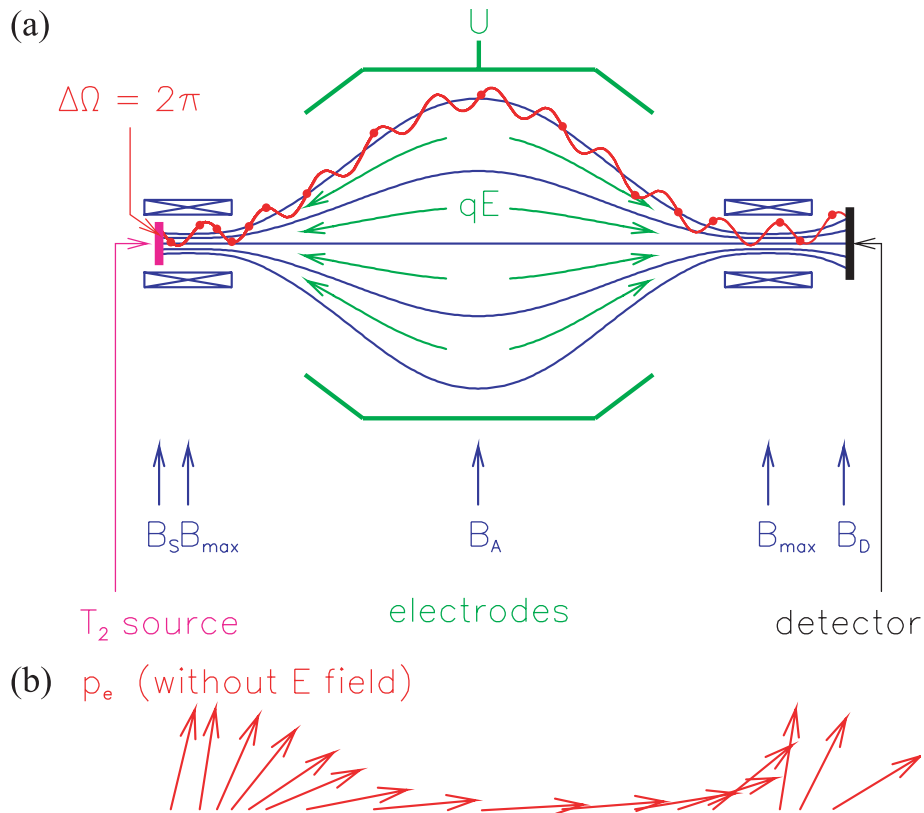


Figure 2.2.: Operating principle of a MAC-E-Filter - (a) The schematic indicates the path of the electric and magnetic field lines. The electrons follow the magnetic field lines in a cyclotron motion (the change in the cyclotron radius by the magnetic field strength is not indicated). (b) The arrows visualize the adiabatic transformation of an initial transversal momentum into a longitudinal momentum (no retardation potential is used in this example). From [3].

of the longitudinal momentum is reversed: The electron undergoes the effect of magnetic reflection. The maximum angle Θ_{\max} electrons can have without being reflected is given by [3]

$$\Theta_{\max} = \arcsin \left(\sqrt{\frac{B_S}{B_{\max}}} \right) = 51^\circ \quad (2.6)$$

This angular limitation reduces the overall electron rate being measured by KATRIN and therefore downgrades the statistics. But on the other hand electrons with a larger angle $\Theta > \Theta_{\max}$ have a longer absolute path to reach the spectrometer. This significantly increases the probability of scattering processes with gas molecules. Hence, the reduction of the electron flux density by the acceptance angle Θ_{\max} has advantages.

Within the KATRIN beamline set-up two MAC-E-Filters are used: The pre-spectrometer and the main spectrometer. Both of them have inner wire electrode built in. These are set to a slightly more negative voltage than the vessel itself and determine the electric potential in the spectrometer volume. These wires in combination with the remaining magnetic field shield the inner flux tube from electrons that are released from the stainless steel vessel by muons. Compared to the main spectrometer the pre-spectrometer is smaller and has a reduced energy resolution and the task of filtering the large part of low energetic electrons from the β -spectrum that are irrelevant for the neutrino mass measurement.

The main spectrometer provides the integrated precision measurement of the tritium β -spectrum close to the endpoint with its high energy resolution. Due to the small magnetic

field in the analysis plane of $B_A = 0.3$ mT the main spectrometer needs a diameter of at least 9 m just to contain the widening flux tube inside. To reach the target low magnet field it requires fine forming of the flux tube and the compensation of the earth magnetic field. Therefore, the stray fields of the superconducting magnets at both ends of the spectrometer are supplemented by a large air coil system which surrounds the MAC-E-Filter. For the precision measurement the stability of the retardation voltage is very important. The high voltage is constantly monitored by a very precise high voltage divider [41]. Additionally, a third MAC-E-Filter, the so called monitor spectrometer, placed outside of the beamline is set on the same potential and analyzes a Krypton-based nuclear standard to detect any drifts in the potential [42].

2.1.4. Main detector

The spectrometrically analyzed electrons are finally registered by a silicon detector which limits the flux tube at the end of KATRIN. The detector is a monolithic PIN-diode with a diameter of 9 cm to cover the flux tube of 191 Tcm^2 . The detector is segmented into a total of 148 pixels of equal areas. With this rough spatial resolution it is possible to take inhomogeneities of the electric and magnetic fields in radial and azimuthal direction into account. The detector has 4 pixels in the center continued by 12 rings in radial direction and each of these rings has 12 angular segments. Each pixel is handled as independent detector channel and its signal is amplified, carried via feed-through out of the vacuum system to the data acquisition system.

The detector energy resolution of about $\Delta E_{\text{FWHM}} \approx 1.5 \text{ keV}$ [43] helps to separate background events outside the energy range of 16-20 keV from signal electrons. In order to keep the background signal of the detector below the limit of 1 mHz, the detector is enclosed by an active scintillator-based myon veto. Inside of the veto a passive shield of copper and lead is placed to absorb most of the surrounding radioactive events that could hit the detector. The β -electrons that passed the main spectrometer can be accelerated by up to 35 kV using a post-acceleration electrode to shift the kinetic energy of the beta-electrons into a low background window of the detector system.

2.1.5. Rearsection

On the other side of the WGTS the Rearsection is connected and finally completes the primary vacuum tight containment of KATRIN. Since the Rearsection forms the central topic of this thesis, it is described in more detail in section 2.3. Before this part the competitive and complementary monitoring methods of WGTS parameters will be described (section 2.2).

2.2. Monitoring methods for the KATRIN tritium source

The tritium source of KATRIN must be monitored and calibrated in several ways to reduce the systematic uncertainties. The main variables of the WGTS to be monitored are source activity and gas density. Even at a constant activity, variations of the gas density have an impact on the systematic uncertainty, because the probability of inelastic scattering of the β -electrons with the gas molecules depends on the column density. Figure 2.4 shows the systematic error caused by an unrecognized relative shift of the column density compared to the assumed value. The upper limit for a single contribution to the systematic uncertainty is represented by the black line. This limit is the result of the evaluation what errors are acceptable to reach the target sensitivity of $0.2 \text{ eV}/c^2$. This limit makes clear that, depending on the analyzing energy interval below the tritium end point, a monitoring of the column density on the per mill level is ultimately required.

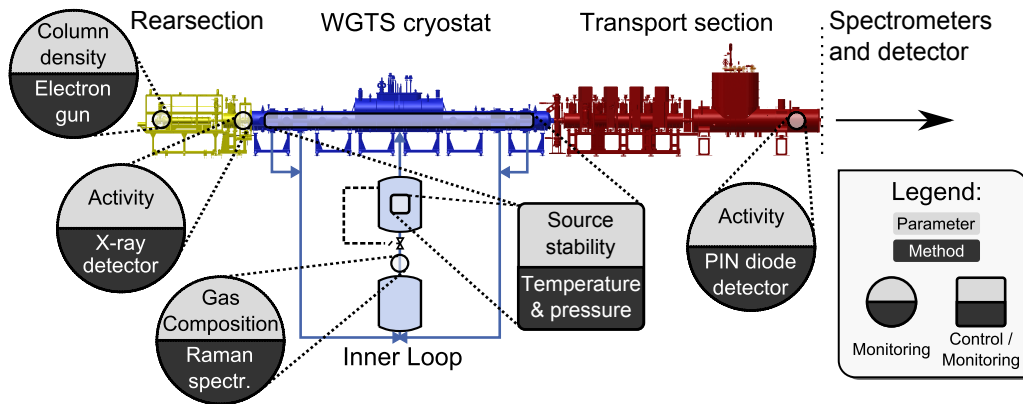


Figure 2.3.: Overview of control and monitoring methods at the source and transport section - Showing different parameters of the tritium source and which measures are used to control or monitor them. Most of these methods are described in detail in section 2.2. (adapted from [44]).

The amount of tritium molecules and the directly linked activity in the inner flux tube depends according to formula 2.2 on the area of the flux tube, the isotope composition and the column density. Therefore, a precise measurement of these 3 parameters and the resulting activity provides redundant information about the status of the source. The combination of all this information shall enable a continuous monitoring of the WGTS with a precision of 0.1%. Using the redundancy can also help to recognize and compensate for unconsidered effects or systematic uncertainties affecting the beta-decay.

Monitoring of the area of the inner flux tube will not be further considered. The effective area as given in formula 2.1 is dynamic and dependent on the magnetic fields produced by superconducting magnets. The magnets will run in driven mode hence the currents within the magnets will be very stable ($\leq 2\%$ in 3 months) and their time dependent behavior is well known. In previous measurements with superconducting magnets at KATRIN a relative stability of $5 \cdot 10^{-6}/\text{h}$ has been shown [43]. In the following sections the different methods to measure or monitor the isotope composition, the source activity and the column density are described.

2.2.1. Composition of the gas mixture

The WGTS is filled with a gaseous mixture which consists mainly of tritium (${}^3\text{H}=\text{T}$) to an amount of at least 95%. Other significant components of the gas are hydrogen (${}^1\text{H}$), deuterium (${}^2\text{H}$) and helium (${}^3\text{He}$). The different nuclides occur predominantly in molecular form. But negatively charged hydrogen ions or neutral helium can also exist atomically. By β -decays or by electron interactions the ambient atoms or molecules can be charged to stable positive or negative ions. An isotope monitoring of the gas mixture is important for the measurement of the partial amount of tritium, which defines the relation of activity to gas density. But it is also important to determine the amounts of molecules of tritium combined with any other hydrogen isotope, as in HT and DT. This is reasoned by the effect that the β -electrons from these isotopologues have a slightly shifted spectrum including a different end point. If not taken into account, this may cause a considerable systematic error.

The composition of neutral gas molecules in the source is measured by Laser-Raman (LARA) spectroscopy [45]. For this purpose molecules are excited to characteristic vibrational and rotational states by inelastic Raman scattering with the incident Laser light. The radiation emitted upon molecular de-excitation is analyzed by optical spectroscopy using a filter, an optical gate and a CCD camera. In the resulting spectrum the frequency

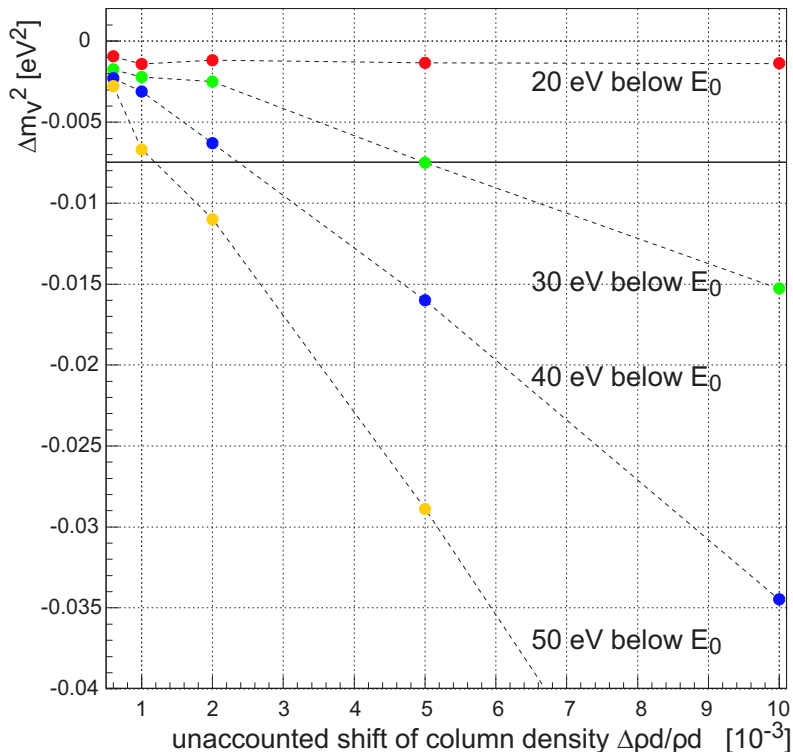


Figure 2.4.: Impact of the column density on the systematic uncertainty - An unrecognized relative shift of the WGTS column density in the order of 10^{-3} during the KATRIN measurement runs can result in an unacceptable large systematic error Δm_ν^2 (from [3]).

and signal height of specific peaks contain information about molecule types and quantities. With the LARA system it is possible to distinguish homogeneous molecules (like H_2 , D_2 and T_2) and heterogeneous molecules (like HD, HT and DT) and to measure their quantitative gas amounts. At the KATRIN experiment the gas composition shall be monitored continuously by LARA. Therefore, the gas mixture which is finally injected into the WGTS is passed through a cell of the LARA system. In this cell the gas mixture is analyzed at 100 mbar pressure and the isotope mixture is determined with a 0.1% precision on a time scale of 100 seconds.

The measurement is supplemented by mass spectrometers for a more conventional way to measure gas compositions. They can be installed at the outlets of the differential pumping systems DPS1-R and DPS1-F. Due to the fact that mass spectrometers separate the gas contents by the masses of the atoms and molecules in the gas, they can not distinguish molecules with the same mass like HT and D_2 . This drawback compared to the LARA analysis is compensated by the possibility to measure noble gases with mass spectrometers. Finally, the ions moving towards the spectrometer are held back in the DPS2 by a Penning trap and analyzed using ion cyclotron resonance. While this last method can provide information about the gas composition, it is rather used for studying the ion behavior in the source and transport section.

2.2.2. Monitoring the WGTS activity

The monitoring of the source activity will be realized in a redundant way using various different methods. At the Rearsection the task is fulfilled by indirect methods using the “Rear Detector”. In the forward direction the activity measurement is done by the Forward Beam Monitor Detector (FBMD) attached to the cryogenic pumping section [17]. Finally,

it is possible to do an explicit non-continuous check of the source activity with the main detector while the spectrometer potentials are reduced. The last method is only considered as backup or cross-check solution since it is non-continuous and would also take important measurement time.

The Rear Detector measures the rate of β -electrons from the WGTS impinging on the Rear Wall by beta-induced X-ray spectrometry (BIXS). The X-rays originate from the gold surface of the Rear Wall where the tritium β -decay electrons react via the inverse photoelectric effect. A part of the produced X-rays can pass through a gold-coated beryllium window and hit a detector. There are two ports in front of the Rear Wall where such a detector system is attached and monitors the X-ray radiation. The measured spectrum is the combined radiation of bremsstrahlung and characteristic X-rays produced by tritium β -electrons in the gold of the Rear Wall. The count rate measured in this process scales nearly linearly with the activity of the source if the deviations from the standard conditions in the WGTS are small. This method avoids most of the typical systematic errors connected with silicon radiation detectors:

- Drifts on the energy scale of the detector: This effect can occur due to small variations in the amplifier electronics. On average, events depositing the same amount of energy in the detector are then registered in a shifted energy channel. The BIXS detector can avoid this by regular self-calibration using the characteristic X-ray peaks of gold in the spectrum.
- Events at the measurement threshold: Every detector has a measurement threshold and primary particles with kinetic energies below this threshold are not detected. This threshold is an inherent risk for any precise counting or monitoring detector because any change in the system leading to a drift of the energy scale or the threshold results in a systematic error for the count rate. This risk is completely avoided by the physics of the BIXS: The minimum energy of the beta-induced X-rays that can reach the detector is larger than the necessary detector threshold energy [46].

The limitation of the BIXS system is the statistical error due to the small conversion rate of the process [47]. The expected count rate is in the order of 10^4 cps [48]. Therefore, an integration time with both SDDs of approximately 100 s is required to reach the target statistical precision of 0.1 %. More details on the implementation of the BIXS system at the Rearsection are available in section 5.5.

There exists an idea of implementing a further activity monitoring method at the Rearsection in an upgrade of the Rear Wall - the “Faraday cup method”: An indicator for the actual source strength is given with the current caused by the β -electrons impinging on the Rear Wall. The current will be at a precisely measurable value around 1 nA and the high statistics enable fast measurements with small statistic uncertainties. The measurement becomes complicated by the ions and secondary low-energy electrons which also hit the Rear Wall. To get a clear measurement signal which scales linearly with the source activity it is necessary to split these events by a multi-layered Rear Wall including a thin but high-resistance insulating layer. Investigations on this multi-layered Rear Wall were not successful on a full-sized Rear Wall prototype but the measurement principle remains an option for a future Rear Wall upgrade.

The forward beam monitor detector (FBMD) in the CPS differs significantly from the BIXS detector already described. It is attached at a port after the cryogenic part of the CPS and has an UHV manipulator to drive a small detector into the KATRIN flux tube [17]. Hence, the electrons of the tritium β -decay are measured directly. The KATRIN measurement itself must not be disturbed by the FBMD measurement. Therefore, the detector is placed in the “outer flux tube” area which is not imaged onto the main detector. Due to the

high source luminosity a sufficiently small-sized, conventional silicon detector is able to measure the activity in the flux tube element. With appropriate amplifier electronics and pulse processing within the data acquisition system (DAQ) it is possible to measure the β -electrons actually energy resolved. Only a few seconds of integration time are necessary to reach the target statistical precision so the measurement's precision is dominated by the systematic uncertainty [49]. Systematic errors can be caused by event rates that are too high to be resolved by the DAQ (generating pile-up events), by drifts in electronics or detector affecting the events close to the detector or by long-term defects and charging caused by tritium molecules or the high luminosity beta radiation. The 2D manipulator is not only designated to drive the detector to its measurement position but can also be used to scan over the whole flux tube. The result is an activity image of the source which can be used to detect inhomogeneities.

2.2.3. Measurement and stability of the gas density

The β -electrons in the WGTS can lose energy by inelastic scattering processes with the gas molecules. The impact of these scattering effects increases the complexity of the spectroscopic measurement of the original electron energy. The black, dashed line in figure 2.5 shows the transmission probability for an electron without scattering effects in dependence of the electron energy E minus the retardation potential $\Phi = e \cdot U$. The rising shape is only caused by the transmission function of the main spectrometer: If the kinetic energy is too small ($E - \Phi \leq 0$) the electron is not transmitted. In the scope of the main spectrometer's energy resolution ($0 < E - \Phi < \Delta E = 0.93 \text{ eV}$) the transmission depends on the starting polar angle (angle to the magnetic field line) of the electron. If the energy difference is larger ($E - \Phi > \Delta E$) the electron always passes the high-pass filter.

The response function takes into account both the transmission function of the spectrometer and the effects of inelastic scattering. The solid blue line in figure 2.5 shows the expected response function for the standard column density of $\rho d = 5 \cdot 10^{17} \text{ cm}^{-2}$. The probability for electrons averaged along the source to reach the main spectrometer without any inelastic scattering is given by $P_0 = 41.3\%$ [44]. Whenever an electron undergoes inelastic scattering, it loses at least 10 eV of kinetic energy by the process [50]. Due to this the unscattered electrons result in a clearly recognizable plateau. With increasing values of the surplus energy $E - \Phi$ also electrons which have been scattered once or twice can be transmitted. Any change in the column density modifies the height of the plateau and also consequently the probabilities for single or multiple scattering.

This effect on the response function can be used to measure or monitor the column density itself. It is possible to monitor the scattering effects quantitatively using an electron beam with 0° polar angle and well defined energy that passes the gas mixture in the source and transport section and is then analyzed in the spectrometer. This measurement requires a high short-term stability (relative 0.1%) of the electron beam. If the absolute rate of the beam is not precisely known at least two measurements with the response functions are necessary. If the long-term rate stability of the beam cannot be guaranteed with sufficient accuracy measurements with at least 3 different, fixed energies should be made. By comparing the ratios one can decouple the absolute beam rate from the scattering problem. In the figure 2.5 such 3 exemplary points are indicated. The measurement will use the Rearsection electron gun, the spectrometer and the detector and will be scheduled every 2 hours according to [3]. The target precision for the measurement is 0.2% with an integrating time for 2 minutes. Due to high experimental and theoretical uncertainties on the scattering cross sections the absolute accuracy will be worse by at least one order of magnitude. The column density is therefore the only parameter among the source strength parameters which can not be monitored continuously. Still this limitation is considered as uncritical: The parameters which define the column density and the gas conditions in the

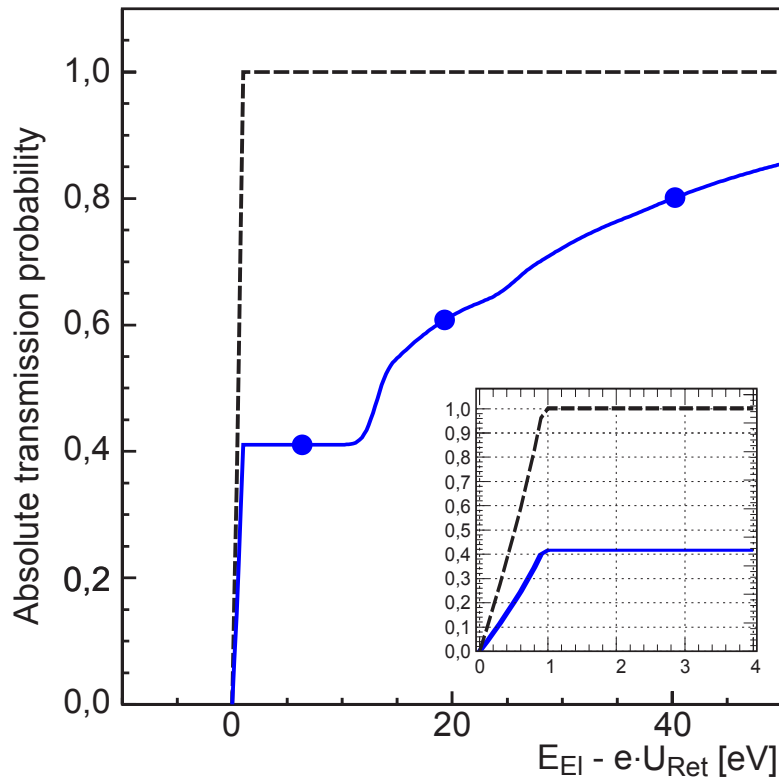


Figure 2.5.: Transmission and response function - The diagram shows the transmission probability at the MAC-E-Filter for electrons in dependency of the potential difference (electron kinetic energy - retardation potential). The black, dashed line is only valid without stray effects (“transmission function”) while the blue, solid line includes scattering effects (“response function”) (adapted from [3]).

source like temperature, the tritium inlet and outlet flow are all designed for a stability of 0.1 % [3].

2.3. Physics objectives of the Rearsection

The windowless gaseous tritium source allows gas and particles to stream equally towards the front side and rear side. Since the pumping, analyzing and detecting parts only continue to one side of the bi-directional tritium source the other end of the WGTS is connected to the system “Rearsection” which has the task to calibrate and monitor different properties of the source section. Therefore, the Rearsection is assigned to the group of “Calibration and Monitoring Systems (CMS)” for the source and transport section.

The Rearsection shall integrate two independent physics instruments: At the front of the Rearsection close to the DPS1-R part of the WGTS the Rear Wall is installed. The main purpose of the Rear Wall is to expose a stable and well defined surface towards the magnetically confined WGTS plasma. Due to the plasma properties the Rear Wall can have a significant influence on the electric potential - this effect is further described in section 5.1.1. Additionally, the Rear Wall provides the opportunity for an in-line and near real-time monitoring of the source activity. The details of the physics implementation of this monitoring method are given in section 5.5.

The other main component of the Rearsection is an electron gun which produces electrons based on the photoelectric effect [3]. An electron source with adjustable electron energy and momentum can reproduce any effects of the β -decay electrons as well as calibrate

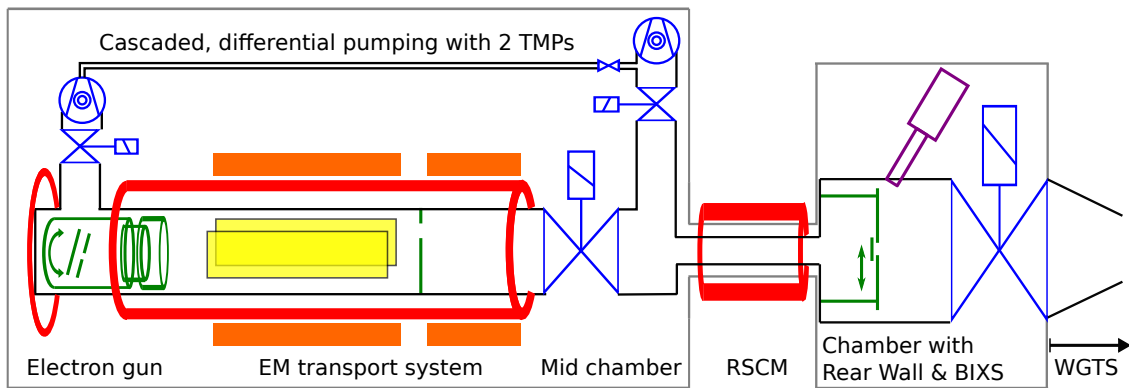


Figure 2.6.: Schema of the Rearsection - Different instrumentations as they are designated for the Rearsection in order to achieve the physics objectives: Primary vacuum system (black) and tritium safe second containment (gray). Pumps and valves are indicated in blue. The main physic instruments electron gun (left) and Rear Wall (right) are drawn in green. The electromagnetic components are solenoids (red), dipole coils (orange) and dipole electrodes (yellow). The BIXS system is indicated in purple.

other KATRIN components with reference electrons. Section 2.3.3 gives an overview of the intended calibration measurements using the electron gun.

2.3.1. Reference potential for the WGTS plasma

The products of the tritium β -decays in the WGTS generate a plasma within the volume of the source pipe. The decay electrons have a certain probability to ionize neutral gas molecules which increases the count of free charges. The number of created secondary electrons and ions depends on the track length of the primary electron - on average a β -decay electron produces about 15 low-energetic secondary electrons [50]. These low-energetic, secondary electrons and the low-energetic ionized gas molecules form the cold, magnetically confined plasma in the WGTS. In contrast, the decay electrons are able to quickly leave the plasma either towards the spectrometer or by entering the grounded, current-draining Rear Wall. The main processes for charge removal in the cold plasma are

- Re-combination of electrons and ions to neutral gas molecules
- The ions moving into spectrometer direction getting removed by the electric dipole in the DPS2
- Removal or neutralization of charge carriers upon contact with the Rear Wall

The magnetic confinement by the superconducting solenoids of the WGTS leads to a very small mobility of the charged particles transversal to the magnetic field lines. Only the plasma ions have a non-vanishing transversal conductivity due to stray processes with other gas molecules [51]. However the magnetic field does not restrict the mobility and conductivity longitudinal to the lines. The large differences in longitudinal or transversal conductivity play an important role in the definition of the plasma potential in the WGTS. The plasma potential defines the electric potential for unbound charges within the plasma (equivalently to the description of electric potentials in vacuum by the vacuum potential). The plasma potential gains its importance for the KATRIN experiment because it gives the reference potential for the β -electrons at the moment of their decay. This reference potential can be added linearly in the kinetic energy measurement at the spectrometer since the MAC-E-Filter measures the potential difference between the filter analysis plane and the WGTS plasma potential. Consequently, unrecognized spatial or temporal instabilities in the plasma potential lead to a systematic uncertainty in neutrino mass measurement.

As mentioned before the anisotropic conductivities in the WGTS have an impact on the potential distribution in the plasma: The vacuum potential in an evacuated vessel is dominantly influenced by the electric potentials of the closest surfaces. The vacuum potential inside an evacuated WGTS then is defined by the cylindrical wall almost in the whole volume except at both ends of the pipe. By contrast, plasma potential distributions do not only depend on the distances to different surfaces but also on the conductivities on the way to these surfaces: The WGTS plasma with its comparably large longitudinal conductivity will transport the electric potential of the surfaces at the WGTS ends to the volume. On the other hand the small transversal conductivity will not be able to transport the potential of the cylindrical side walls deep in to the plasma. Since there is no solid surface at the front side of the WGTS, only the surface at the back side, the “Rear Wall”, has the increased impact on the electric potential inside of the source plasma.

Given the importance of the Rear Wall’s electrical potential it is foreseen to apply an additional voltage to it shifted by ± 10 V towards the WGTS potential. Going deeper into detail the electric potential of the Rear Wall surface is not simply defined by the voltage it is connected to: Just as any metallic surface it has its own surface potential which depends on the voltage difference between the Fermi level inside of the metal to the vacuum level. This difference is also called work function and is a material specific characteristic [52]. The absolute value of the Rear Wall work function is not important for KATRIN since this is a constant shift applied on the measured total electron energy and this energy is a free parameter in the fit calculations for the neutrino mass. But any variations in time or over the surface of the Rear Wall, have a strong impact on the systematic errors. For this reason the requirement of a work function precision of < 20 meV [53] in space and time has been added. This requirement only applies to an area of 0.86 cm² at the Rear Wall surface which equals the flux tube size of one detector pixel - this softening of the requirement is acceptable because the KATRIN analysis will handle and fit each single detector pixel individually.

2.3.2. Monitoring of the source activity with beta-induced X-ray spectroscopy

The Rear Wall as the surface which is hit by most of the charges produced in the WGTS provides an excellent opportunity to monitor properties of the tritium source. Additional to the other available WGTS activity monitoring methods (compare section 2.2.2) an activity monitoring system is planned to be installed close to the Rear Wall. The main challenge for this monitoring system is to provide an in-line and near real-time monitoring without any interference in the flux tube or in the plasma. The activity must be measurable to a precision of better than 0.1 % in less than 100 s to match adequately to concurrent WGTS monitoring systems. This measurement must be able to efficiently distinguish apart the primary electrons of the beta decay from all the other charges - otherwise the signal of the primary electrons is overwhelmed by the secondary electrons and ions created by ionization. The count rate of secondaries does not necessarily follow the count rate of beta decays to the necessary precision. Therefore, the non-removal of secondaries for any activity measurement method could produce a systematic error which exceeds the required precision of 0.1 %.

The established method for the WGTS activity monitoring is beta-induced X-ray spectroscopy (BIXS): All the tritium beta-decay electrons of the source hit the Rear Wall. Unlike the low-energy secondaries and ions the high-energy primary electrons have a non-vanishing chance to produce X-rays on their relaxation process in the Rear Wall matter. The physical requirement of a minimum electron energy to produce X-rays is a sufficiently reliable and intrinsic feature to split the primary electrons from the low energetic electrons and ions. The surface film of the high-Z material gold at the Rear Wall increases

the resulting bremsstrahlung X-rays intensity I according to Kramer's law [54]

$$I(\lambda)d\lambda = \frac{KiZ}{\lambda^2} \left(\frac{\lambda}{\lambda_{\max}} - 1 \right) \quad (2.7)$$

with the Kramers constant K , the incoming electron current i , the atomic number of the electron beam target Z and the X-ray wavelength λ [55].

The generated low energetic X-rays cannot penetrate through the Rear Wall. Therefore, the X-rays emitted into the direction of the WGTS must be used for the BIXS measurement. So the detectors which shall measure the X-rays must be placed closely in front of the Rear Wall but they must not touch the flux tube - otherwise they would disturb the neutrino mass measurement. But it is possible to measure a sufficient rate of beta-induced X-rays from the Rear Wall if detectors are attached at the sides of the Rear Wall chamber in a geometric alignment which fits the cone of sight of the detector chip exactly to the Rear Wall surface. This measurement setup is possible due to the broad angular emission of X-rays from the Rear Wall surface. The detectors are protected from the KATRIN primary volume by X-ray transparent gold coated beryllium windows. The detectors used in the monitoring system are silicon drift detectors (SDD) [46]. An SDD combines a large active area with a very good energy resolution. Despite the large active area the event rate at the detector will be small enough for a full digital pulse processing including single event energy and time measurement. The most important advantage of a spectral measurement with high energy resolution is the possibility to measure sharp X-ray fluorescence lines in the spectrum. This can be used for a continuous energy calibration and for studying any occurring systematic effects during the KATRIN runtime. More details about the implementation of the BIXS system at the Rearsection are provided in section 5.5.

In case of a direct current measurement of the primary β -electrons impinging on the Rear Wall the statistical error can be neglected after 1s of integration time. This was the main motivation for investigations by the UCSB group in a Faraday cup based activity monitoring. As described in section 2.2.2 this method had difficulties in the production of working prototypes and with the systematic errors during test measurements. The Faraday cup option has not yet been completely discarded but postponed to an upgrade option for the Rear Wall in the future. A Rear Wall prototype which can be used for a direct current measurement has then to pass all qualification tests as the other prototype samples before it is used productively at KATRIN. So far only BIXS is an established method for activity monitoring and therefore the Faraday cup method will not be considered furthermore in this thesis.

2.3.3. Calibration methods using an electron source

The last important feature of the Rearsection is the photo-electric electron gun. This system provides a well defined electron beam for different calibration tasks of KATRIN. The distinct measurement modes of the E-gun are described in table 2.1. The electron gun is designed to be a versatile and flexible instrument for regular calibration as well as for the investigation of unexpected effects. To achieve this the design specifications require the E-gun to tune the following beam properties:

- **Electron energy:** The kinetic energy can be adjusted directly with the acceleration voltage which is a common tuning parameter at electron guns. The Rearsection E-gun uses the main spectrometer high voltage as reference potential and adds a custom potential offset in positive or negative direction. The design specifications require a sharp energy distribution with $\sigma < 0.2$ eV in the high resolution mode. The main contribution to the uncertainty in the energy distribution is given by the mismatch of the photon energy of the incoming UV light to the energy necessary to

emit an electron from the surface (“work function”). Therefore, a precise tuning of the photon energy distribution is required.

- **Emission rate:** The resulting emission rate from a photo-electric electron gun is a folding of different parameters: The UV-light intensity at the cathode surface, the quantum efficiency of electron production which is increasing with the surplus energy of the photons towards the work function barrier and the probability of the excited electrons to drift to the surface and leave the metal. The UV-light wavelength dependence concerning the electron energy uncertainty and the emission rate are contradictory to each other. Hence, the emission rate requirement is defined in dependence of the accepted energy distribution: In the high resolution mode ($\sigma < 0.2$ eV) the rate will be $\lesssim 10^5$ /s. In the high rate mode ($\sigma > 2$ eV) the rate will be $\gtrsim 10^5$ /s. In the high resolution mode the E-gun rate is required to achieve a relative stability of better than 0.1 % within two hours of measurement time.
- **Average angle of the electron momentum towards the guiding magnetic field line (“polar angle”):** The kinetic energy of the electrons and their polar angle defines the kinetic energies parallel (E_{\parallel}) and transversal (E_{\perp}) to the solenoid magnetic field lines. This is particularly important since the magnetic moment of the electrons ($\mu = E_{\perp}/B$) is conserved through the Rearsection as well as the complete KATRIN experiment. Any deviation of a perfectly conserved magnetic moment (“adiabatic motion”) broadens the distribution of the polar angle. Apart from non-adiabatic effects the angular and positional distribution of the low energetic electrons emitted from the cathode surface can contribute to the uncertainty in the final polar angle. The overall requirement is that the polar angle shall be adjustable in the whole range of accepted electron angles in the KATRIN experiment with a distribution sharpness of $\sigma < 4^{\circ}$ in the WGTS at a magnetic field of 3.6 T.
- **Beam size and position:** The beam size is initially defined by the spot size of the UV light that hits the cathode surface. The design requires a light spot size of less than 1 mm with more than 99 % of the light intensity inside. The size of the photo-electron beam then varies according to the conservation of the magnetic flux tube $\Phi = B \cdot A$. The beam position is also dependent on the magnetic flux tube and can be manipulated by dipole fields in the Rearsection. While the dipole fields in the Rearsection can not be strong enough to position the beam across the full KATRIN flux tube, there are superconducting dipole coils available in the WGTS which can be used to move the beam to any position of the full KATRIN flux tube. These WGTS dipole coils are not in the responsibility of the Rearsection task group and do not cause any requirements for the Rearsection.

The way the E-gun was specifically implemented at the Rearsection is described in detail in section 4.3. Various simulations and calculations have been completed to optimize the given parameters above in order to fulfill the ambitious requirements. The simulations will be presented in section 4.3.

Table 2.1.: Electron gun measurements modes - Two of them are source related with the goal to measure the scattering probability and energy loss on scattering (2.) and to use this information later to monitor for source column density changes (1.). The other operation modes are spectrometer related: On request the transmission function can be measured, a check of work function shifts at the spectrometer electrodes can be performed or a high intensity electron beam can be used to search for particle traps or systematic effects. For each of these measurements the most important electron gun parameters and measurement configurations are provided.

Measurement mode	1. Column density monitoring	2. Energy loss function	3. Transmission function	4. Work function calibration	5. Spectrometer trap tests
E-gun parameter					
Energy					
Absolute (eV)	18600	18600	18600	18600	0-18600
σ_E (eV)	< 2	< 2	< 0.2	< 0.2	< 2
Polar angle in WGTS					
Absolute ($^\circ$)	0	0 or 51	0-51	0	0-51
σ_Θ ($^\circ$)	< 4	< 4	< 4	< 4	< 4
Rate					
Absolute (1/s)	O(10^4)	O(10^4)	O(10^4)	O(10^4)	O(10^6)
Relative stability	0.1 % over minutes	0.1 % over hours	0.1 % over minutes	1 % over minutes	not important
Beam shifting					
Off-axis	No	On request	Yes	Yes	On request
Flux tube scan	No	On request	On request	On request	On request
Measurement Schedule					
Conditions	Periodic Normal run	Calibration Modify WGTS pressure	On request WGTS evacuated	On request Normal run	On request Depends on specific test

3. Mechanical design of the Rearsection

The mechanical design fully complies with to the main tasks of the Rearsection: To build a tritium safe containment which closes the vacuum system of the WGTS and to support for the important physics instruments of the Rearsection - specifically the electron gun with its electromagnetic transport system (described in chapter 4) and the Rear Wall with its source activity monitoring instrumentation (described in chapter 5). The design evolved stepwise with changes in concepts or requirements of the contained instruments. For the parallel development of the electromagnetic design and the mechanical design mutual influences have always been considered. The basis for the mechanical design is an ultra-high-vacuum system since a low pressure is ultimately required for the functionality of the electron gun. To achieve the required pressures the system uses a state-of-the-art combination of UHV-compatible parts and sealings, turbomolecular pumps, pressure sensors, valves and a bake-out system. The fore vacuum for the turbomolecular pumps is provided by a tritium compatible, 2-stage pumping system of the Isotope Separation System (ISS) [56].

The vacuum system is encased by a second containment - this is a requirement for tritium safety by the Tritium Laboratory Karlsruhe. The double contained system needs a support structure to adjust and align the position of the overall system with respect to the WGTS. Additionally, a mounting system within the containment is required to fix the vacuum system in the correct position and alignment to connect the WGTS/DPS1-R connection flange. The technical details of the mechanical design of vacuum system, 2nd containment and support structures have been laid down in a Technical Design Report (TDR) which has been approved by a review committee. The following sections describe details about the vacuum system (3.1), the 2nd containment (3.2) and the interfaces to neighbor systems 3.3.

3.1. Vacuum system

The vacuum system comprises all components or surfaces that separate the vacuum volume from the surrounding atmosphere which is close to ambient pressure. All these components and surfaces are contaminated with tritium by definition due to the tritium gas streaming from the WGTS into the Rearsection. Hence, the vacuum system is a tritium primary system and must fulfill all safety requirements as defined in the TLA [4]. To comply with these requirements appropriate vacuum standards which already fulfill the demands of the TLA were utilized. The chosen wall material for primary containment pipes and chambers

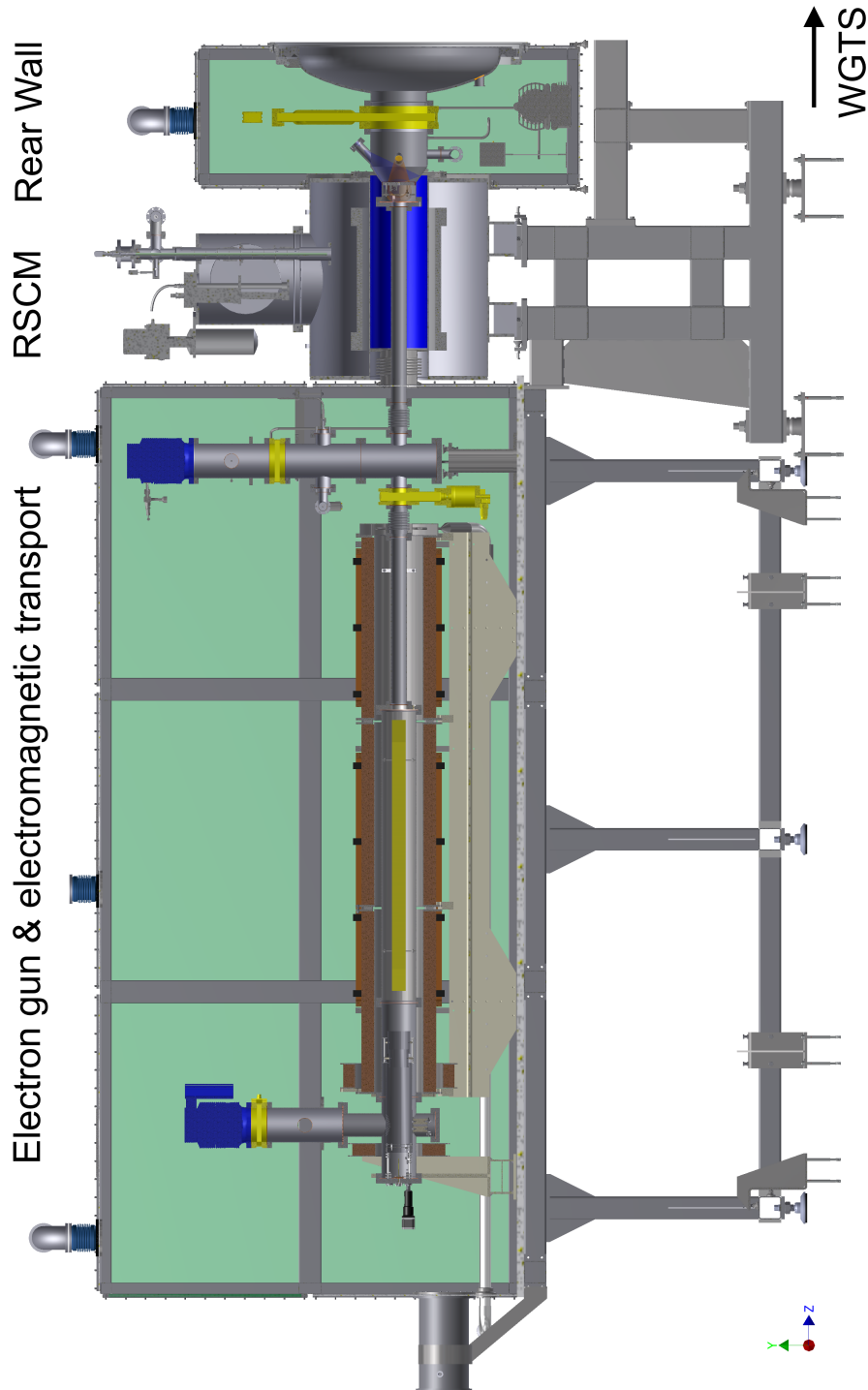


Figure 3.1.: Side cut view of the full system - The most recent status of the Rearsection CAD model in a half cut view. The WGTS and further KATRIN components will be connected at the right end. The drawing showing support, boxes, vacuum system and interior instrumentation shall give an overview and point of orientation for the following detailed description of the individual parts.

is stainless steel (most preferably the type 316LN but also 316L and 304L when 316LN is not available) and the parts are connected with full metal seals using the CONFLAT¹ or the VCR² standard. These connection standards will not only be used at all chambers and piping but also at all valves, feed-throughs and attached sensors (e.g. pressure sensors). Assuming the connection standards are applied properly they ensure fulfillment of the TLA since the first containment is fully metal sealed and they provide a helium leakage rate of better than $< 10^{-9}$ mbar · l/s for a single sealing and $< 10^{-8}$ mbar · l/s for the integral system. Furthermore, all custom pipes and chambers have to undergo several qualification steps in design and production, e.g. an X-ray test of at least 50 % of the weldings seams. More details on the safety requirements can be found in the TLA[4].

The resulting design, considering the space demands by physically relevant instruments and the described safety requirements, is displayed in the CAD drawing 3.2. Most of the primary volume is enclosed by CF-standard components because standard components are more cost-effective and their production process often complies already to the TLA requirements. While every single sealing increases the flexibility in design, construction and replaceability, it also necessarily increases the construction effort and the chance of a sealing failure. Therefore, long pipes are implemented as single pipes of custom length, if the required accessibility allows it, and chambers with many connections are realized as custom welded chambers. The main constructive parts from right to left as seen in figure 3.2 are:

- **Rear Wall chamber:** The Rear Wall chamber connects to the right to the WGTS / DPS1-R. In between there is a VAT³ CF250 valve placed which enables a vacuum-safe separation of the two large components. The custom designed chamber houses the Rear Wall and reduces the flange sizes from CF250 to CF160. There are 4 access ports available with CF40 flange size where two silicon drift detectors for beta-induced X-ray spectroscopy can be installed, one port is used for an optical window to provide UV-light illumination to the Rear Wall and the last port is used for sensor installation and electric feed-throughs. More details on the Rear Wall and corresponding instrumentation are described in chapter 5. The connection to the mid chamber is realized by a long CF63 pipe which guides through the superconducting re-condenser magnet.
- **Mid pumping area:** The “mid chamber” is rather important for creating good vacuum conditions than for providing physical instrumentation. Since this part has its own support while the Rear Wall chamber positioning is defined by the connection to the DPS1-R/WGTS, the mid chamber uses bellows for mechanical decoupling. The mid chamber consists of multiple CF160-63 reduction crosses - the large diameter connection pipes result in a large gas conductance towards the turbomolecular pump and the CF63 ports are used for pressure sensors, small valves and piping connections and of course for the beam line connection itself. Towards the turbomolecular pump a large VAT CF160 valve is installed to safely disconnect the pump in case of a failure. Towards the electron gun the mid chamber has a CF63 VAT full metal gate valve attached which enables a tritium safe separation of the electron gun parts from the front and mid area of the Rearsection.
- **Electron gun:** The electron gun area includes more than the E-gun chamber itself. Especially the transport section between mid pumping area and E-gun chamber contains electrodes and is surrounded by coils of importance for the electron beam path. The connection to the mid chamber is again decoupled by a CF63 bellow and

¹Registered trademark of the company Varian, Inc.

²Registered trademark of the company Swagelok, previously Cajon Company

³VAT Inc., 500 West-Cummings Park, MA 01801 Woburn, United States

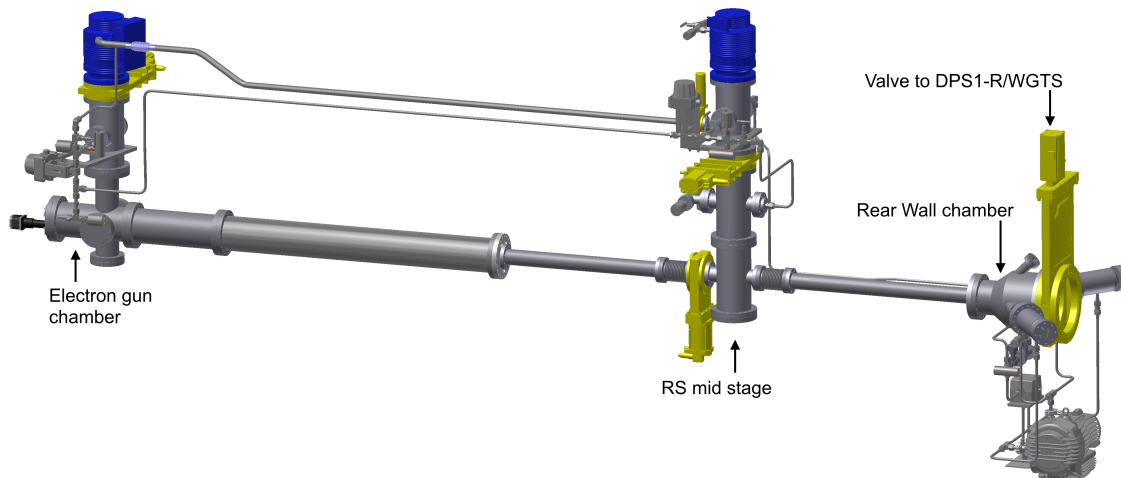


Figure 3.2.: Vacuum system of the Rearsection - Only parts that enclose an evacuated volume are shown. At the front right are the large valve and the Rear Wall chamber which are connected to the WGTS. In the center the mid stage is located, followed by the electron gun chamber on the back left.

continues into a CF63 pipe. This pipe is just extending the distance to the electron gun which is only required to increase the length over which magnetic dipole fields act on the beam path. Consequently, the pipe diameter is downsized to the minimum, which is required for proper transport of the electrons, to reduce the gas conductance to the electron gun. For a further reduction of the gas conductance a small aperture is included in the following CF63-160 adapter flange. The aperture hole, with a 3 mm diameter, has an offset of 10 mm to the symmetry Z-axis. This breaks the direct line of sight from the central Rear Wall hole to the E-gun and thus reduces the amount of tritium molecules reaching the E-gun even further. The aperture flange is connected to 2 CF160 pipes which contain large electrodes. All the named pipes of the electron gun area are surrounded by beam steering solenoids and dipole coils. The electron gun chamber itself is a custom 6-way cross with 2 ports CF160 and 4 CF100 ports. All optical, mechanical and electrical feed-throughs required for the E-gun are attached to this chamber. To the upper side another cross is attached to provide ports for piping and sensors continued by another CF160 valve and a turbomolecular pump.

3.1.1. Design of the vacuum and pumping system

The vacuum layout comprises the choice and positioning of adequate pumps and sensors to be able to reach and measure the target pressures. The most important requirement for the vacuum design is the target pressure value of $< 10^{-7}$ mbar in the E-gun chamber. This target pressure does not appear to be very challenging with the given choice of metal sealed UHV standard components and turbomolecular pumps. However, the WGTS brings a comparably high gas load into the Rearsection: The inlet pressure in the center of the WGTS is fixed to 10^{-3} mbar and this gas load is reduced by two orders of magnitude by the pumping section in the DPS1-R. This also defines the maximum pressure in the Rear Wall chamber - and likewise of the remaining high vacuum vessels in the Rearsection - to approximately 10^{-5} mbar. For further vacuum calculations it is recommended to determine whether the gas motion is in molecular, laminar or transitional flow. This can be determined via the Knudsen number,

$$\text{Kn} = \frac{\lambda}{l} \quad (3.1)$$

[57] where λ is the mean free path and l the characteristic length. If the Knudsen number exceeds 2 the gas can be approximated by molecular flow, in case the number is smaller than 0.2 the formulas of laminar flow have to be applied and if the Knudsen number is in between the gas is in transitional flow. At the given maximum tritium pressure of 10^{-5} mbar the gas has a mean free path of $\lambda > 1000$ m [58] while the characteristic length equals the typical diameter of the vacuum piping in the Rearsection with 160 mm. Therefore, the Knudsen number in the Rearsection is $Kn = 6250$ and higher (in lower pressure regions). Hence, the formula set for molecular flow can be applied. The gas conductance of a cylindric pipe in the molecular flow regime is calculated by

$$C_{\text{Pipe}} = \sqrt{\frac{\pi RT}{18M}} \cdot \frac{d^3}{l} \quad (3.2)$$

with the gas constant R , the temperature T , the molecular mass M , the pipe diameter d and the pipe length l [59]. The conductance of an aperture in the molecular flow regime is given by [60]:

$$C_{\text{Pipe}} = A \sqrt{\frac{RT}{2\pi M}} \quad (3.3)$$

with the aperture area A , the gas constant R , the temperature T and the molecular mass M .

Simple vacuum calculations can be implemented by defining volumes which are connected to each other by a certain gas conductance. In the first place the pressure in each chamber is calculated separately as a result of incoming gas by leakage & outgassing and gas removal by pumps. In the next iteration the pressure in each chamber is corrected by the gas streaming between the chambers, taking the conductance of their inter-connections into account, to arrive at the final equilibrium value. In simple cases this approximation already delivers sufficiently precise results without solving differential equations of gas dynamics. For the calculation of the Rearsection it is necessary to split the Rearsection into 3 pseudo-separated volumes: The first volume is the chamber connected to the DPS1-R and ends at the Rear Wall, the second volume is the first pumping chamber and ends at the aperture and the last chamber comprises the E-gun chambers and the other turbomolecular pump (compare sketch 3.3). The chamber interconnections with low conductance are on the front side the combination of Rear Wall with following CF63 pipe and in the mid of the Rearsection the aperture. For the further calculations the following general assumptions are made: The average specific outgassing of out-baked steel surfaces is smaller than $q_{\text{SS}}/A = 10^{-10}$ mbar \cdot l/(s \cdot cm²) [61]. The turbomolecular pump used for the calculations is a Leybold MAG W 600 with magnetic bearing, a geometrically reasonable CF160 connection port and a pumping speed of $S_{\text{H}_2} = 4101$ /s for hydrogen and $S_{\text{He}} = 5701$ /s for helium [62]. The tritium pumping speed is estimated as $S_{\text{T}_2} = 5001$ /s. The resulting pressure in a chamber is then determined by the total gas ballast q_{total} (caused e.g. by outgassing or leakage) divided by the pumping speed S [58]:

$$p_{\text{res}} = \frac{q_{\text{total}}}{S_{\text{TMP}}} \quad (3.4)$$

First iteration step: The Rear Wall chamber has a volume of approximately 16 liters and no pump to evacuate the volume. It is connected to the DPS1-R with a fairly high conductance which allows the following worst-case assumption: The pressure is exactly the same as in the DPS1-R which is expected to be 10^{-5} mbar. The estimated surface of 0.3 m² does not significantly contribute to the preconditioned pressure. All gas emanated from the surfaces will be pumped by the turbomolecular pumps of the DPS1-R. The partial pressure due to stainless steel outgassing will not exceed 10^{-8} mbar which is negligible compared to the pressure caused by tritium gas.

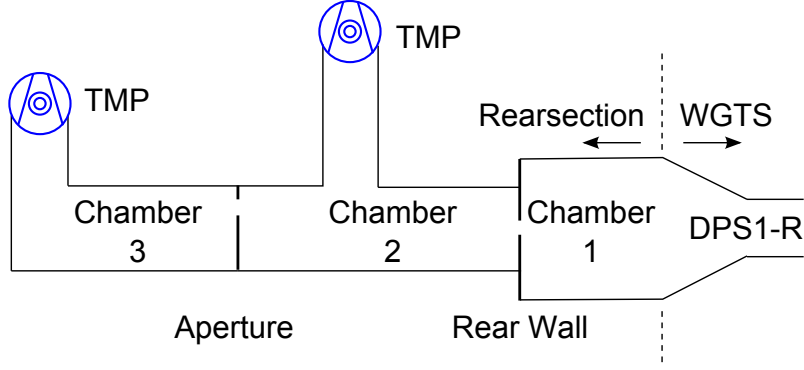


Figure 3.3.: Schema for vacuum pressure estimation - The sketch defines the 3 pseudo-separated volumes. Chamber 1 and DPS1-R/WGTS are not physically but only logically separated. Between the chambers 1 to 2 and 2 to 3 a small hole aperture limits the gas flow. Chamber 2 and 3 are evacuated by turbomolecular pumps.

The mid chamber has a turbomolecular pump with a pumping speed of 4101/s (for H_2 [62]) which is not limited by the connection pipe with a conductance of approximately 9001/s. The inner surface of about 1 m^2 puts a gas load of $10^{-6}\text{ mbar} \cdot \text{l/s}$ on the system. Combined with an assumed leakage rate of $10^{-9}\text{ mbar} \cdot \text{l/s}$ (after out-baking) this results in a pressure in the mid chamber of

$$p_{1,\text{Mid chamber}} = 2 \cdot 10^{-9}\text{ mbar} \quad (3.5)$$

The E-gun chamber is evacuated by the same turbomolecular pump as the mid chamber and the pumping speed is also not reduced by the connection since the pipe has a conductance of above 10001/s. Again the sources of gas load are outgassing from surfaces (in this case $3.5 \cdot 10^{-6}\text{ mbar} \cdot \text{l/s}$ by a surface size of 3.5 m^2) and leakage (with a rate of $10^{-9}\text{ mbar} \cdot \text{l/s}$). The surface size estimation takes the interior installations in the E-gun chamber into account. The following pressure is expected in the idealized E-gun chamber:

$$p_{1,\text{E-gun chamber}} = 7 \cdot 10^{-9}\text{ mbar} \quad (3.6)$$

In the second iteration step the interconnection between the 3 chambers has to be considered in pressure calculations. To get to the resulting pressures the gas conductances between the chambers are calculated: The Rear Wall is assumed as thin aperture with a central hole diameter of 5 mm and a further 1 mm gap between the RW boundary diameter of 148 mm and the surrounding steel walls. The effective surface for gas transmission is therefore 4.9 cm^2 . As result the Rear Wall as a gas aperture has a conductance of 1251/s. This conductance is comparably large for an aperture for differential pumping, especially due to the small gap between the Rear Wall and the surrounding walls. This can not be avoided since the Rear Wall needs a certain electrical and mechanical safety margin to the walls. Though the gas conductance is further reduced by the CF63 piping which connects the Rear Wall chamber and the mid chamber. With a total length of 1066 mm and an inner diameter of 63 mm it has a conductance of 671/s. The combined conductance can be calculated through $1/C_{\text{eff}} = 1/C_1 + 1/C_2$, resulting in an effective conductance of $C_{\text{eff}} = 431/\text{s}$. With this result and the pressure difference between the Rear Wall chamber and the mid chamber a new pressure value for the mid chamber can be calculated using the streaming rate q [58]:

$$q_{\text{Ch1} \rightarrow \text{Ch2}} = \Delta p \cdot C = (p_{\text{Ch1}} - p_{\text{Ch2}}) \cdot C_{\text{eff}} = 4.4 \cdot 10^{-4}\text{ mbar} \cdot \text{l/s} \quad (3.7)$$

$$p_{\text{Ch2}} = \frac{q_{\text{Ch1} \rightarrow \text{Ch2}} + q_{\text{Leakage}} + q_{\text{Outgassing}}}{S_{\text{TMP,mid}}} = 8.8 \cdot 10^{-7}\text{ mbar} \quad (3.8)$$

To continue the second iteration to the E-gun chamber the conductance of the aperture in-between has to be evaluated: The aperture only has a 3 mm diameter central hole to transmit gas, resulting in a gas conductance of 7.31/s. The pressure difference of mid and E-gun chamber puts an additional gas load through the aperture to the chamber with the smaller pressure. Therefore, the final pressure in the E-gun chamber is expected to be $1.9 \cdot 10^{-8}$ mbar which is well within the specification requirement of $< 10^{-7}$ mbar. According to this calculation the layout of the vacuum system with two turbomolecular pumps and two apertures in a differential pumping system fulfills the vacuum requirements. In order to check whether the ultimate pressures can be reached also the compression ratios of the TMPs have to be taken into account: The data sheet states a maximum compression ratio of $3.4 \cdot 10^4$ for hydrogen and $1.7 \cdot 10^6$ helium [62]. The assumption of a compression ratio of $1.0 \cdot 10^5$ for tritium is rather conservative since this ratio heavily depends on the molecular mass of the pumped gas [58]. To reach the target pressure in the mid chamber with the given compression ratio the fore line pressure at the mid chamber TMP must definitely be better than 0.1 mbar. This is a new requirement concerning the fore vacuum pressure provided by pumps in the ISS box which also affects the design of the pumping pipe connection between Rearsection and ISS box. Instead, the E-gun turbomolecular pump would require a fore pressure even better by two orders of magnitude which is definitely not feasible with the ISS pumps. This can be solved by cascaded pumping: The outlet of the E-gun TMP is fed in directly in front of the high vacuum side of the mid chamber turbomolecular pump.

The above calculations delivered important input for the planning of the Rearsection vacuum design. The main challenge is the tritium gas streaming freely through the WGTS towards the Rearsection which can be compared to an huge, but unavoidable leak in the system. The design with two cascaded and differentially pumped chambers fulfills the pressure requirement for the E-gun chamber. If required there are still options for improvements:

- The conductance of the Rear Wall is high although it is designed as an aperture. The main part of the conductance is caused by the 1 mm gap towards the vessel wall for electrical insulation. This gap can be filled with a vacuum compatible electric insulator (e.g. PEEK⁴). This is already foreseen in the current technical design. Nevertheless, the one millimeter gap remained in the calculation as a worst-case approximation to take potential mechanical imperfections into account.
- Adding any type of getter pumps could significantly improve the vacuum. But such pumps need additional maintenance and (re-)activation when they are saturated. An installation of such pumps is only foreseen in case the need arises during test measurements or KATRIN measurements.
- Exchange of the turbomolecular pump by another model with increased pumping speed: The options here are very limited since the only reasonable flange connection size is CF160 and the number of manufacturers and bearing types that have been tested with tritium [63] is very small. The pumping speeds of optional TMPs for the Rearsection do not vary much from the selected type. Changing the pump type might only be desirable if higher compression factors or better compatibility with magnetic fields are ultimately required. The issue of turbomolecular pumps and magnetic fields is described in the next section.

3.1.2. Magnetic shielding for the turbomolecular pumps

All turbomolecular pumps (TMPs) work at high rotation speeds with a vulnerability concerning high temperatures or mechanical forces. Due to this, TMPs may react very sen-

⁴Abbreviation for Polyether ether ketone polymers

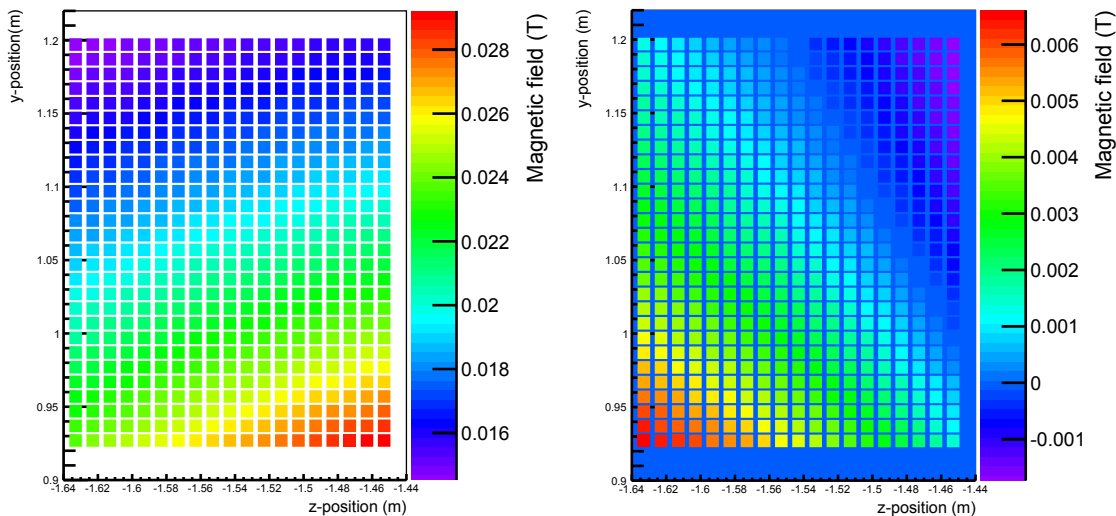


Figure 3.4.: Magnetic field at the turbomolecular pump position - Field maps at the final TMP position in the symmetry z-y-plane without any shielding. Left: B-field component parallel to the rotor axis. Right: Radial component to the rotor axis. Without shielding the acceptable field values are exceeded for both field directions.

sitive to any magnetic fields that significantly exceed the earth magnetic field - they can stop or even be damaged by magnetic fields. This issue is of high importance for most of the KATRIN components since the TMPs in use are situated in strong magnetic fields close to superconducting magnets. Therefore a test stand has been developed to measure and monitor the behavior of TMPs in magnetic fields [64]. The following list shows the main limits for critical operations depending on the magnetic field strength and alignment:

1. Magnetic field perpendicular to the rotor axis: Eddy currents are induced in the rotor blades which constantly produces heat in the blades. The rotor blades expand with temperature increase up to the critical length where they touch the inner side of the TMP encasement. The critical temperature for this effect is 120°C but for continuous operation 90°C should not be exceeded ([65]). The maximum acceptable field for continuous operation concerning this effect has been measured to 3 mT for a different pump model (Leybold MAG W2800) which uses a similar magnetic bearing [66].

Another limit is caused by the electromagnetic motor which slows down and finally stops in a too high magnetic field when the sufficient current can not be provided by the power supply anymore. Still, the critical field strength for this effect is typically much higher than for the first effect $> 10\text{ mT}$.

2. Magnetic field parallel to the rotor axis: The turbomolecular pumps at the Rearsection have a magnetic bearing to reduce the amounts of lubricants in the primary containment which could be affected by the radio-chemistry of tritium. This magnetic bearing or the corresponding position sensors lose their functionality if the superimposed external magnetic fields becomes too strong. In this case the pump is automatically stopped by its controller. The maximum acceptable field to avoid this effect has been measured to 12.5 mT for a different pump model (Leybold MAG W2800) [66].

These limits are relevant at the Rearsection for the turbomolecular pump of the mid chamber which is positioned close to the superconducting magnet. Since the magnetic field lines of the flux tube behind the RSCM are opening up without being “compressed” again by another superconducting magnet, the magnetic field can be strong at the final TMP position (especially in the radial direction). To reduce the magnetic field the TMP

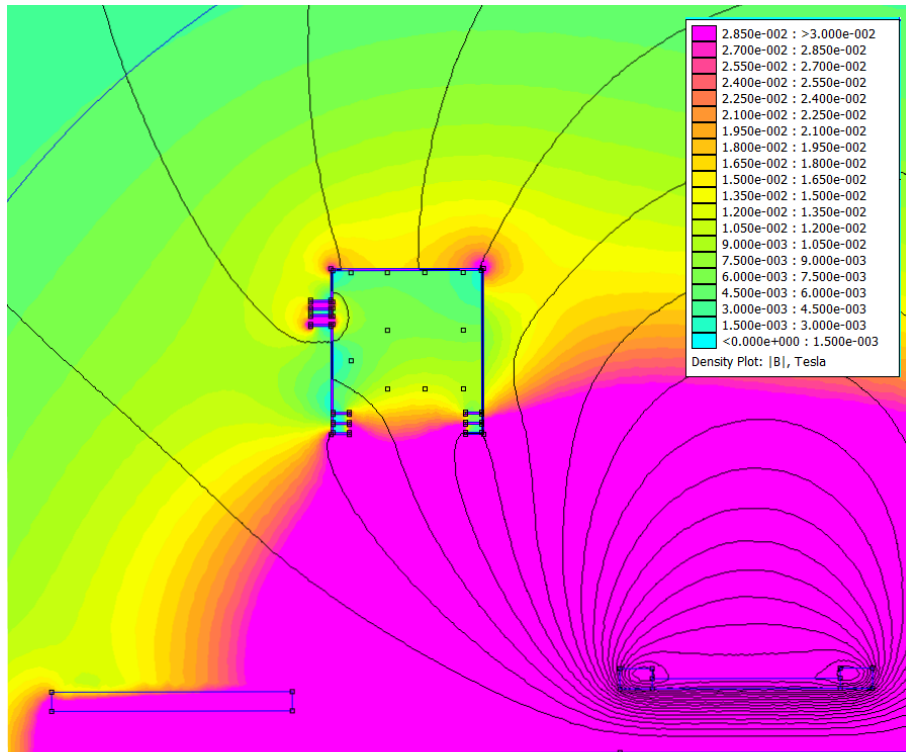


Figure 3.5.: Magnetic shielding calculations with FEMM [68] - Fields are generated by the superconducting coil bottom right and the normally conducting coil bottom left. The intensity map ranges from 0 mT to 30 mT. The 5 mm iron shielding is strengthened to the lower opening (TMP inlet) and the side feed-throughs. Position of the TMP and its controller is indicated. The absolute field in the area of the pump is successfully reduced to < 15 mT.

for the mid chamber has been positioned further away by increasing the length of the intermediate piping compared to the TMP at the E-gun chamber. A map of the magnetic fields at the position of the turbomolecular pump without shielding is given in figure 3.4 (simulated with Magfield3 [67]). The fields parallel and perpendicular to the rotor axis are more than an order of magnitude too high compared to the acceptable field strengths measured for a similar pumping model (Leybold MAG W2800) with magnetic bearing. This calculation shows that a magnetic shielding is ultimately required.

First designs for magnetic shieldings have been made with the software FEMM [68] implemented as axially symmetric calculations with respect to the Z-axis. Simulations using a variety of materials showed that a high saturation magnetization is more important like the magnetic permeability. A good candidate is ST-37 steel - a non-austenitic, cost efficient and easily machinable material with a saturation magnetization of slightly above 2 Tesla [65]. The FEMM-simulations use the magnetization data from ST-37 steel measured by the TMP test stand, the real positioning of the axially symmetric coils at the Rearsection and realistic dimensions for the magnetic shielding of the TMP. The magnetic shielding has a minimum diameter of 280 mm due to the size of the TMP and its integrated controller along the largest axis and is limited in height by a valve between TMP and mid chamber. Holes in the shielding are integrated to take account of cabling and gas outlet of the turbomolecular pump. The overall setup and the resulting field with an exemplary shield design are shown in figure 3.5. The results showed that even with thick or sophisticated shields the magnetic field strength exceeds 3 mT perpendicular to the rotor axis at some positions within the prospected TMP rotor position. The perpendicular field strength of 3 mT has been the limit of operation for another TMP at previous measurements [66]. On

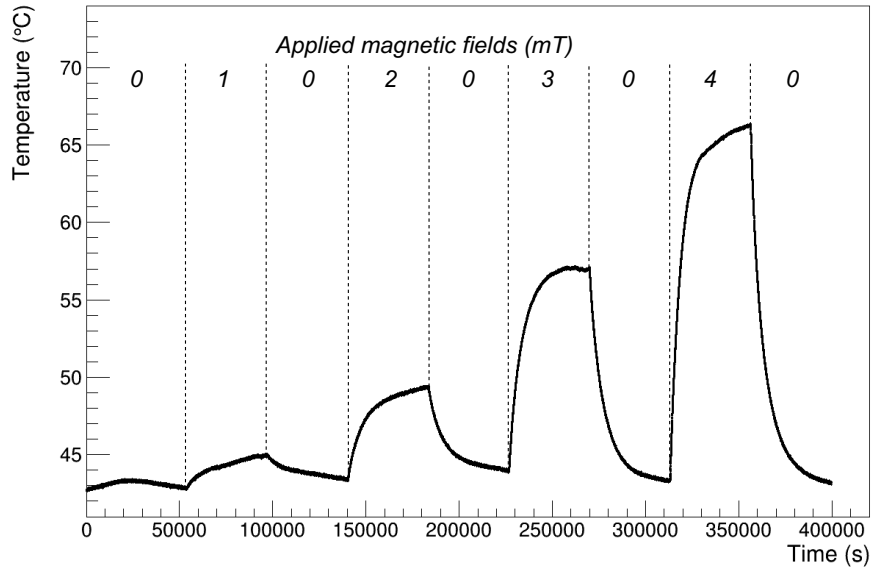


Figure 3.6.: Magnetic heating of a turbomolecular pump - Measured temperature increase of the TMP rotor blades by the application of a magnetic field transversal to the rotor axis. Each heating cycle is followed by a cooling cycle with 0 mT external field until the field-free value is reached again. Due to the water cooling the pump remains in an acceptable temperature range even at a field of 4 mT.

the other hand the magnetic shielding reduces the field strength parallel to the rotor axis below any limits that have been found in the previous measurements [66]. The limitation of these calculations are very obvious: It is not assured that the same maximum field ratings are valid for the final TMP model of the Rearsection. Even in the case the maximum ratings are still valid, there is an important difference of the designed magnetic shielding to a real one: The complete simulation is axially symmetric which does not only apply to the axisymmetric solenoids but also to the magnetic shielding. Therefore, the magnetic shielding is not shaped like a local cylindric or elliptic container but more like a large torus which is opened in one direction. This will definitely change the field strength within the shielding. Hence, the calculations with FEMM helped for the first design steps but more detailed investigation has been necessary.

The strategy to design a reliably sufficient magnetic shielding should consist of 3 independent steps: At first the performance of the selected TMP in magnetic fields must be measured with the available test stand. Next is the measurement of the efficiency of a generic magnetic shielding made of the preferred material to calibrate the shielding simulation. The last step is to design a magnetic shielding with the calibrated simulation which reduces the magnetic field inside of the shielding to a range which has been measured to be acceptable in step one. The measurements of the maximum rating for the turbomolecular pump has been carried out at the test stand. A picture of the test stand is available in figure 3.7. The measurement conditions should replicate the situation at the Rearsection - the TMP orientation is equal and in both cases water cooling (20°) is used. Measurements have been conducted with the magnetic field created by the Helmholtz coils parallel and perpendicular to the TMP rotor axis. The field was increased until the pump controller stopped the pump or the pyrometer measuring the rotor blade temperature indicated a value of $> 90^\circ\text{C}$. The magnetic field dependence of the reached equilibrium temperatures is provided in graph 3.6. More details about the measurements procedures at the magnetic field test stand are available in [66].

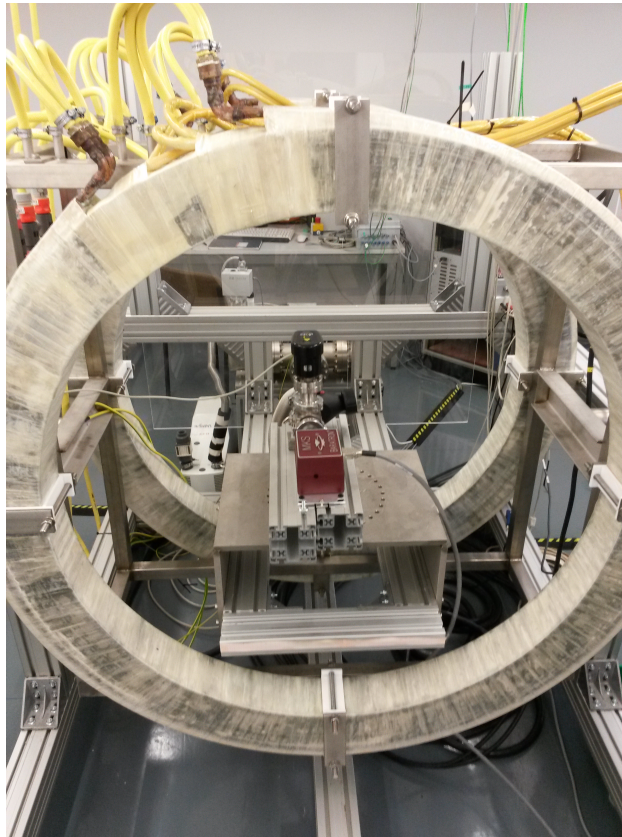


Figure 3.7.: Magnetic field compatibility test stand - The large water-cooled Helmholtz coils can create a homogeneous magnetic field of up to 50 mT in the central test volume. In this case two pressure sensors are installed for the field compatibility tests.

The maximum acceptable fields and the corresponding temperatures in the TMP are listed in table 3.1. The most important results were the limitation of 4 mT for a magnetic field perpendicular to the rotor axis and 8 mT for a parallel field. The maximum parallel magnetic field was found at a unusual small value and with a high directional dependency. Since the magnetic field of KATRIN is directed from the main detector towards the source [69], the TMP in the Rearsection is operated in the sensible orientation. Hence, the magnetic field limits for both directions have been successfully found at the field compatibility test stand. Knowing these limits the magnetic shieldings were designed by an expert from CERN with the finite element software Opera 3D by COBHAM⁵. After several design iterations the result is an TMP shielding of 8 mm thick ST-37 steel with an inner diameter of 224 mm and a height that extends over the TMP height by 105 mm [70]. At the bottom on the last 66 mm the diameter is restricted to 174 mm in order to further reduce the field strength entering the TMP through the shielding opening. With the applied shielding at the Rearsection electromagnetic design the maximum magnetic field perpendicular to the rotor axis is $B_{\perp,\max} = 2$ mT and the maximum parallel field is $B_{\parallel,\max} = 5$ mT. The field maps are available in figure 3.8. No calibration with a experimentally measured steel shielding has been performed yet. Still, OperaFEA is a professional software package which was successfully tested and used in many large scale experiments with strong magnetic fields (an example for a dedicated test is given in [71]). Therefore, the results are considered reliable and the shielding will be realized as recommended in the report. The shell will be made of two parts which overlap when they are connected. Any hole in the shielding which is necessary for feed-throughs (electric connections, gas inlet/outlet, water cooling) will be enclosed by a small cover of the same steel as the shielding.

⁵Cobham plc, Brook Road, Wimborne, Dorset, BH21 2BJ, UK

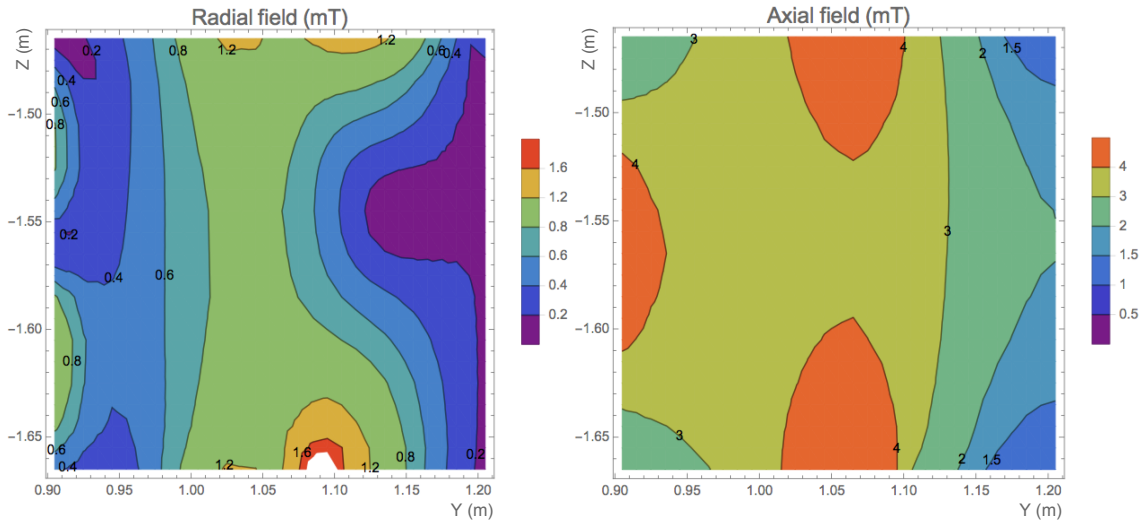


Figure 3.8.: Magnetic shielding calculations with OperaFEA - Map of the resulting B-field in radial (left) and axial (right) direction with respect to the TMP rotor axis. The TMP opening is directed to the left. The designed 8 mm shielding with bottom extension & restriction and a coil current safety margin of 20 % are applied. Due to the successful shielding the remaining radial B-field is smaller than 2 mT and the axial B-field stay smaller than 5 mT. The highest values result of the uncovered ports for the gas outlet and the electric connections at top and bottom (calculations and graphs by [70]).

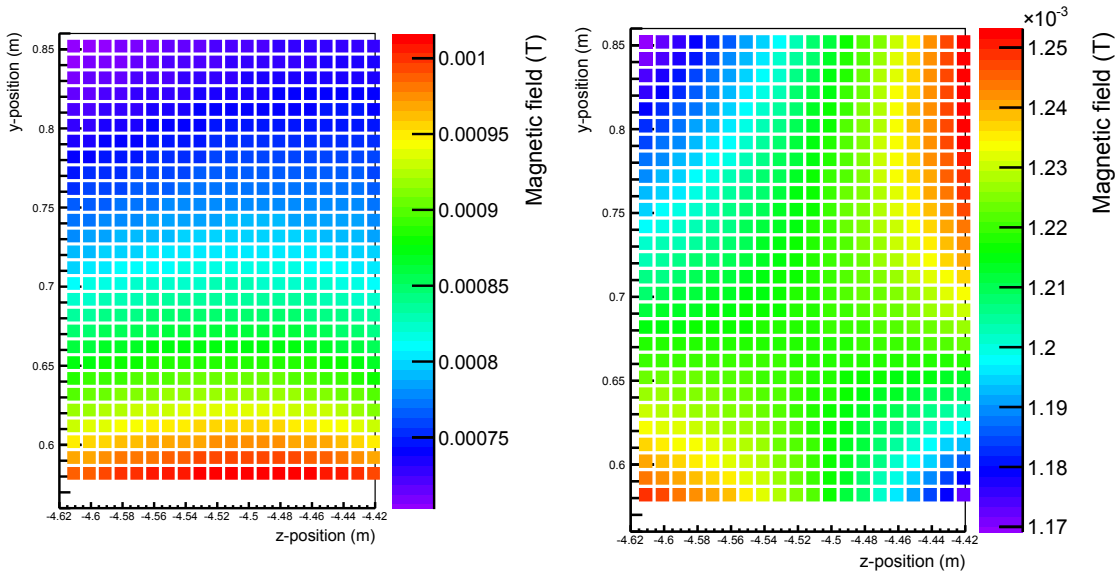


Figure 3.9.: Magnetic field at the E-gun TMP position - Field maps for the turbo-molecular pump evacuating the electron gun chamber. The fields have been calculated for the final TMP position in the symmetry z-y-plane without any shielding. On the left is the B-field component parallel to the rotor axis and on the right the component radial to the rotor axis. Without shielding the B-fields are always in the accepted range and therefore no shielding is required for this pump.

Table 3.1.: Magnetic field limits for Leybold MAG W600 Turbopump - In dependence of the field direction relative to the turbo-pump rotor axis. In radial direction the magnetic heating of the rotor blades limits the maximum field. Measurements at a relatively strong radial field of 4 mT still resulted in an acceptable temperature for long term operation. In axial direction the controller can indicate a bearing failure resulting in an undesired pump stop. The pump was only sensitive if the magnetic field was directed from high vacuum (HV) to pre vacuum (PV) flange and not vice versa. At KATRIN the TMP runs in the HV->PV mode. The pump was installed with the HV side to the floor as at the Rearsection. In the case HV flange upwards the field limits for HV->PV were even lower by up to 2 mT.

B-field direction	B-field strength	B-field pulsed	Pump status	Failure reason
Axial (PV->HV)	40 mT	no	No failure	-
Axial (PV->HV)	40 mT	yes	No failure	-
Axial (HV->PV)	9 mT	no	Failure indicator	Bearing stability
Axial (HV->PV)	5 mT	yes	Failure indicator	Bearing stability
Radial	1 mT	no	T = 45 °C	-
Radial	2 mT	no	T = 49 °C	-
Radial	3 mT	no	T = 57 °C	-
Radial	4 mT	no	T = 68 °C	-

The other TMP which evacuates the electron gun chamber is not threatened by magnetic fields, since the closest solenoids are only normal conducting coils. With magnetic fields of 1 mT along the rotor axis and 1.25 mT transverse to the rotor axis the TMP will work properly without magnetic shielding. The corresponding field map is given in figure 3.9. But there are three further instruments close to the re-condenser magnet that might be influenced or disabled by the magnetic field: An MKS⁶ Baratron 690A pressure sensor, an MKS cold cathode type 903 and a scroll pump (Edwards⁷ nXDS6). The cold cathode pressure sensor is placed in the large second containment, while the other 2 instruments are placed on the floor of the small front second containment of the Rearsection. All three instruments have also been tested for their maximum magnetic field in the test stand in order to design appropriate shieldings or change the operating position. The test of the scroll pump is a rather simple functionality test: At increasing magnetic fields the pump is supervised for malfunction or failure. In contrast to that the pressure sensors are continuously operated at increasing fields and changes in their readouts are recorded. This can be used to calibrate the sensors with the magnetic field at their operating position.

The Edwards XDS scroll pump is a fore vacuum pump that is used to evacuate the detector volumes of the BIXS system (compare section 5.5). In the magnetic compatibility tests it was possible to completely stop it with a field of at least 45 mT in the most sensitive field direction. In the other directions an audible stress noise was created at fields of 30 mT and 40 mT respectively. Still the pump continued running at fields up to 50 mT in these directions. But with regard to a safe long-term operation the magnetic limit is defined to 20 mT. As consequence the pump definitely needs a displacement or a dedicated magnetic shielding because without modifications the fields at its position reach up to 60 mT. A map with absolute magnetic fields at the preliminary position at the Rearsection is provided in figure 3.10.

⁶MKS Instruments, 2 Tech Drive, Suite 201, Andover, MA 01810

⁷EDWARDS GLOBAL HEADQUARTERS, Manor Royal, Crawley, West Sussex, RH10 9LW

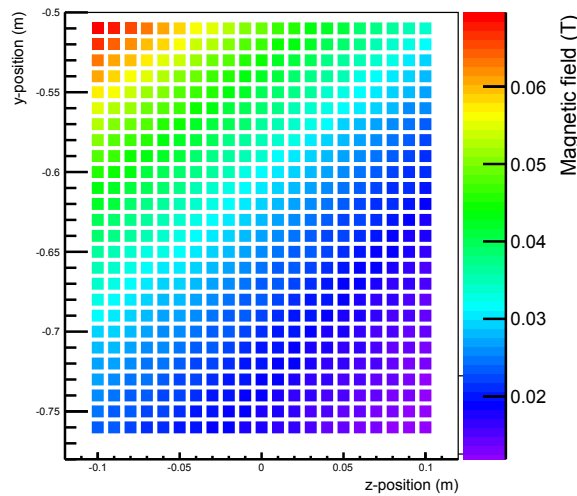


Figure 3.10.: Magnetic field at the Edwards scroll pump - Map of the absolute B-field at the preliminary position of the scroll pump which evacuate the small detector volume for the BIXS system. The simulation results show that a shielding is required which reduces the magnetic field strengths in the area of the pump by at least a factor of 2.

The cold cathode pressure sensor MKS 903 (compare figure 3.11) measures the vacuum pressure by the electric conductivity of ionized rest gas. The sensor uses a strong permanent magnet to measure the pressure with a gas type dependent calibration. Because of the internal permanent magnet, this sensor has been expected to react sensitive to the external magnetic fields. But the test measurements proof that the sensor acts robust in an external magnetic field: The cold cathode continues to measure at fields up to 30 mT in any field direction. Still, the sensor's accuracy suffers under the external field and the readout drifts (dependent on the field direction) by up to 10 %. The pressure dependence of the analog readout value are given in the graph 3.12 and 3.13. Because all cold cathode sensors at the Rearsection will be used in magnetic fields smaller than 30 mT, there is no risk of a magnetic field correlated failure. To receive more accurate values the sensors can either be calibrated for the magnetic field at their operating position or encased by a small magnetic shielding.

The last instrument tested was a MKS Baratron 690A (compare figure 3.11) with the high precision option and temperature stabilization. It is foreseen to measure the pressure in the Rear Wall chamber down to 10^{-5} mbar with a higher accuracy than the usual hot or cold cathode sensors. The sensor measures the pressure in a gas type independent manner by actually measuring the mechanic force on a membrane. The readout works by a precise readout of capacitors which are coupled to the membrane. The working principle itself is not dependent on magnetic fields but the sensor is placed in a position close to the superconducting magnet which makes a test of the compatibility reasonable. The results of this test were unexpected: In the direction along to the VCR connector the sensor is extremely sensitive on the magnetic field. The readout remains stable for field values of 0 - 1.6 T but at a higher value > 1.75 T the readout value changes to 0.1 mbar which is the full scale value of this sensor. This behavior could either be caused by a slight magnetism of the membrane and/or the capacitors or an extremely sensitive readout electronics. The perpendicular direction in the horizontal plane is also very field dependent. In the measured magnetic field range 0-23.4 mT the readout values vary between $4 \cdot 10^{-6}$ mbar and $6 \cdot 10^{-4}$ mbar while the repeatedly measured value with no field is steadily at $1.1 \cdot 10^{-4}$ mbar. This might be another strong magnetic field dependency or it is caused by a slight misalignment resulting in a small partial field into the extremely sensitive direction. Compared to these figures the pressure sensor is relatively robust in the vertical direction



Figure 3.11.: Pressure sensors tested for magnetic field compatibility - Pictures of the MKS 903 cold cathode (left) and the MKS Baratron 690A (right). The definition of the coordinate system allows to differentiate the field directions and is valid for both sensors. Photos used with permission of MKS Instruments.

where it was tested up to 30 mT. The readout value increases continuously from $2.6 \cdot 10^{-4}$ mbar to $4.9 \cdot 10^{-4}$ mbar. In the graphs 3.14 and 3.15 the dependency of the readout values on the magnetic fields are shown. The results of the Baratron sensor are the most unexpected and clearly show that a magnetic shielding is required. The original close position to the superconducting magnet and Rear Wall chamber, chosen to shorten the pipe length and improve the accuracy of the pressure measurement, can not be kept. The maximum absolute B-field in the used volume would have been in a range from 120 mT to 260 mT which can not be shielded down to a compatible value. The sensor must be aligned that it uses the field free direction of the axisymmetric KATRIN field for the most sensitive direction of the MKS 690A. Furthermore, the pressure sensor will be moved 10 cm to 20 cm away from the superconducting magnet and will be tightly enclosed by a thick, possibly multi-layered magnetic shielding. The shielding will be designed by a professional company but this process is not yet completed. Another recommendation derived from the measurement results is to check all Baratron type sensors which are placed in strong magnetic fields regions - not only for the Rearsection but for the whole KATRIN experiment. Concerning the Rearsection there are two further Baratron sensor types (MKS 626 and MKS 722) installed at not less than 5 potentially hazardous positions.

3.1.3. Sensors and controlling

The vacuum system of the Rearsection requires more instrumentation than just the vacuum containment and pumps. To monitor pressure development and stability during evacuation and operation the installation of different pressure sensors is required. Also the large valves installed at the primary system (compare section 3.1) are insufficient to control the Rearsection gas flow and must be completed by small manual and automated valves. To achieve the pressures of an ultra high vacuum ($\leq 10^{-7}$ mbar) it is necessary to bake out the system which requires heating tapes for bake-out and temperature sensors for monitoring. Finally, the system shall be vented with purge gas which requires an appropriate purge gas connection and a flow controller to vent the system in a regularized way. Venting with a purge gas has two benefits: On the one hand it transports fewer impurities and water into the system compared to venting with atmospheric gas and on the other hand it is possible to reduce the tritium inventory by flushing the system multiple times (e.g. with hydrogen). In the following all the named sensors and control instrumentation are

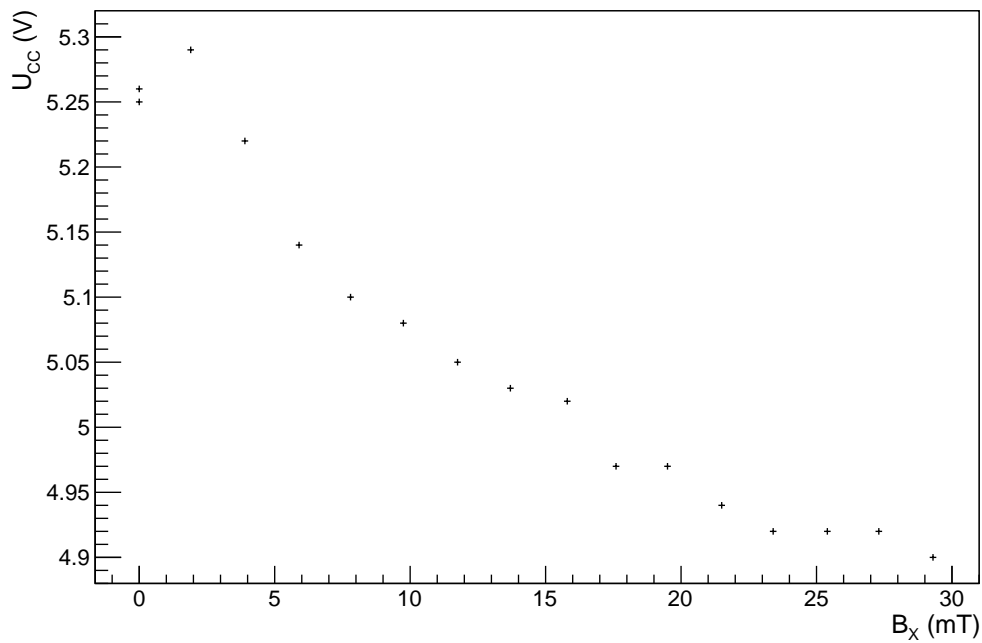


Figure 3.12.: Cold cathode pressure sensor readout value in dependency of the magnetic field - With a B-field in x-direction (the behavior for y-direction is nearly identical) the linearized analog output value drops by about 0% within 30 mT. The main error source is the instable pressure as indicated by the double measurement for the zero-field case which differs by 10 mV before and after the field measurements.

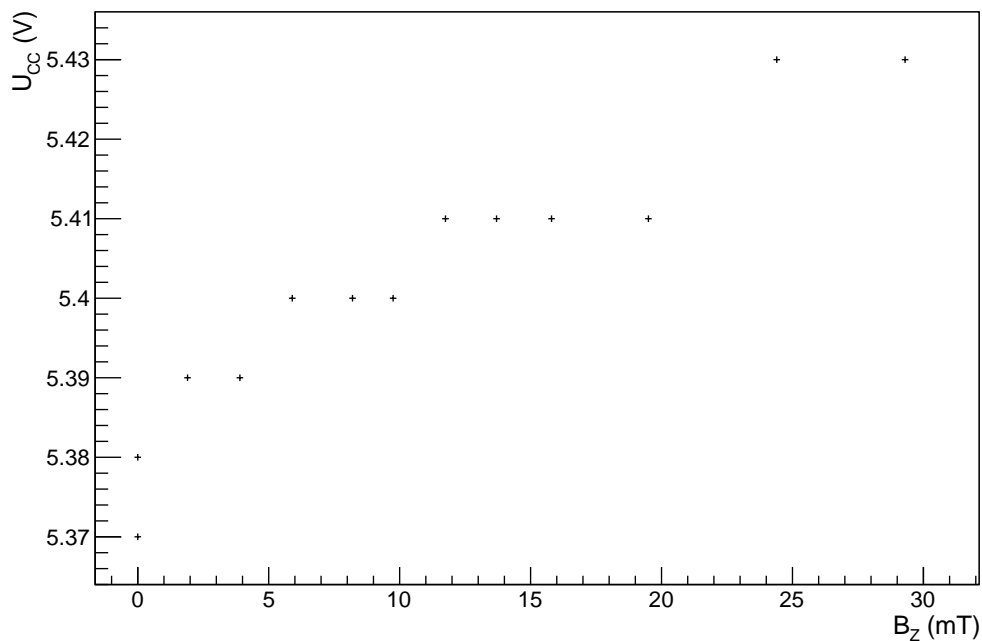


Figure 3.13.: Cold cathode pressure sensor readout value in dependency of the magnetic field - With a B-field in z-direction the analog output value is only weakly affected. Results stray at about 1%. The error is again approximately 10 mV caused by the instable pressure.

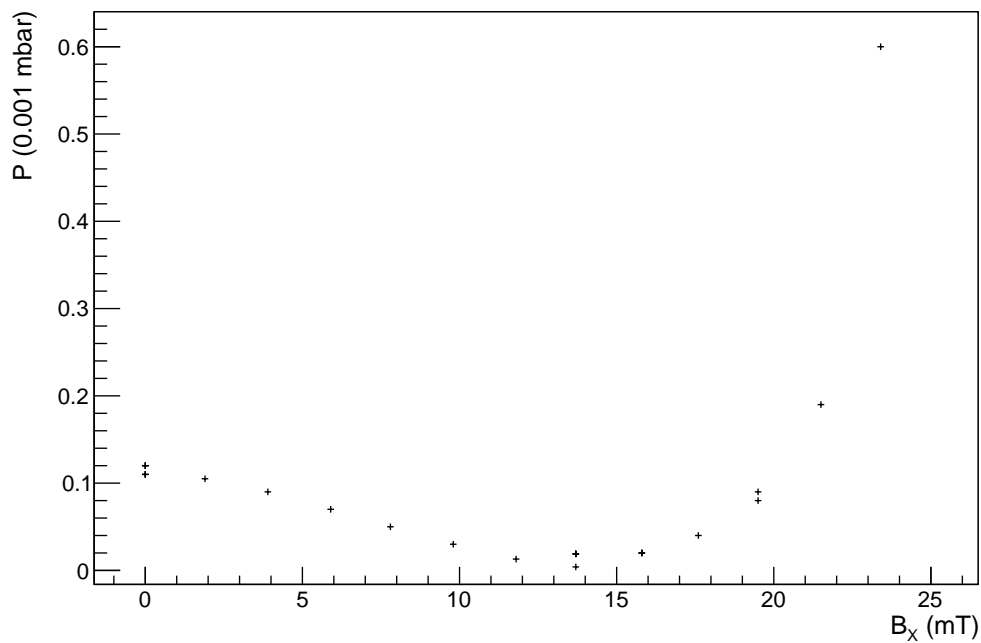


Figure 3.14.: Baratron pressure indicator value in dependency of the applied magnetic field - This sensor reacts very sensitive to changes of the magnetic field in x-direction while the pressure remain relatively stable. The even more critical y-direction is not shown because it equals just a step function when the critical B-field (1.75 mT) is exceeded.

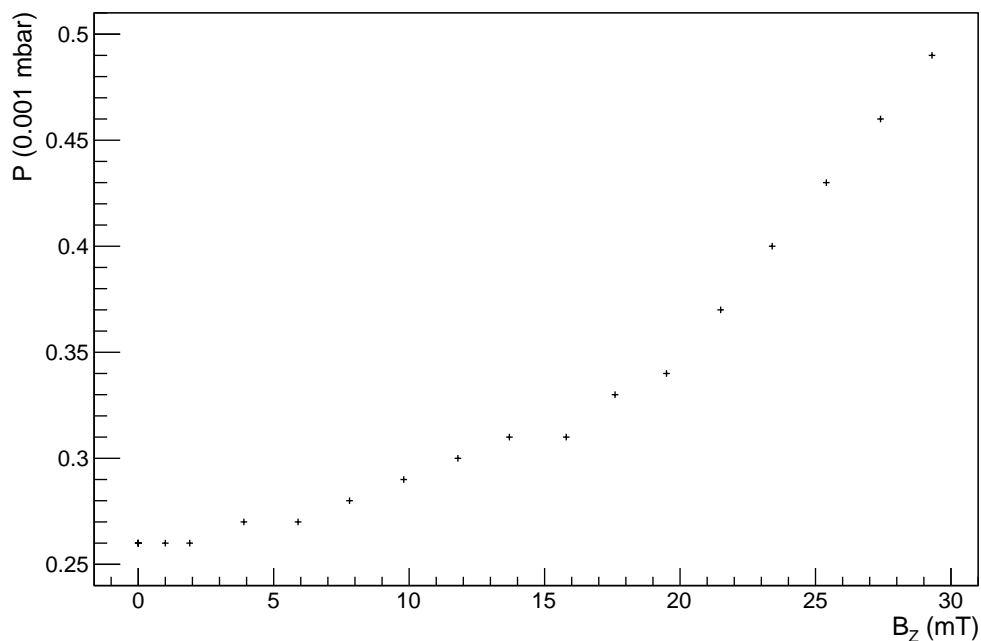


Figure 3.15.: Baratron pressure indicator value in dependency of the applied magnetic field - A vertical magnetic field change by 30 mT results in a doubling of the pressure output value at the MKS 690A. Still this field direction is the least sensitive for the Baratron pressure sensor.

described in more detail.

The pressure sensors must be able to cover a pressure range from 10^{-8} mbar up to atmospheric pressure. There is no commercially available pressure sensor with a single measurement principle to cover the full measurement range. This can be solved by combining pressure sensors of different types. The following measurement principles and pressure sensors are used at the Rearsection:

- Piezo resistive pressure sensor: This sensor covers only the coarse vacuum range from $\mathcal{O}(1 \text{ mbar})$ up to atmospheric pressure. The principle uses the mechanical force of gas pressure on a surface. The sensitive surface in this case connects to a piezo resistive material which changes its resistance depending on the force which is applied to the crystal. Only one pressure sensor of this type is used - the MKS 902.
- Pirani based pressure sensor: The measurement principle uses the pressure dependence of thermal conductance of gases. This allows measurements up to atmospheric pressure but with a larger range than piezo-based sensors. The disadvantage is the strong dependence on the gas elements in the gas mixture. The Rearsection will have several MKS type 317 with a pressure range from $1.3 \cdot 10^{-3}$ mbar to 1333 mbar installed.
- Capacitive pressure sensors: This type of sensor also measures the mechanical force on a surface. In this case the surface is a sensitive membrane which is as well part of a capacitor. Very small forces on the membrane change the shape and the capacitance of the membrane to a reference electrode. The method is gas independent but the range is limited to typically limited to 3 to 4 orders of magnitude in pressure while the full scale pressure can be chosen from 0.1 mbar to atmospheric pressure. At the Rearsection there are 2 MKS 720 planned with a full scale of 13 mbar and one MKS 690 A sensor with a full scale of 0.13 mbar.
- Cold cathode sensors: For the high vacuum and ultra high vacuum range, cathode pressure sensors are required. These instruments measure the pressure of the remaining gas by its electric conductivity. Currents are transported by ions which are either excited with a filament (hot cathode sensor) or available in the rest gas which is then further ionized by electric fields (cold cathode sensor). At each, the mid and the e-gun chamber, one of these sensors is planned.

A combination of pressure sensors for rough vacuum (piezo resistive or pirani based) and fine vacuum (capacitive or cold cathode) are planned at every high vacuum chamber of the Rearsection. The goal is to cover the full range from atmospheric pressure down to the prospected vacuum pressure as determined in the calculation in section 3.1.1. The detailed usage of pressure sensors is visualized in the flow plan in figure 3.16. Besides the sensors for pressure monitoring in the main chambers of the Rearsection, some other sensors are required to measure the pressure at the inlets or outlets of pumps, the pressure in the BIXS chambers or the pressure in the purge gas line. These pressure sensors can be used to define interlocks to safety valves which react if a certain pressure value is exceeded. The safety valves are all automated and steered by compressed air. The large CF valves installed at the Rearsection are complemented by smaller Swagelok VCR valves which control the gas flow in the outer area of the Rearsection. The small valves are automated if required or manually steered otherwise. The valves can be set-up to individually evacuate or vent any of the 3 Rearsection chambers (Rear Wall chamber, mid chamber, E-gun chamber) additionally to the normal operation. All valves and pressure sensors are part of the primary system and in contact with tritium. Therefore, they only use full metal seals to close the vacuum system and expose only metals and ceramics to tritium. The large CF250 valve between WGTS and Rearsection and the two CF160 valves to shut off the

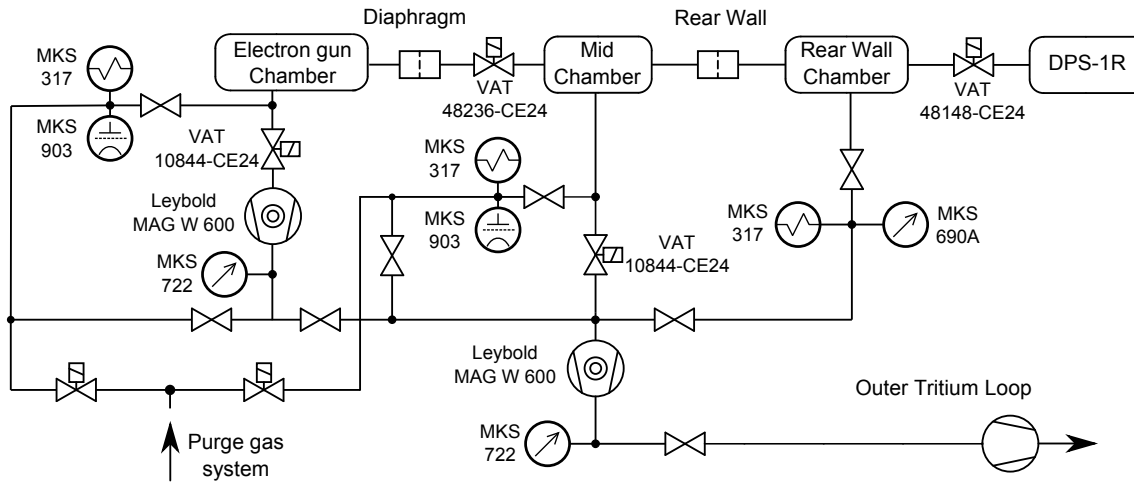


Figure 3.16.: Vacuum schema of the Rearsection primary system - The schema shows the main chambers and the apertures in between for differential pumping. Multiple valves (automatic and manual) and pressure sensors allow to control and monitor the vacuum system. Two turbomolecular pumps evacuate the vacuum chamber and pump the gas towards the outer loop. Roughing pumps at the outer loop prepare the necessary fore vacuum for the TMPs. If required purge gas can be inserted at different sections of the system.

turbomolecular pumps are an exception of the previous rule: They expose an internal VITON⁸ seal to the vacuum volume - nevertheless they use only full metal seals between vacuum and ambient. Similar valves are also in use between other main components like WGTS/DPS and DPS/CPS.

A system bake-out of all high vacuum chambers is possible by redundant systems of heating conductors and temperature sensors. The intention is to use heating tapes from Thermo-coax⁹ which can be directly welded to the stainless steel CF pipes. The maximum target bake-out temperature is 150 °C to protect the sensitive in-vacuum installations of the Rearsection like thin deposited layers or electronics. The heating power in the thermocoax is limited since they are supplied by an adjustable transformer and additionally regulated by a controller. This controller uses the feedback from either thermo couple or Pt100 temperature sensors to steer the heating current. The temperature sensors are always installed nearby to the corresponding heating tapes. A system bake-out is necessary prior to the first start-up and after each venting process to remove water from the surfaces and reach a better final vacuum pressure. For a well-defined venting a dedicated purge gas connection is foreseen at the system. Any gas source stored in a gas cylinder can be installed to the purge gas connection and vent the system controlled by a flow meter. Since the gas source is placed outside of the tritium safety containments, a one-way valve shall avoid any back streaming of tritium.

3.2. Tritium safe second containment

The second containment is an additional safety measure to protect the environment in the laboratory from the tritium inside of the primary system. Its properties are also defined in the TLA documentation (AK II) similar to the requirements for primary system components (AK I). The containment is a barrier for tritiated gases or fluids in any moment the primary system has either leaks or is intentionally opened (e.g. for construction or maintenance). The leak tightness of a second containment can not match up with the leak tightness of a properly closed primary system. The TLA requires a maximum leakage

⁸VITON is a trademark of the company DuPont Performance Elastomers

⁹Company THERMOCOAX SAS, 40 bd Henri Sellier, 92156 SURESNES CEDEX, FRANCE

rate of 0.1 % of the contained AK II volume per hour (at a pressure difference of < 5 mbar towards the laboratory atmosphere). To ensure that tritium in the second containment can not diffuse to the ambient laboratory atmosphere, the containments are kept at pressure below the atmosphere and the contained air is circulated and filtered 5 times per hour by tritium retention systems (TRS). Additionally, a permanent tritium activity monitoring of the air inside a second containment needs to be installed which is always realized by a sensitive windowless ionization chamber with active gas pump system. To enable manual access to the components stored inside the second containment it is common to attach polycarbonate windows with multiple glove ports at the side walls of the containment. As a result 2nd containments are often also referred as “glove boxes”. The windows are bordered by a steel frame, attached via bolts and welded threaded bolts and sealed with Ω -shaped sealings. The bolts are placed with a maximum distance of 150 mm to each other to ensure a uniformly pressed sealing. These glove boxes are completed by feed-throughs to transport signals, electric power and possibly gaseous or liquid media between the inside and outside of the box. Interfaces between boxes, for example a gas transport line, maintain the principle of double containment: These lines are always constructed as double-shell pipes. Components and instrumentation can be transported into a box using airlocks if available. In rare cases a box needs to be opened which is possible in an operation called “intervention”. In the scope of an intervention it is possible to take windows or side wall modules off in strict accordance with the TLK safety requirements for this kind of operation. There is an exception concerning the requirement of enclosing an AK I primary systems in an AK II second containment: A closed second containment or a glove box is only required if the activity in the primary system exceeds 10^{10} Bq. Below this threshold a partially closed box or a fume hood can be sufficient. The discussion if an AK II conformal second containment is necessary and how it is realized at the Rearsection is described in the following section.

3.2.1. Second containment implementation at the Rearsection

The decision if a second containment is required at the Rearsection depends on the contained total activity in the primary system. The tritium amount in the gas phase can be derived from the pressure and volume calculations in 3.1.1. The gas amount of tritium in the Rear Wall chamber is $6.9 \cdot 10^{-9}$ mol and the resulting activity is 14.8 MBq. In the mid chamber the amount is reduced by the first turbomolecular pump to $2.4 \cdot 10^{-12}$ mol which equals to an activity of 5.2 kBq. In the volume backwards from the CF63 full metal valve to the E-gun chamber the remaining amount of tritium is $1.5 \cdot 10^{-11}$ mol corresponding to an activity of 32.8 kBq. Summed up the overall activity in gaseous phase within all high vacuum chambers of the Rearsection is only 14.8 MBq and therefore significantly lower than the threshold for a glove box ($> 10^{10}$ Bq). But in fact the gaseous tritium in the high vacuum chambers during normal operation contribute only a small part of the real or potential contamination in the system. To these amounts an unknown amount of tritium dissolved into the stainless steel has to be taken into account. Although stainless steel is considered as impermeable material significant amounts of hydrogen isotopes can be absorbed in the bulk [72].

Another major contribution to the radioactivity within the system is the fore-line vacuum line of the mid chamber TMP. The volume within the box is comparably small with 0.5 l but the pressure in the volume is many orders of magnitude larger compared to the high vacuum chamber. The precise end pressure which is achieved in the fore line depends on pumping performance and gas conductance towards the ISS outer loop. This issue will be discussed in more detail in section 3.3.2. Further on a worst case assumption with a pressure of 1 mbar in the fore line is used. This adds an amount of $4.3 \cdot 10^{10}$ Bq to the total activity. Obviously the worst-case value exceeds the threshold where a designated

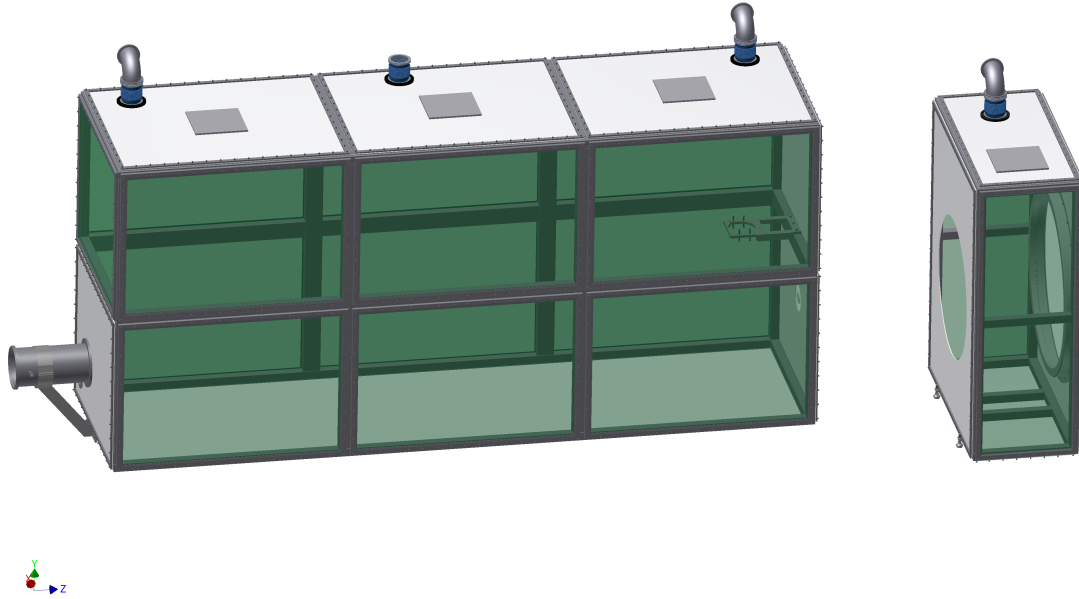


Figure 3.17.: Second containments of the Rearsection - Both glove box designs as they were submitted to a manufacturer. Distance and position equals to the situation in the final setup. By the design the following parameters have been defined: Dimensions, usage of steel plates/glass, usage of an airlock, TLK infrastructure connections and flexible mounting panels on top.

second containment as described in the TLA is required. Therefore, the cautious decision has been made to realize the Rearsection with a full glove box system - especially due to the additional unknown amount of tritium which can be absorbed in the vessel walls over time. With this decision a 2nd containment for the Rearsection has been implemented in several iteration steps. The glove box is optimized for construction and handling of the contained primary system while it also needs to fulfill all safety and space requirements by the TLK. A CAD drawing of the second containment design is presented in picture 3.17.

In the following the 2nd containment is described from the WGTS-side to the further end of the Rearsection. The Rear Wall chamber is surrounded by a very compact glove box due to space constraints on both ends: On one side the end cap of DPS1-R/WGTS and on the other side the re-condenser magnet which has a maximum distance to the DPS1-R to avoid an unacceptable drop of magnetic field strength. Mainly the box design is common practice with a stainless steel frame which is closed by either windows with glove ports or metal sheets. On the front side a deviation from the standard is required since the end cap of the DPS1-R cryostat reaches into the box. This is necessary since the DPS1-R has no dedicated connection interface for the second containment of the Rearsection. Instead, this is solved by a custom adapter ring which installed to the cryostat end cap connection sealing the glove box to the atmosphere according to the TLK safety standards. On the back side of the glove box follows the superconducting re-condenser magnet. An important design goal was to keep the superconducting magnet outside of second containments. This ensures easy access for cryogenic refilling and enables in case of a magnet defect the withdrawal of the uncontaminated magnet from system for repair action. To achieve this the Rear Wall chamber connects to a pipe which continues the second containment through the superconducting magnet. On the other end of the pipe the large containment of the Rearsection is attached. The containment pipe includes a metallic bellows below to avoid a rigid mechanical coupling of the two containments. The large glove box

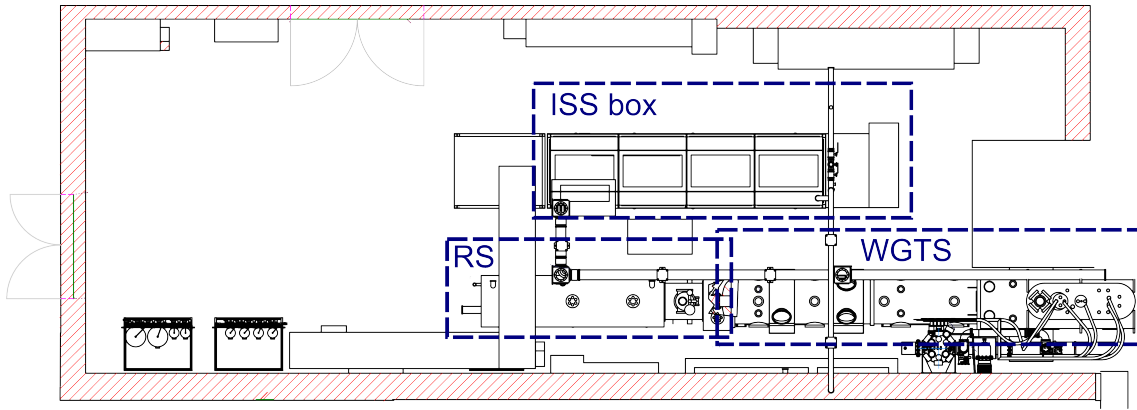


Figure 3.18.: Rearsection placed in building 452 - Drawing of the most recent Rearsection model placed at the final position in the experimental hall. It is connected to the WGTS with an overlap by the second containments connections. The nearby ISS box is an essential system for the tritium handling.

comprises the mid and the E-gun chamber as well as all other related instrumentation for the electromagnetic design. The glove box has an overall size of $4 \times 1.1 \times 1.85 \text{ m}^3$ ($l \times w \times h$) and is again implemented as steel frame closed with polycarbonate windows and steel sheets. In contrast to the small glove box it has an air lock of the diameter 220 mm and a tritium gas interface to the ISS box (compare section 3.3.2).

Both second containments share several other properties and requirements. Both systems use an activity monitoring with gas ionization chambers of the contained atmosphere as required for tritium safety. Any tritium amounts that is released into the air of the box is reduced by filtering the air through the tritium retention system (TRS). For this purpose the air in the containment has to be ventilated and fed through the TRS. The ventilation with a speed of 5 complete air changes per hour ensures that a tritium leak anywhere in the primary system can be quickly detected and the released tritium does not bottle up in the glove box. The two containments and the superconducting magnet are all placed on support structures of welded steel profiles to position the center of the contained vacuum parts on to the beam light height of KATRIN which is approximately 1.80 meters above the floor level. The large containment requires its own support but the superconducting magnet and the small glove box share a welded support system. These two support frames can be locked to each other by screws with the goal to fix their relative positions but not to share forces among them. Besides the normal weight of all boxes, parts and instrumentation, the support frames must be able to withstand an earthquake as safety requirement. Furthermore, the frame structure for the superconducting magnet has to withstand the horizontal attractive force of the magnet to the WGTS magnets. The force difference of approximately 15 kN (compare section 5.1.2) between the switched off and the fully ramped superconducting magnet must not cause a movement of more than 1mm in either support or magnet. Both support frames use fixed feet and floor plates to position them within the building. To move the Rearsection it is necessary to use air cushions at the support frames.

3.3. Interfaces to neighbor systems

Since the Rearsection is an end part of the KATRIN experiment, the amount of interfaces and restrictions by neighbor systems is reduced compared to all other components of the source and transport section (STS). Especially the length of the system could be adjusted incomparably easy because the Rearsection is only attached at one side to KATRIN components. Hence, the main dimension limitation are given by the laboratory

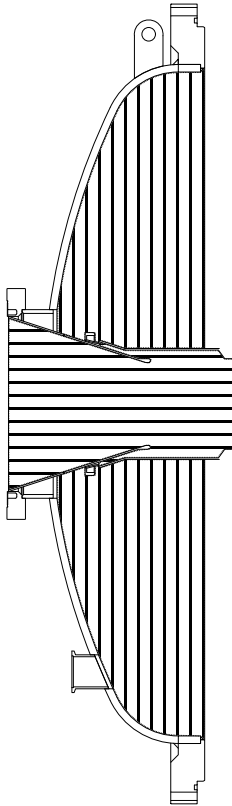


Figure 3.19: DPS1-R/WGTS end cap - simplified drawing of the DPS1-R end cap region. The cryostat encloses the second containment (vertically hatched) and the beam tube encloses the primary tritium system (horizontally hatched). At the DPS1-R ending flange towards the Rearsection both containments merge without a possibility to connect the Rearsection glove box. Adapted from [74].

and installations within the laboratory like control cabinets. The space limitations for the length of the Rearsection is naturally given by the WGTS to the front side and to the back side by a large stationary control cabinet. The control cabinet is a hard limit since its doors reach up into the z-axis of KATRIN when opened. The Rearsection in the current room planning of the designated laboratory space (TLK building 452) is visualized in drawing 3.18. The interfaces to the most important neighbor systems, the DPS1-R and the tritium infrastructure, are described in the following sections. Other technical relevant interfaces like floor load or media supplies have been evaluated and approved in the scope of a technical design report [73] and will not be described in the following sections.

3.3.1. Interfaces to the DPS1-R

The DPS1-R is the rear-side differential pumping section of the WGTS and the decisive interface component for the Rearsection to connect to the KATRIN experiment. The interface comprises the connection of the primary systems, the second containments and physical interfaces like the magnetic flux tube. The Rearsection has to adapt to the framework conditions given by the WGTS which has its parameters fixed since this component is in the end phase of construction.

The primary system of the DPS1-R ends with a non-rotatable CF250 flange. With the superconducting magnet in the configuration of the Rearsection the complete magnetic flux tube of the WGTS is transported further backwards. This enables the installation of a CF250 valve which officially separates the WGTS/DPS1-R from the Rearsection while the valve itself can not be clearly assigned to either of these components. The connection to a non-rotatable CF250 flange is the only definite technical requirement for the Rearsection at this point. Another requirement comes from the electromagnetic design which limits the distance between the most backward magnet in the DPS1-R and the most forward magnet of the Rearsection (the re-condenser magnet). If this limit is exceeded the magnetic flux tube touches the inner walls of the primary system (e.g. inside the valve) and is hence not fully transported anymore. This EMD limit is discussed in more detail in section 4.2.2.

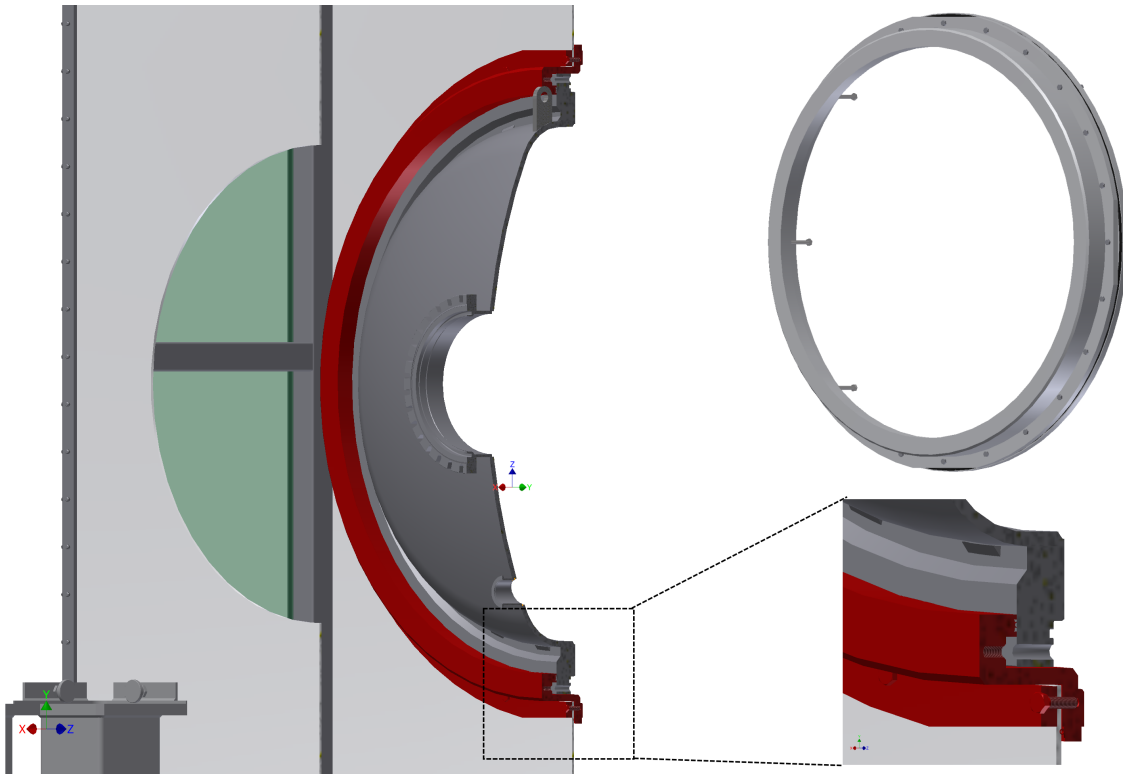


Figure 3.20.: Second containment adapter - The metallic ring allows to connect the Rearsection's 2nd containment to the WGTS cryostat while both containments remain hermetic. The left side shows the adapter installed at the WGTS, the top right shows the ring only and on the bottom right is a zoom view to the sealed interconnection.

The second containment situation is rather difficult at the interface of WGTS and Rearsection. The WGTS cryostat is a leak-tested encasement of stainless steel and therefore qualifies itself as second containment. But at the end flange of the DPS1-R towards the Rearsection, the first and second containment of the WGTS recombine to only one layer (compare drawing 3.19). Thus, the 2nd containment of the Rearsection has to be extended to include the CF250 valve and the DPS1-R end flange and hermetically¹⁰ connect to the DPS1-R cryostat. Especially this connection to the cryostat is challenging since the WGTS does not offer appropriate flat surfaces nearby the Rearsection and on the other hand any modifications of the design of the source component should be avoided. The final solution is an adapter ring additionally attached to the DPS1-R at the position where the end cap is fixed to the main cryostat by screws (compare figure 3.20). The adapter ring needs only a small part of the screws to connect in comparison to the amount of screws required to safely connect the end cap. The adapter ring provides a flat surface, a circular array of blind tapped holes and a sealing to connect the second containment of the Rearsection in a tritium safe way.

3.3.2. Interfaces to the tritium infrastructure

The tritium infrastructure systems enable the reduction of the amount of tritium in the first and second containment of the Rearsection again. The reduction of tritium is not only required for safety reasons but also with the goal of recycling of this rare gas. The Rearsection treatment is very similar to the handling at the DPS2 since both components can expect a similar inventory of gaseous, adsorbed and absorbed tritium.

¹⁰The overall system has to be conformal to the leak tightness requirements by the TLK.

The primary containment of the Rearsection connects to the TLK infrastructure via the fore gas line of the front turbomolecular pump. It ends at the outer tritium loop within the isotope separation system (ISS). The connection between the Rearsection and the ISS must be realized using a double shell pipe to maintain the safety concept of double containments. The fore pressure in this gas line required for a proper operation of the turbomolecular pump is provided by a TLK compliant system of two roughing pumps¹¹. The inlet pressure at the roughing pumps is approximately 10^{-2} mbar which results in a fore line pressure of approx. 1 mbar with the given gas conductance of the intermediate pipe of 1.91/s. Since the TMP can work with fore pressures up to 6 mbar, the pressure in the fore line is sufficient. All gas in the outer loop is not directly cycled within the ISS - instead it is forwarded to further TLK infrastructure for purification.

Finally, the gas in the volume within the Rearsection glove boxes requires appropriate handling. Tritium that evaporates from the primary system into the 2nd containment must be removed from the enclosed volume. This is independent if T_2 leaks from the primary system or evaporates when the primary system is opened on purpose for example for maintenance operations. To detect tritium within the glove box the volume is continuously monitored by an ionization chamber. The measured amount of activity is also reported to the TLK safety system to enable a fast reaction to excesses in the box activity. To reduce the tritium quantities evaporated into the second containment is the task of the Tritium Retention System (TRS). This method can only reduce but not completely remove the tritium within a box which means activity can remain in the second containment air or at the inner walls. The Rearsection has an advantage concerning long time contamination due to the small amounts of tritium in the primary systems in normal operation. These considerations about interfaces shall complete the description of the technical and mechanical details of the Rearsection. The next chapter will describe the electron gun and the electromagnetic design of the Rearsection in detail.

¹¹A combination of a metal bellows pump and a Normetex scroll pump

4. Rearsection electron gun and electromagnetic transport

The electron gun (E-gun) of the Rearsection is an important instrument of the calibration and monitoring systems (CMS) of KATRIN. The electrons from this artificial source shall imitate the full range of electron parameters which also occur at the tritium β -decay electrons in the WGTS. Furthermore, the parameters can be chosen precisely and are well known which enables many different calibration procedures for the source and transport sections, the spectrometers and the main detector.

The Rearsection consists of two essential parts required for an operational electron gun: The electron gun itself which is responsible for production and acceleration of electrons and an electromagnetic transport section to guide the electrons and optimize beam parameters. In the following sections, development and simulations of the E-gun and the transport section will be described independently. After defining all components and individually presenting their effects, the results of the simulated system, combined of electron gun and all the electromagnetic field sources of the transport section, are discussed. This chapter concludes with test experiments completed at KIT to develop or test essential instruments that are correlated with the E-gun functionality of the Rearsection.

4.1. Design of the electron gun

The following sections describe the working principles and different specific features of the Rearsection electron gun. The E-gun uses photoelectric emission from a metallic surface for electron production and a first acceleration step between two rotatable plates. The electrons are adiabatically guided into a stronger magnetic field followed by another acceleration step to the final kinetic energy in the so called “post-acceleration” stage. For a reliable long term operation of the electron gun the high voltage stability is important: Discharges can damage the E-gun or prevent a continuous operation. To clarify the high voltage stability, calculations have been completed and are presented in the upcoming sections. Finally, different UV light sources and options for the optics design are discussed.

4.1.1. Principles of photoelectron sources

The photoelectric emission of electrons from metallic surfaces is an understood effect since the beginning of the 20th century [75]. The emission is possible if a photon excites an

electron close to the surface with an amount of energy that is larger than the difference of the electron binding energy to the vacuum energy level. The minimum amount of energy required to release an electron via photoelectric effect is a metal surface specific value called “work function” W_F . A photon with an energy of $h \cdot f$ can emit electrons with a remaining kinetic energy of up to $E_{\text{kin}} = h \cdot f - W_F$. The concept of a work function simplifies the details about electron states within the solid and can be calculated as the difference of the Fermi level of the metal to the vacuum energy for perfectly clean and undisturbed surfaces at a temperature of 0 K. For real surfaces the work function is a distribution by thermal broadening and can be effectively changed by adsorbents, absorbents, impurities and electric fields. The work function is also an important property of the Rear Wall because of its impact on the source plasma potential. Further details about impact and evaluation of the Rear Wall work function are given in chapter 5. The effect of photoelectric emission to get free electrons is the preferable method to run the electron gun in the Rearsection. Theoretically there are other possibilities for the production of free electrons like thermionic emission or field emission from metallic surfaces. But these concurrent methods do not provide the target beam properties: The energy broadness and emission rate is difficult to control and the typical emission rates are orders of magnitude higher than the target electron gun rate of $\leq 10^5$ /s.

Once the electrons have been raised onto the vacuum energy level, their movement can be controlled with electric and magnetic fields according to the Lorentz force.

$$\vec{F} = q(\vec{E} + \vec{v} \times \vec{B}) \quad (4.1)$$

Typically an axisymmetric magnetic field is used to guide the electrons while an electric field parallel to the magnetic field lines accelerates the electrons away from the cathode. The resulting electron beam can further be guided or manipulated with electromagnetic fields. If the electrons kinetic energy transversal to the magnetic field line is not exactly zero, the electron will follow a cyclotron motion with non-vanishing cyclotron radius. If the electric and magnetic field in the acceleration region are not exactly parallel, the electrons will undergo an $\vec{E} \times \vec{B}$ drift.

4.1.2. Acceleration electrodes design

The electron gun acceleration stages are required to accelerate the emitted photoelectrons to the target kinetic energy. The absolute value of the electrons kinetic energy is only defined by the difference of the potential at the electrons point of emission and the electrons endpoint, which is the ground potential. It is not dependent on the precise behavior of the electrostatic potential in between. But the detailed electrode design determines another important parameter of the beam electrons: The polar angle Θ between the electron momentum and the magnetic field line. With the goal of adjustable angle and energy combined, with a narrow distribution of these two parameters, the E-gun electrodes have been designed as follows:

The itemization below refers to “adiabatic” or “non-adiabatic” acceleration. In this case the movement can be described as adiabatic when the kinetic energy transversal to the magnetic field lines $E_{\text{kin},\perp}$ is conserved. A more detailed discussion about adiabaticity is given in section 4.2.1.

- Non-adiabatic acceleration after photo emission: The electrons emitted from the gold surface of the cathode are directly accelerated by the electric field between the two rotatable plates towards the anode. For this purpose design value for the potential difference between the cathode and the anode (ΔU_1) is 1 to 5 kV. The absolute value of the cathode is set according to the kinetic energy the electrons finally shall have

when they arrive in volumes at ground potential. The anode potential is shifted into positive direction by ΔU_1 . At the beginning of the acceleration the electron velocity is small therefore the strong electric field dominates the electron movement. At this point of the electron path the magnetic moment increases if the plate normal is not parallel to the magnetic field. On the way through to the hole of the anode the electric field strength will drop and the influence of the magnetic field increases due to the higher velocity. After the electrons passed the hole, they enter a volume surrounded by an electrode on the same potential as the electron gun anode. Therefore, this region is free of electric fields and the kinetic energy of the electrons stays unchanged until it arrives at the post-acceleration system.

- **Adiabatic post-acceleration (PA):** In the post-acceleration area the electrons undergo several, approximately equidistant electric potential steps to finally reach the ground potential at which the electrons have the target kinetic energy. The design goal of the post-acceleration is to increase the electrons kinetic energy without broadening their angular distribution width. The PA electrodes are placed in a stronger magnetic field than the E-gun. By this and by splitting the potential difference into multiple smaller steps the electron kinetic energy should only increase $E_{\text{kin},\parallel}$ in the direction parallel to the magnetic field lines.

The combination of rotatable plates at the first acceleration stage and a post-acceleration stage increases the flexibility to condition the electron beam. By turning the plates to a non-zero angle α , any acceleration potential between cathode and anode will result in a beam of electrons with a non-zero polar angle Θ . The amount of transversal energy $E_{\text{kin},\perp}$ can be further adjusted either by changing the plate angle α or by changing the proportions of the acceleration voltage steps of the plates compared to the post-acceleration. This over-determined way to adjust the electron angle can be used to cover the full range of 0° to 90° electron angle in the magnetic field of the superconducting pinch magnet of KATRIN. An additional advantage of the post-acceleration system is the effect of decreasing the electron angle within the low magnetic field region of the Rearsection. This is beneficial to scale the absolute electron polar angle in the high magnetic field regions of KATRIN because the change in magnetic field increases the angle and the magnetic momentum by adiabatic transformation. Finally, the concurrent effects of the E-gun plate tilt angle and the post-acceleration electrodes make a spectrometer independent angular calibration of the produced electrons possible. These effects are described in more detail and covered with test results of simulations in section 4.3.

4.1.3. High voltage calculations at the electron gun

The various high voltage potentials up to 20 kV for the electron acceleration entails two risks: All charged particles within KATRIN are confined by the magnetic field-lines that are generated through the whole experiment by solenoids. Wherever electric potentials additionally create a potential sink for charged particles, the result is a charged particle confinement - a penning trap. Penning traps can be filled rather rapidly due to the high luminosity source or secondary ionization. If the local amount of free charges in the trap becomes too high (the precise limit depends on the used geometry and potentials) the insulation breaks down and the high voltage discharges. This can damage susceptible surfaces and increase the pressure within the vacuum chamber by ion sputtering on surfaces during the discharge. The previously mentioned traps are filled even faster if the high voltage electrodes in the system have sharp edges producing a sufficiently strong electrostatic field. Then direct field emission from the electrode is possible. In this undesired case the traps can fill and discharge repeatedly. The worst case is a constant high voltage break-through due to local field strengths above the vacuum insulation limit. If this current exceeds its

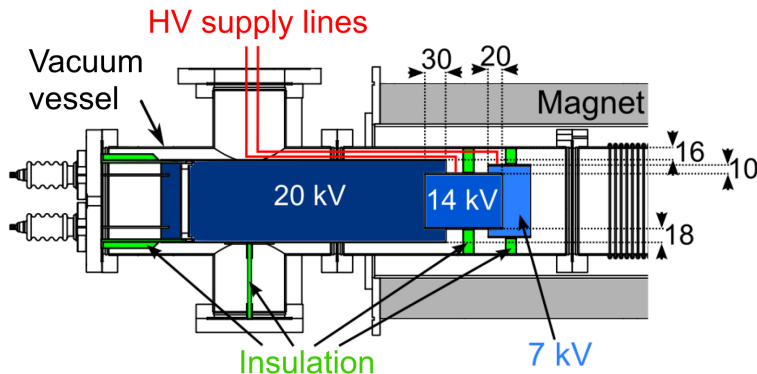


Figure 4.1.: High voltage electrode configuration at the E-gun - Defines the essential distances and potential gaps that are necessary for the high voltage field calculations. The electric supply lines for the post-acceleration are only indicated but have been defined properly during the model creation. Schema according to [76].

limitation set up at the power supplies the overall voltage is reduced until the current is within its limits. In every case of a steady HV break-through the pressure in the system will increase by ion bombardment of surfaces. Therefore, to ensure a long-term reliable operation of the electron gun a careful examination of the electrodes is required.

To find possible weaknesses at maximum electric potential and to proof the insulation layout to be a sufficient protection from direct electric break-throughs, the electron gun design has been checked in cooperation with the Institute for electric energy systems and high voltage technology (IEH) at KIT campus south [76]. For this test a slightly simplified electrode system has been defined to enable a full 3-D simulation of the charge distribution and field strengths by the IEH. Image 4.1 shows the configuration as defined for simulation. The acceptable limit for electrostatic fields before a high voltage breakthrough occurs, can be derived by empirical Paschen's law [77]. It defines the maximum voltage U between two surfaces in dependence of the product of pressure and distance $p \cdot d$ (compare figure 4.2). But for the high and ultra high vacuum pressure ranges, Paschen's law can not be used to make very accurate predictions because the break-through voltage rapidly increases for low pressures. This increase in the break-through voltage can not take into account surface and geometry details that may lead to field emission or other effects previously mentioned. As a compromise, a maximum acceptable field strength between the different electron gun parts of 3 kV/mm has been chosen. On the one hand this limit has a large safety margin when the chamber is operated at the target design pressure of $p < 10^{-8}$ mbar and on the other hand it minimizes risks for the case that the electrodes are powered while the chamber is at ambient pressure: The break-through field strength for dry ambient air at atmospheric pressure is at slightly more 3 kV/mm [78].

At the model displayed in the drawing 4.3 the geometry is overall simplified but still all details that could affect the calculation are maintained. The chamber walls are set on ground, the main electrode (green) surrounding the electron gun is set to -20 kV and the post-acceleration electrodes (brown and orange) to -14 kV and -7 kV respectively. The supply lines are included with their corresponding potentials. Insulators (cyan) are included with an estimated electric conductivity of 10^{-14} A/(Vm). The electron gun plates are removed because there are comparably large safety distances available while the potential differences are comparably small. The simulation by IEH does not include any magnetic fields or particle tracking. On the search for potential electrostatic weaknesses it is possible to define 3 high risk groups:

1. The main electrode's potential towards the walls. This electrode is at the most negative potential and therefore carries a high risk of causing a high voltage discharge.

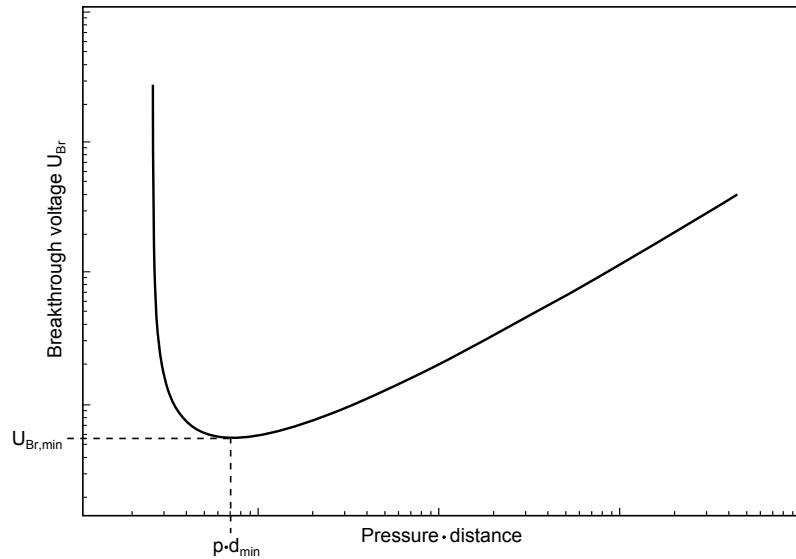


Figure 4.2.: Representation of Paschen's law - Indicates how the breakthrough voltage of a gas depends on the product of gas pressure and electrodes distance. The curve has a minimum breakthrough voltage $V_{Br,min}$ at a certain $(p \cdot d)_{min}$ (e.g. for air $V_{Br,min} = 352$ V at $(p \cdot d)_{min} = 7.3$ mbar · mm [78]). The quantitative shape of the curve is determined by gas type dependent heuristic parameters in Paschen's law.

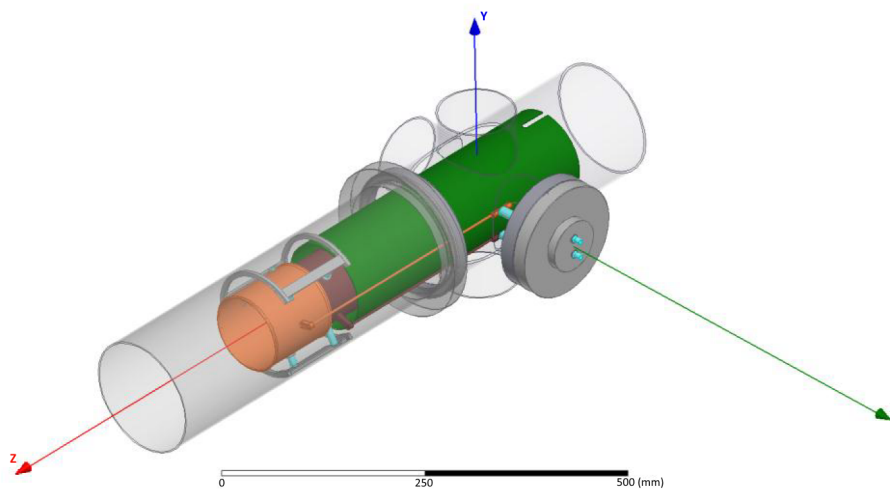


Figure 4.3.: Model for the FEM field calculation - The chamber walls (gray) are grounded, the main electrode (green) is at a potential of -20 kV and the post acceleration (brown and orange) are at potentials of -14 kV and -7 kV. Insulators (cyan) are included as well. The orientation of the coordinate system is according to the global KATRIN coordinate system. [76]

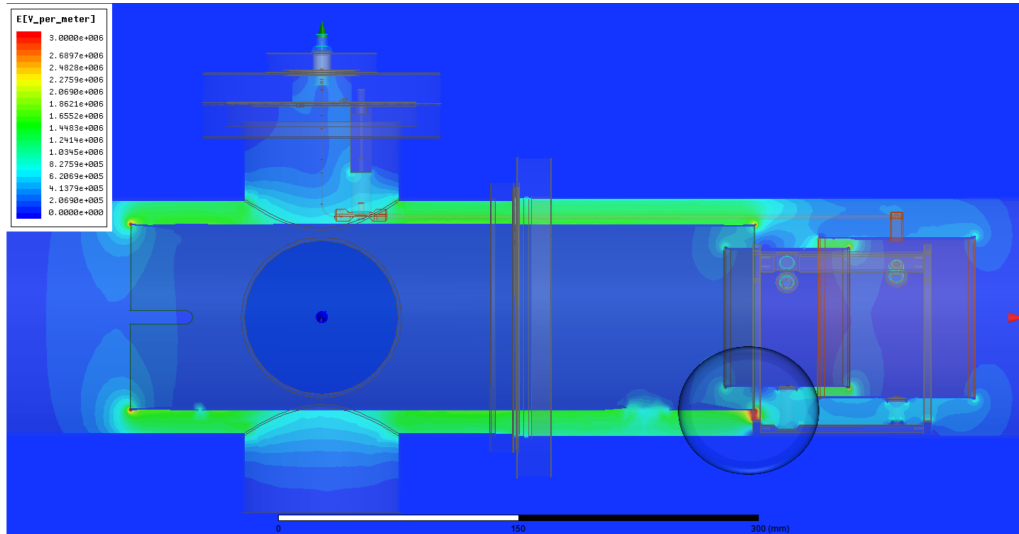


Figure 4.4.: Electric field check at the main electrode - A side view on the E-gun electrodes. The color range equals field strengths of 0 kV/mm (blue) to 3 kV/mm (red). The analysis revealed a critical field strength at the gap of main electrode towards the grounded clamp of the post-acceleration electrodes. [76]

The electrode mounting is safely disconnected from ground by large (60 mm long) massive insulators. The distance towards all other potential carrying elements has been maximized within the tolerable size of the surrounding walls and the enclosed E-gun plates and post-acceleration.

2. The supply lines which are enclosed by electrodes and walls to either side. To connect the post-acceleration electrodes massive wires are used. But since they have to be positioned between electrodes and grounded wall, their distance to surfaces with different potential is small. With a voltage of up to -7 kV and -14 kV the supply lines bypass all the electrodes. A careful check is required if the maximum allowed field strengths are complied in the volume around the supply lines.
3. The post-acceleration electrodes among each other and towards the grounded wall. Compared to the previous two points the post-acceleration electrodes are a small thread: The potential differences are significantly smaller. On the other hand the small distance between the two electrodes certainly justifies a careful validation.

After implementation and simulation of the electron gun model all areas of high electric field strength have been investigated and IEH collected the results in a report [76]. As the main result this report states that the overall design is uncritical. All electrode edges shall be rounded and electro-polished. For all components a careful high voltage conditioning is required after each cycle of venting and evacuating the system.

In the following the most critical positions of the simulation are discussed: The first risk part - the main electrode - causes in general acceptable field strengths towards the grounded walls of up to 2 kV/mm (compare illustration 4.4). It shows some critical field strengths towards the grounded holder of the post-acceleration electrodes of ≥ 3 kV/mm. This can be resolved by increasing the distance for example either by slightly shortening the holder or by moving the holder structure including the ceramic insulators (but not the electrodes itself) further away from the main electrode. The supply lines produce acceptable field strengths even in the most dangerous area along the main electrode (compare figure 4.6). The limit of 3 kV/mm field strength is only hit very close to the curved surface but not on the full path to the main electrode or the grounded walls. The supply lines take advantage of the fact that their potential is close to the medium potential which is caused at this

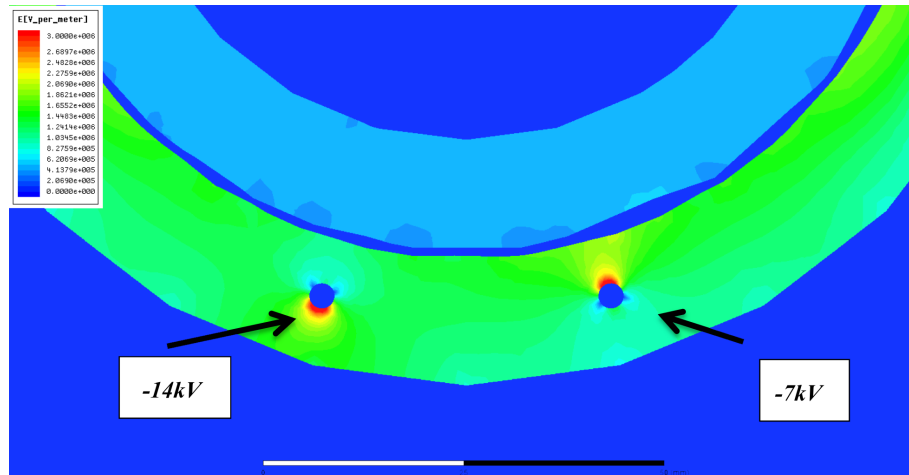


Figure 4.5.: Electric field check of the high voltage supply lines - A front cut view through the main electrode and the post acceleration electrodes. The color code ranges from field strengths of 0 kV/mm (blue) to 3 kV/mm (red). The field strengths are overall uncritical. The FEM calculation shows how the field polarization turns because the vacuum potential at the wiring position is about -10 kV. [76]

position by the potential difference of main electrode to ground. This is also the reason for the opposed polarities of the electric fields caused by the -14 kV conductor (more negative potential than the environment) and the -7 kV conductor (more positive potential than the environment). As expected the post-acceleration electrodes themselves are overall non-critical - neither to each other nor to the walls. There is no complete path between these components which exceeds a field strength of 2 kV/mm.

The report identifies a new component as the highest risk part which has not been considered as risk part in the previous listing: The pin of the atmosphere sided feed-through for the post-acceleration supply lines shows peak field strengths of 23.9 kV/mm (compare figure 4.6). Although this value is very high it can be neglected even in the case it is not caused by numeric effects: The simulation misses the appropriate connector cable at this pin which includes a large ceramic insulator. Furthermore, the feed-through is used within its specification of 15 kV [79] and it is unreasonable if the feed-through as commercially available product has electrostatic flaws on the atmospheric side in normal operation. All in all the recommendations of the report have been included in the final CAD model of the electron gun and realized in the prototype. In high voltage conditioning tests and productive use at UCSB the prototype showed no electrostatic weaknesses, discharges or high voltage break-throughs.

4.1.4. Optics and UV light source

The ultraviolet light source is essential for a photoelectric electron gun and does also influence key parameters of the E-gun: First of all the electron rate but also the broadness of the kinetic energy distribution. The precise implementation of the cathode illumination can also effect the angular distribution of the electrons when they are emitted from the cathode surface. To understand how the UV light source influences key parameters like electron rate and energy distribution it is necessary to have a closer look at the different steps of the outer photoelectric effect:

1. Before photons enter the target material the standard diffractive effects on the incident light at the surface have to be considered. In particular, the reflected light reduces the amount of energy transported into the volume.

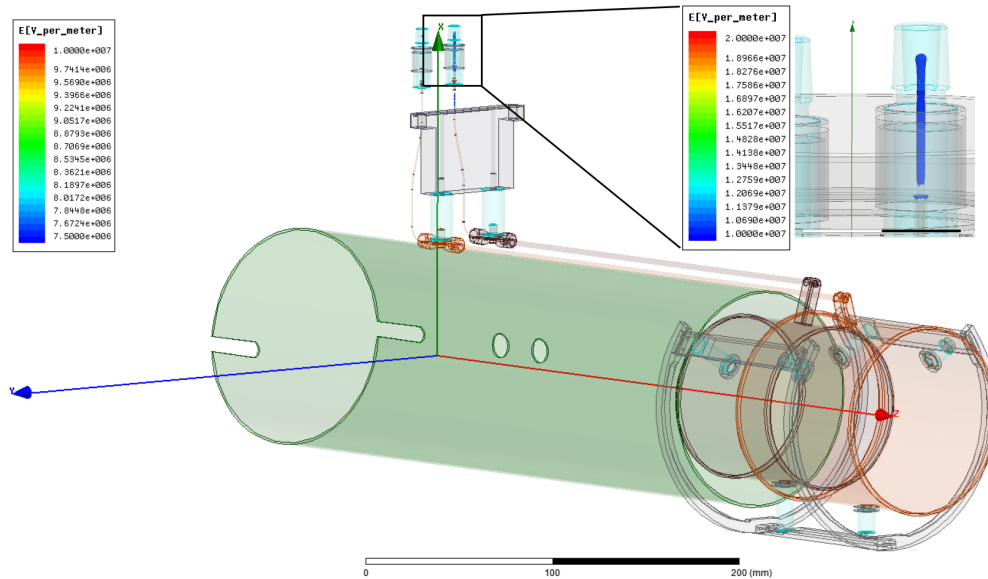


Figure 4.6.: Electric field check at the high voltage feed-through - This object has been identified as the source of the strongest fields within the field calculations. To find the regions with highest fields a cut is applied to the lower end of the color palette: On the overview image the colored range is from 7.5 kV/mm (blue) to 10 kV/mm (red) and at the detail view from 10 kV/mm to 20 kV/mm. The high fields are uncritical though, because the model misses the high voltage connector and the corresponding insulation material. Adapted from [76].

2. In the material photons are absorbed by different interactions according to the Beer-Lambert law [80]. This effect reduces the amount of available photons exponentially with the material depth.
3. Photons that are absorbed by interaction within a metal can excite conduction electrons from an energy level of the Fermi sea level and below to an energy level above the vacuum energy which is corresponding to the energy of a free electron in vacuum.
4. The excited electron can drift inside the solid until it scatters inelastically, is de-excited or in any way recaptured. For this process calculated and measured inelastic mean free path (IMFP) lengths are available depending on the electron's kinetic energy [81]. Very important is the fact that the MFIP can be comparably large with up to 100 nm when the electrons carry a kinetic energy slightly above the work function $E_e - E_{WF} < 1$ eV. In this situation the small kinetic energy of the electron leads to a small cross-section for some inelastic interactions or is even completely insufficient to trigger some processes.
5. In the case the electron reaches the surface of the solid before it is re-absorbed in any inelastic interaction it can be emitted from the solid volume. To evade from the solid the electron needs a kinetic energy which exceeds the work function of the material. This is already a simplified model: The probability of emission can further be modified by effects like the momentum orientation of the electron compared to the surface, quantum mechanic reflection at the potential wall at the surface and the electric potential that is applied to the metal.

Hence the effect of photoelectric emission can be complex if it is evaluated in detail. For quantitative analysis the model of Fowler [82] and DuPont [83] is used to attain the photoelectric yield per photon depending on the incident light wavelength. The model is extended by refractive effects at the gold surface/vacuum interface and by volume effects in



Figure 4.7.: Picture of the EQ-99X - the laser driven light source (LDLS) consists of the plasma enabling laser and the lamp itself with a proprietary xenon light bulb. The high intensity UV light is transmitted through the large window. [84]

the metal. To understand the optimization problem for the E-gun light source it is sufficient to know that the electron emission rate starts to increase roughly around the average work function of the metal (excluding shifts by electrostatic potentials and broadening by temperature effects and the inherent distribution of work functions over the solid surface). Once the photon energy is sufficient to emit photoelectrons, the emission rate scales at first exponentially with the surplus energy of the photons over the work function $E_\gamma - E_{WF}$. If the goal is to maximize the emission rate the light source should be chosen to have a large spectral power above the target metal work function and a broad spectrum of photons with high surplus energies. On the other hand such a light source results in an electron stream emitting from the surface with a very broad energy distribution. Such a resulting electron energy distribution is unacceptable for a high precision mode demanding for $\sigma_E < 0.2$ eV. The small starting energy caused by the surplus energy of the UV-light photons is the largest contribution to the energy broadening of the final E-gun beam. This is expected because the only other dependency of the final electron energy is the very stable potential difference between E-gun back plate and ground potential as described in section 4.1.2. On the other hand the effects by UV light wavelength on the kinetic energy distribution is also shown in the full electron gun simulations in section 4.3.1. The effects described above are the reasons why the search for the optimal E-gun light source is an optimization problem of electron rate versus the minimal kinetic energies of the electrons. Hereafter follows the description how the UV-light source is implemented at the electron gun to fulfill its requirements within the framework of the previously described optimization problem.

A high intensity laser-driven Xenon lamp of the type ENERGETIQ¹ EQ-99X LDLS will be used as ultraviolet light source in the first generation of the Rearsection electron gun. This low-pressure gas-discharge light source is an instrument that can be used for spectroscopy and produces a broad spectrum down to 170 nm [85] in the ultraviolet range. Due to the overall broadband optical power of 0.5 W the lamp still provides a comparably large spectral power in the relevant wavelength range. A comparison of different considered UV light sources like a UV-Laser, a deuterium lamp, a UV-LED and the EQ-99X is sketched

¹Energetiq Technology, Inc., 7 Constitution Way, Woburn, MA 01801 USA

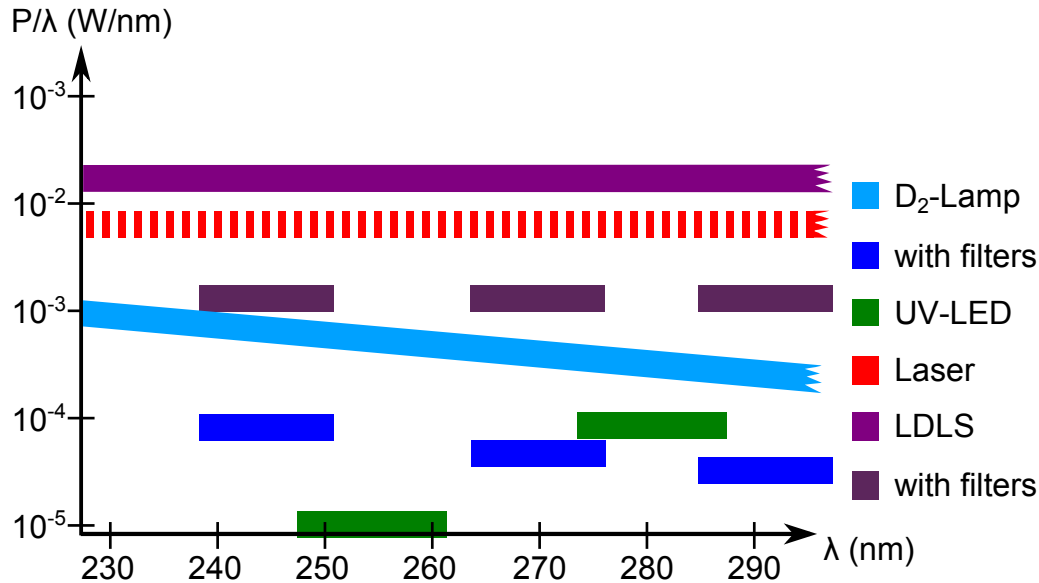


Figure 4.8.: Deep UV light sources considered for the Rearsection E-gun - The rough figures for spectral range and power are linked to concrete products but are mainly given for a relative comparison among the light sources. The spectral power of an UV laser can be significantly higher but needs to be capped to avoid a too high rate by the E-gun.

in scheme 4.8. The goal is a sharp spectral range matched to the gold work function combined with a large spectral power for a high E-gun rate. Deuterium lamps are very common products and deliver a broad spectrum and high power. To limit the spectral range, optical filters must be used (which are available for many wavelengths). But their usage reduces the spectral power by an order of magnitude. The resulting light power is similar to UV light emitting diodes (LEDs) in that range. Both light sources are considered to have not enough reserves for the photo-emission when the work function of the cathode is precisely matched. Tunable, deep UV lasers have very sharp spectral ranges combined with an extremely high spectral power - which would therefore be capped to a value as estimated in figure 4.8. However, such a laser is rather cost-intensive and the tuning of the wavelength is not an easy and automatable task. The laser driven light source (LDLS) is a compromise providing a larger spectral power than the deuterium lamp combined with the flexibility in the spectral range by the use of optical filters in an automated filter wheel. Overall each possible light source has advantages and drawbacks but an exchange will remain possible as potential future upgrades of the electron gun.

The light of the EQ-99X is collected by a lens and passed through a narrow-band UV light filter (compare in the sketch 4.9 of the optics system). Multiple of these filters are installed on a filter wheel where each is capable to select an approximately 10 nm broad part of the lamp spectrum. By this it is possible to adjust the UV light spectrum to match closely to the work function of the gold cathode and therefore to minimize the broadening in the electron's kinetic energy. Furthermore, the light passes a mechanical chopper for light pulsing and a beam splitter. One of the beam splitter outputs is connected to a UV photodiode to monitor the stability of the light source and to enable corrections in the case of intensity drifts. Finally, the light is focused with a lens system through a window into the vacuum system. Inside the Rearsection primary system it is coupled into an optical fiber of 200 μm diameter which guides the light towards the gold coated E-gun cathode. The fiber on the E-gun end is glued into the cathode and gold coated itself which ensures a fixed surface from which the electrons are emitted. For redundancy reasons and to be able to switch between different positions on the electron gun cathode, there are several of these fibers available in the vacuum system. The fiber selection occurs by mechanical

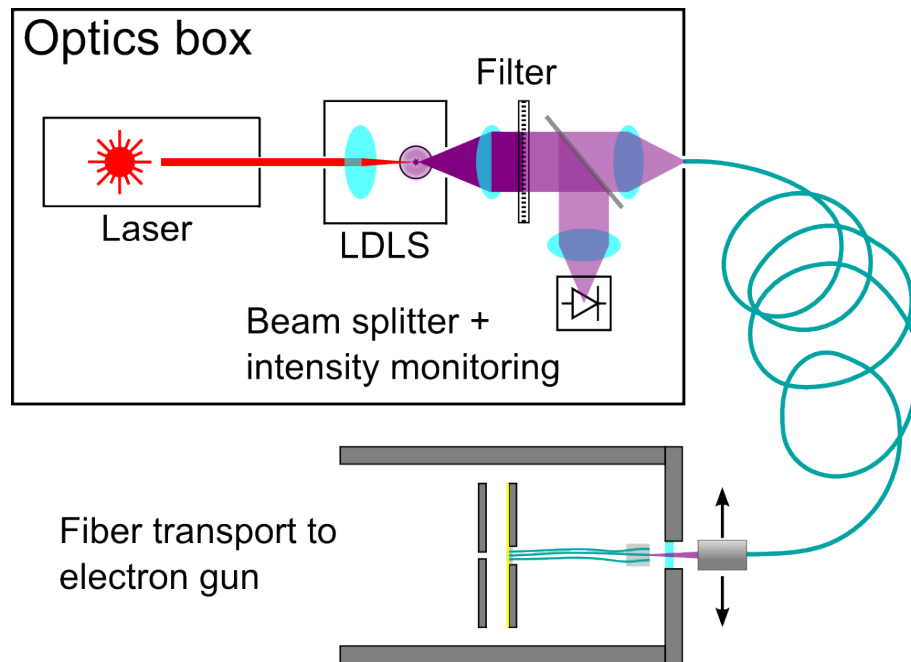


Figure 4.9.: Ultraviolet light path at the photoelectric electron gun - The laser ignites the Xenon plasma in the laser driven light source (LDLS). The intense ultraviolet light from the LDLS is collected by a lens and filtered by UV optical filters. A beam splitter and a stable UV diode is needed for a constant monitoring of the light intensity. The remaining light is focused into a fiber and guided towards the E-gun. Then the steerable fiber end focuses the light through a UV transparent window into a selectable fiber in the vacuum system. Since the fibers are fixated at the electron gun cathode, the UV photons end up in the cathodes gold coating.

movement of the fiber positioned outside of the vacuum system and focusing into the desired fiber. The values for light attenuation by the different optical components can be combined with the theory of photoelectric emission to estimate the final E-gun rate. In the high precision mode the filtered light is further attenuated by optics, feed-throughs and fibers. The probability of electron emission by the photons reaching the gold layer is defined by the processes that are described at the beginning of this section. As result of detailed calculations and related test experiments an E-gun rate of 1 kHz to 10 kHz is expected - the quantitative analysis will be described in detail in [86].

4.2. Electromagnetic transport section simulation

Calculations and simulations are essential for the electromagnetic design (EMD) of each single KATRIN component. The Rearsection is one of the most delicate systems concerning EMD because it comprises not only axially symmetric magnetic fields but also electric and magnetic dipoles. These fields steer and manipulate the electron beam on its path through the Rearsection. Electron properties like energy and polar magnetic moment must be conserved on this track. This is ensured if the electromagnet transport part is designed to ensure the adiabatic movement of the electrons. In the following, the term of adiabatic transport is discussed in more detail and the simulation results with different fields are shown. In these parts the electron gun itself is excluded from the system because this part is always non-adiabatic. The simulated electrons start with positions, energies and momentums as they shall be produced by the electron gun. This method was the key to deconvolve effects by the transport EMD and the electron gun itself. The combined system of electron gun and the transport EMD is described in section 4.3.

4.2.1. Adiabatic transport

The term of “adiabatic” concerning in the further discussion is in no way connected to the adiabatic term in thermodynamics - where processes can be fast enough or well isolated that no heat exchange occurs in the process. Electrons can do “adiabatic movement” when the changes in the electric and magnetic field are small during one cyclotron motion. A good indicator of adiabatic conservation can be the magnetic moment $\mu = E_{\parallel}/B$: Assuming an electron starts in a homogeneous magnetic field and transverses a space of different magnetic fields & electric fields ending up again in only a homogeneous magnetic field - if energy and magnetic moment are equal to their starting values the motion has been adiabatic. On computer based simulations the effect of adiabatic motion occurs automatically when the fields are well-formed and the Lorentz force

$$\vec{F} = q(\vec{E} + \vec{v} \times \vec{B}) \quad (4.2)$$

is correctly applied.

The simplified definition via the magnetic moment is often used to describe or proof adiabatic movement, also within the KATRIN design report [3]. In fact adiabaticity of motion depends only in the lowest order on the magnetic moment μ alone and is complemented by higher order effects which depend on electric fields or inhomogeneities in the magnetic field [87]. This is important when evaluating the transport adiabaticity with the help of the magnetic moment: The motion is still adiabatic if the magnetic moment always returns to the same value at locally static fields but it may change significantly at positions where the fields have non-vanishing spatial dependence. In the following calculations the magnetic moment μ is used to determine adiabaticity whilst taking into account the true nature of adiabatic motion.

4.2.2. Simulations with axially symmetric fields

The coils responsible to create the magnetic field which is axially symmetric to the z-axis are always referred as “solenoids”. The z-axis at the Rearsection is aligned to the z-axis of the KATRIN global coordinate system going along the experiment from the Rearsection to the main detector. The axisymmetric field forces all charged particles into a cyclotron motion and therefore the overall beam of all charged particles is confined within a magnetic flux tube². The tasks of the Rearsection solenoids are to guide the flux tube from the WGTS up to the Rear Wall and in the other direction to adiabatically guide the electron beam from the E-gun to the WGTS. Concerning the magnetic flux tube there are 3 quantities of relevance:

- The **Outer flux tube** has a size of 229 Tcm^2 and corresponds to the WGTS pipe diameter of 9 cm multiplied with the design magnetic field strength in the source of 3.6 T. Since the β -decay electrons mainly originate from the source, it is obvious that the WGTS defines the maximum of the flux tube.
- The **Inner flux tube** has a size of 191 Tcm^2 and corresponds to the main detector diameter times the design magnetic field strength at the detector of 3 T. This flux tube comprises all electrons which can be detected by the main detector and therefore can contribute to the neutrino mass measurement.
- The **Technical flux tube** has an intermediate size compared to the previous two with a value of 210 Tcm^2 . It is a purely technical definition and not related to a certain system at KATRIN. It is defined that all components of the experiment

²This is only valid for the center of motion of the particles when other fields are neglected. For the real dimensions of the beam, drifts and their cyclotron radii have to be considered.

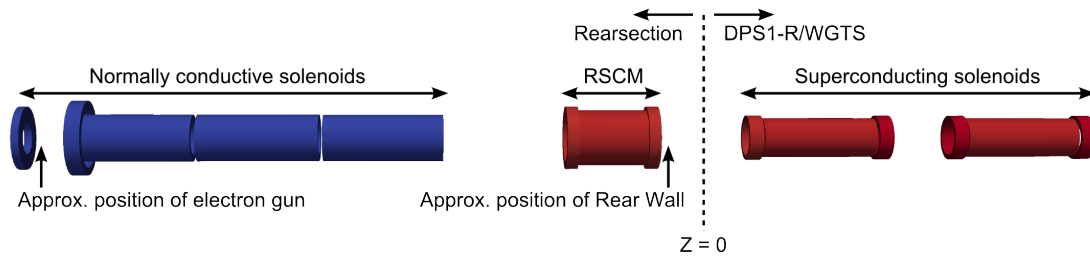


Figure 4.10.: Solenoid setup as used for the electromagnetic simulations - additionally the reference Z-position and the positions of Rear Wall and E-gun are indicated. The coils are colored by their current density. In contrast to the following simulations this view has already been realized with the most recent KATRIN simulation package KASSIOPEIA.

are required to provide enough space to let this flux tube pass through the system without losses. This adds a safety margin for technical designs to the physically relevant inner flux tube.

Only on the WGTS side of the Rearsection a superconducting magnet is required to force the magnetic flux tube on the Rear Wall (compare design simulations in section 5.1.2). All other solenoids can be normally conducting because their magnetic field is only needed to guide the E-gun beam but not the WGTS flux tube. Yet some requirements are put on the field strength of these normally conducting (NC) solenoids: The adiabaticity conservation is generally improved with the strength and the smoothness of the axisymmetric magnetic field. In the process of EMD the solenoids took several iterations to fulfill the requirements for adiabaticity conservation and the limitations by the feasibility of construction. The basic geometric set-up of the most recent configuration is shown in image 4.10. From right to left the following magnets are planned:

- Superconducting re-condenser magnet (RSCM): This magnet has a strong field with a maximum of 4.7 T in the center produced by $2.99 \cdot 10^6$ ampere-turns in total. This field strength is sufficient to compress the flux tube opening at the rear side of the WGTS again. The superimposed field of RSCM and the DPS1-R magnets of the WGTS contains the flux tube to dimensions which can be surrounded by a vacuum vessel system working with standard CONFLAT sizes.
- The main solenoid modules shall provide a smooth magnetic field in the transport area. It must be strong enough to ensure adiabaticity conservation although the E-gun beam is manipulated by electrodes and dipole coils. The magnets on the right and in the mid resume the strong field of the superconductor and therefore only need 27195 ampere-turns. The coil system is split into 3 modules for constructive reasons and to increase the modularity. In the axisymmetric field simulations it has been tested if the 3 module setup has significant disadvantages compared to a long, single coil. The left coils close to the E-gun chamber needs a stronger individual field by 31080 ampere-turns to avoid a steep field drop.
- The electrode booster coil is added at the end of the magnet module at the electron gun side. By this a too steep drop of the field strength at the magnet ending shall be avoided. This compensation is of special importance because at this position the post-acceleration of the electron gun occurs. The sensitivity of the beam electrons in the post-acceleration region on the magnetic field strength is shown in 4.3.1. Therefore, this compensation coil needs to be comparably strong with 4872 ampere-turns.
- The last solenoid is the E-gun booster coil which increases the homogeneity and overall field strength at the electron gun plates. Between the plates the B-field has a

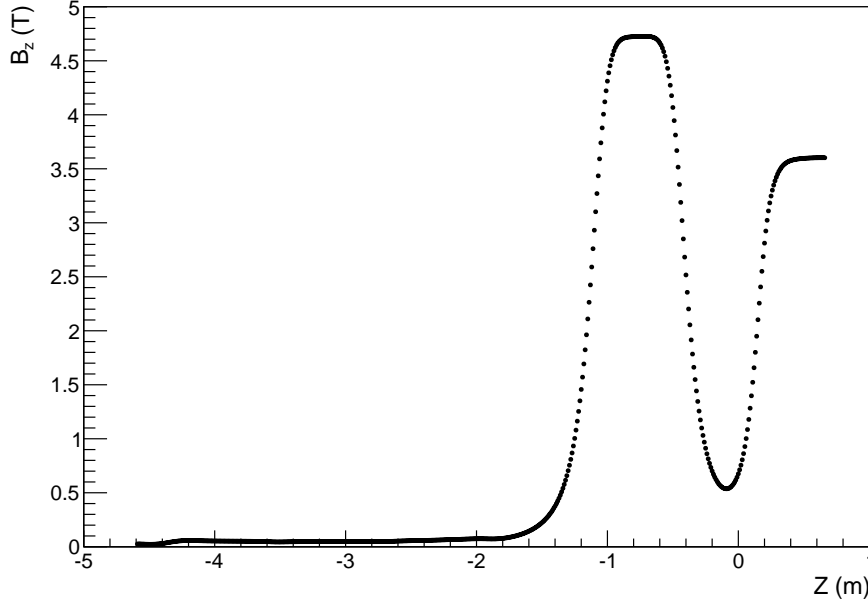


Figure 4.11.: Solenoid field strength in the Rearsection - from the electron starting point into the DPS1-R. The Rearsection superconducting cryogen-free magnet (RSCM) and the first superconducting module of the WGTS dominate with their maximum magnetic fields of 4.7 T and 3.6 T.

local maximum and is therefore very homogeneous. A locally intensified and homogeneous field improves the quality of the electron gun beam. For this achievement a coil strength of 4620 ampere-turns is required.

The magnetic field strength along the symmetry axis of the solenoids is diagrammed in the plots 4.11 and 4.12. It shows a smooth development towards the high B-field region with a roughly stable part at approximately 50 mT within the large solenoid modules. Inside of the center of a single magnet module at nominal current a field strength of 41 mT is produced meaning the maximum cyclotron radius of a 18.6 keV electron measures 1.2 cm. The reduced field leads to a significantly smaller value for the electron polar angle which is able to pass through the whole KATRIN experiment (“pitch angle”). The pitch angle is defined by magnetic reflection at the strongest magnetic field (6 T pinch magnet between detector and main spectrometer [3]). With the formula for adiabatic transformation of the polar angle

$$\frac{\sin(\Theta_1)}{\sin(\Theta_2)} = \frac{B_1}{B_2} \quad (4.3)$$

the pitch angle can be calculated to 51° in the source and to only 5.2° at a Rearsection typical field strength of 50 mT. In EMD simulations including only the solenoids the adiabaticity violation has always been very small with relative changes of $\Delta\mu/\mu < 0.1\%$ which is within the specifications of $\Delta\mu/\mu < 1\%$ and leads to a negligible shift in the electron’s polar angle Θ . Splitting the solenoids into 3 modules has no impact on the adiabaticity compared to a single module of 3 times the length. The adiabaticity violation in dependence of the maximum field strength in the NC-solenoids is shown in graph 4.13. Even if only the axially symmetric coils are in use, a certain minimum field strength is required to conserve the transport adiabaticity. In the following sections further EMD components and their requirements on the axially symmetric magnetic field are described individually.

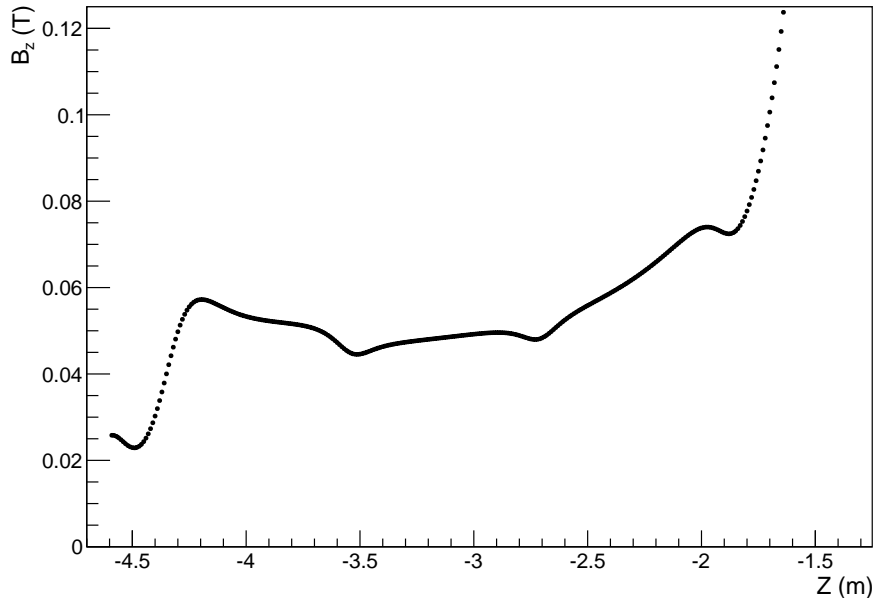


Figure 4.12.: Magnetic field of the normally conducting solenoids - detailed view of the smaller solenoid field in the electron transport section of the Rearsection. At the very left is the electron gun emission field while in the center of the graph the field is produced by the 3 solenoid modules. The gaps between the modules are visible in 3 small dents in the field. Towards the more positive Z-positions the field is constantly rising due to the RSCM stray field. The relatively strong field at the beginning of the first solenoid module ($Z \approx -4.2$ m) is caused by a slightly increased current at this solenoid and an additional booster coil at this position.

The NC coil modules have been designed according to the results of these simulations by the company Custom Coils³ and delivered to UCSB. The coils are wound on 3 equal stainless steel mandrels. The windings consist of 1/4 inch square copper wires with 111 windings along the coil and 7 windings in the height. Surrounding these copper windings there is one winding of 3/4 inch copper tube for water cooling. Each module is over-specified and can be driven with up to 50 A current but the target design values are 35 A for the Rear Wall sided module, 35 A for the center module and 40 A for the E-gun sided module. The booster coils have been wound on mandrels with large inner diameter to fit around a solenoid module or the E-gun cross respectively. They are made of square copper wires with 3 water cooling layers in-between to drive them with high currents up to 58 A. Both coils have 84 windings.

The superconducting re-condenser magnet has been built by Cryomagnetics Inc.⁴ and delivered to KIT. It is the exactly same magnet as it is used 5 times at the new DPS2. Due to its superconductivity the magnet can produce fields up to 5.5 T [88] but is only used with 4.7 T maximum field at the Rearsection. The coil core has 25125 windings and at both ends small boosters with 8798 windings are attached. The re-condensing technology enables a long-term usage of the magnet with a small helium consumption and slow (less than every 9 months [88]) refill cycles. All magnets used at the Rearsection are designed or fitted into the system with the verification by EMD simulation and consecutive iterations with the mechanical design. The technical details of every single magnet including its dimensions, wiring count and nominal currents are given in table 4.1.

³Custom Coils, Inc., 4000 Industrial Way, Benicia, CA 94510

⁴Cryomagnetics Inc., 1006 Alvin Weinberg Dr, Oak Ridge, TN 37830, US

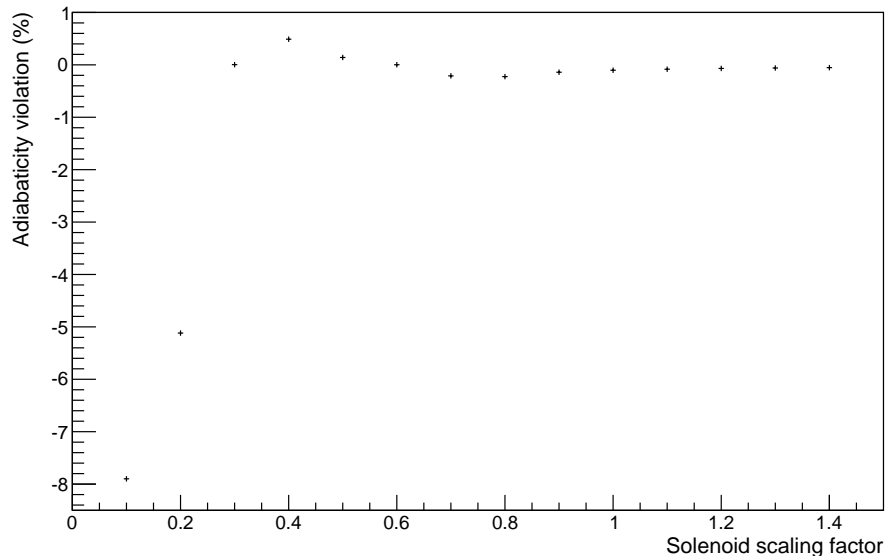


Figure 4.13.: Adiabaticity of the solenoid transport field - at differently scaled solenoid field strengths. The scaling factors range is from 0.1x to 1.4x of the nominal solenoid current. Small field strengths (factor < 0.3) lead to non-adiabatic transport even with only the axially symmetric coils activated. Minor variation in the transport properties occur with field strength factors of 0.3x to 0.8x. At the nominal current (factor 1.0x) the magnetic transport works just as well as at higher fields.

4.2.3. Test of the dipole coils

Without further electric or magnetic field sources the electron gun beam would simply follow the starting magnetic field line on a linear path in a cyclotron motion. In this case the electron path from the E-gun through the gas flow reducing aperture to the Rear Wall equals a straight line. But as a consequence there is also a line of sight available from the WGTS to the sensitive cathode surface of the electron gun. Neutral tritium molecules can move this way unhindered because the pressure is in the range of molecular streaming. Although the solid angle is small (Rearsection length > 4 m and E-gun front plate hole ≤ 5 mm), the amount of tritium close to the E-gun cathode must be further minimized to avoid background events for KATRIN or E-gun damages by radio-chemistry or ion-sputtering. Therefore, the aperture between E-gun and Rear Wall has a design offset of 10 mm to the Z-axis which blocks the mentioned direct line of sight. This aperture ensures that neutral gas molecules need at least one deflection to target the gold coated cathode from the source. With the introduction of this offset aperture some mechanism for beam steering and bending is required to guide the electrons through the chicane. At the Rearsection, “dipole coils” will be used which is a quite common technique to steer collimated charged beams precisely. These are not the only dipole coils installed at KATRIN: Dipole coils in the DPS1-R and DPS1-F of the WGTS can be used to shift the electron gun beam to any position of the KATRIN flux tube. The main spectrometer also is surrounded by large dipole coils to do a fine positioning of the flux tube in the spectrometer against interfering external fields like the earth magnetic field.

In this scope every coil creating a magnetic field with field lines intentionally perpendicular to the field lines of the solenoids is defined as dipole coil. The effect of the dipole coils is simply caused by its superposition with the stronger (already present) axisymmetric field. This superposition affects all the field lines, the center of motions of the charged particles and flux tube which is enclosed by the dipole field. Because the field lines itself are affected, the charged particles are shifted bidirectional depending in which direction they are moving on the axially symmetric field line. The shift Δy for a dipole field of B_y

Table 4.1.: Magnet configurations for the simulation - Most important parameters for the simulation of solenoid and dipole magnets. Grouped by type and ordered by the increasing distance to the WGTS. For the simulation only current densities or ampere-turns were required but the table already includes the as-built winding counts. For the solenoids inner radius (IR) and outer radius (OR) are provided, for the dipole coils width of the rectangle and the thickness of the wire package is given. The last parameter for solenoids (Ampere-turns per meter length) is a qualifier for the strength comparison of a cylindrical coils.

Solenoid Name	Windings	Nom. Current (A)	Z center (m)	Length (m)	IR (m)	OR (m)	$I \cdot n/L$ (A/m)
RSCM booster front	8798	70	-0.490	0.081	0.160	0.211	7.65E+06
RSCM	25125	70	-0.760	0.470	0.160	0.186	3.74E+06
RSCM booster rear	8798	70	-1.040	0.081	0.160	0.211	7.65E+06
Module Front	777	35	-2.300	0.796	0.110	0.154	3.42E+04
Module Mid	777	35	-3.120	0.796	0.110	0.154	3.42E+04
Module Rear	777	40	-3.950	0.796	0.110	0.154	3.90E+04
Booster Rear	84	58	-4.280	0.100	0.194	0.243	4.87E+04
Booster E-gun	84	55	-4.600	0.050	0.105	0.205	9.24E+04
Dipole coil name	Windings	Nom. Current (A)	Z center (m)	Length (m)	Width (m)	Thickness (m)	
Steering coil	144	0.97	-3.410	1.095	0.285	0.020	
Comp. coil	144	0.76	-2.300	0.675	0.285	0.020	

locally crossing the axisymmetric field B_Z on a length of l_Z can be estimated to

$$\Delta y = \frac{B_Y}{B_Z} \cdot l_Z \quad (4.4)$$

This is only an estimation because it ignores boundary region, inevitable stray fields and inhomogeneities of the fields. For a better understanding, the dipole coils have been included in the simulation. In the following the details of the implementation and the results concerning the impact on the electron beam path and the adiabaticity are described.

The field calculation for long axisymmetric coils can be done with high speed and acceptable precision by the zonal harmonics expansion [67]. This is not possible anymore for the dipole coils because their shape is in no direction axially symmetric. Magnetic dipole fields for arbitrarily shaped coils can be calculated by discretization of the coil into line elements and then calculating the contributions to the magnetic field via the law of Biot-Savart [89]:

$$d\vec{B}(\vec{x}) = \frac{\mu_0}{4\pi} \frac{Id\vec{l} \times \vec{x}}{x^3} \quad (4.5)$$

The coil elements with a current I contribute to the magnetic field B at a position defined by the radius vector \vec{x} . The total magnetic field is obtained by summing up the finite-element values. For this purpose a new discretizer has been written to implement the Rearsection's dipole geometry in the KATRIN global simulation (KGS) package. The

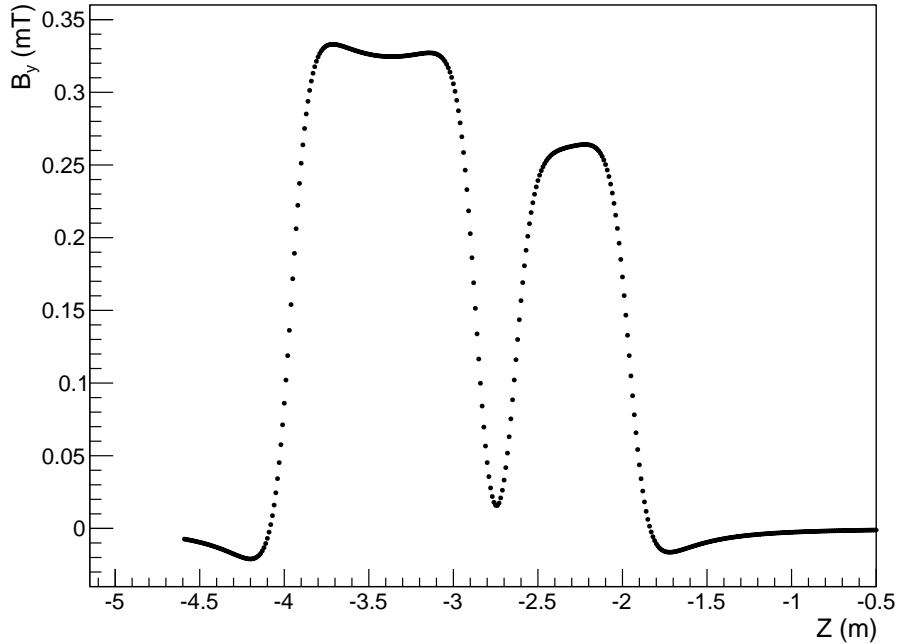


Figure 4.14.: Magnetic field of the dipole coils - Field strength in y-direction (upwards) over the z-axis. A weak field with $B_y < 1$ mT is sufficient for the electron deflection. The fields of the two independent dipoles (steering on the left, correction on the right) are clearly separated except for a small intercept.

shape of the coil must be optimized for the purpose of steering: The width of a dipole module must be similar to the diameter of a solenoid (to ensure full penetration of the axisymmetric field) module while the length along the z-axis can be longer. In fact a long dipole coil is desirable because formula 4.4 shows, the longer the dipole coil is, the more shifting effect it has or the less current is needed for the same shift. Different geometric shapes have been tested but the final design of a dipole module is mainly a rectangle with rounded corners. The shape at the corners is necessary for constructive reasons but not from the perspective of electromagnetic design. A pair of these modules installed oppositely around the solenoid creates a dipole coil. To get the maximum steering capacity 2 pairs of coils are used: One for steering the beam upwards-downwards (y-direction) and on to steer the beam horizontally (x-direction). One pack of 2 dipole coils is simulated on the E-gun side of the aperture with a length of 1.095 m and totally 140 ampere-turns. These dipole coils are designed to steer the electron beam through the aperture without violating the adiabaticity conservation. To achieve this goal they are designed with a rather small current but in a long shape. There exists a further pair of 2 dipoles on the Rear Wall side of the aperture with a smaller design of 0.675 m length and a larger maximum current of 110 m. They can be used for further fine adjustment of the beam or to compensate the stray field from the previously mentioned superconducting dipoles in the WGTS. Nevertheless, the demands on these “compensation dipoles” have been significantly reduced when the superconducting re-condenser magnet has been added to the Rearsection design: The RSCM pushes the weak axisymmetric field area further away from the WGTS which reduces the impact of the dipole stray fields significantly. They are typically not required to shift the E-gun beam “back” to the z-axis because the electrons are forced closer to the axis anyway by the compression of the flux tube in the other KATRIN regions with higher axisymmetric magnetic field.

In figure 4.14 the strength of the dipole field B_y is displayed along the z-axis. As expected, both dipoles provide a large plateau of maximum field and fast field rise and drop at the coil

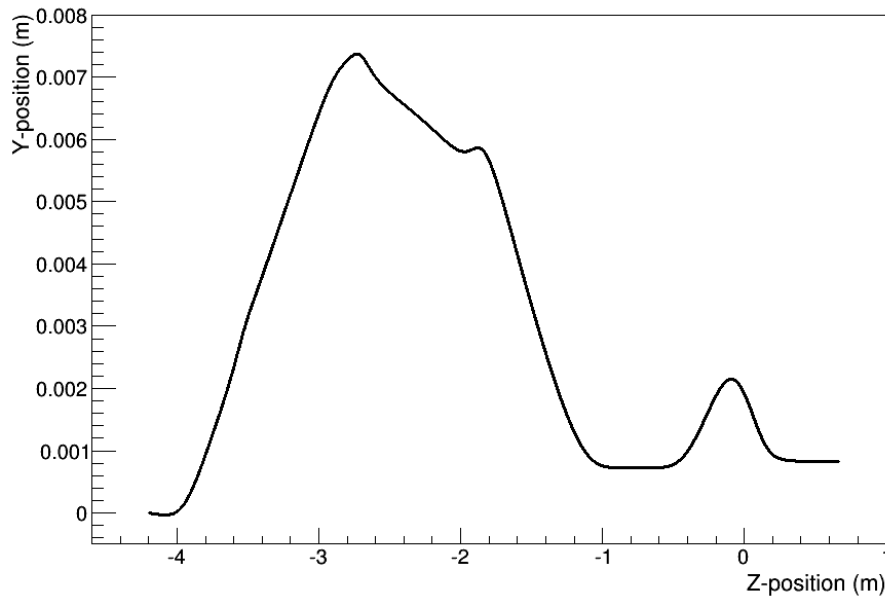


Figure 4.15.: Shift of a field line by the magnetic dipoles - At nominal current the magnetic dipoles shift the field line more than 7 mm. At the point of the largest shift the aperture will be installed ($Z \approx -2.67$ m). For $Z > -2.7$ m the path is no further deflected by magnetic dipoles - the changes in the Y-position are caused because the field line is following the magnetic flux tube. Depending on B_Z the flux tube becomes compressed or relaxed towards the solenoid symmetry axis Z .

endings. The resulting shift on the center of motion of a charged particle by the aperture steering dipole coil is shown in figure 4.15. The shift steadily increases while the electron is located in the dipole field ending with a maximum shift of 7.5 mm to fit through the fixed offset aperture. The adiabatic violation by this combined system remains acceptable with a value of 0.2% for electrons starting in the most left solenoid module with the maximum angle of 5.6° and a kinetic energy of 18.6 keV. The theoretical proof of principle for the compensation coil is displayed in graph 4.16 - the compensation coil combined with the diaphragm steering coil can completely compensate the shift of the DPS1-R dipole stray field if it should be required.

The final constructive design is again strictly orientated at the design which was successfully verified in simulations. Similar to the solenoids, the technical feasibility had reverse impact on the EMD. The modules were also manufactured by Custom Coils Inc.⁵ in a massive winding process without a mandrel at the finalized module. They only consist of 144 windings of copper wires with a cross sectional area of 3.31 mm^2 wound and glued together to a massive object. The maximum allowed current for the dipole coils is about 10 A (AWG12 wire) - so the dipole coils are also over-specified in their maximum rated ampere-turns. All dipole coils are installed at the Rearsection by clamping them to a frame which surrounds the solenoid modules. Separate water cooling is not required because the maximum power dissipation can still be cooled by air convection. The technical details of the two dipole coils including its dimensions, wiring count and nominal currents are given in table 4.1.

4.2.4. Evaluation of the dipole electrodes

The combined magnetic fields of solenoids and dipoles are sufficient to guide the electrons from the E-gun by passing the two holes in the aperture and the Rear Wall towards the

⁵Custom Coils, Inc., 4000 Industrial Way, Benicia, CA 94510

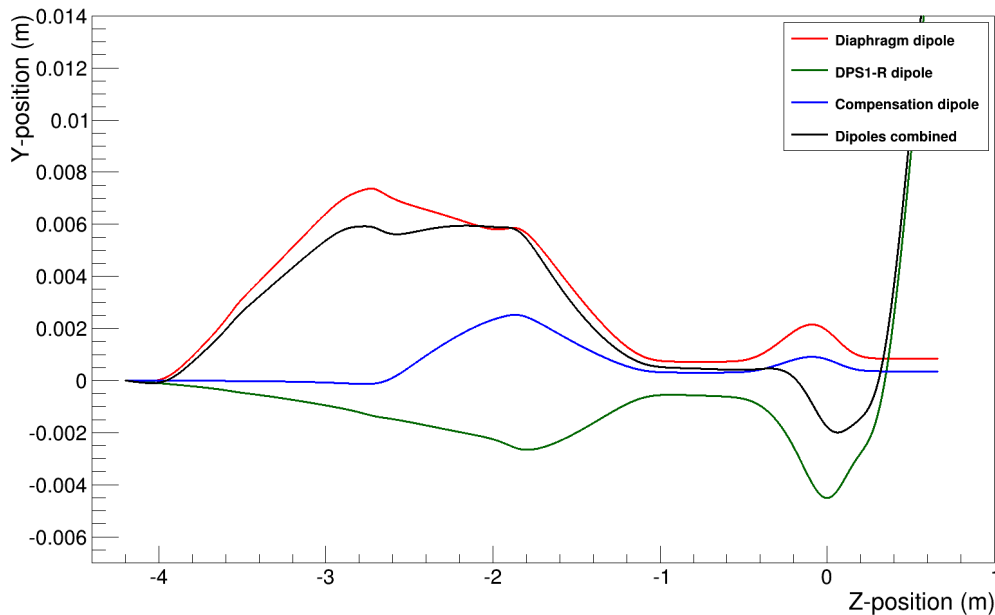


Figure 4.16.: Displacement effects by the magnetic dipoles - listing the effects of the aperture steering coil, the compensation coil, the (stray field) of the DPS1-R dipole and all dipole coils combined (Y-direction only). The compensation dipole can add a shift in opposite direction to the DPS1-R coil effect. With all dipoles combined the superconducting dipole in the DPS1-R can only dominate the beam path at the exit of the Rearsection for $Z \geq 0$. With this design the electron path passes the Rear Wall hole with less than 1 mm off the Z-axis.

WGTS. But charged particles can also follow the path in reverse direction from the source to the electron gun which can lead to the following undesirable effects:

1. Low energetic ions can be guided towards the E-gun and accelerated by the negative potentials towards the cathode. With a final kinetic energy of more than 18 keV the tritium ions can potentially damage the thin gold coating of the cathode. To avoid this sputter-like effect the tritium ion flux from the WGTS must be suppressed.
2. A part of the electrons in the E-gun beam will be reflected during the electron gun measurements. This reflection can occur e.g. by scattering with the rest gas or detector substrate or by magnetic reflection at the pinch magnet or electrostatic reflection in the MAC-E-filter. The electrons may return on the same magnetic field line up to the E-gun cathode to be reflected again by the electrostatic potential. The process of reflection is very non-adiabatic and can result in an nearly arbitrary new polar angle towards the magnetic field line. The double reflected electrons can mix with the primary beam and blur the narrow and well-defined angular spectrum. Therefore, the angular selectivity of the electron gun can only be ensured when reflected electrons are removed from the beam.
3. Finally the beta-decay electrons themselves can approach the E-gun and undergo electrostatic reflection. They can also mix with the E-gun beam but the risk of ambiguity is very small: The E-gun rate outnumbers easily the rare events of tritium beta-decays around the endpoint. Hence, this effect is the least problematic of all the effects mentioned. A removal of these electrons in the Rearsection is still desirable to reduce the amount of rest gas ionization within the vacuum system and close to the electron gun (compare first argument of this list).

All the required particle removal can be complied with a single EMD component - an electric dipole. Any electrode system which generates electric field lines transversal to the

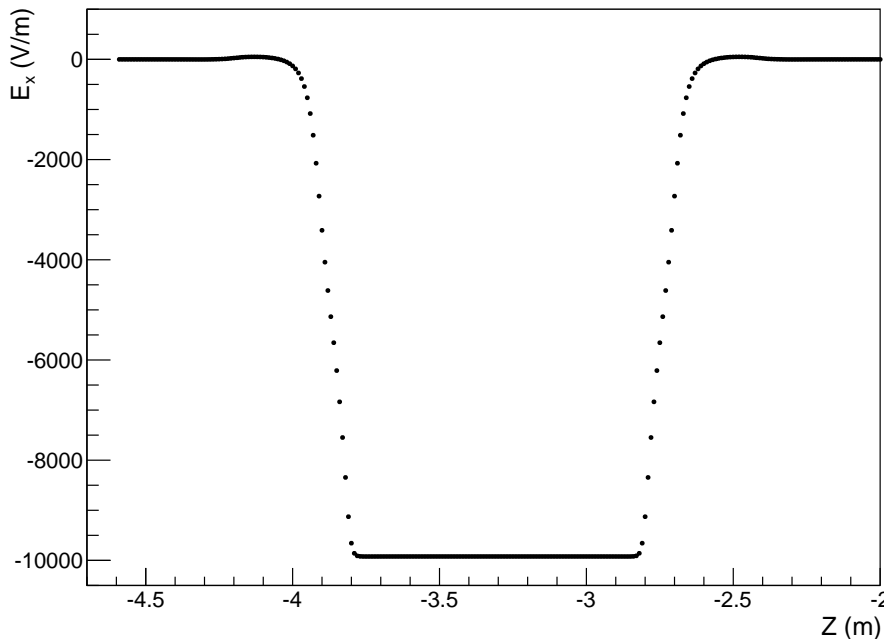


Figure 4.17.: Electric field of the dipole electrodes - in x-direction along the z-axis. The maximum field nearly reaches $E_{x,\max} \leq 10000$ V/m as it can be estimated. The length of the electrode is necessary to accumulate a sufficient drift effect. The smooth field progress at both exits of the dipole electrode is achieved by the special electrode design.

axisymmetric magnetic field lines and does not accelerate charged particles that are passing through is called “electric dipole” in the further. The result of such a field constellation is the so called “E-cross-B” drift which affects charged particles with the drift speed

$$v_D = \frac{\vec{E} \times \vec{B}}{B^2} \quad (4.6)$$

The drift speed is independent of the sign of the charge or the moving direction of the particle. Due to these properties an electric dipole resolves all the undesired effects mentioned above:

1. The ions passing into the Rearsection have a typical mass of 3-6 u and a kinetic energy of the order of 10 meV. Hence, the ions are orders of magnitudes slower, than the lighter and more energetic electrons. When the E-cross-B drift is large compared to the ion speed, the ions can not pass through the dipole electrode because they are forced away from the guiding magnetic field line towards the vacuum vessel wall. This behavior is checked in simulation.
2. Reflected E-gun electrons pass the dipole electrode a second time and finally a third time if they are reflected at the electron gun potentials. Each time they pass the dipole electrode they are drifting in the same direction. The dipole electrode must be designed in a way, that the two additional shifts of a double reflected electron (relative to the primary beam) are large enough to prevent further passing of the aperture. This is ensured if the shift is at least twice as large as the diameter of the aperture.
3. The argument above is also valid for any other electron that moves from the WGTS towards the electron gun. The electrons pass the aperture once and are shifted by the dipole electrodes two times in the same direction and the total shift is too large to pass the aperture hole a second time.

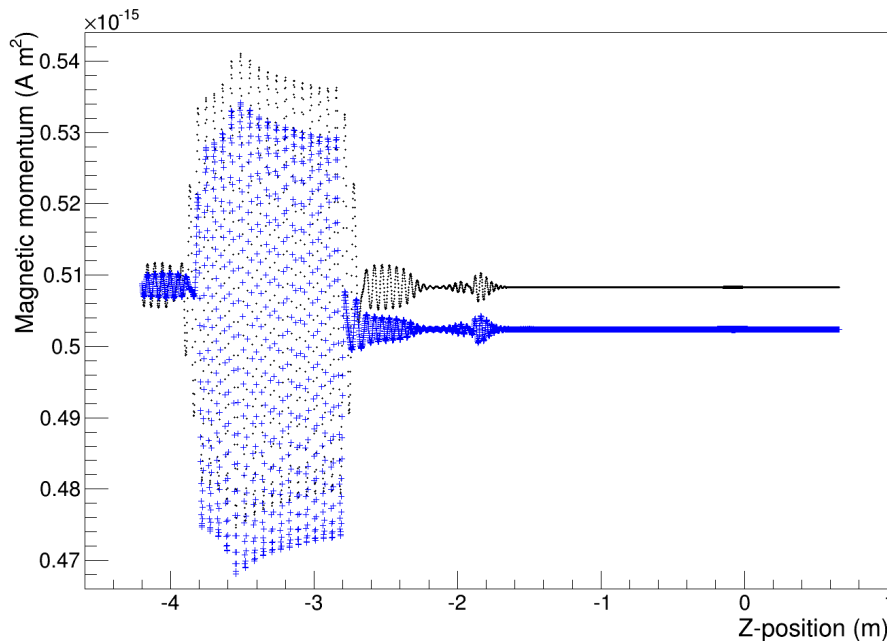


Figure 4.18.: Importance of the dipole electrode design - showing the progress of the electron's magnetic moment while passing through dipole electrodes either in a simple design (blue crosses) or the advanced design with kinked plates (black points). In the new design the magnetic moment remains nearly unchanged. In the old design the dipole electrode causes a adiabaticity violation of $> 1\%$, which is larger than the value allowed for the sum of all electromagnetic transport components.

The dipole electrodes had to be designed very carefully because the required strong electric fields can break the adiabaticity conservation and change the polar angle of the electrons. The design works basically like a plate capacitor with two parallel plates on opposite potential. To maximize the drift effect, the electrodes are designed to be very long in the direction of the beam path (the z -axis). Between the plates, the field should be nearly homogeneous - this is achieved by a plate height of 6 cm which is limited by constraints of the vacuum vessel and still larger than the plate distance of 4 cm. With the target design voltages of +200 V and -200 V the electric field between the plates can be estimated to

$$E = \frac{\Delta U}{d} = \frac{400 \text{ V}}{4 \text{ cm}} = 10000 \text{ V/m} \quad (4.7)$$

First simulations showed a too large adiabaticity violation at the entrance and exit of the dipole electrode. To avoid the sudden change of the electrostatic field, the dipole electrodes were slightly modified with additional plates at both ends with a kink to the main plate. These kinked plates act like an infinite amount of capacitors with smoothly increasing/decreasing distance and therefore create a slow electric field decrease/increase. The following simulations will mainly show results achieved with this modified electric dipole.

For field simulation and particle tracking, these non-axisymmetric electrodes need to be calculated (similarly to the dipole coils) by a finite element method. For this purpose the electrode plates are discretized in many rectangular elements. The potential of each single element is calculated with a numerical implementation of equation 4.8 ([89]) optimized for a finite rectangle. The total potential at any point of the system can be calculated by summation of all rectangular elements.

$$\Phi(\vec{R}) = \frac{1}{4\pi\epsilon_0} \int \frac{\rho(\vec{r})dV}{|\vec{R} - \vec{r}|} \quad (4.8)$$

The method for discretization of rectangular shaped electrodes has been implemented into the simulation package. The code includes optimization like a higher density of rectangles at the shape corners, load reduction by symmetries and the calculation with a simplified model (with less elements) when the distance between tracked particle and dipole electrode exceeds a threshold. In figure 4.17 the electric field strength in dependence of the position on the z-axis is visualized. The rise in field strength at the electrodes entrance and exit is significantly smoother with the new design compared to the simple design without kinked plates (not shown). The effect by this difference becomes obvious in plot 4.18 which shows the magnetic moment of particles passing through either of the designs. The smooth field progress avoids adiabaticity violation at the both ends of the electric dipole and reduces the relative change of the magnetic moment from 1.3 % down to 0.14 %. The latter value is within the specification for the electron gun of 1 %. Of course it is not sufficient to show that an EMD component is not harmful to the experiment; also the usefulness has to be proven: Figure 4.19 shows an electron that is reflected in a generic way in forward and backward direction. The reflection is implemented by an inversion of the z-component of the momentum while the exact cause of the reflection is irrelevant for this simulation. The result shows how the double reflected electron becomes shifted twice compared to the original path. The total shift relative to the normal beam path is 5.2 mm which completely excludes the possibility of an electron passing the 3 mm hole of the aperture after two reflections. On the other hand the ions deliver a more secure picture in figure 4.20. Due to their low speed they are strongly deflected already at the beginning of the electric dipole. The short path within the dipole will always end up with hitting the vacuum vessel independent from the possible starting positions defined by the aperture's hole size and position. With the simulative proof that the dipole electrode can remove even the highest energetic particles that are expected at KATRIN it also ensures that there is absolutely no accumulation of charged particles between the electron gun and the main spectrometer. This possible penning trap is completely cleared by the combination of aperture and electric dipole of the Rearsection.

The electric dipole alone enables to build a high precision electron gun and also protects the sensitive device from large penning traps and ions. Since the shape is well defined, the construction of the dipole electrodes was a very linear task. The electrodes have been manufactured by the workshop of UCSB. They are welded of 4.7 mm stainless steel and all necessary support and insulation is positioned on the “back side” of the electrodes. This is important because any additional elements on the “front side” (visible to the particles and the z-axis) can influence the homogeneity of the electric field. On the backside there is an additional steel sheet welded to the electrode for stabilization. Small ceramic tubes insulate the dipole electrode from the mounting rings which are fitted into the CF160 pipes to hold the instrument. The electric connection is done with KAPTON insulated wires which are conducted outside of the vacuum system by Sub-D feed-throughs on the aperture reduction flange.

4.2.5. Adiabaticity of the post-acceleration electrodes

The previously described parts - the solenoid system, the magnetic and electric dipoles - can all be clearly assigned to the transport EMD and they do not change the kinetic energies of the electrons. In contrast to that, the post-acceleration electrodes accelerate the electrons in multiple steps. But by design request, they still shall be adiabatic because they only accelerate along and not perpendicular to the magnetic field lines. Due to this the post-acceleration can be considered as adiabatic EMD component and the magnetic moment $\mu = E_{\perp}/B$ may be conserved or only slightly changed when electron pass through. The purpose of the post-acceleration system becomes most obvious in simulations of the combined system with electron gun in section 4.3. In the following the main advantages by

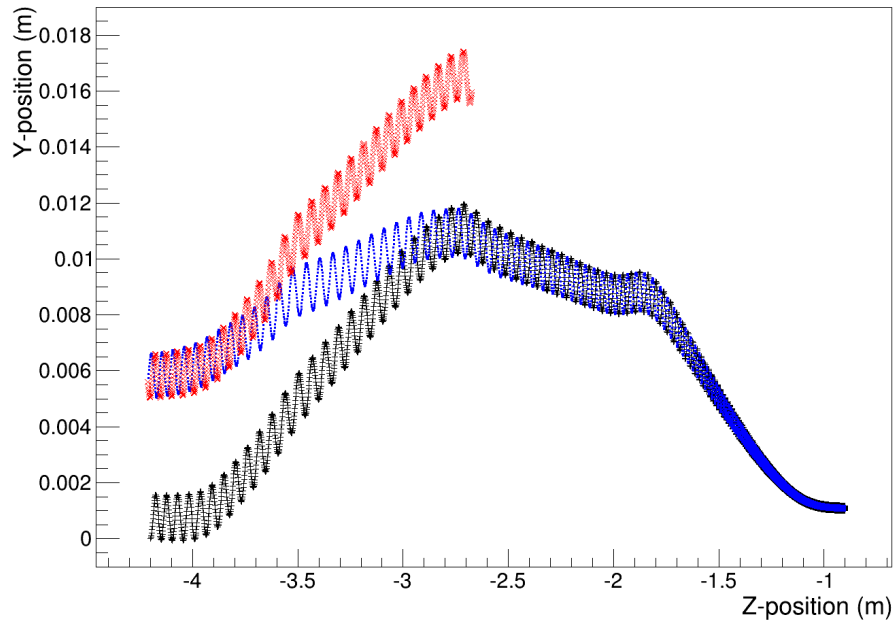


Figure 4.19.: Removal of reflected electrons by the dipole electrodes - An electron is tracked through the dipole electrodes with reflections at $Z = -0.9$ m and $Z = -4.21$ m. The electron starts at -4.2 m for the first pass (black crosses), turning after the first reflection (blue points) to be reflected again for the 3rd pass (red diagonal crosses). Each pass through the electrodes adds the E-cross-B shift into the same direction. Even in the case the electron should be reflected again at the E-gun (despite a 6 mm), offset the reflected beam particles are definitely stopped at the first aperture.

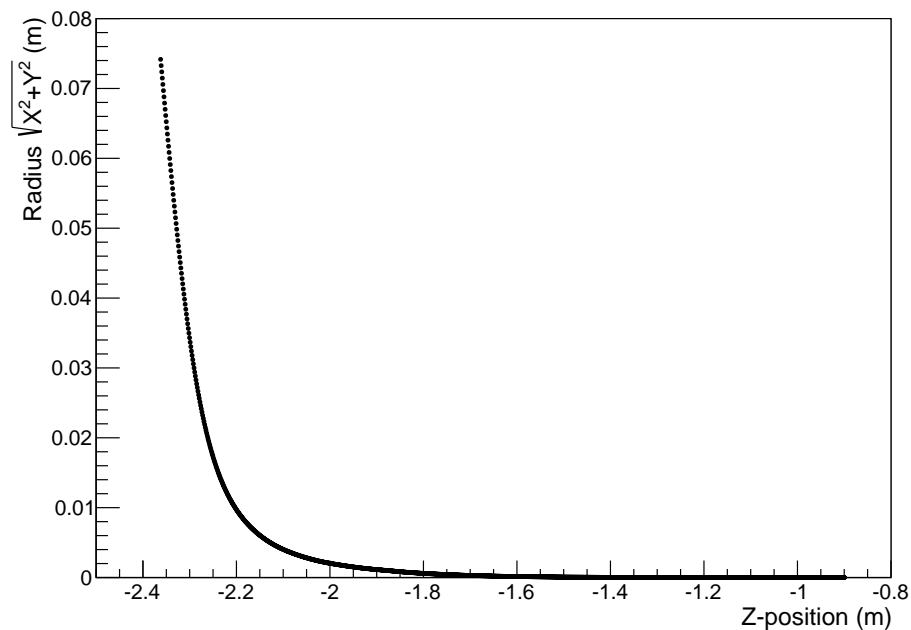


Figure 4.20.: Removal of incoming tritium ions by the dipoles electrodes - The simulated tritium ion reflects the worst case with an unusual high kinetic energy of 10 eV and 0° angle. The velocity of the ions is small compared to the drift speed caused by the electric dipoles. Already a small electric field E_X causes large drifts in X- and Y-direction. Once the overall radial shift from the Z-axis reaches 0.075 m the ion hits the wall of the vacuum pipe and adsorbs on the surface.

a combined system of rotatable E-gun plates and post-acceleration electrodes are listed:

- Without a post-acceleration, the full potential difference must be applied between the two E-gun plates. The cathode must be set to -18.6 kV in normal operation and has only a distance of 10 mm available to the grounded anode plate and possible even less to the surrounding grounded vacuum vessel. This setup is a high voltage risk especially for the gold plated cathode which will be vulnerable to high voltage discharges. Due to the post-acceleration system only a small potential difference of less than 4 kV is necessary for E-gun standard operation.
- As already stated previously the low magnetic field strength in the Rearsection leads to a small pitch angle ($\approx 5^\circ$). The fine tuning between the small pitch angle and zero degree electrons can become difficult depending on the accuracy of the plate turning mechanism. Small errors in precision or reproducibility of the turning mechanism does also result in a large error on the electron's polar angle. The post-acceleration electrodes increase only the kinetic energy parallel the magnetic field line while the perpendicular energy remains unchanged. As consequence the electron polar angle is reduced, which allows the production of initially larger angles at the E-gun plates. Therefore, the requirements on the turning mechanism are reduced.
- Similar to the previous argument the post-acceleration can also improve the angular distribution: If the full acceleration takes place between the plates small differences in the initial electron configuration (starting point, emission energy) can be "boosted" to a broader angular distribution. This effect is reduced if the electrons undergo a smaller acceleration and are afterwards all handled completely equivalent by the post-acceleration electrodes.
- The combination of rotatable plates and post-acceleration creates a redundant and flexible system to adjust the polar angle of the electrons. This angle can either be modified by turning the plates to a different angle or by redistributing the electric potential differences at the E-gun plates and the post-acceleration electrodes while the cathode potential remains constant. This redundancy can be used to perform tests to check the correct understanding of the E-gun and even for a spectrometer-independent angular calibration (compare section 4.3.2).

The post-acceleration electrodes are axially symmetric to the z-axis. Their fields are simulated by Elfield2 [67], as many discretized cylinder elements making use of the symmetry to improve the calculation efficiency. The electric potential along the z-axis caused by the post-acceleration electrodes is presented in graph 4.21. It shows the stable potential within the main electrode and the 3 potential steps on the way through the 2 post-acceleration electrodes to the ground electrode. A tracking simulation starting with a 3.6 keV electron at the designated E-gun position shows the acceleration analogously (figure 4.22). Apparent in figure 4.23 is, that the electric field strengths at the E-gun are significantly stronger than at the dipole electrodes. As previously explained, the post-acceleration in general always results in an angular transformation towards smaller polar angles. The concrete case of an electron with maximum polar angle (8.6°) and a starting kinetic energy of 3.6 keV which is accelerated to a final energy of 18.6 keV is visualized in graph 4.24. It shows that the post-acceleration reduces the angle from 8.6° to 5.3° although the axisymmetric magnetic field increases from 25.8 mT to 51.6 mT on the path.

Finally, the adiabaticity of (only) the post-acceleration is verified by checking for changes in the magnetic moment before and after passing the acceleration stage (compare figure 4.25). The magnetic moment for this single track changes by -0.48 % which is within the allowed specification of 1 % for pitch angle electrons. This result is also valid when electron parameters are varied like the starting positions (offset in x- or y-direction of ± 1 mm) or

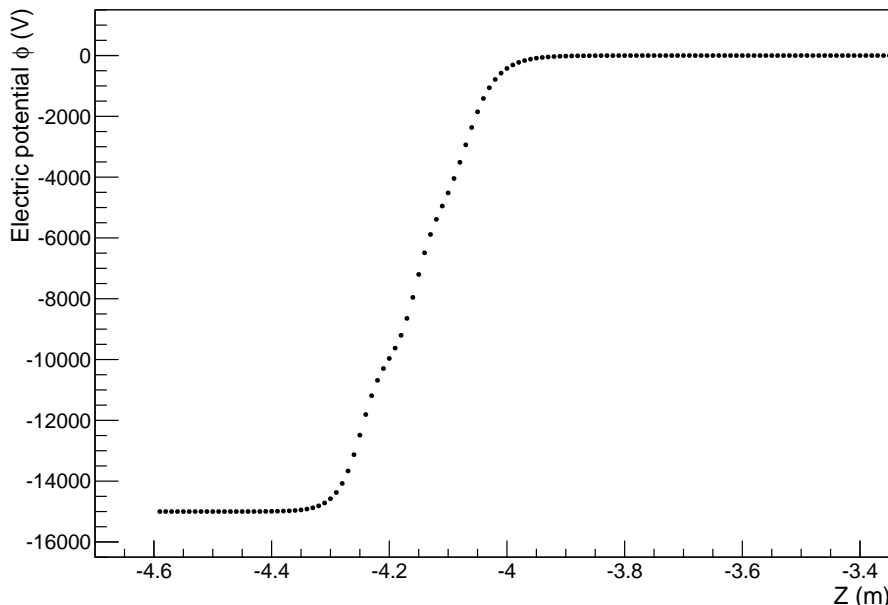


Figure 4.21.: Electric potential within the post-acceleration electrodes - assuming the main electrode is set to -15 kV and therefore the post-acceleration electrodes to -10 kV and -5 kV. Within the main electrode the potential is constant till the adiabatic acceleration stage follows in a higher magnetic field. The short electrode design does not cause a plateau in the potential instead it is a continuous potential increase up to 0 V. After passing this stage the E-gun electrons have the maximum kinetic energy.

the azimuthal angle ϕ (varied for the full range of 2π). The resulting adiabaticity violations stay in the acceptable range of -0.2% to -0.92%. Larger offsets of the initial beam position can lead to adiabaticity violations larger than 1% therefore high requirements have to be set for the mechanical alignment of magnets and electrodes.

The successful adiabaticity tests of the transport EMD are followed by the combined simulations with the E-gun (compare section 4.3.1). The finalization of the calculations also allowed the completion of the mechanical design of electron gun, post-acceleration electrodes and the surrounding vacuum containment. This mechanical design has been checked for high voltage peak and potential discharges as described in section 4.1.3. After these verifications, the electrodes were built of stainless steel at the UCSB workshop. The main electrode is insulated, fixed and aligned towards the bottom flange. The post-acceleration electrodes are mounted to a minimal stainless steel frame that is fitted into the vacuum tube. All electrodes are insulated by standard ceramic insulator standoffs of MDC⁶ and their voltage supply is transported into the vacuum by CeramTec⁷ feed-throughs. The technical details of the cylindrical electrodes like length, insulation strength and radius are provided in table 4.2.

4.2.6. Optimizations at the transport section

Each single component of the electromagnetic design is thoroughly described in the previous sections. But this shows only the design and constructive results of many different optimization steps. Therefore, this section will sum up the most important changes during the development of the transport EMD to achieve the required adiabatic conservation. The requirement of an adiabaticity violation of less than 1% is an intermediate goal for the E-gun angular requirement of $\sigma_{\Theta} < 4^{\circ}$.

⁶MDC HQ, 23842 Cabot Boulevard Hayward, California, United States

⁷CeramTec, One Technology Place Laurens, SC 29360, United States

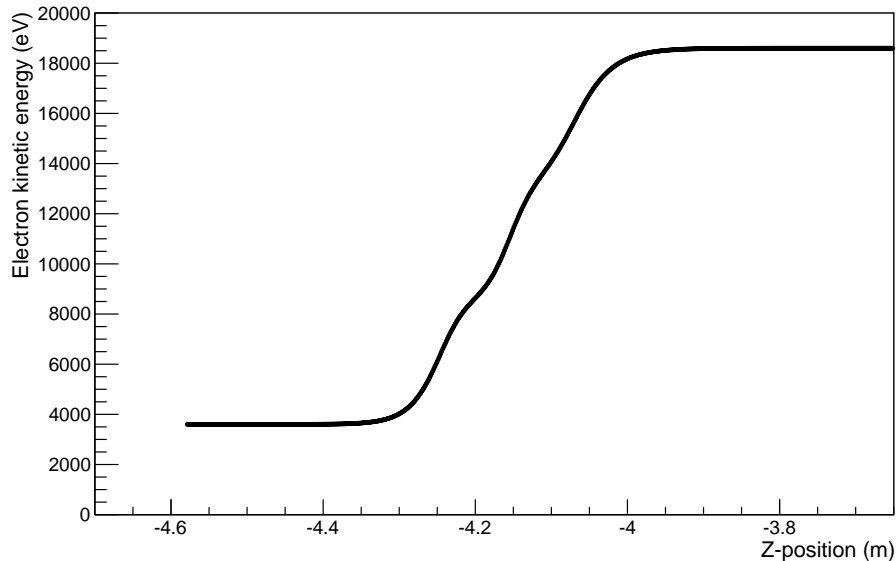


Figure 4.22.: Electron post-acceleration - progress of the kinetic energy of a single electron starting at the designated E-gun position with 3.6 keV energy. Within the main electrode the electron velocity remains unchanged. By passing the post-acceleration system the electron’s kinetic energy increases to the target 18.6 keV. The post-acceleration electrodes decrease the overall slope of the velocity and are visible in slight mitigations of the acceleration process at $Z = -4.2$ m and $Z = -4.1$ m

The solenoids for the axisymmetric magnetic field have been the first elements simulated and changed several times with the evolution of the Rearsection. Nearly any axially symmetric magnetic field with $B_Z > 10$ mT is sufficient to conserve the adiabaticity of electrons in the KATRIN energy range but the requirements have increased due to the other EMD components at the Rearsection. As a result, the solenoids must enclose the beam pipe very tight within the reasonable range and steep changes in the magnetic field must be avoided. The booster coils and the increased solenoid current towards the electron gun improves the performance at E-gun and post-acceleration. The superconducting magnet (RSCM) has been added to the Rearsection design late in the year 2012 which did not change the principle EMD design because the normally conducting solenoids still continued the magnetic field to a superconducting magnet with roughly comparable field

Table 4.2.: Electrodes configuration for the simulation - Details of the axisymmetric main and post-acceleration electrodes. Since they are aligned to the simulation Z-axis their geometry is fully defined with the center Z-value, their length and radius. The values for “typical potential” are used for most simulation runs. The rated insulation results from the official specifications of the used insulators and the high voltage calculations described in section 4.1.3.

Name	Z-center (m)	Length (m)	Radius (m)	Typ. potential (V)	Insula- tion (V)
Main electrode	-4.418	0.395	0.058	-15000	-20000
First postacceleration electrode	-4.200	0.079	0.043	-10000	-12000
Second postacc. Electrode	-4.129	0.100	0.050	-5000	-7000

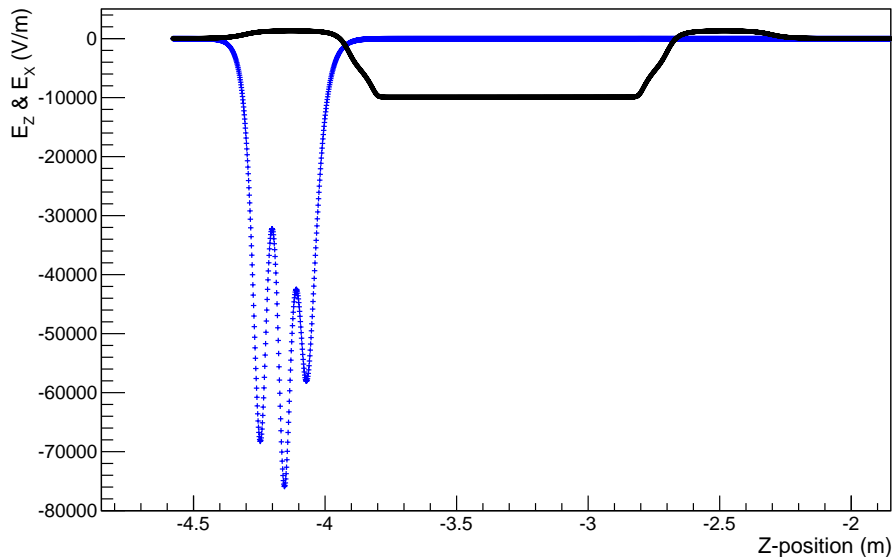


Figure 4.23.: Comparison of electric field strengths at the dipole and post-acceleration electrodes - the simulation shows that the absolute field E_Z by the post-acceleration (blue crosses) can be locally more than 7 times stronger than the absolute field E_X (black points) produced by the dipole electrodes. It also proves that the intersection area of the two different fields has been successfully minimized.

strength and distance. The field strengths necessary in the simulation resulted in a design requirement for the normally conductive solenoids: The electric power consumption by the coils was too high for conductive air cooling and therefore an additional water cooling has been added.

The dipole coils have been more challenging design components. An early consideration to place dipole coils of smaller dimensions inside of the solenoids had to be reverted. Due to the reduced homogeneity of the smaller dipole coils the adiabaticity gets violated unacceptably in this setup. The shape of the dipole coil finally came within the process of technical design and the planning of winding and mounting. The original dipole coils were of a curved shape which fits around the outer diameter of the solenoid module. This change required an update of the wire discretization code and subsequently another test concerning the beam quantities. The dipole coils to compensate the stray field of the superconducting dipole coils of the DPS1-R have been challenging before the RSCM was added to the design. Without the RSCM the compensation dipoles needed many ampereturns (≈ 1000 A) and the resulting electron path had still large offset positions to the z-axis. With the RSCM the requirements on the compensation could be relaxed by a factor of 6. Even without the compensation coils the electron beam remains close to the z-axis. Nevertheless, the compensation coils remained in the design to ensure a proper beam guidance through the Rear Wall aperture.

Optimizations of the dipole electrodes have rather slow iteration steps due to the amount of computing time which is required for three dimensional finite element electrostatic calculations within the KATRIN simulation package. The most important finding is that the electric dipole produces a large contribution to the adiabaticity violation but this does not happen while the electrons are moving within the maximum field between the plates. Instead, the steep changes in the electric field at the entrance and exit of the plates could introduce a relative change in the magnetic momentum of more than 10%. Therefore, the slope had to be reduced and the option to attach plates with smaller voltages at both ends was discarded due to its mechanical and electrical complexity. Instead, wings with

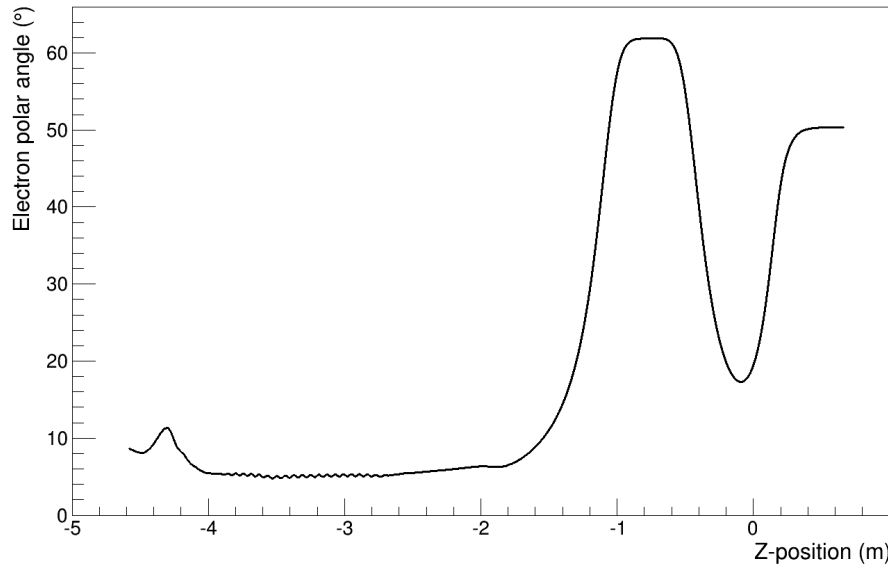


Figure 4.24.: Electron polar angle in dependence of the path through the transport section - The two main factors influencing the electron polar angle from the E-gun position to the first solenoid in the DPS1-R are the post-acceleration and the solenoid field strength: The post-acceleration increases the longitudinal kinetic energy and therefore decreases the electron angle in the area $Z < -4$ m. The angle is everywhere transformed adiabatically by the solenoid field strength (compare graphs 4.11 and 4.12. The variations in the area $-3.8 \text{ m} < Z < -2.8$ m are caused by the electrode dipole field leading to local increases/decreases of the transversal energy by the cyclotron motion.

a kink angle of 18° have been attached which are on the same electric potential as the main plate but produce a smaller field on the z-axis because of the increasing electrode distance. With the given shape and potential of the electrode, a length of 1 m showed a sufficient diversion by the E-cross-B drift. The other dimensions of the dipole electrode were maximized with respect to the constraints by the vacuum beam tube. With the increase in size the field becomes more homogeneous leading to improved simulation results. The post-acceleration electrodes followed the general scheme of the Rearsection EMD: Increasing the magnetic field and the homogeneity of the electric field while the damping the slopes improves the adiabaticity conservation. The magnetic field strength is increased by the post-acceleration booster coil. The diameters of the electrodes are maximized but constraint by the vacuum tube and requirements of electrostatic insulation. The application of conical instead of cylindrical shapes (similar to the dipole electrode) did not improve the transport qualities. More and therefore smoother post-acceleration steps would have improved the results but this comes at the cost of mechanical and electrostatic supply complexity. Two post-acceleration electrodes to smoothen the potential drop between main electrode and ground are a compromise of simulation and feasibility. After all, simulations with the post-acceleration electrodes delivered good results when the electrons offset to axis was not too large (> 3 mm) and the distance to the dipole electrode was not too short (< 15 cm).

Concerning the electrons that passed through the transport system, all parameters have been varied in a broad range. This approach delivers conservative or even pessimistic results. But a design simulation also has to deal with the limitations of the constructions. Most important are the possible misalignments between the electromagnetic components. To reduce the effects of misalignment each component has been designed to provide a similar homogeneous and directed field within a certain volume around the target beam position. The most critical positions (begin/end of a dipole system) is always placed

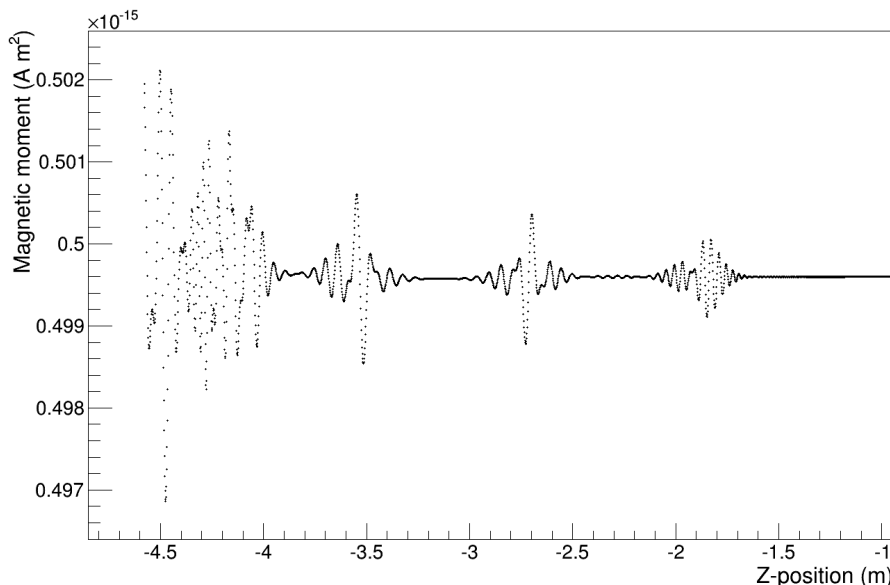


Figure 4.25.: Electron magnetic moment in dependence of the path through the transport section - the progress of the magnetic moment μ shows the major offset by non-adiabatic effects occurs right at the start caused by the post-acceleration and the instable magnetic field close to the electron gun. The variations of μ for $Z > -3.8$ m are examples for adiabatic movement with a locally instable μ which stabilizes again in homogeneous electric and magnetic fields.

within a solenoid module. The complete mechanical system can have large mismatches and misalignments (several centimeters) as long as alignment and positioning of the vacuum system to the magnets are maintained. Therefore, all electromagnetic components have their positions and alignments defined towards the next solenoid module with more rigid constraints than the mechanic construction itself. Different alignment options have been added to the mechanical design to fulfill these requirements. Several explicit misalignment and mismatch simulations did not indicate problems for small deviations (< 2 mm, $< 2^\circ$). With the fixation of the transport electromagnetic design it is possible to add the electron gun to the simulation for the full system calculations. The results of these simulations will be discussed in the next section.

4.3. Implementation of the electron gun to the simulation

In the simulation, a virtual electron gun can be added to study the results of the transport system combined with the Rearsection electron gun. The following results are presented using either a methodical approach by iteration through the multi-dimensional starting parameters or Monte Carlo simulations with random starting parameters from the configuration space. Optimizations on the E-gun parameters have been the task of UCSB since they are also responsible for the final design, prototyping and construction of the electron gun. Nevertheless, the development was supported and the calculations were cross-checked to find the optimal operation conditions. The final simulation must reflect a rather pessimistic setup between worst-case and realistic and still deliver results for the electron energy and angular distribution within the official specifications [53]. The initial implementation of the E-gun by [90] has been rewritten for a usage with the KATRIN simulation package including compatible field calculations and physical collision checks.

The E-gun field calculation itself uses the existent analytic solution [89] for a system of two infinite large plates with a distance d while one of the plates (equivalent to the E-gun anode) has a thickness t and a central hole with the radius r . An analytic solution is very

fast for the field calculation but has the disadvantage of being only an approximation. To be able to use this approximation, two requirements must be fulfilled: The outer diameter of the finite plates must be much larger than the plate distance d or the hole radius r . This requirement is necessary anyway to achieve a homogeneous electric field between the plates and is incorporated in the final design. Another requirement is that the asymmetric electrostatic induction on the E-gun plates by surrounding electrodes must not invalidate the assumption of infinite large symmetric plates. There are several important arguments why the approximation should still hold, although the boundary conditions are different: Again the outer diameter is much larger than the plate distance d , which reduces the impact of the surrounding electrodes. Furthermore, the only relevant space concerning the trueness of the electric field calculation is at a small area around the center of the plates where there is the least effect of induction by surrounding electrodes. Finally, the E-gun plates are surrounded by the main electrode with only few millimeters distance but the potential of this electrode is the same as the anode. As a consequence, there is definitely no inductive effect on the anode by the environment and a comparably small effect on the cathode. This is, because the absolute potential difference between cathode and main electrode is much smaller than the one between cathode and ground electrode. For particle tracking this field calculation is then combined with all previously described field calculation methods for the axisymmetric electrodes, solenoids, electric and magnetic dipoles.

Concerning the electron generation the detailed mechanism of photo-emission (compare section 4.1.4) is not included in the following simulations. Hence, any effect contributed by the electron emission itself must be calculated in preparation before the simulation. The tracking simulation must get the correct starting parameter space to replicate angular distribution, energy distribution and the positions of emission as it is caused by the back-illuminated gold surface.

- **Angular distribution:** Concerning the resulting angles of photo-emission close to the work function it is possible to use geometric assumptions or rely on available literature [91]. Both options have been considered but it was decided they are not secure enough for the evaluation. The simulation assumes an isotropic 2π emission from the gold surface which is a worst case approximation concerning the final angular distribution. From other sources one would expect a distribution which is non-isotropic and aggregated to the plate normal but there is no data available which exactly corresponds to the given setup.
- **Energy distribution:** The starting energy distribution is the result of the photons surplus energy to the gold work function. Although this kinetic energy is small compared to the electron's final kinetic energy ($< 1\text{ eV}$ to 18600 eV), this effect is the main source of the energy error. It can be minimized by precisely filtering the UV light range to match the gold work function. This optimization is difficult since it causes a strong reduction of the E-gun rate, because the quantum efficiency for emission increases exponentially with the photon surplus energy according to the Fowler function [82]. It is possible to calculate the resulting energy spectrum and the total emission efficiency by multiplying the filter function with the fowler function (compare figure 4.26). The sharpness of the energy distribution depends on the conditions at which the required rate can still be achieved. Since these values were not experimentally determined yet, the simulation uses the official energy requirement of the E-gun which is given as $\sigma_E < 0.2\text{ eV}$ [53]. This is again a worst-case approximation since this value must be achieved by the requirements but may improve if an acceptable rate can be realized with less photon surplus energy in the final setup.

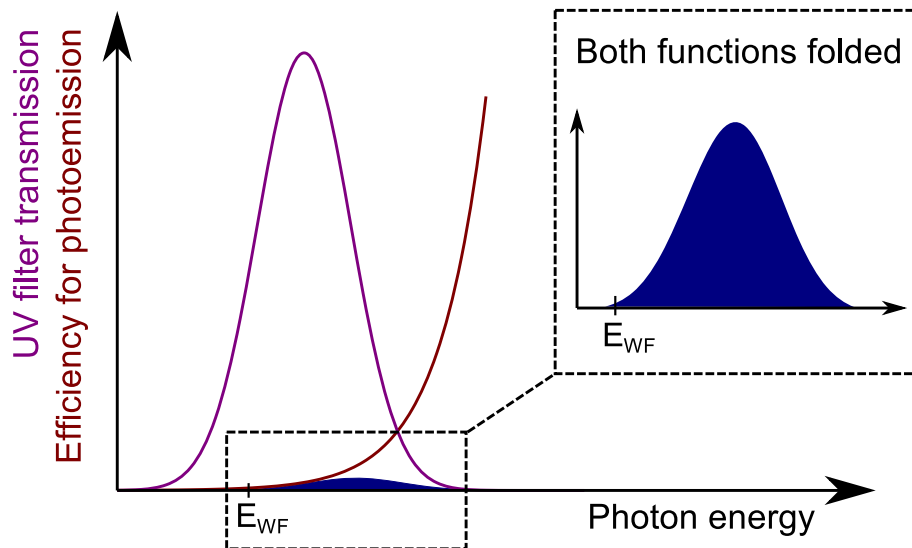


Figure 4.26.: Energy distribution of the photo-emission electrons - To narrow the energy distribution of the E-gun electrons, the ultraviolet filter must be selected appropriately. Then the Gaussian-shaped transmission function of the filter may be matched to the photon-energy dependent quantum efficiency for photo-emission (Fowler function). When the two functions are multiplied the result provides an estimate for the photo-electron energy distribution - which again can be approximated as a Gaussian distribution for the simulation input.

- **Positions of electron emission:** The possible starting positions of electrons are given by the ultraviolet light spot size which is very well defined by the use of gold coated UV fibers. The fiber is illuminated homogeneously on the side of the UV light source and due to the very thin gold layer compared to the fiber diameter the affected area can not be increased significantly by the fiber opening angle. If the area and position of the electron emission are set exactly to the corresponding fiber surface, this should give a good estimate of the real system.

Before the simulation results are presented in the next section, it is also useful to consider the complex field interactions at the electron gun. The fields between the plates determine where and if the electrons pass the anode hole in dependence of the starting position on the cathode. The dominating fields at the electron gun are on the one hand the electric field caused by the potential difference of cathode/anode and on the other hand the magnetic field produced by the solenoid and booster magnets. The electric field is aligned parallel to the plate normals, directing from anode to cathode. An exception is the center of the front plate where the hole leads to axially symmetric field distortions. Because the electric field is directly related to the plate potentials, it equivalently changes its direction when the plates are turned. The magnetic field is caused by the static solenoids and boosters and therefore remains constant independent of the E-gun plate angle.

If the E-gun angle is set to 0° (plate normal aligned to z-axis and magnetic field line) the electric and magnetic field lines are parallel and the electrons are accelerated along the field lines. The impact of the electric field distortion close to the front plate hole can be neglected because the electrons target for the center of the axisymmetric distortion. Already within the E-gun, the electrons bind to the magnetic field lines with increasing velocity. The result is a zero-angle beam on the z-axis with possible small offsets caused by the electron starting conditions.

The situation is more difficult when the E-gun plates are turned to a non-zero angle. In that case electric and magnetic field lines are not parallel anymore and the cross products

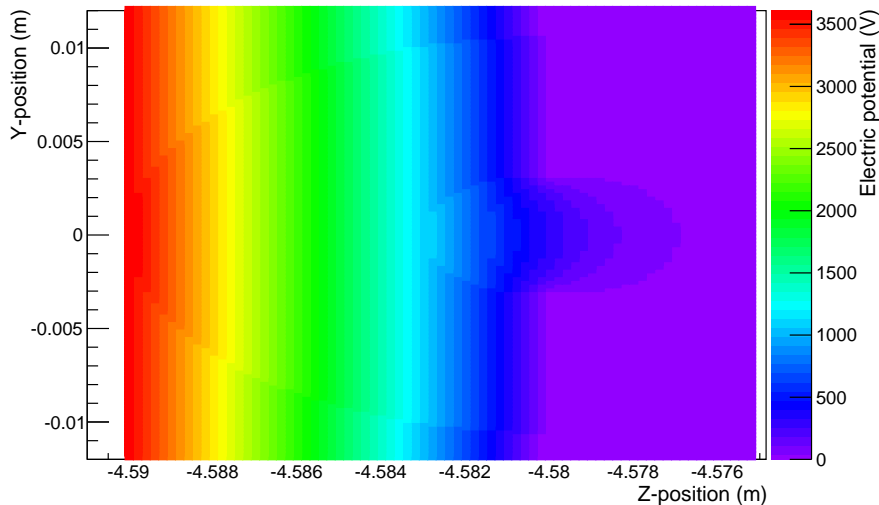


Figure 4.27.: Absolute electric potential between the E-gun plates - as calculated by the analytic formula. The potential drops very homogeneously between the two plates located at $Z = -4.59$ m and $Z = -4.58$ m. The front plate hole located at -0.003 m $< Y < 0.003$ m allows the back plate potential to continue further into the positive Z-direction and to slightly “shine” through the hole.

$\vec{E} \times \vec{B}$ and $\vec{v}_e \times \vec{B}$ do not vanish. The surface emitted electrons are at first accelerated and gain momentum with a non-zero angle to the magnetic field line. While the velocity of the particle increases and the electric field strength decreases on the way to the front plate, the magnetic part of the Lorentz force becomes increasingly important compared to the electric part. The magnetic field forces the electron into a cyclotron motion while the electron’s kinetic energy and cyclotron radius continue to increase. In addition to that, the electrons undergo an $\vec{E} \times \vec{B}$ drift like at the dipole electrode. Finally, the starting conditions of the electrons can still vary in energy, polar/azimuthal angle and starting position as already described. All these effects combined determine the properties of the electron beam and are included in any tracking simulation which provides an appropriate implementation of the fields. The goal of the design simulations is to steer the beam through the front plate hole without losses and optimize for a minimized distribution width concerning energy, polar angle and beam spot size. The results of these simulations and their impact on the mechanical and electrical design of the electron gun are described in the following section.

4.3.1. Results for the combined system

This section gives an overview on the results on E-gun simulations and tracking results with the combined system of E-gun and transport EMD. Some simulations are aimed to point out certain effects or dependencies and are therefore configured with fixed starting parameters (varied in discrete steps). But when evaluating statistic properties like the angular or energy distribution of the final electrons, a Monte Carlo simulation is used which randomly chooses starting parameters from the configuration space.

Figure 4.27 shows the resulting potential at the E-gun plates by calculation with the analytic formula (the plates are at 3.6 kV potential difference). The electrostatic potential is homogeneous, apart from the anode hole which can be expected because the solution bases on infinitely large plates. The influence of the more negative potential of the back plate reaches inside the front plate hole. Close to the circular corner of the aperture the potential increases rapidly - resulting in a strong electric field close to these corners. The electric potential inside the plates is set to the corresponding plate potential. On the front

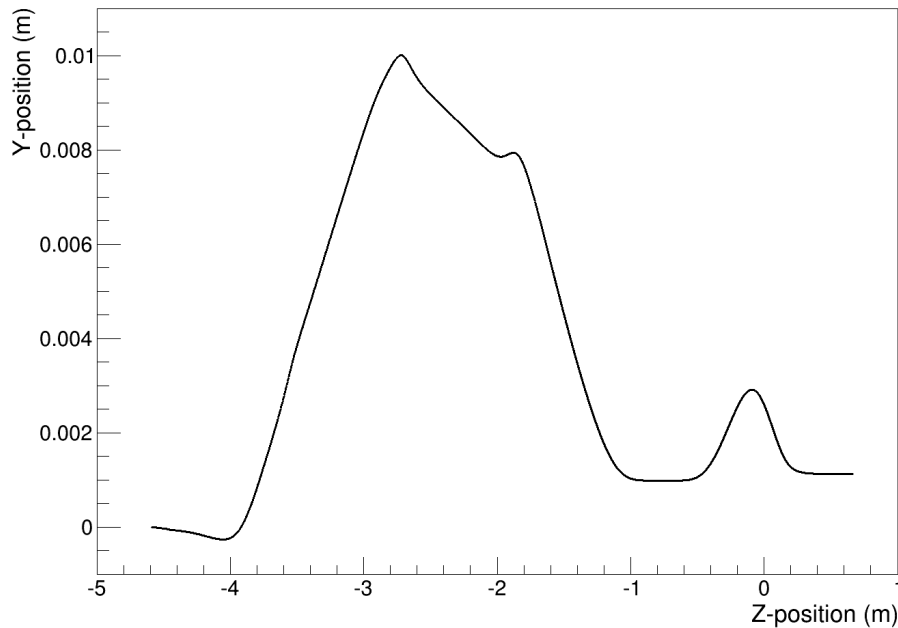


Figure 4.28.: Electron path starting from the electron gun with a plate tilt angle of zero degree - as required the electron passes through all components and does not take up any polar angle which would lead to a cyclotron motion. Besides the E-gun electrodes also the electric and magnetic dipoles are also active in this simulation which leads to a beam offset of up to 10 mm at the position of the aperture.

side of the anode the potential is set constant to the anode potential. Correspondingly the potential at the back side of the cathode is set to the cathode potential, though electrons can not move to this space.

The simple case with the full setup but the electron gun plates turned to 0° angle is evaluated next. The track through this system is visualized in the plot 4.28. Within the electron gun and post-acceleration region the particle stays on the z-axis. It is shifted in y-direction by the active electric and magnetic dipole systems. After passing the aperture, the particle is guided closer to the z-axis due to the shrinking magnetic flux tube. There is no cyclotron motion visible because the polar angle of the electron's momentum is parallel to the magnetic field lines after the electrons passed the only system which can cause non-zero polar angles - the electron gun. Figure 4.29 shows the progress of the electron's kinetic energy on the acceleration path. The smaller amount of 3.6 keV is gained between cathode and anode followed by the drift in the main electrode where the kinetic energy remains unchanged. The acceleration to the final kinetic energy happens step-wise between the post-acceleration electrodes. Here again only slow changes in the fields are tolerable in order to conserve the adiabaticity of the electron motion.

In a next step the electron gun tilt angle has been configured to produce electrons of the maximum acceptance angle for KATRIN (51° in the WGTS field of 3.6 T) or the reflection limit at the pinch magnet with 6 T). The angular behavior during an electron track is given in figure 4.30. In this case the path also shows the characteristic cyclotron motion (compare figure 4.31). Besides the non-zero polar angle, the center of motion of the particle track is also slightly shifted off the z-axis within the main electrode. The theoretical description of the E-gun principles in section 4.3 uses the forces at the electron to understand the resulting motion between the plates. The electrostatic and the magnetic force on an electron during its path through the E-gun are visualized in diagram 4.32: The increasing magnetic force exceeds the rapidly decreasing electric force close to the anode position. Because of this the electrons follow this path of combined acceleration and

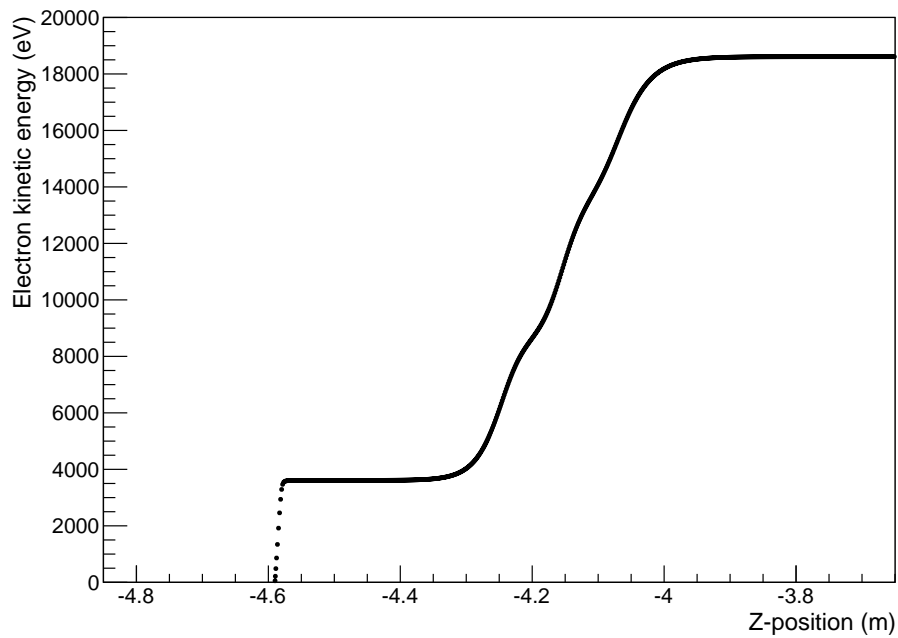


Figure 4.29.: Kinetic energy of an electron passing through the E-gun electrodes - The main difference to figure 4.21 results from the additional acceleration step between the electron gun plates. About 10 particle steps are calculated between the plates.

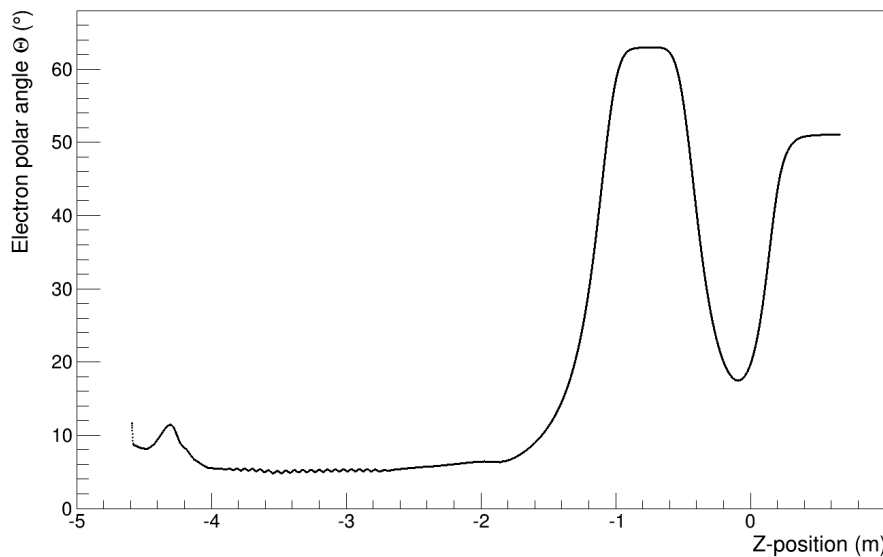


Figure 4.30.: Electron maximum polar angle behavior at E-gun simulations - starting with the lowest Z-values the polar angle drops rapidly at the E-gun when the magnetic force starts to dominate the electric acceleration force. From this point on, the angular progress resembles graph 4.24. At the very right, the electron ends up in the WGTS with the required 51° polar angle.

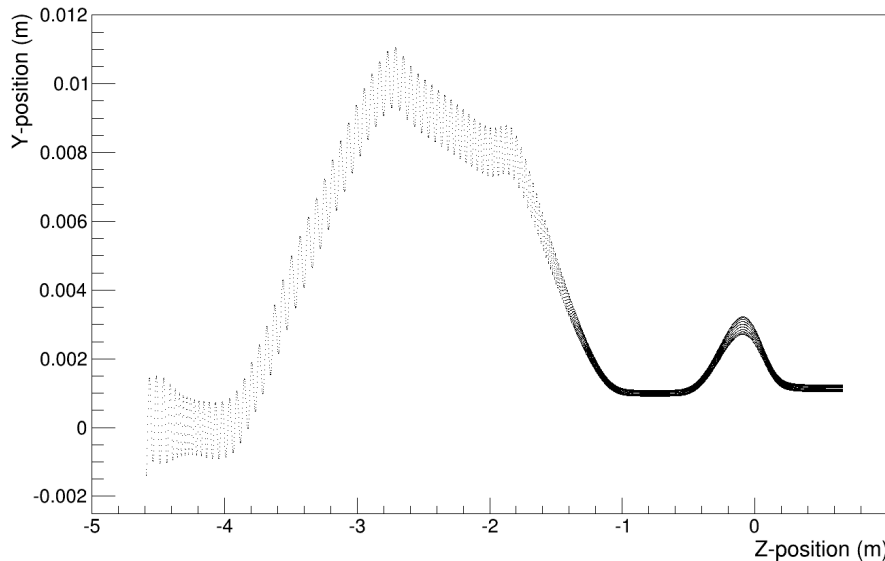


Figure 4.31.: Electron path with E-gun at maximum polar angle - as required the electron passes through all components and takes up the maximum polar angle by the E-gun plate tilt. Besides the E-gun electrodes the electric and magnetic dipoles are active in this simulation which leads to a beam offset of up to 10 mm at the position of the aperture.

cyclotron motion.

These basic simulations have been repeated while iterating through the parameters that can be optimized at the electron gun. In this case only the solenoids, the electron gun itself and the post-acceleration are activated to isolate the effects on the final beam properties from any modifications by the magnetic or electric dipoles. For a plate tilt angle of 0° there are not many possibilities to optimize the E-gun because the most parameters are already predefined (emission spot position, plate angle) or do not significantly affect the resulting beam. Therefore, the optimization is focused on the simulation of electron beams with the maximum acceptable angle for KATRIN. Intermediate angles will then work correspondingly and are only separately evaluated for the optimal starting position. The electron gun EMD design and optimization have been carried out in cooperation with [92, 90]. The final electrons' polar angle is defined by the interplay of plate tilt angle and the part of the electron acceleration that occurs between cathode and anode compared to the final energy. This dependency to create a maximum acceptance angle of 51° at the WGTS field strength of 3.6 T is presented in diagram 4.33. A smaller tilt angle can be compensated by a larger potential difference between cathode and anode - the result is a line with infinite possible configurations resulting in the same polar angles for the electrons. Following the line of possible configurations enables to compare the resulting angular distributions for electrons with comparable and realistic starting conditions. The parameters plate tilt angle and the potential difference between the plates can be adjusted anytime at the final electron gun and tuned with the result of real measurements.

In contrast to the previous easily adjustable parameters, the plate distance can not be changed without disassembling the electron gun. On the other hand this parameter is also more restricted: The plate distance must not be too small (≤ 5 mm) to securely avoid high voltage breakthroughs between the plates or at the plate mounting system. Likewise, the plate distance must not be too large (≥ 15 mm) because otherwise the field between the plates can become inhomogeneous and the turning body of 2 plates becomes so large that it can collide with the main electrode when it is turned. The effect of the plate distance on the electron gun beam has been investigated in [90]. As a compromise of optimization

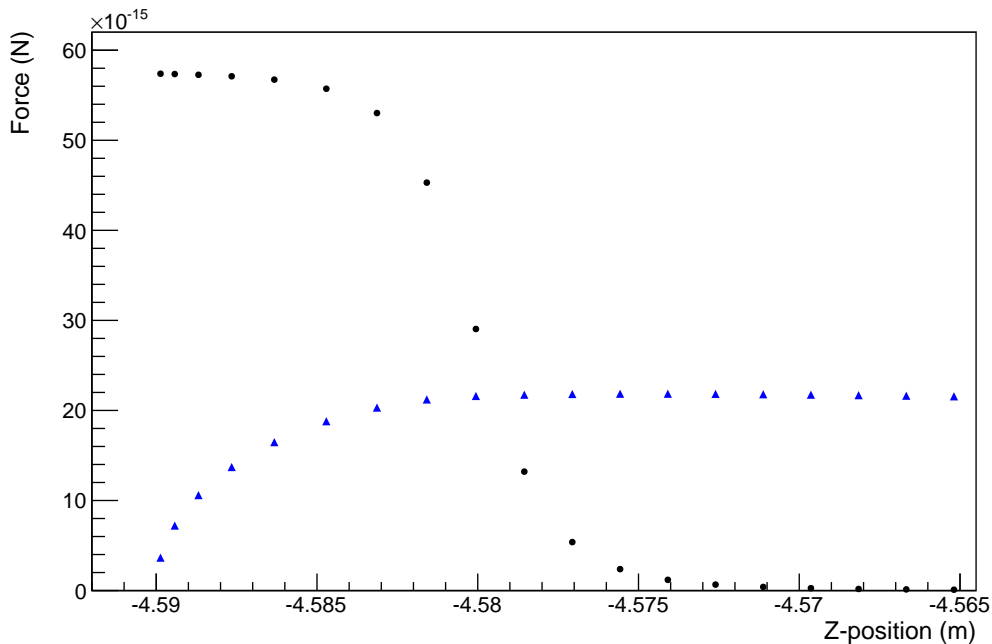


Figure 4.32.: Absolute electric and magnetic forces at the E-gun - Between the electron gun plates ($-4.59 \text{ m} < Z < -4.58 \text{ m}$) the electric acceleration force (black dots) dominates the magnetic force of the solenoid guiding field (blue triangles). However, the increasing magnetic force is sufficient to bend the electron to an initial cyclotron turn. Once the electron passed the anode the electric force drops to zero while the magnetic force remains stable due to the unchanged electron velocity. Simulation carried out with a plate angle of 11.7° and a plate potential difference of 3.6 kV.

and the mechanical and electrostatic feasibility a plate distance of 10 mm has been chosen.

The influence of the magnetic field strength was also investigated by [90]. The main conclusions of these calculations were that the electron beam properties improve with magnetic field strength and homogeneity at the E-gun as well as the post-acceleration electrodes. But increasing the magnetic field at the electron gun also has the undesired effect of the reduction of the mean polar angle. As a result the booster solenoids at the E-gun and at the post-acceleration position have been added to the transport EMD design. With the booster coils a very homogeneous field with a strength of approximately 30 mT at the electron gun and a field strength with more than 50 mT in the post-acceleration area is reached. This solenoid configuration did not need further improvement and has been used in all previous and following simulations.

The spot size of electron emission again is constrained by the technical details of the E-gun construction: The electrons are emitted in the surface area which is illuminated by the ultraviolet light. And the ultraviolet light targets the gold surface from within a UV fiber, which is why the fiber diameter determines the beam spot size. The fiber diameter $200 \mu\text{m}$ has been chosen, being a compromise of the difficulty to couple the light into the fiber and the mechanical flexibility of the fiber. Another reason the beam spot size on the gold surface does not require optimization are previous investigations [90] showing that the beam properties are nearly independent of the beam spot size as long as the spot size is less than 1 mm. More important than the emission spot size is the actual position of the spot in dependence of the plate tilt angle. The impact of the starting positions on the final beam properties is only of minor importance but if the starting position is not adjusted to the plate angle the electrons might hit the front plate instead of passing through the hole. Any case resulting in the beam stopped at some surface is not tolerable and must be avoided in the safest possible way. In the previous simulations the center of

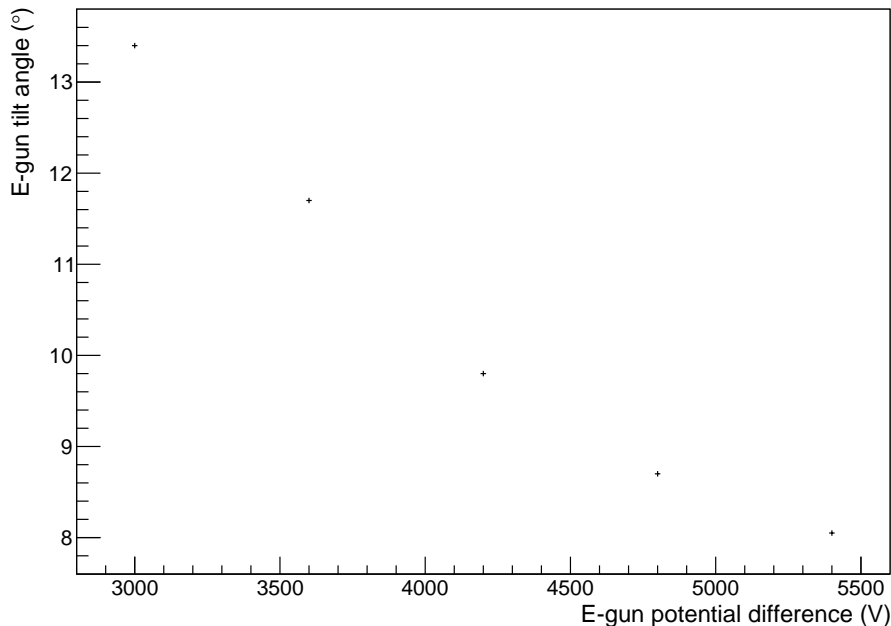


Figure 4.33.: Electron gun configurations to generate electrons with maximum polar angle - like expected the E-gun plate potential difference and tilt angle are linked parameters. For a certain plate potential difference, there exists a plate tilt angle to generate maximum polar angle electrons (51° in the WGTS). The simulation used an automatic algorithm to pick the right fiber for each plate tilt angle.

the emission spot has always been the intersection of the system z-axis and the E-gun back plate. Simulations also show that in the coordinate system of the E-gun back plate an appropriate starting spot needs to move with the plate angle. In the final setup multiple fibers are glued into the cathode. A dynamic moving of the spot requires the fibers to be placed at the right positions and an automated switching between the fibers. To find these positions simulations at different tilt angles have been performed to find in total 8 optimized positions [93]. The coordinates of the fiber positions and the E-gun settings with which they can run are summarized in table 4.3.

Now that all parameter dependencies are resolved and optimized in the range of feasible values the final full Rearsection simulations can be completed. These simulations use the previously described emission points and spot sizes. The photo-emitted electrons have an energy according to the Rearsection specification and the pessimistically assumed isotropic momentum directions. The designs of electron gun, post-acceleration electrodes and transport EMD fully comply to the results of the individual simulations and optimizations. Full Monte Carlo simulations have been carried out for the zero degree and the maximum polar angle with plate tilt settings of $\alpha = 0^\circ$ and $\alpha = 11.7^\circ$. For each simulation 2000 particles have been tracked through the full Rearsection setup including all magnets and electrodes with positions and dimensions as designed. The diagrams 4.34 and 4.35 show the angular and energy distribution for a simulated 0° beam. The angular distribution for this beam is 0.73° wide and the energy distribution has an uncertainty of 69 meV. Some remaining absolute polar angle at a field of 3.6 T can not be completely avoided. A mean angle of less than 2° in such a strong solenoid field should not restrain the electron gun functionality in any way. Correspondingly the simulation has been done for a maximum polar angle beam with the results given in the figures 4.36 and 4.37 respectively. At maximum angle the angular distribution is 2.2° wide and the energy distribution has an uncertainty of 71.5 meV. The absolute polar angle matches the target of $\Theta = 51^\circ$ considerably well. Such a distribution would be cut off above 51° by the KATRIN pinch magnet resulting in an

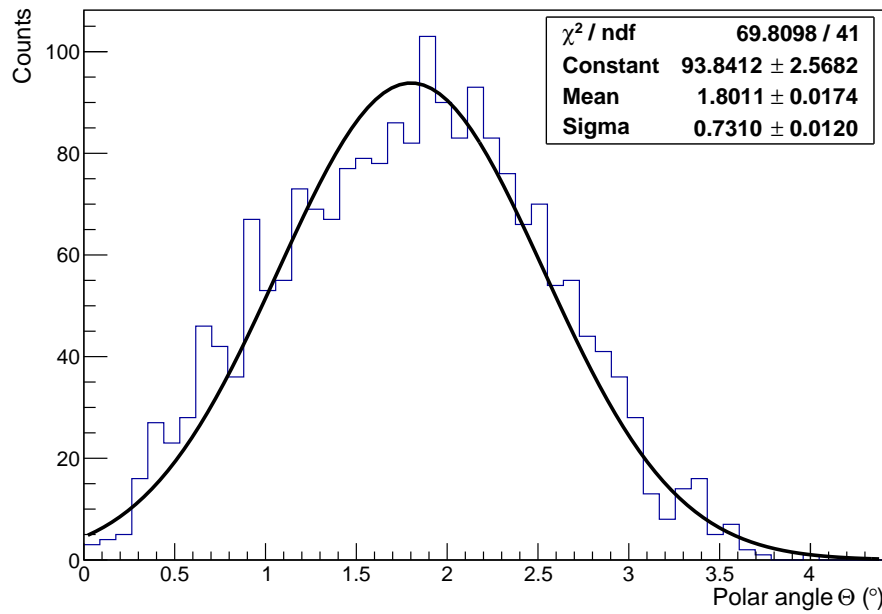


Figure 4.34.: Angular distribution of a full Rearsection electron gun simulation at zero degree plate tilt angle - Monte Carlo simulation of 2000 electrons passing through all previously described electromagnetic components. The plate tilt angle is set to zero and the plate potential difference to 3.6 kV. The final angular distribution is sufficiently narrow and close to 0° .

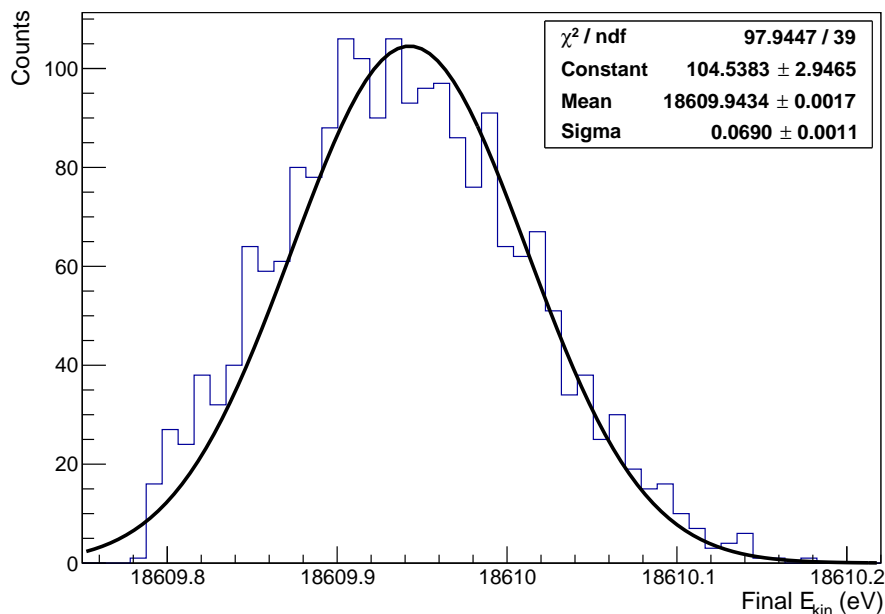


Figure 4.35.: Energy distribution of a full Rearsection electron gun simulation at zero degree plate tilt angle - Monte Carlo simulation of 2000 electrons passing through all previously described electromagnetic components. The plate tilt angle is set to zero and the plate potential difference to 3.6 kV. The broadness of the final energy distribution is completely caused by the initial electron surplus energy originating from the photoelectric effect.

Table 4.3.: Electron gun fixed fiber positions - These positions are an optimization result of simulations and are accordingly realized in the prototype design. They are selected to cover the full range of plate angles and to work redundant if a fiber should fail. Each fiber also has a “best” plate angle range where the resulting electrons keep a large (≥ 2 mm) distance to the anode aperture. These best plate angles for each fiber have been implemented in the Rearsection simulation.

Name	Fiber ID	X-shift (mm)	Y-shift (mm)	Best plate angles ($^{\circ}$)	Working plate angles ($^{\circ}$)	Symmetric to ID
Central fiber	0	0	0	-3 to 3	-6 to 6	-
Non-diagonal offset	1	0	-0.6	3 to 6	0 to 8	-1
First diagonal offset fiber	2	0.6	-0.6	6 to 10	2 to 11	-2
Second diagonal offset fiber	3	1.1	-1.4	10 to 15	7 to 15	-3
Non-diagonal offset	-1	0	0.6	-6 to -3	-8 to 0	1
First diagonal offset fiber	-2	-0.6	0.6	-10 to -6	-11 to -2	2
Second diagonal offset fiber	-3	-1.1	1.4	-15 to -10	-15 to -7	3

even narrower angular distribution of the final beam. In both cases the energy distribution width directly replicates the electron emission surplus energy which was defined as Gaussian distribution with a mean value of $E_{\text{kin,mean}} = 150$ meV and $\sigma_E = 75$ meV. The absolute value of the energy is augmented by approximately 10 eV which is caused by a minor flaw in the potential calculation of the E-gun plates module. The potential at the starting position is overestimated by 0.27% of the plates potential difference. Since rather the broadness of the energy distribution is important and furthermore the effect is purely virtual, it may be disregarded.

Although some assumptions in the simulations are quite pessimistic, the results exceed the Rearsection requirements. The results can always be improved at cost of electron count rate by a better matching of the UV light to the gold work function which directly narrows the electron emission energy distribution and reduces σ_E . Additionally, this small starting energy with a momentum in isotropic direction causes the largest contribution to the uncertainty of the polar angle.

Parallel to the electron gun design a simplified mechanical design has been implemented to enable checks for conflicts and mechanical incompatibilities. The final CAD drawings have been produced by [94] and an E-gun prototype has been built at UCSB. Some optimization like the beam spot positions have been included at a very late part of the development. For testing and calibration the electron gun with all electrodes and the full transport EMD has been assembled at UCSB. First measurements with an optical filter at 297 nm that should match closely to the gold work function (compare section 5.3) delivered count rates of about 17000/s. First tests of the electron polar angle have been conducted recording the electron beam phase shift in dependence of the solenoid field. The preliminary results showed a 5° angular spread at a polar angle of 20° . The energy and angular distribution will be measured more precisely with a small electron spectrometer during the E-gun

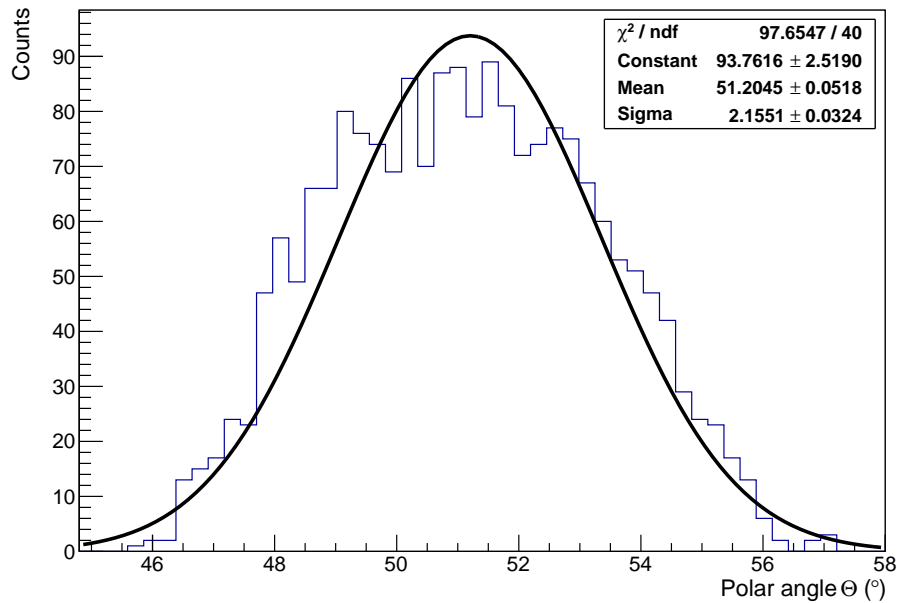


Figure 4.36.: Angular distribution of a full Rearsection electron gun simulation for maximum electron polar angle - Monte Carlo simulation of 2000 electrons passing through all previously described electromagnetic components. The plate tilt angle is set to 11.7° and the plate potential difference to 3.6 kV. The final angular distribution is sufficiently narrow and close to the target maximum electron angle of 51° at the WGTS field of 3.6 T.

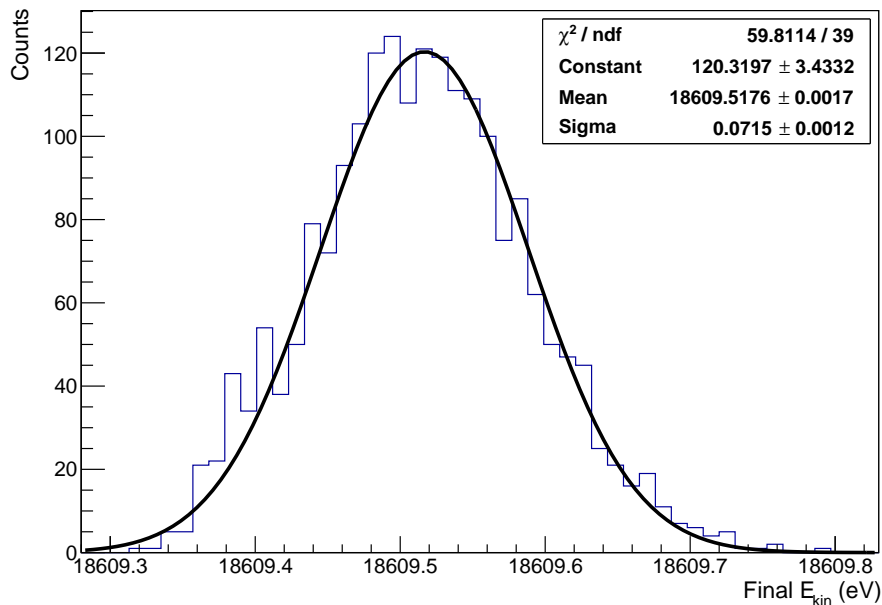


Figure 4.37.: Energy distribution of a full Rearsection electron gun simulation for maximum electron polar angle - Monte Carlo simulation of 2000 electrons passing through all previously described electromagnetic components. The plate tilt angle is set to 11.7° and the plate potential difference to 3.6 kV. The broadness of the final energy distribution is completely caused by the initial electron surplus energy originating at the photoelectric effect.

commissioning at UCSB. Once the measurements are completed and the electron gun fulfills all requirements it will be shipped to KIT for assembly and integration with the Rearsection.

4.3.2. E-gun calibration procedures

Even after detailed simulations of every single component it is necessary to have a set of calibration procedures available to check different E-gun properties and monitor the long-term reliability. Parts of the KATRIN experiment shall be calibrated by the electron gun. This makes the search for appropriate E-gun calibration procedures, without using circular arguments, challenging. The key to an appropriate calibration is to use the flexibility of the electron gun to setup measurements in which the other KATRIN components have improved precision compared to the normal experimental run mode. The most relevant parameters for calibration measurements with the E-gun are the electron rate, the electron energy and angular distribution. In all cases the mean values, the uncertainties and the time development of the values can be important. The precise beam position is of minor importance because it can be steered at high magnetic field strengths by the superconducting magnetic dipoles in the DPS1-modules of the WGTS. The beam size is also not of high relevance for the further KATRIN experiment because by the aperture of 3 mm diameter at a magnetic field of 50 mT the effective flux tube size of the E-gun beam is limited to $< 3.53 \cdot 10^{-3} \text{ T} \cdot \text{cm}^2$. This small flux tube size leads to a negligible beam diameter of $177 \mu\text{m}$ in the WGTS and an acceptable beam diameter of a few centimeters in the main spectrometer. As a consequence in the following list possible calibration and monitoring methods are only discussed for the most important parameters of the electron gun.

- Electron rate:** The absolute electron rate is important to reduce the time for measurements where only small statistical errors can be tolerated. The E-gun specifications demand for a rate of 10^5 1/s in the high precision mode with $\sigma_E < 0.2 \text{ eV}$ and a rate up to 10^6 1/s in the high rate mode with reduced energy requirements ($\sigma_E < 2 \text{ eV}$). The rate stability in time is necessary for scanning operations like the response function measurement or repeated column density checks. Required is a stability of $\sigma \leq 0.1\%$ on a time scale of hours. The absolute rate as well as the rate stability are both tested within the commissioning tests. With an energy resolving silicon detector it is possible to measure the rate with single event counting. On short time scales the ultraviolet light source is the highest risk concerning stability. Therefore, a monitoring of the light source will be implemented using a beam splitter. The correlation of UV intensity monitoring and the E-gun rate is also calibrated during commissioning. The intensity monitoring will be included in the final Rearsection setup. A precise measurement of the E-gun rate or stability can be done with the main detector while the E-gun energy exceeds the spectrometer filter voltage. Of course scattering at tritium gas in the source section rules out the calibration of the absolute rate and can disturb the stability measurement if the gas density is not stable. If a very precise check of the rate parameters is required the WGTS has to be evacuated which is possible on a short time scale by closing the tritium gas inlet. But still the source evacuation is an undesired action because it can destroy the stability and equilibrium inside the WGTS. This is why the high precision rate measurement with the main detector will be carefully pondered before it is used.
- Electron energy distribution:** The absolute electron energy is defined by the cathode potential which is again linked to the main spectrometer potential. A precise low-voltage power supply is added to compensate the surplus energy by the UV light

and to shift the electron energy relative to the filter potential. With this voltage supply design no significant absolute shifts or temporal drifts are expected. More important is the broadness of the energy distribution. This is measured during the commissioning with an appropriate electrode which applies a counter potential to the electrons. After this high-pass filter, a detector measures the rate in dependence of the filter voltage. In the same way the energy distribution shape can be measured at KATRIN with the main spectrometer as filter and the main detector as counter. With the absolute energy set to a value above the tritium endpoint there is no contribution by the β -decay to the measurement. The precision can be improved when the electron gun uses a polar angle of zero degree because for 0° electrons the MAC-E-Filter has a significantly improved energy resolution (compared to the 0.92 eV energy resolution for isotropic sources). The measurement of the electron energy distribution by the main spectrometer requires a short interruption of the neutrino mass measurement.

- **Electron angular calibration:** Basically the main spectrometer can also be used for angular measurements because the transmission dependency on the electron angle is well known (e.g. the analytic transmission function [3]). But the MAC-E-Filter will already be used for the determination of the energy distribution - if the angular calibration would be done with the same device the uncertainties can become difficult to unfold. Instead, it was proposed to not use electrostatic but magnetic transmission/reflection for the angular calibration. With the KATRIN pinch magnet a strong magnetic field for reflection tests is available. Magnetic reflection only depends on the adiabaticity conservation, electron angle and field strength in a weaker field and the reflection field strength (compare equation 2.6). The independence of the electron energy makes this kind of reflection to an ideal candidate for angular calibration. In this measurement the E-gun can be tested for all large plate tilt angles (except when the resulting electron angles are too small for magnetic reflection). At each plate tilt angle the potential steps between cathode/anode compared to the post-acceleration are varied until magnetic reflection occurs. The total energy of the electrons may differ from the typical values around 18.6 keV during this calibration. The resulting data can be used in simulations or analytic calculations to precisely reconstruct the E-guns angular behavior (absolute angle and uncertainty on the angular distribution). This working principle has been tested and proven with partially blinded simulations in [90]. The angular calibration can be done during normal KATRIN operation. Only the four most inner pixel of the main detector will be blocked by the electron gun beam - except for that the neutrino mass measurement can continue.

4.4. Piezoelectric motor performance test

So far in this chapter details how an electron beam is produced and guided within the Rearsection have been described. In fact the electron gun is switched off most of the time because it is only activated for limited calibration runs. During the downtime periods of the E-gun the central hole in the Rear Wall must be closed. By this the tritium gas flow into the Rearsection is reduced and the Rear Wall can expose a complete surface towards the WGTS beam tube. The features of the Rear Wall and the importance of a gapless surface are discussed in chapter 5. To complete the surface a cover, which will be moved above the hole, is placed on the backside of the Rear Wall. The cover surface directed towards the source is also gold coated. For the closing operation a mechanical movement of the cover by more than 5 mm is required within a complicated environment. In the following the requirements for the motor, linear stage or moving mechanism (hereafter called “motor”) are listed:

- The motor has to work in a vacuum environment. Although the pressure in the chamber is not in the ultra high vacuum (UHV) range the outgassing rate of the motor should be as low as required for the UHV range. By this the impact on the gas purity of the tritium source is reduced.
- Due to the connection to the WGTS there will be a significant amount of tritium and β -radiation that can reach the motor. The resulting ions can act similar to an acid. In addition, they can be activated to reactions, which do not occur at room temperature because they are too endothermic, by the energy from the decay. By the safety requirements of tritium handling the material choice for the motor is also restricted [4]: Preferable are metals and ceramics, while plastics and hydrocarbons in general must be limited to the necessary minimum. Furthermore, the usage of halogen elements is completely forbidden to avoid chemical reactions resulting in strong acids like hydrofluoric acid (HF) or hydrochloric acid (HCl). This also excludes most of the modern UHV compatible lubricants.
- The close superconducting magnets produce a magnetic field of more than 1 T at the Rear Wall. At such a strong field it is impossible to use UHV compatible electro-motors. Also outside of the vacuum system, conventional electro-motors need a certain distance to the Rear Wall chamber to avoid being blocked by the magnetic field.
- The environmental conditions are typical to favor a solution using a mechanical feed-through while the motor is placed outside of the vacuum system. But in this case the mechanical access is only possible in the backside direction of the Rear Wall and would require a complicated mechanical translation to connect to the feed-through which must be placed inside of the Rearsection superconducting re-condenser magnet (RSCM). Placing the motor directly at the feed-through is not acceptable because of space constraints.
- Similar to the mechanical access the supply access in general is challenging. The space for device connections is very narrow and allows a few electrical connections but can not be used for pneumatic or hydraulic supplies.
- Finally, the maintenance or exchange of the motor will be a very complex operation. The motor should therefore be able to handle many driving operations before it stops moving: Mean time before failure (MTBF) must be at least > 50000 , better > 100000 end-to-end cycles. A high MTBF gives the chance that the motor never needs replacement in the runtime of KATRIN.

After the requirements have been carefully evaluated a motor based on the piezoelectric effect has been considered as ideal instrument to realize the mechanical movement of the Rear Wall cover. The manufacturers assure the vacuum and B-field compatibility of their motors and an appropriate choice of materials for the usage in a tritium environment. With such a small motor no direct mechanical access is required and only a few wires are required to connect the device. But still an explicit test is needed to guarantee the endurance of the motor within the aggressive, radio-chemical tritium environment. In the following section the experimental setup and the measurements performed in this stress test are described.

4.4.1. Experimental setup

The central element of the setup is the small motor which works with the inverse piezoelectric effect. The piezoelectric and the inverse piezoelectric effect describe a dependency of mechanical stress on the one hand and charge separation and voltage at the solid surfaces on the other hand. In technical products crystals or ceramics are used which are

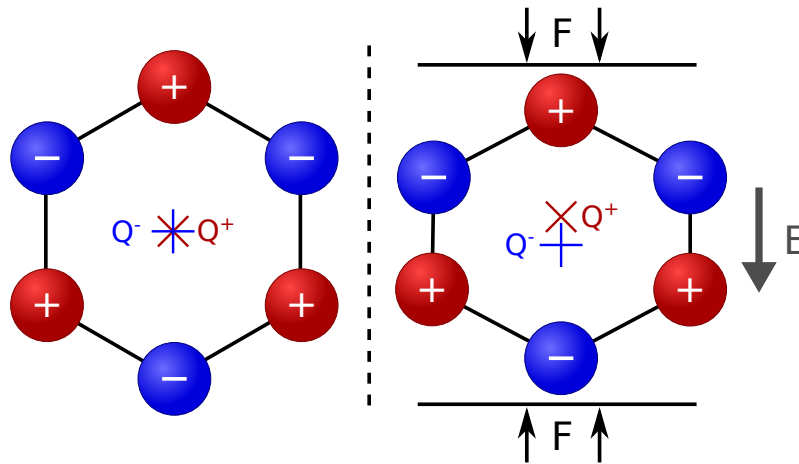


Figure 4.38.: Simplified visualization of the piezoelectric effect - If a mechanical deformation of a solid leads to an overall charge separation and a voltage on the crystal surfaces, the solid is piezoelectric. Typically, the microscopic charge separation occurs on the level of a symmetric cell like the elementary cell. The piezoelectric effect may work in both directions: It reacts with a surface voltage to an outer mechanical force or with a crystal length change on an outer electric field.

non-inversion symmetric and their elementary cells show charge separation when they are deformed in a certain direction (compare figure 4.38) [95]. This microscopic effect can be retained up to the macroscopic crystal or ceramic. If a force is applied on such a solid a voltage can be measured between the surfaces (direct piezoelectric effect) and if a voltage is applied to the surfaces the solid can change its length or shape (indirect piezoelectric effect). Still these solids can not be used directly to build a linear stage covering the required 5 mm range - the typical stroke depending on the exact piezo crystal is within the range of nanometers up to a few micrometers [95].

The motor that has been chosen for the test and might be applicable in the given environment is the ANPx101eXT20/RES by Attocube⁸ with 20 mm stroke. The motor works with the “slip-stick” mechanism to reach this macroscopic stroke: The voltage applied to the piezoelectric solid is relatively slowly increased. By this the piezoelectric solid extends/contracts and pushes the loosely connected movable part in the same direction (“stick” phase). After this step the voltage is rapidly reset resulting in a quick contraction/extension to its original size and shape. The movable part which is only loosely connected to the piezoelectric solid will not follow this quick movement due to the inertia of momentum (“slip” phase). By repeating the slip-stick process it is possible to achieve a macroscopic movement. For this macroscopic movement the applied voltage must be a sawtooth signal with appropriate frequency and peak-to-peak voltage. Due to the working mechanism the allowed forces and loads for a slip-stick motor are relatively small compared to conventional motors (e.g. maximum 4 N static force along the axis for the ANPx101eXT20/RES).

A CAD image of the ANPx101eXT20/RES is shown in figure 4.39. The motor has a footprint size of 24 mm × 48 mm moving a platform with top surface dimensions of 24 mm × 24 mm along the axis. The piezoelectric ceramic in use is PZT (lead zirconate titanate) and the motor body is made of titanium. The maximum load or force along the axis is 2-4 N while the maximum speed is 3 mm/s. The motor includes an absolute resistive position sensor. Totally 5 UHV-compatible and KAPTON insulated copper wires are used to connect the piezo-motor: Two wires for the moving mechanism and three wires for the position sensor. According to the manufacturer the motor only consists of titanium and

⁸attocube systems AG, Koeniginstrasse 11a, 80539 Munich, Germany

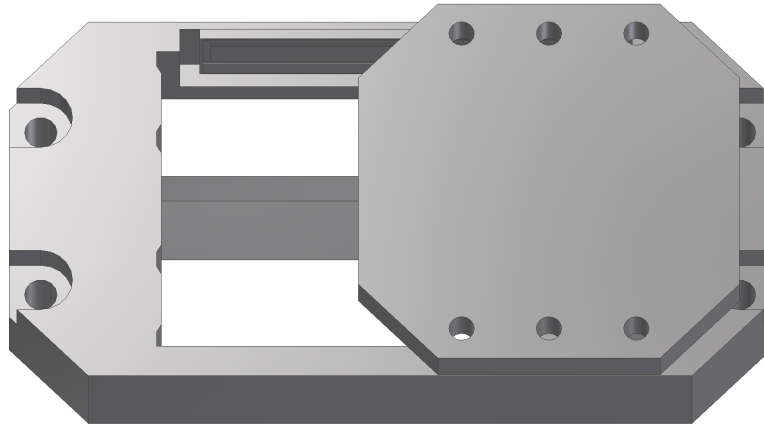
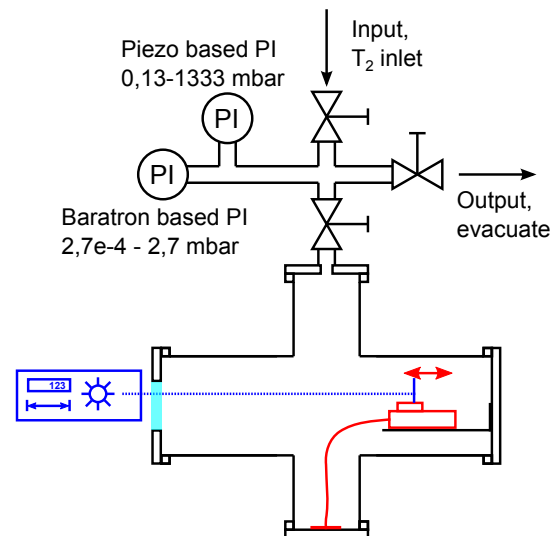


Figure 4.39.: CAD picture of the piezoelectric motor Attocube ANPx101eXT20 - The top platform can move along the axis while the axis and the body of the motor stays fixed. The body can be installed to a surface with 4 screws. Several screw holes are available to fixate the object that shall be positioned by the motor. CAD data property of attocube systems.

Figure 4.40: Schema of the Attocube motor test experimental setup - The motor itself is installed in a vacuum chamber and the electric supply is realized in form of an electric feed-through flange. The motor position can be checked independently via laser distance measurement. Pressure sensors allow a quantitatively controlled evacuation, venting and filling of the vacuum system.



the PZT ceramics and there are no materials in use (including vacuum-sided cables and connectors) that do not comply with the tritium and UHV requirements [96]. A special controller (Attocube ANC350) was used to power the slip-stick motors and read out the resistive sensors. A common PC was used to communicate with the ANC350 via USB and the included LabVIEW drivers.

The motor was placed into an ultra high vacuum system based on a CF100-63 CONFLAT reduction cross as chamber. The setup of the vacuum system is visualized in the schema 4.40. On one CF100 flange the piezo-motor has been installed using an elbow connector in between. At one of the CF63 flanges an electrical feed-through is installed to connect the in-vacuum motor with the controller placed outside of the vacuum system. At the opposite CF63 flange the gas control system is attached. It consists of pressure sensors and further connectors for gas inlets and evacuation outputs. Using the outlet the system can be evacuated via a pumping system consisting of turbomolecular pump (TMP) and fore pump. Once the system is evacuated it is possible to inject and test specific gas mixtures including hydrogen or tritium in combination with the motor. The pressure indicators in use are MKS 902-1213 and MKS 626B02TBE - both based on the mechanic force of the pressure and hence independent of the gas type. Combined, the sensors cover

a measurable pressure range from 10^{-5} to 1000 mbar. Both pressure sensors are read out with the measurement PC and included in the custom LabVIEW software. The final remaining flange of the cross is used to install an UHV compatible sight glass. By this the status of the piezo-motor can be visually checked. Furthermore, the driving distance can be verified more quantitatively with a Bosch GLM150 laser distance measurement device [97]. In order to have an appropriate target for the laser another elbow connector is installed on the moving platform of the ANPx101eXT20. The unconnected side of the elbow connector offers its surface towards the measurement laser. The laser distance measurement is only foreseen in cases when the measurements by the resistive, absolute position sensor of the piezo-motor should be doubtful. The vacuum system is used with the flange supporting the motor downwards. As a consequence, the piezo-motor drives upwards-downwards to do a driving cycle. Finally, the vacuum system is placed into a second encasement which was formerly used for the TRAP experiment [98]. This enclosure is considered as safe as a fume hood concerning the TLK safety regulations. By this the handling of tritium amounts with a radioactivity smaller than 10^{10} Bq inside of the CF100-63 cross is allowed. The motor can then be tested in a tritium atmosphere with pressures and intensities of radioactivity which are several orders of magnitude higher than at the designated deployment position at the Rear Wall of KATRIN. As consequence the compatibility measurement time of the test experiment can be significantly reduced compared to the KATRIN operational time.

4.4.2. Motor performance evaluation

The first driving operations with the motor were performed at ambient air to ensure the proper functionality of the custom LabVIEW program. The software uses closed loop driving commands for either manual drive to a given position or automatic driving operations. The automated drive runs either from end to end of the driving scope or to random target positions. It is possible to configure a certain pause between the automatic driving operations. Additionally, the pressure of the sensors is read out and displayed. The data of motor and pressure sensors can be written to a measurement file after every single driving operation. The software was successfully tested with the motor at ambient conditions. After motor and controller worked well in the first tests the hardware was integrated in the described vacuum system.

One of the final checks before the continuous stress test is the cross check of the motor positions with the laser distance measurement device. In this test the distance measurement device and the absolute position encoder agreed on several driven distances within ± 0.5 mm. This result is within the valid scope to proof the proper functionality of the absolute position sensor since the precision of the laser distance measurement device is only ± 1 mm [97]. The simple calibration test was repeated whenever the results of the absolute position sensor were doubtful and required an independent cross check. Another task handled during the beginning of the measurements was the optimization of the configurable motor parameters. The optimization was required because in rare cases (probability $\approx 1\%$) the motor got stuck or did not reach the target position with the expected precision (deviations > 10 μ m are considered as failure). There are 2 parameters available that can be configured at the motor controller: The amplitude and the frequency of the sawtooth voltage that is applied to the piezoelectric ceramic of the motor. Both parameters have been varied within a reasonable range and the result is given in table 4.4. In general a higher voltage increases the power of the motor and the chance to reach the target position. But a high supply voltage has the inherent problem of faster deterioration and depolarization of the piezoelectric ceramic. Concerning the frequency the motor runs best in the range from 500 Hz to 1000 Hz. But the system acts very efficient on certain frequencies which can be considered as resonance frequencies. During the stress tests the voltage and frequency parameters have been adjusted in order to achieve continuous and

flawless driving operations. In case of driving failures the recommendation by the manufacturer Attocube was followed to re-polarize the ceramic with a few steps at 70 V with a repetition rate of one step per second. In the further the behavior of the piezo-motor during the measurements within vacuum and tritium atmosphere is described in detail.

Table 4.4.: Performance of the piezo-motor - depending on the 2 configurable parameters: Amplitude and frequency. The table shows a search for a working parameter set after the motor showed first signs of wearout. If the motor runs both directions further qualities like the driving time or accuracy have been tested. The measurement revealed the motor needed at least 40 V to achieve accurate driving without getting stuck. The limited power of the motor shows by the difference of gravity when the motor is driving upwards or downwards.

Amplitude (V)	Frequency (Hz)	Time: Down (s)	Time: Up (s)	Accuracy	Motor stuck
20	1000				yes
30	100				yes
30	500				yes
30	750			low	no
30	1000	36	stuck		yes
30	1200				yes
30	1400				yes
30	1600			low	no
30	1800				yes
30	2000			moderate	no
35	1000	36	stuck		yes
40	500	45	135	high	no
40	1000	18	42	high	no
40	1500	10.5	19	low	no

The first part of the stress test is realized without tritium but just in rough or fine vacuum. The remaining gas at these pressures is expected to have a similar gas composition as ambient air. The pressures covered in these measurements were ≈ 13 mbar and $2 \cdot 10^{-3}$ mbar to $2 \cdot 10^{-2}$ mbar. Especially the lower pressure range is close to the target partial pressure of tritium in the second part of the stress test. During the cold measurements also the previously described optimizations and calibrations have been carried out. Overall 11000 random driving cycles have been conducted in this phase. At the beginning the motor showed a performance completely sufficient in every concern of the Rearsection like reliability, repeatability, precision and speed. In most cases ($> 95\%$) the target position and the measured position were met within $2 \mu\text{m}$. At the end of the cold measurement after 9000 driving operations the motor shows first signs of abrasion: The error rate goes up to 30 % (compare figure 4.41) of the driving operations and the deviations are large (several millimeters). In this case and in the further evaluation all driving operations when the original target is missed by more than $10 \mu\text{m}$ are considered as erroneous. With some optimizations and repeated re-polarizations the error rate could be reduced again with the goal of continuing the test in tritium atmosphere. The test in the radioactive tritium atmosphere starts with a tritium gas mixture of $> 90\%$ tritium purity at a pressure of 0.08 mbar. During the experiment the pressure increases by outgassing and leakage up to 0.12 mbar. The measurement is conducted with an already erroneous motor trying to detect a different behavior in the radioactive atmosphere. Due to the optimization the motor starts running with a reduced but non-zero error rate. After 3500 random driving cycles during 2.5 days in tritium atmosphere the error rate started to rise steadily (compare figure 4.42). After more than 5500 driving operation and 4 days in tritium the motor is stuck completely and reaches therefore an error rate of 100 %.

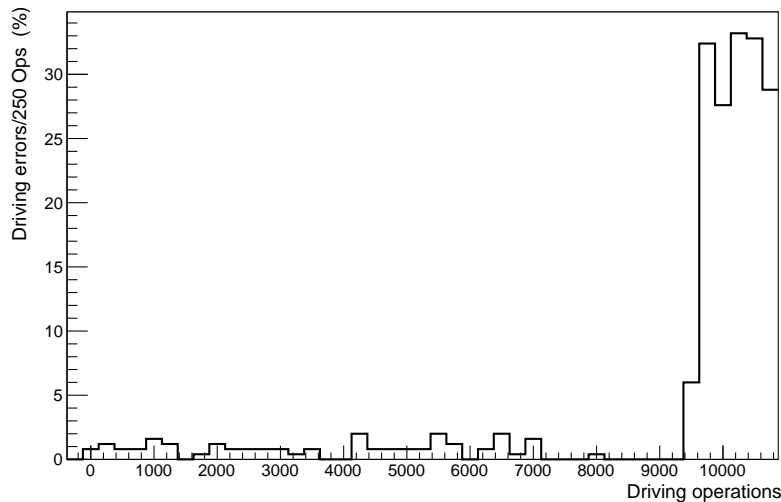


Figure 4.41.: Piezo-motor driving operations in vacuum - At the beginning the motor performed precisely and accurately. After 9000 driving operations (Ops), the first signs of wear appeared - about 30% of the commands were not completed successfully

The first and most important result of the performance test of the piezoelectric motor is that the motor fails by abrasion-like effects before it reaches the target minimum driving cycles of 50000. Already when conducting the warm test the manufacturer Attocube has been contacted for trouble-shooting. In several discussions important information could be gained concerning the motor: The amount of driving cycles without maintenance by the manufacturer is limited. The mean time before failure is not precisely known to the manufacturer but was estimated to 10000 end-to-end cycles [99]. This MTBF value is neither available in any product specifications nor was it stated during the product research. The reason for the limited lifetime is an organic coating that is applied to the motor axis. It ensures the right friction for the slip-stick mechanism and is essential for the motor to work. The existence of such a coating was repudiated during the product negotiations asking for any lubricants, organics or materials that differ from the used titanium and ceramics [96]. Recommendations of Attocube to sent back the motor for maintenance and re-coating were neither applicable at the test experiment nor later for the Rearsection due to the tritium contamination.

The experiment could not definitely show if the radiochemistry of tritium does any harm to the motor, but it could definitely proof that such a slip-stick piezoelectric motor can not be used for moving the Rear Wall cover at the Rearsection. During the disassembly of the experiment the motor has been checked visually. Picture 4.43 shows a close-up of the motor axis. The stains on the axis are a visible sign of damage and abrasion. While the piezoelectric moving mechanism failed completely, the absolute position sensor did never fail and was helpful for diagnostics. Concerning the final Rearsection setup the closing mechanism at the Rear Wall must have some position indicating mechanisms. An absolute position sensor allows closed-loop operations and detailed information if the motor gets stuck or changes its speed. But when the motor works reliably limit switches are sufficient to have well defined Rear Wall cover positions and it remains possible to detect a motor failure. This test experiment was very important to render an advanced technology within the Rearsection as unusable. As a result some Rearsection requirements were modified and several design changes had to be done:

- The robustness requirement on the moving mechanism has been increased. Any mechanism to implement the cover movement of the Rear Wall needs an explicit testing with and without tritium. At least 100000 successful end-to-end driving

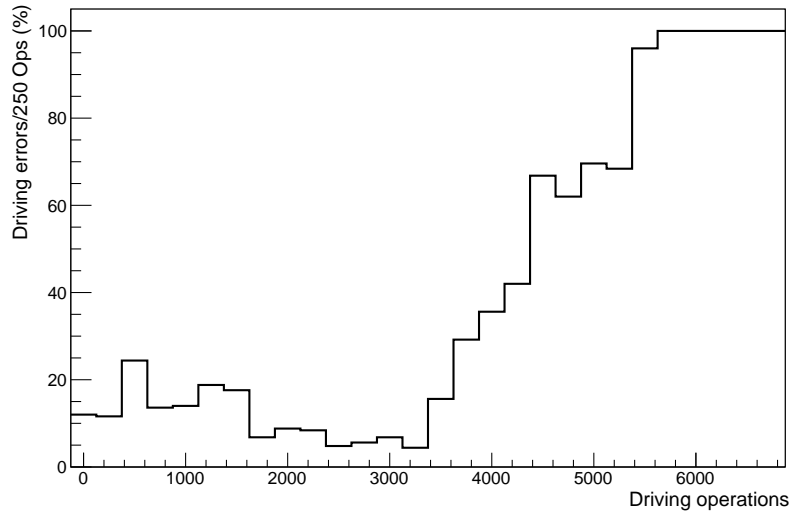


Figure 4.42.: Piezo-motor driving operations in tritium atmosphere - Due to the previous stress test at atmosphere the motor did not start flawlessly. With optimizations and re-polarization of the piezo-crystal the motor operation could be improved at the beginning and during the tritium measurements. Later the error rate increased rapidly until to the total failure of the motor.

cycles are required. For safety reasons this is a factor of 2 to 3 higher than what is expected as cycle count at KATRIN.

- The lifetime of every mechanical system is limited. Therefore maintenance plans are required to exchange any component that is likely to fail at the Rearsection during the regular KATRIN maintenance phases. The moving mechanic for the Rear Wall cover is such a component with a dedicated repair plan.
- An alternative way to integrate a mechanic movement in the Rear Wall environment had to be found. For this another motor based on the piezoelectric effect has been carefully selected. It is a custom adapted development by Physik Instrumente⁹ and uses a different mechanism than “slip-stick”. The tests in vacuum and tritium were successful and fulfilled the requirements. The details about tests and measurements with this motor are given in [86].
- Originally not only the Rear Wall cover but also the electron gun aperture should be a movable part within the Rearsection. This option was abandoned because a maintenance at this position is hardly possible. The aperture is now placed at a fixed offset position of 10 mm and the steering magnets must be used to steer the beam through the hole.

4.5. The electron gun beam tracker

The Rearsection electromagnetic transport section includes 2 small apertures, one at the Rear Wall and one off-axis in the center of the solenoid, and multiple electromagnetic field sources to steer the beam. Furthermore the earth magnetic field and the stray field of the DPS1-R magnetic dipoles have a significant steering impact on the electron gun beam. Even with the support of detailed electromagnetic simulations there is a large degree of freedom concerning the configuration of dipole fields to successfully steer the beam through the apertures. To solve this problem a small detector system has been designed, built and tested. Such a detector system can either help to reduce the effort at

⁹Physik Instrumente GmbH & Co. KG, Auf der Roemerstr. 1, 76228 Karlsruhe

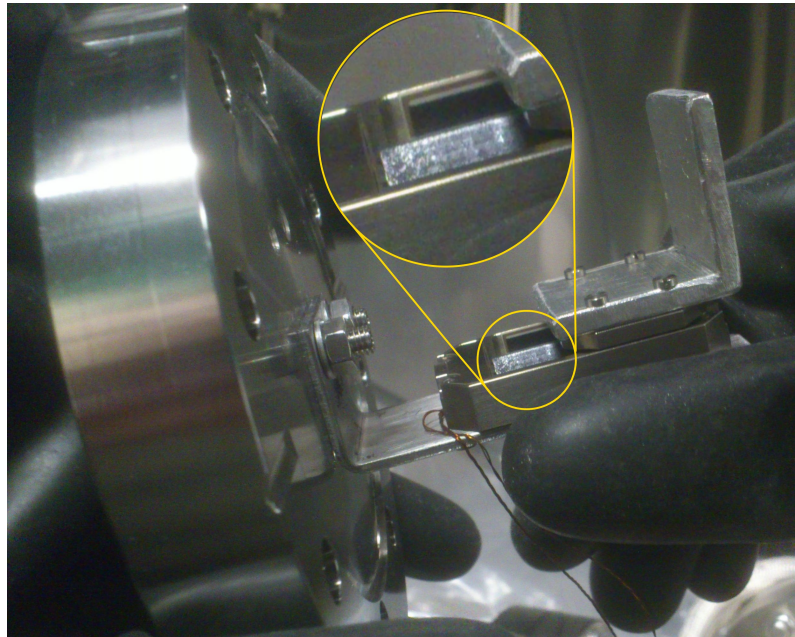


Figure 4.43.: Picture of the piezoelectric motor after the measurements - recorded during the system disassembly after complete failure of the motor. The stains visible on the motor axis may be an indicator for a destroyed friction layer.

the initial configuration of the E-gun or even enable a closed-loop operation of the detector and the beam steering magnets.

4.5.1. Design of the electron gun beam tracker

The minimum requirements for the e-gun beam tracker are a detection system with a hole equal to the planned aperture size and an electric output signal that indicates when the hole is missed by the e-gun beam. This can be improved if a rough position indicator is included. Silicon PIN-diode based detectors are typically among the first choices for a custom simple, compact and reliable radiation detection system. In this case a special PIN detector is required because it needs a central hole, a thin dead layer to detect low energy electrons and segmentation for position resolution:

All silicon detectors have a designated surface where the particles which shall be detected enter the sensitive silicon volume. This surface is called detection window and the doping atoms are typically placed close to the surface. The deepness of the implantation depends on the production process and has a direct impact on the size of a depletion zone which is the effective detection volume of a silicon detector. Due to this inherent production property, all silicon detectors have an area of reduced detection efficiency between the detection window and the sensitive volume. This area is called the dead layer of a detector and its impact strongly depends on the particle type and energy which shall be detected. Charged particles i.e. electrons with an energy in the low keV-range, like the β -decay electrons of tritium, have an inelastic mean free path of $O(10\text{ nm})$ in silicon [81]. This is the same order of magnitude as dead layers of commercially available silicon detectors for electron detection. This leads to the following 2 consequences:

- The electron energy can be completely or partially deposited in the detector's dead layer. How these incomplete or missing events influence the E-gun beam tracker will be described in the scope of the output signal estimation later in this section.
- The other outcome for the E-gun beam tracker is that the usage of a special detector with thin entrance window (equals to small dead layer) is required which is optimized

for low energy electrons.

Overall the geometric requirements on the total size as well as the size of an inner hole and the suitability for use with low energy electrons are quite specific demands. But after an inquiry among common semiconductor companies a suitable detector for the purpose of an E-gun beam tracker was found at Micron Semiconductor¹⁰. The LL series as catalog product contains a wide range of quadrant electron detector with central holes and a variety of hole diameters (1050 μm - 5600 μm) and outer diameters (10600 μm - 19000 μm). For the test system the 4-segment Micron LL14 has been ordered. It has a inner hole diameter of 3.3 mm, an eight sided outer shape with a Flat-to-Flat chip distance of 10.6 mm, an inner active area diameter of 4.22 mm and an outer active area diameter of 10.08 mm.

A silicon detector like the LL14 is based on a reverse biased PIN-Diode. This is the same working principle like a pn-junction but with an intermediate “intrinsic” layer which is only slightly doped. By this, the space charge region of the pn-junction is extended to maximize the sensitive volume of the detector. When particles deposit energy in the space charge region electron-hole-pairs are created and separated by the electric field in the space charge region. Since silicon has an indirect band gap the average energy to excite an electron-hole-pair exceeds the band gap of 1.1 eV [100]. The average energy for the excitation of an electron-hole-pair by electrons in the low keV-scale is given by:

$$w = 3.65 \text{ eV} \rightarrow \langle N_{\text{E-P-Pairs}} \rangle = \frac{E_{\text{deposited}}}{w} [101] \quad (4.9)$$

Inherent in every silicon detector there is a statistical variance to average the number of created electron-hole-pairs $\langle N_{\text{E-P-Pairs}} \rangle$ given by the Fano-factor F :

$$F = 0.115 \rightarrow \sigma_{N,\text{Fano}} = \sqrt{F \cdot \langle N_{\text{E-P-Pairs}} \rangle} [101] \quad (4.10)$$

The required energy per electron-hole-pair w is an important parameter to design an appropriate signal amplifier. The other important factor for the amplifier design is the decision which type of electric signal from the diode is used.

- Charge source: Detectors can act as charge source since they provide a burst of electric charges with every single event. For the measurement of charges a charge-sensitive preamplifier is necessary. This option is typically used when the impinging rate of primary particles is small ($< 10^7/\text{s}$) and the energy of each single primary particle shall be measured.
- Current source: The continuous stream of charge bursts by events can also rather be interpreted as current source. This can be measured with a transimpedance amplifier or with a precision electrometer. There is no information about single events but the current scales linearly with the event rate and there is no limitation to the maximum measurable rate.
- Voltage source: The charge separation to the surfaces of the diode creates an electric potential difference just as charges separated on a plate capacitor. Since the capacitance and the amount of charges are very small the diode is discharged quickly. For this type of measurement the voltage must be measured with a high input resistance and a high impinging rate of primary particles.

For the electron gun beam tracker the detector is used as current source which is turned into a signal voltage by a transimpedance amplifier. The current produced by the detector consists of its temperature dependent leakage current and the signal current caused

¹⁰Micron Semiconductor Ltd., 1 Royal Buildings, Marlborough Road, Lancing Business Park, Lancing, Sussex, BN15 8SJ, England

by the electron-hole pair production by impinging electrons. The Rearsection electron gun produces electrons with rates ranging from $dN_e/dt = 10^4 - 10^6$ 1/s at energies of approximately 18.6 keV. With this we can calculate the minimum detector current to:

$$I_{\text{signal}} = \left(\frac{dN_e}{dt} \right)_{\text{min}} \frac{E_e}{w} e = 8.2 \text{ pA} \quad (4.11)$$

With the Fano-factor the signal noise current calculates to:

$$\sigma_{I, \text{signal}} = \sqrt{F \frac{dN_e}{dt} \frac{E_e}{w} e} = 0.39 \text{ fA} \quad (4.12)$$

Here reflection of electrons or absorption of electron energy in the dead layer is neglected. This assumption leads to a significant error but the estimated values are still in the correct order of magnitude. To measure currents of few picoampere a transimpedance amplification of at least 10^9 V/A is reasonable. With this amplification the electron beam at minimum rate results in a sudden signal change of a few millivolts at the moment the beam hits one of the detector quadrants - which is a comfortably measurable signal by precision A/D converters or voltmeters. The contribution to the electric noise by Fano-noise is 4 orders of magnitude smaller and can therefore be neglected in the original current and the converted and amplified voltage. But other current sources have to be considered as well, since the exact number of charges transported every second can vary according to Poisson statistics: For these current sources we get $\sigma_{N_e} = \sqrt{N_e}$. The two other main noise sources for current production are:

1. The detector leakage current at room temperature is rated by Micron Semiconductors to a typical value of 1 nA and a maximum value of 30 nA [102]. With the worst case assumption of a leakage current of $I_L = 30$ nA one can derive a noise contribution in an average measurement time of the ADC/voltmeter of one second:

$$\sigma_{I, L} = \sqrt{I_L/e \cdot 1 \text{ s}} \frac{e}{1 \text{ s}} = 69 \text{ fA} \quad (4.13)$$

2. Another noise source is the operational amplifier which is a necessary part of the transimpedance amplifier. Every operational amplifier produces some current between its two polar inputs - the "Input Bias Current". To minimize the noise contribution an operational amplifier with a very small input bias current is used, namely the AD8669 by Analog Devices¹¹. The AD8669 is a low-noise, precision operational amplifier with totally 4 channels, a low offset voltage of maximum $175 \mu\text{V}$ and a low input bias current of $I_{\text{OPA}} = 45$ pA [103]. Assuming Poisson statistics the current noise can be calculated to:

$$\sigma_{I, \text{OPA}} = \sqrt{I_{\text{OPA}}/e \cdot 1 \text{ s}} \frac{e}{1 \text{ s}} = 2.7 \text{ fA} \quad (4.14)$$

The conclusion is that any of the existing noise sources which contributes to the measurement in a time interval of one second is at least 2 orders of magnitude smaller than the signal current itself: The projected signal-to-noise ratio is approximately $S/N \approx 117$. The largest current noise source is produced by the detector leakage current which is an inherent noise source of the detector. All these calculations are only valid for stable, steady-state conditions. If the temperature at the detector is not stable the leakage current will change significantly due to the strong temperature dependence of the leakage current at p/n-junctions:

$$I_L = I_0 e^{-\frac{eV}{kT}}^{-1} [100] \quad (4.15)$$

¹¹Analog Devices, Inc., One Technology Way Norwood, MA 02062-9106

Temperature changes at the detector system may lead to a slow drift in the total output current, respectively total output voltage after the amplifier. In contrast to the noise sources the drift amount can exceed the detector current I_{signal} . Nevertheless, it is possible to distinguish the E-gun beam hitting the detector which induces an immediate signal change to the temperature effects which manifests itself as a slow continuous drift on the scale of minutes or hours.

With the detailed design considerations for the E-gun beam detector above the electronics for the test system can be finalized. The detector Micron LL14 and the pre-amplifier AD8669 are already defined. For the target signal transimpedance amplification of 10^9 V/A each of the 4 detector pixel outputs must be fed into one of the 4 negative operational amplifier inputs. The corresponding other input is always grounded while the outputs need a feedback connection to the corresponding detector pixel with an $1\text{ G}\Omega$ resistor in between. This resistor defines the amplification of 10^9 V/A. The outlet then also provides the amplified signal voltage which must be transported out of the vacuum system via feed-through. For an optimized signal quality the wires used for the signal voltage are coaxial cables in- and outside of the vacuum system with a BNC feed-through in between. Small resistances of $10\ \Omega$ and capacitances of $1\ \mu\text{F}$ and $10\ \text{nF}$ are used for lowpass filters at the asymmetric supply voltages ($\pm 5\text{ V}$) of the operational amplifier. The signal chain uses $47\ \Omega$ resistances and $15\ \text{pF}$ capacitances to avoid too large currents and self over-steering at the operational amplifier. All parts are mounted on a circuit board of aluminum oxide ceramic which was preprinted with silver conductor paths. These material choices reduce the outgassing of the printed circuit board (PCB) to allow the usage in an ultra high vacuum system [49].

The Institute of Data Processing and Electronics (IPE) of KIT helped with consultation in the design process and printed & mounted the ceramic board. The circuit board is a cut aluminum oxide of 99.6% purity with mounting holes and a total size (length x height x thickness) of $50\ \text{mm} \times 50\ \text{mm} \times 0.6\ \text{mm}$. All parts are standard SMD¹² in the size 0805 except for the operational amplifier which has a TSSOP14 package. The detector chip is glued on the ceramics with a conducting epoxy resin (EPO-TEK H20E) which also connects to the detector bias. The quadrant pixels are connected to the transimpedance amplifier inputs via bond wires. This kind of system is not specifically vacuum optimized but it has been shown that small SMD electronics have an acceptable outgassing rate for high vacuum and ultra high vacuum applications [49]. A picture of the printed PCB and the mounted ceramics can be found in figure 4.44. The circuit layout is shown in detail in Appendix A.

Before and after the mounting of the amplifier electronics the working principle has been manually tested at atmospheric pressure and without detector. The circuit layout amplifies $1\ \text{nA}$ reproducible to $1\ \text{V}$ within the uncertainty of Gigaohm-resistor (5%). The test also showed a stability of the output value of better than 1% which is sufficient for the electronics. Succeeding the “cold test” of the electronics the combination of amplifier and a small external circuit board including a LL14 detector for test purposes (reverse biased at $5\ \text{V}$) has been tested outside of vacuum and without any radiation. The windowless detector in combination with the high-gain amplifier acts as very light sensitive system. Nevertheless, the basic offset voltage caused by the detector leakage current and the electronic circuit could be measured during an overnight measurement using a double visual cover for the detector. The graph 4.45 shows the recorded values of the amplifiers output voltage in a time range of totally 750 minutes. At the evening of measurement begin (after sunset) one of the visual covers could be removed without significant change in the signal. Overnight the signal has been overall stable with a small drift of about $40\ \text{mV}$ in

¹²Surface Mounted Devices

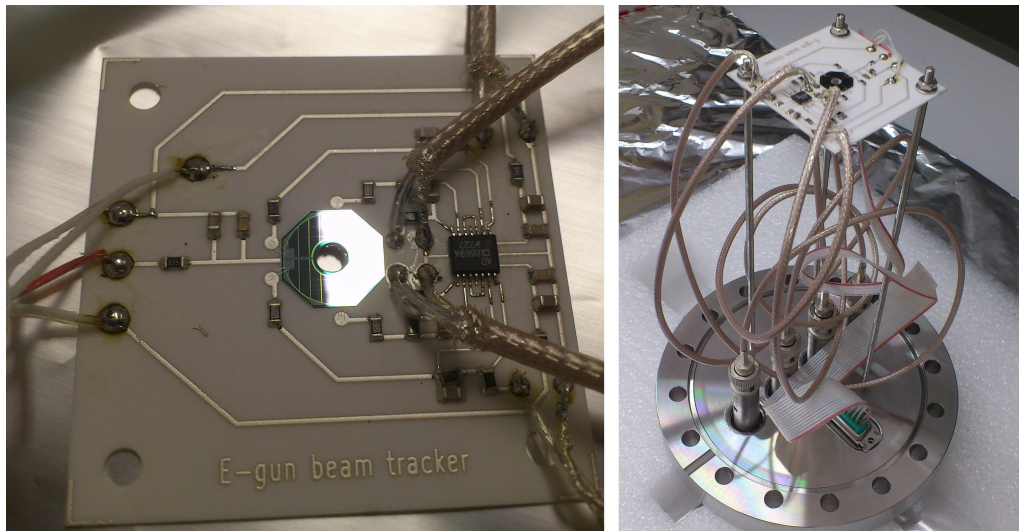


Figure 4.44.: Pictures of the prototype for the electron gun beam tracker - On the left is a close-up picture of the printed, mounted and cabled ceramic PCB. The quadrant electron detector is glued and bonded in the center. On the right the detector is installed on threaded rods to its mounting and feed-through CF100 flange. All cables are generously oversized to have a comparable signal quality to the final installation at the Rearsection.

55500 seconds which equals to an average drift speed of $0.72 \mu\text{V}/\text{s}$. The maximum change between two consecutive measurements (before the steep rise at the end of the graph) is 1.16 mV. The beginning of the steep rise at the end of the graph occurred in the morning of the next day in the time range of 5:45 a.m. and 6:00 a.m. This fits well to the calculated beginning of the astronomical morning twilight at 5:57 a.m. on February 8th, 2013 [104].

The pre-tests at atmospheric pressure without radiation have shown a sufficient precision, sensitivity and reliability of detector and electronics. The most important result is the offset voltage of approximately 100 mV. The detector diode is rated with a maximum leakage current of 30 nA - this would have led to an offset voltage of 30 V which could not be created by the transimpedance amplifier. Since the leakage current is the largest contribution to the offset voltage, it is possible to estimate the real leakage current of the LL14 to approximately 100 pA by using the transimpedance amplification factor. After the pre-test, the detector has been operated together with a photo-electron source. In the following sections the different beam measurements that have been conducted are described.

4.5.2. Implementation with an electron gun

For the implementation together with a photoelectric electron gun the detector system has been build as described in the previous section. The system is mounted on a custom CF100¹³ flange via threaded rods and the mounting holes. The cabling for voltage supply is using KAPTON insulated copper wires which end in a female Sub-D connector. All signal voltages are transported in a TEFLON insulated coaxial cable which is shielded with the reference ground. For the electric feedthroughs the flange provides four BNC feedthroughs with floating shield for the signals and one Sub-D 15 male-male feed-through for all remaining electric connections. The detector system has been installed and connected on the flange without any adjustment to the cable lengths in order to test realistic cable lengths as they are necessary in the Rearsection (compare figure 4.44). On the atmospheric side conventional power supplies with small ripple ($< 50 \text{ mV p-p}$) provide the

¹³CF is the abbreviation for the CONFLAT vacuum standard

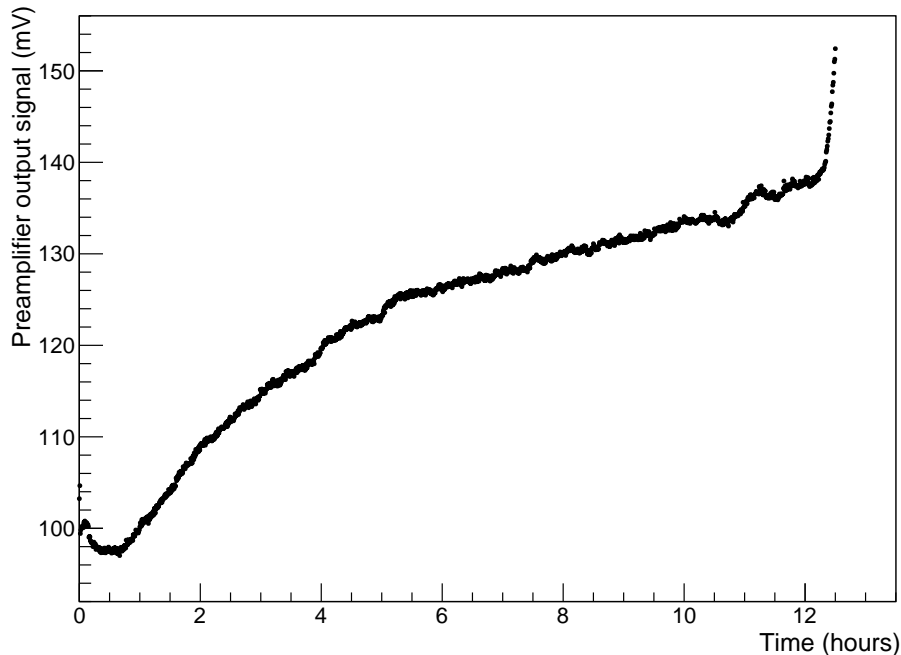


Figure 4.45.: Dark measurement of the detector signal - Measurement of the signal stability by intrinsic voltage and current sources. This measurement could only be realized overnight with a double visual cover. The continuous increase might be caused by slow warming of detector and electronics. The rapid rise at the end is caused by the morning twilight.

supply voltage 0 V, +5 V and -5 V. The signal voltage is measured by a Fluke¹⁴ 8808A multimeter.

The detector system has been installed at an electron gun of the Institute of Nuclear Physics (IKP) which is available for general research purposes connected to the KATRIN experiment [105]. It emits electrons from a gold surface with UV light via the photoelectric effect similar to the working principle of the Rearsection E-gun as described in section 4.1. The UV light source is an unfiltered 30 W deuterium lamp including one focus lens which shines on a gold-coated quartz glass tip in a distance of approximately 15 cm. The gold tip is connected to the negative high voltage which can be set-up from 0 to -30 kV. After emission and acceleration the electrons are guided magnetically to the target measurement device. To minimize the amount of stray light at the detector the E-gun is bended in the middle by approximately 60°. The electron beam is turned accordingly by rotation magnets and additionally focused by focus coils before and after the bend. On the remaining path to the target measurement device the electrons are guided by a long solenoid which is surrounded by two magnetic dipole coil pairs. The magnetic dipole coils can be used to steer the electron beam in left-right or up-down direction. The beam path ends at a CF100 port where the E-gun beam tracker has been attached as electron measurement device. Once the vacuum system is closed the volume has been evacuated by a Pfeiffer¹⁵ HiCube 80 Eco down to a pressure of $\leq 10^{-5}$ mbar which is sufficient to produce and transport the E-gun beam.

4.5.3. Detection measurements

The detection measurements started with a test series looking for possible influences on the voltage signal offset to find potential systematic errors. When only the detector electronics is powered and the PIN-diode is biased the output voltage of two channels is

¹⁴Fluke Deutschland GmbH, In den Engematten 14, 79286 Glottertal

¹⁵Pfeiffer Vacuum GmbH, Berliner Strasse 43, 35614 Asslar

approximately 100 mV, the third channel is about 300 mV and the fourth equals to the operational amplifier full scale of 5 V. The first two channels show the default behavior as found in the pre-tests before the detector has been glued and bonded on the circuit board. The third channel might have an increased offset voltage due to an increased leakage current in this quadrant of the diode or creeping currents in the circuit - nevertheless except for the increased offset voltage this quadrant has proven to be fully functional later on. The last quadrant pixel is not functional since it is not possible to measure any offset voltage if the signal is permanently in the amplifier overflow. This might be either caused by a significantly higher leakage current in this detector quadrant or by some failure like an electric short in the circuit for this pixel.

The E-gun beam tracker is quite robust concerning environmental conditions compared with other non-encapsulated silicon-based detector systems. The signal is not affected by other electric devices even if they produce noise on the power line or have electromagnetic impact like the air-conditioning, the magnets or the magnet power supplies. The E-gun construction efficiently shields from light: Neither the UV-light nor the room light has a measurable effect on the detector signal. There is no indication that the ripple of the electronics power supply ($50 \text{ mV}_{\text{P-P}}$) has a significant impact on the signal: The output voltage is longterm stable with $\sigma_V < 1 \text{ mV}$. Nevertheless, this stability can not be reached in use with the E-gun beam due to the warm up of the magnetic solenoids: The main solenoids can only be water-cooled by a cooling pipe laying on the topmost outer layer of the coil windings. Additionally, the heat transport is not very efficient in transporting the thermal energy from the inner coil layers to the outside. This important design flaw at the electron gun leads to a significant warm up of the E-gun vacuum pipe and also to all connected components by conductance and all instruments inside the pipe by radiation. There is no access to measure the real temperature of the beam pipe and the E-gun beam detector prototype has no temperature sensor included. For those reasons the measurement intervals of the beam tracker have always been limited to a few hours to avoid damage to the detector or the electron gun. During this time the offset voltage steadily increases since the PIN-diode leakage current rises exponentially with temperature (compare formula 4.15). This effect will not occur at the final Rearsection if the following requirements are fulfilled:

- The magnets are cooled more efficient.
- The equilibrium temperature is reached on a shorter time scale.
- The equilibrium temperature does not significantly exceed the specified design value of 3°C temperature variation from the most inner to the most outer copper layer. The temperature of the outer copper layer is defined by the pipe which supplies the cooling water with of a typical temperature of $18\text{-}22^\circ\text{C}$.

With the given experimental conditions of a magnetic solenoid introducing a long term drift of the detector system's signal voltage the measurement of electrons have to occur on short time scales. The quadrant channel has been selected manually by connecting the voltmeter to the corresponding BNC connector. To distinguish electron effects from slow drifts in the signal voltage the electron beam has been directed alternatingly on and completely off the detector. The regular disable of the beam has been ensured either by switching off the high voltage or the rotation magnets. Except for the beam switching the electron gun usage has been used in normal mode with normal parameters:

- UV-light switched on and the lamp got a warm up time of at least half an hour.
- The electron gun has been evacuated to a pressure $\leq 1.5 \cdot 10^{-5}$ mbar.
- The high voltage for electron acceleration was set in a range from 3 kV to 18 kV. A

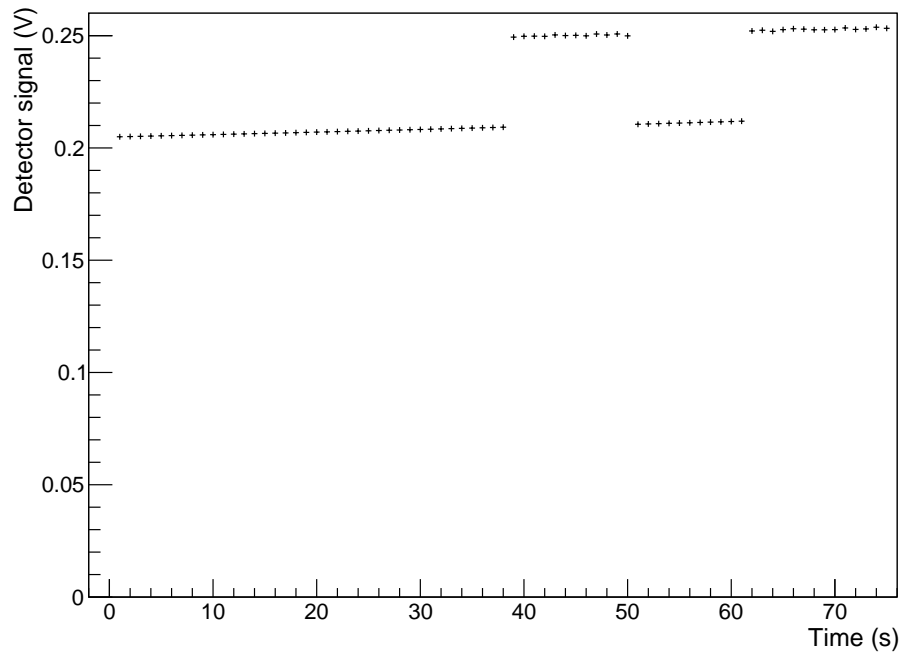


Figure 4.46.: Signal events with the beam tracker detector - the recorded output voltage in this graph shows how slow drifts can be distinguished from electron events. The slow drift is caused by the increasing detector temperature which leads to increasing diode leakage current. Electron events cause an immediate jump of the signal by several millivolts and the signal also returns to the previous value when the electron gun is deactivated. In further the difference of the raw signal leap is considered as “detector signal”.

higher voltage is not recommended at the given pressure due to potential damage at the E-gun gold tip by ion sputtering.

- All magnets switched on. The solenoid has been driven at 3 A, the currents for the rotational coils were calculated by the LabVIEW controlled software, the focus magnet current was manually optimized depending on the acceleration voltage and the detector quadrant.

The first measurements aim for the overall detection of the electron beam on the three different working detector quadrants. An example of beam detection is presented in figure 4.46. In contrast to the slow voltage drift there is a comparable sudden leap and a consecutive offset in the signal voltage when the beam hits the detector and also a regression to the signal background when the electron beam targets offside of the detector again. The detector recognizes electrons in the energy range from 7 keV to 18 keV with the smallest definite signal response of 3 meV at 7 keV. Using the formulas in section 4.5.1 the signal corresponds to 3 pA which can be estimated to a rate of approximately 10000/s of 7 keV electrons which fully deposit their energy in the detector. This detection limit exactly matches the expected detector capabilities: The detection of 7 keV electrons with a rate of 10000 electrons per second which fully deposit their energy in the detector ensures a detection limit for the Rearsection with 18 keV electrons at a real impinging rate of 10000/s. The reduced rate of deposited primary electrons due to reflection or absorption in the silicon dead layer is compensated by the 2.5 times higher kinetic energy of primary electrons. This leads to a reduced energy loss on the path through the dead layer and a 2.5 times higher amount of electron-hole pairs excitations. All four detector quadrants have been measured individually through the energy range from 3 keV to 18 keV.

After this first qualitative test the system is further evaluated and optimized by changing available E-gun parameters. The correct estimation of the measurement errors is difficult -

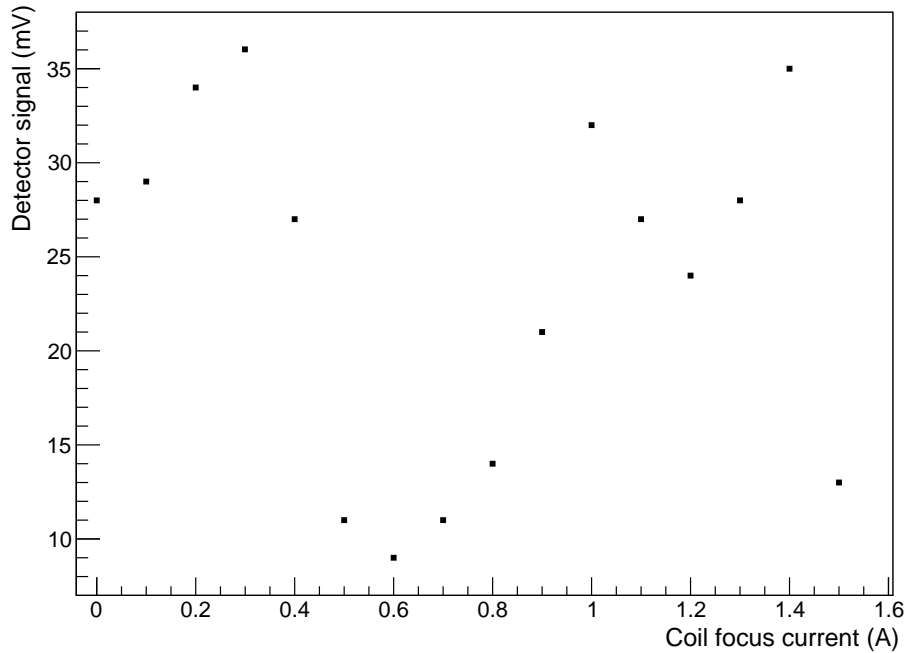


Figure 4.47.: Beam tracker signal dependence on the focus coil current - The detector signal clearly changes when the focus current is modified. The reason is the influence of the magnetic field on the phase of the cyclotron motion. As a consequence, the signal should change in a sine like periodic function. This effect is hardly visible because the electron beam is diffuse and also becomes slightly shifted with the focus coil current.

the system has been designed rather as a logical than a quantitative beam detector. Most of the following measurements successfully overrun the initially planned precision. At least an error of $\sigma_V = 1.5 \text{ mV}$ has to be assumed for the detector signal because of the output variation while the signal was read out. All these measurements have been performed without any changes in the coil currents of the focus coil or the dipole coils. The results of the measurement using beam positioning are presented in the following section.

4.5.4. Calibration measurements

At first the effect of the focus coil has been tested while the acceleration voltage has been kept stable at 12 kV. The results are displayed in table 4.5. The measured signal at the detector clearly depends on the focus current but not in a trivial way. The focus coils are obviously not just focusing the beam to allow the beam to pass through an aperture - in this case the dependence of the focus current would be a step like function increasing the signal at a certain focus current at the moment when the electron beam is sufficiently focused through the aperture and other obstacles. But the focus coils do not only focus the beam they also modify the axially symmetric, magnetic field which changes the cyclotron motion of the electron. Finally, they reach the detector with a different phase of the cyclotron motion and consequently with a completely different position on the detector surface. This can explain artifacts similar to resonances when plotting the detector response over the focus coil current like in graph 4.47. The resonances are very broad and unpredictable due to the unknown size of the electron beam and the imperfect alignment and centering of the complete system of electron source, guiding and steering magnets and detector. These results are helpful for further measurements implementing beam alignment which use not only the focus coils but also the magnetic dipoles.

In the further measurements, the maximum achievable signals at one channel have been investigated. The maximum intensity has been determined by varying the 3 parameter

Table 4.5.: Effect of the focus coil current - Detection voltage steps of all 3 working quadrant detectors at different focus coil currents. The task of the focus coils is mainly to compress the electron beam at the 2 apertures of the E-gun. Additionally, it modifies the phase of the electron cyclotron motion. The combined effect has a large impact on the measured signal and can lead to one or multiple maximum(s) on the coil current scan.

I_{Focus} (A)	ΔV_1 (mV)	ΔV_2 (mV)	ΔV_3 (mV)
0	0	1	28
0.1	2	1	29
0.2	1	2	34
0.3	0	2	36
0.4	1	2	27
0.5	4	4	11
0.6	4	5	9
0.7	8	7	11
0.8	12	9	14
0.9	16	6	21
1	17	1	32
1.1	15	20	27
1.2	19	25	24
1.3	22	35	28
1.4	1	87	35
1.5	13	135	13

space of coil currents in the focus coil, the dipole coil for horizontal deflection and the dipole coil for vertical deflection. The electron gun acceleration voltage has been varied between 7 kV and 18 kV. The most important coil current to modify is the focus coil current which changes the phase of the cyclotron motion at the detector. Close to the maximum achievable rates via variation of the focus coil current the dipole coils have been used to steer the beam to an optimal position. The results are listed in table 4.6. The smallest signal voltage change is 53 mV at electron energies of 7 keV and the highest measured signal voltage change is 329 mV at 16 keV. In the graph 4.48 the measured signal in dependence of the electron energy is diagrammed. Investigating the energy dependence is an additional assurance that the signal is not caused by stray light. In the theory of semiconductor detectors (compare section 4.5.1) the amount of secondary charges is proportional to the primary ionizing particle. But the detector dead layer introduces non-linearity and threshold effects at low energetic electrons. The given graph shows a threshold like effect: No electrons are detected for acceleration voltages below 7 keV. This changes the dependence of output signal to primary electron energy from proportional to a linear relation with offset. Fitting a linear function to the data results in:

$$U_{\text{Det}} = (0.026 \pm 0.003) \text{ mV/eV} \cdot E_e - (130 \pm 40) \text{ mV} \quad (4.16)$$

The four measurement points of the highest electron energies show a relatively too high signal which distorts the spectrum. The effect is too large to be explained only by the suppression of the smaller energies by dead layer effects. The measurement is reproducible, but though they could be caused by a lack of ultimate control of the E-gun beam position and beam spot size. Due to this limitation it is also necessary to adjust the focus coil current after every change in the electron energy. Nevertheless, the measurement still shows an energy dependence very close to the theoretical expected and exceeds the requirements on the electron gun beam detector: The device shall detect an off-steering of the beam rather

Table 4.6.: Maximum measured signal at different electron energies - The table includes the parameters set-voltage & the calibrated voltage measured with a voltage divider, the currents of the steering dipole coils, the focus coil and the rotation coil currents. For each of the given, optimized configuration the measured output voltages with inactive and active E-gun and the difference are given.

U (V)	U _{calib.} (V)	I _{Up/down} (A)	I _{ILeft/right} (A)	I _{Focus} (A)	I _{Rot} (A)	V _{3off} (mV)	V _{3on} (mV)	ΔV_3 (mV)
7000	6956	0.8	0.05	1	1.5	267	320	53
8000	7950	0.11	-0.05	1.1	1.6	243	353	110
9000	8943	0.11	0	1.3	1.7	256	369	113
10000	9937	0.06	-0.03	1.1	1.8	116	240	124
11000	10931	0.08	-0.06	1.3	1.9	124	279	155
12000	11925	0.15	-0.08	1.5	1.9	137	289	152
13000	12918	0.12	-0.08	1.6	2	145	307	162
14000	13912	0.15	0.08	1.7	2.09	160	353	193
15000	14906	0.15	0	1.4	2.09	173	488	315
16000	15900	0.1	-0.05	1.6	2.2	183	512	329
17000	16893	0.1	-0.05	1.7	2.3	197	520	323
18000	17887	0.17	0.04	1.8	2.3	208	534	326

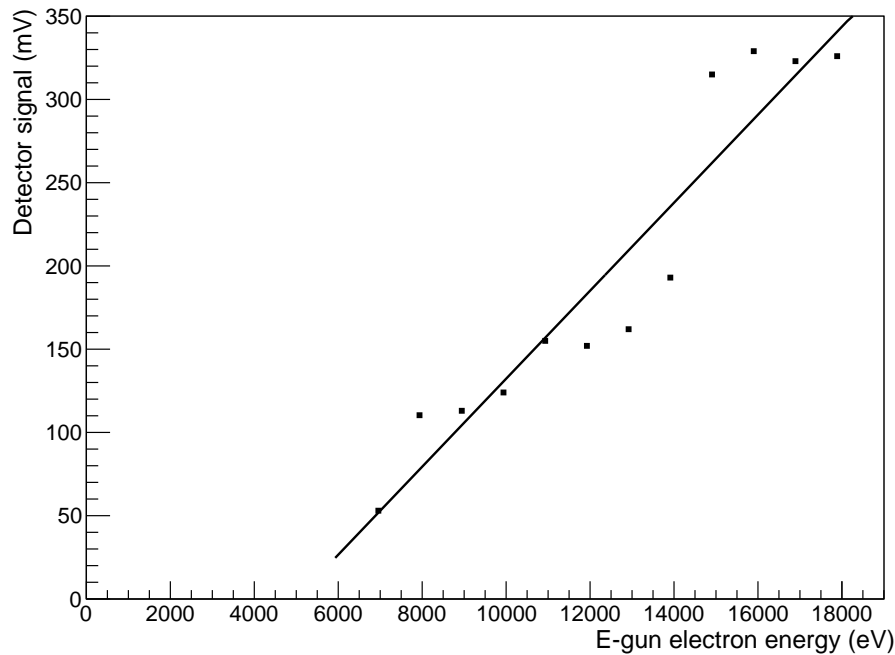


Figure 4.48.: Beam tracker signal dependence on the electron energy - As expected from theory the silicon detector/preamp output scales with the energy of the primary electrons. Although the detector is not designed for quantitative analysis a rough linear dependence can be recognized in the graph. No electrons could be detected below 7 keV due to the limited detector precision and silicon deadlayer effects.

than its energy. This effect is finally investigated with the dipole coils and described in the next paragraph.

The main purpose of the electron gun beam detector is the recognition of the 18.6 keV electron gun beam when the beam is too off-centered to pass through the aperture holes. In order to test the position recognition a beam sweep over the single quadrant surfaces has been performed using the magnetic dipole coils for steering while the focus coil current is

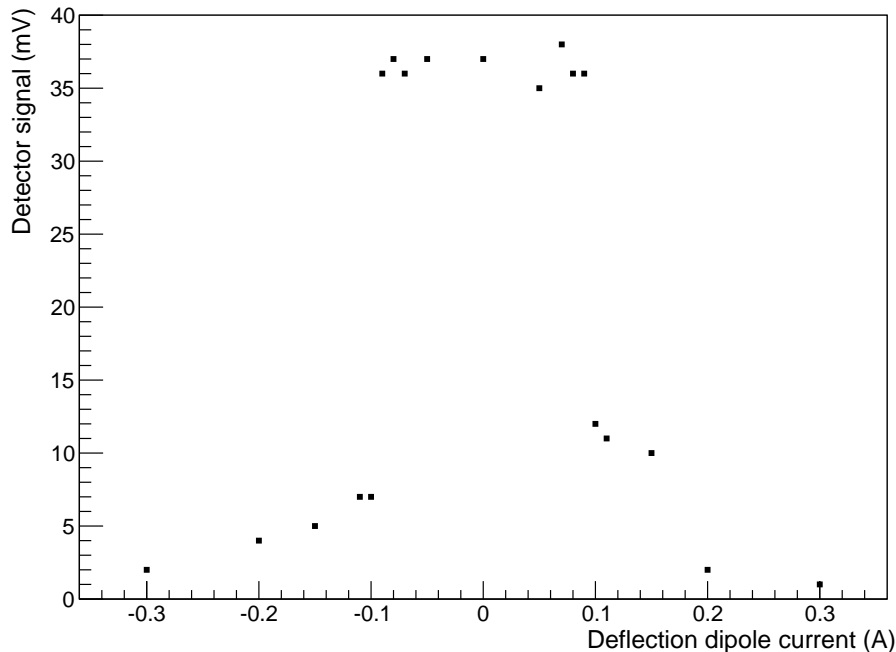


Figure 4.49.: Electron beam sweep over a detector quadrant - The electron beam is steered with left-right magnetic dipoles over the top quadrant. The signal shows a broad plateau in the center when the complete beam hits the quadrant. When the beam is deflected too far, the signal drops rapidly with some remaining event rate due to the beam’s diffuseness.

fixed. Plot 4.49 shows a scan over the top detector quadrant (3) with horizontal deflection by the left-right dipole coil. The y-axis symmetry proves that the beam and the detector have been well aligned at a focus coil current of 1.9 A. If the dipole coil current is in the range $-0.1 < I_{\text{Dipole-coil}} < 0.1$ the output signal is significantly higher ($\gtrsim 35$ mV) than in the other region (maximum signal 12 mV). Outside of the central region the signal voltage does not immediately drop to zero but it is slowly reduced up to the maximum tested dipole currents of ± 0.3 A. This proves that the detector quadrant and the beam spot have a measurable spread. The LL14 quadrant extends in horizontal direction in the range from 3 mm to 7 mm depending on the precise vertical position. The beam spot diameter is expected to be ≈ 1 mm from previous measurements [49]. But the beam spot is not completely described by a sharp defined circle which explains the slow reduction of the signal voltage once the beam center left the quadrant area. If either the beam spot of the electron gun is sharply defined or the beam profile is well known it is possible to detect when the beam hits one of the quadrants instead of passing through the central hole. The final confirmation of the beam detector principle is done by tracking the beam steered from one quadrant to the opposite one. The results of the measurement are displayed in graph 4.50. It shows the shifted areas of maximum plateaus but no region where the signal voltage drops to zero for both channels which means the electron beam spot is too diffuse to fit through the detectors central hole. Furthermore the focus coil current had to be adjusted to hit both quadrants properly. These limitations do not apply later on: The Rearsection electron gun has and requires a more precise dipole coil steering and a sharper defined, smaller beam spot size.

As a result of the intensive testing of the electron gun beam tracker, it is possible to state that the system is overall working and acting as expected. The signal detection is reliable and reproducible and can be easily automated by signal differentiation with threshold detection in the differentiated spectrum. The transimpedance amplifier acted robust against outside influences like noise on the supply voltages or typical sources of

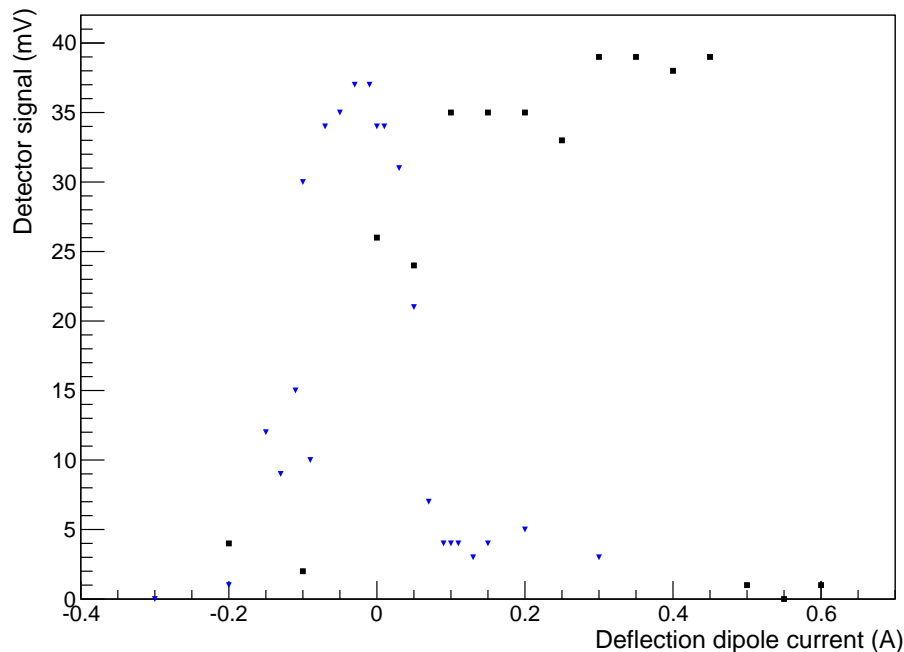


Figure 4.50.: Beam crossover with two opposed quadrants - Up-down sweep of the electron beam in order to show a crossover of the two working opposed quadrants top (blue triangles) and bottom (black quadrants). The crossover can be recognized at a dipole coil current of about 0 A. Still the beam is too diffuse to see a gap between the two quadrants where the electrons precisely pass through the central hole.

electromagnetic incompatibilities. The energy dependence of the signal has been proven and the reaction to a sweep of the electron beam over the quadrant surface by the magnetic dipoles has been checked. But also some limitations of the system appeared: The main intrinsic problem is the wide spread of the signal offsets at the four different channels. The reason for the failure of one of the channels could not be determined definitely. Hence, the detectors for the final system will be ordered with stronger requirements on the detector leakage currents (< 0.1 nA) to reduce the spread in the signal voltage offsets. Except for the failure of one channel and the wide distribution of offset voltages most difficulties during the test measurements have been caused by the electron gun. The limitation due to the not circular-focused beam spot will not occur at the Rearsection because a better shaped beam spot and beam steering is required by design specification. Also the temperature conditions are expected to be more stable at the Rearsection because of a better cooling system and a comparable long-term operation. Nevertheless, after the experiences with the test measurements, adding a temperature sensor to the updated possibly 2-sided board layout of the electron gun beam tracker is recommended. In conclusion the usage of electron gun beam trackers at the final Rearsection is reasonable and will be helpful for beam steering especially in the early commissioning of the freshly assembled system.

5. Rear Wall and WGTS activity monitoring

Besides the electron gun, the Rear Wall (RW) and its monitoring capabilities is the other important system component for calibration and measurement within the Rearsection. The Rear Wall can be abstracted as a disc installed on the WGTS-facing side of the Rearsection. It exposes a gold surface towards the stream of charged particles and neutral gas coming from the WGTS. This surface absorbs or neutralizes all incoming electrons and ions and hence acts as the electric termination of the source plasma. In the center the disc has a small hole to enable the electrons from the electron gun to pass into the WGTS and the other KATRIN beam line elements.

The Rear Wall properties and its electrostatic potential may influence the electric potential of the entire tritium source. This would have an important impact on the systematic errors of the neutrino mass measurement. The details and quantitative calculations concerning this impact are described in section 5.1.1. The precondition for the correct functionality of the Rear Wall is that the magnetic flux tube of the WGTS is fully transported to the Rear Wall. In section 5.1.2 the flux tube calculations and the consequences for the Rear Wall are discussed. The final concept of the Rear Wall implementation within the Rearsection closes the section about the Rear Wall design. This implementation considers the experimental and simulated results of the flux tube, the piezoelectric motor and the electron gun beam tracker. It also includes the technical designs of mounting, installation and supply instruments.

Due to the Rear Wall's impact on the KATRIN systematics several qualification tests are required to find an acceptable prototype. The qualification tests have been carried out by KIT, UCSB and University of Mainz. Each available sample has been tested unless its usability could be excluded by a previous test. The Rear Wall samples are disc-shaped prototypes with the same production mechanism but reduced diameter compared to the final Rear Wall. Typical sample sizes have diameter of 2 or 3 inch diameter. The qualification tests, realized in the scope of this thesis with a Kelvin Probe and the KATRIN monitor spectrometer, are described in sections 5.2 and 5.3 respectively. Finally, the Rear Wall acts as passive source for X-ray radiation which is used to monitor the source stability. The X-rays can be produced by the de-excitation processes of the tritium β -decay electrons. Section 5.5 shows how Beta-Induced X-ray Spectroscopy (BIXS) can be used to monitor the WGTS activity and how this system is implemented at the Rearsection.

5.1. Design of the Rear Wall

In the final Rearsection assembly the “Rear Wall” designates to a more complex component than just a gold-coated disk. In the following sections the complex requirements affecting the design and position of the Rear Wall will be discussed. The associated moving mechanism to shut the Rear Wall aperture is treated in section 4.4. Similarly, the BIXS system for activity monitoring is handled in the separate section 5.5, because this important monitoring tool uses the Rear Wall passively and does not imply any requirements on the component Rear Wall.

The most important role of the Rear Wall is its interaction with the charged particles coming from the gaseous tritium source. As a result of β -decays and ionization processes many low energy electrons and ions are produced, so the source may be treated as a mixture of plasma and neutral gas. Due to the strong axially symmetric magnetic field the mobility of the plasma particles is confined to the remaining z-axis leading from and to the Rear Wall. As a consequence, the influence of the electrostatic potential of the Rear Wall on the plasma potential will be evaluated in the following. It is equally important to ensure that all particles of the WGTS flux tube do arrive at the Rear Wall. For the electrons impinging on the Rear Wall, a maximized ratio of absorption to reflection is desirable. This is because reflected electrons may pass through the entire KATRIN beamline with a shifted energy and thus might end up as background to signal electrons. Finally, the technical implementation of the Rear Wall as component is presented. This implementation refers to all requirements and previous findings and includes the concepts for assembly and maintenance. Furthermore, instrumentation related to the electron gun such as the piezoelectric motor (compare section 4.4) and the E-gun beam tracker (compare section 4.5) is included as well.

5.1.1. Work function and the source potential

All charged particles moving in backwards direction in the WGTS are most likely absorbed or neutralized by the Rear Wall. This can also happen to electrons which start from the source into the direction of the detector but are reflected somewhere within the beamline. On the other hand the ions traveling into forward direction are removed from the magnetic flux tube by the electric dipoles at the DPS2 [106]. Still, the Rear Wall remains the most important surface for charge neutralization and free electron capture of the entire beamline. By the fact that the Rear Wall is on a fixed potential and that charged particles are magnetically guided along the z-axis the Rear Wall is considered as the back-sided electric termination of the source. This means any potential that exists in the source plasma is terminated at the metallic Rear Wall and can not reach further into the Rearsection. As the potential of the Rear Wall is fixed, by a direct connection to a power supply the Rear Wall can not charge up. In particular its electric potential cannot be modified by the plasma. Vice-versa it is important to discuss the effect of the Rear Wall on the plasma potential and possible interactions of the plasma and the Rear Wall close to the surface.

When discussing the relevance of different effects the magnetically confined plasma is neglected at first. In this case, charged particles inside an evacuated metallic encasement have their potential energy modified by the vacuum potential. If the encasement consists of one perfect metal the Fermi-level and the vacuum energy level are homogeneous within the whole metallic encasement. An exception to this will occur very close to the metallic surface where a continuous function conveys the vacuum level to the Fermi level inside the metal. This intermediate function can be explained by the image charge of the charged particle close to the surfaces. The potential difference of Fermi level and vacuum energy level is called the material dependent work function. The distance to the surface where the transition of the vacuum potential to the Fermi level occurs is typically of the order

of 10 nm but its size can depend on the geometry and other boundary conditions [107]. In case of a perfectly homogeneous metallic encasement, there is no effect if the potential of the metallic surface is shifted against the experimental ground potential. Due to the homogeneity there is no potential difference and no field existent in the encasement which can affect the enclosed charged particles. This changes when a charged particle is enclosed by metallic surfaces that have a voltage difference applied. In this case a non-zero slope exists in the vacuum energy level and a shift in the Fermi energy level. Charged particles within these surfaces, which act like cathode and anode, will be accelerated according to the Lorentz force. This case is similar to the electrostatic filter measurement that happens at the spectrometers: Electrons will pass the filter only in the case the projected kinetic energy exceeds the difference of the maximum vacuum potential in the spectrometer and the vacuum potential at the starting point in the source (start time and position is defined by the corresponding tritium β -decay). By this it is possible to conclude that the temporal and spatial stability of the vacuum potential in the source is as important as the stability of the main spectrometer potential. At the main spectrometer a stability of better than 60 meV is required [3]. Given the importance of the source potential it is necessary to evaluate the interaction of source and Rear Wall at KATRIN in more detail.

Compared to the previous case of charged particles within a metallic encasement two important details of the physical situation are changed in the KATRIN source: All charged particles are confined by the magnetic field with strengths in the range 0.2 T to 3.6 T [3]. As a result the mobility of electrons and ions along the z-axis towards the Rear Wall is nearly unaffected compared to free particles while the mobility transversal to the magnetic field lines is suppressed by many orders of magnitudes. Additionally, the content of the WGTS can not be handled using a vacuum potential anymore. The high luminosity of 10^{11} 1/s beta-decays and the consecutive secondary ionization results in the formation of a cold plasma. Inside the WGTS a mixed state of neutral gas following the laws of flow dynamics and a quasi-neutral plasma confined by the magnetic field will co-exist. The plasma part of the mixture reacts on the electrostatic potential, e.g. by shielding or conducting of external voltages. Because of this the electrostatic potential of the gas mixture must be handled as a plasma potential instead of a vacuum potential. The plasma frequency is given by the electron/ion density of approximately $n_e \approx 10^{14}$ /m³[108] to

$$\omega_p = \sqrt{\frac{n_e e^2}{\epsilon_0 m_e}} = 564 \text{ MHz} \quad [109] \quad (5.1)$$

Compared to a neutral gas a plasma is characterized by an inherent non-zero conductivity as a result of the charged particle's mobility. In the special case of the WGTS, small potentials can have a significant impact on the cold plasma due to the small kinetic energy of secondary electrons and ions. Furthermore, the strong axisymmetric magnetic fields suppress the conductivity transversal to the magnetic field lines. In longitudinal direction the plasma conductivity is dominated by low energy electrons because the electron longitudinal conductivity is $\sigma_{e,\parallel}/\sigma_{ion,\parallel} \approx 10^3$ higher than the ion longitudinal conductivity [51]. Concerning the transversal conductivity, electrons can be neglected because they are forced on cyclotron motions. On the contrary, ions have an effective transversal conductivity by their scattering processes. Nevertheless, the value is small compared to the electron longitudinal conductivity $\sigma_{ion,\perp}/\sigma_{e,\parallel} \approx 10^{-7}$ [51].

Considering the different mobilities, the impact on the plasma potential should be greater by the Rear Wall compared to the WGTS walls. If a certain voltage is applied to the Rear Wall, one expects that the mobile negative charges are shifted relative to the positive charges with the result that the applied potential is reflected in the whole plasma. On the contrary, if a certain potential is applied to the WGTS wall, the value will not be

transported into the plasma due to the suppressed mobility and conductivity transversal to the magnetic field lines. In a simplifying picture the plasma can be treated like one or multiple wires along the magnetic field lines which are transporting the Rear Wall potential through the complete plasma. This evaluation must be supplemented by the non-zero transversal conductivity of the ions: Although it is 7 orders of magnitudes smaller than the longitudinal electron conductivity, the ions gain importance in view of the WGTS geometry with a very long tube of 16 m compared to the tube diameter of 90 mm.

The expected potential has been calculated to check the previously described effects with the finite element software FEMM [68]. This simulation only uses the metallic surfaces set on certain potentials as boundary conditions and the conductivity in the volume according to the plasma properties. The geometry of the vacuum system in front of the Rear Wall has been simplified to a pipe of 90 mm diameter. To avoid problems with numerical precision the WGTS length of 16 m has been reduced by one order of magnitude while the factor of transversal ion conductivity to longitudinal electron conductivity is increased by 2 orders of magnitude according to the scaling law found by [108]. The voltages of the side walls and the Rear Wall are offset by 1 V to show the difference in influence. The results are displayed in figure 5.1 and show that the volume is clearly dominated by the Rear Wall potential. Only close to the walls an influence exists which increases with the distance to the Rear Wall. Still, the impact of the beamtube walls can not be neglected if their potential differs from the one of the Rear Wall. It can however be partially compensated by the detector segmentation. Furthermore, the effect can be avoided if the surface potential of Rear Wall and WGTS walls is matched which requires the compensation of the work function difference between the different metals.

In case that the surface potential of the Rear Wall varies across the surface these different potentials can also be transported along the plasma. The plasma tubes that have different electric potentials and exist along the magnetic field lines shield amongst themselves by double layer structures [110]. The plasma tubes need a minimum diameter, approximately given by the Debye length ([109]):

$$\lambda_D = \sqrt{\frac{\epsilon_0 k_B T_e}{n_e e^2}} = 3.78 \cdot 10^{-4} \text{ m} \quad (5.2)$$

This calculation assumes a full thermalization of the plasma electrons to the source temperature of 30 K and a reduced charge density of $10^{11} / \text{m}^3$ close to the Rear Wall (according to [108]). As a result, only potential variations on the surface larger than 0.3 mm diameter can propagate along the plasma. This excludes microscopic work function variations as they have been measured with an atomic force microscope [111]. Smaller surface potential variations will be averaged out across the surface because they can not enter the plasma [108].

Because of the possible Rear Wall impact on the source plasma potential, the Rear Wall surface potential has to fulfill a strict requirement: The work function distribution on scales larger than the Debye limit and smaller than a projected detector pixel (0.86 cm^2) must have a variance of $\sigma_{\text{WF}} < 20 \text{ meV}$ to comply with the Rear Wall specification. To ensure that this requirement is fulfilled, the measurement of the Rear Wall work function is part of the qualification strategy. Each prototype sample and all final candidates have to pass work function measurements including investigations of their spacial and temporal dependence. Some of these measurements have been realized with a Kelvin probe (described in section 5.2) and with the photoelectric effect (described in section 5.3). However, a work function difference of several 100 mV will remain between the gold coating on the Rear Wall and the stainless steel of the WGTS tube. Therefore, a possibility to shift the Rear Wall potential

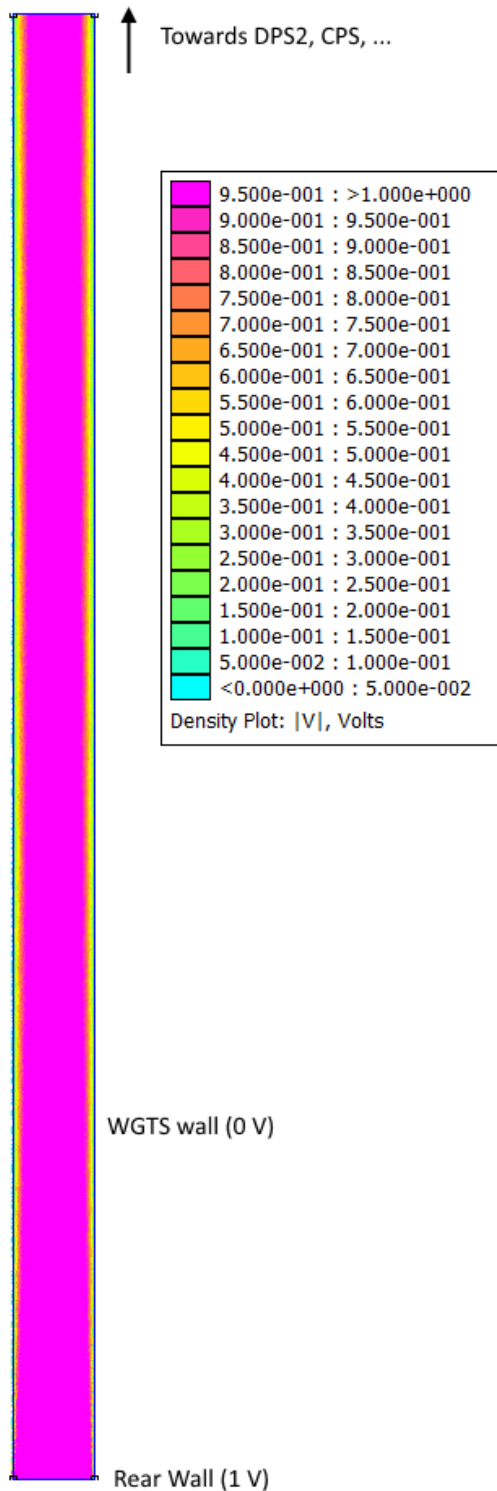


Figure 5.1: Influence of the Rear Wall potential on the WGTS - a finite element simulation shall visualize the importance of the Rear Wall for the WGTS potential. The WGTS is shortened by a factor of 10 to a length of 1.6 m and the conductances are therefore scaled to $\sigma_T/\sigma_L = 10^{-5}$. No plasma or particle streams are included in the simulation. The simplified calculation shows a clear dominance of the Rear Wall potential (1 V) compared to the WGTS walls (0 V) within the tube. The wall potential gains importance with increasing distance to the RW. To avoid similar effects the surface potentials of RW and walls should be balanced during actual experimental runs.

relatively to the WGTS is required. An adjustable voltage at the Rear Wall of at least ± 10 V has thus been added to the requirements. This range is sufficient to match the Rear Wall surface potential to the surface potential of the WGTS walls. The surface potential matching must be tested and repeated during the KATRIN measurements because the effective work function is not a static material property but it can change due to surface modifications, temperature, as well as degradation effects and adsorption of gas molecules on the surface [112]. In particular, adsorption effects of tritium gas molecules have been investigated in more detail as described in section 5.4.1.

The FEMM simulations do not fully reflect the physics in the source plasma. They only represent electrostatic calculations making use of the conductivities that are expected in the plasma. They neglect gas flow and densities, charge generation and annihilation and the overall plasma nature as a collection of single charges. A more comprehensive simulation including charge generation by β -decays and ionization and charge annihilation by recombination in the gas and at the walls will be implemented with the software COMSOL multi-physics¹. First calculations reveal that the implementation of all processes in the source section is quite challenging. The results will be described in [113].

Independent from improved simulations, experimental data can deliver precise information about the dependence of the Rear Wall surface potential and the plasma potential: When a variable voltage is applied solely to the Rear Wall, it is possible to scan through the voltage range and check the event rates on the detector pixels. If the plasma potential is shifted, this is equivalent to a measurement of the tritium beta-spectrum at a different filter potential U_{Filter} . The experiment is very sensitive to such shifts because the integrated rate at the detector scales with the electron surplus energy like $(E_e - e \cdot U_{\text{MAC-E-Filter}})^3$ [3]. There are multiple scenarios on how a variation of the Rear Wall voltage can affect the event rates at the main detector. The rate could increase/decrease at all detector pixels simultaneously, which implies that the plasma potential is fully governed by the Rear Wall. The opposite case is when the detector rate remains unchanged on all pixels and the plasma potential is solely determined by the WGTS walls. Finally, there are the mixed states where the Rear Wall potential influences the rate at the inner rings of the detector and the WGTS walls influence the outer rings of the detector. When the Rear Wall voltage is set to compensate the surface potential difference to the WGTS walls, this effect can be reduced or removed. This dedicated measurement is required with the spectrometer filter voltage set at least 50 V below the endpoint of the β -decay to increase the detector rate and statistics. To quantify the radial influence and the potential difference the measurement has to be unfolded from other radial effects. Also, the precise slope of the response function at the measurement voltage must be compared to the Rear Wall scan voltage. This measurement can be decoupled from other systematic drifts of the potentials by a time-dependent variation of the Rear Wall voltage and a correlated detector measurement. This measurement should be carried out at the beginning of the KATRIN experiment and repeated regularly according to a specific calibration procedure to avoid unaccounted systematic errors by the source plasma potential.

5.1.2. Flux tube transport to the Rear Wall

Most of the Rear Wall functionality such as the electric termination of the plasma, the stabilization of the plasma potential and the Beta-Induced X-ray Spectroscopy require that the full magnetic flux tube hits the Rear Wall. As already defined in section 4.2.2 it is possible to define 3 magnetic flux tubes: The outer flux tube 229 Tcm^2 , the inner flux tube 191 Tcm^2 and the technical flux tube 210 Tcm^2 . The flux tubes of interest are contained by the superconducting magnets of the WGTS and the Cryomagnetism condenser magnet (RSCM). To design the guidance of the flux tube, magnetic simulations are used to optimize the positions and field settings for the superconducting magnets. The results of the electromagnetic design (EMD) is then included in the mechanical design and the coil specifications. The configuration of the WGTS coils has never been modified during the Rearsection EMD, because these parameters were fixed beforehand [114]. Prior to integration of the RSCM to the Rearsection layout, the size of the flux tube increased in an extreme manner towards the end of the DPS1-R. As a result, the flux tube then touched the walls of the WGTS rear side exit cone. Therefore, the Rear Wall had to be placed within the exit cone of the DPS1-R to ensure the full flux tube hits the Rear Wall. In this

¹Comsol Multiphysics GmbH, Robert-Gernhardt-Platz 1, 37073 Göttingen

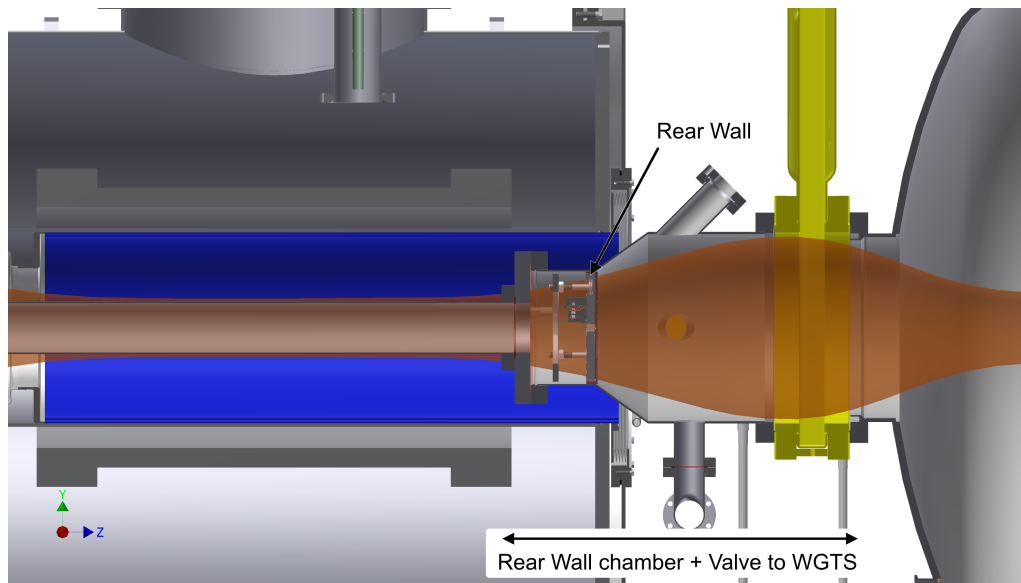


Figure 5.2.: CAD drawing of the Rear Wall domain including the magnetic flux tube - Side cut view of the connection to the DPS1-R/WGTS with the magnetic guidance by the superconducting magnet at 4.7 T. The simulated flux tube (orange) contains the outer flux tube of 229 Tcm^2 which can be fully transported through the Rear Wall chamber. The flux tube continues further to the left but the guided particles will be stopped at the Rear Wall.

earlier setup the vacuum systems of the Rearsection and the WGTS could not be separated anymore because a valve at the end of the WGTS would prohibit any electric connection to the Rear Wall. Placing the Rear Wall within the WGTS implicated several drawbacks and undesirable dependencies of the two KATRIN components. The introduction of the RSCM enabled to place the Rear Wall inside of the Rearsection instead the DPS1-R exit cone. The resulting physical decoupling and the possibility to isolate the two vacuum systems by a valve was one of the strongest arguments in favor of the superconducting magnet at the Rearsection.

When the option to add the additional RSCM coil was adapted, it resulted in to multiple design tasks: The magnet strength and positioning had to be adjusted in a way that it can contain the flux tube inside of the vacuum vessel. Furthermore, the forces of the superconducting magnets had to be calculated and the technical design of the vacuum vessel and the Rear Wall had to be adjusted to fulfill all requirements. The properties of the superconducting magnet RSCM were already fixed being an exact copy of the module design by Cryomagnetics used at the DPS2. In iterative steps the RSCM field strength and Z-position has been varied and the resulting flux tube and the force to the DPS1-R magnets have been calculated. Concerning the parameter space the range of Z-positions was limited to comply with the technical design of the Rearsection: A minimal distance between RSCM and WGTS is required for installation of a valve and all further RW-related installations. On the other hand the maximum distance RSCM-WGTS is rather soft, being limited only by the requirement of a compact Rearsection given the limited laboratory space. First technical designs of a vacuum system for the Rear Wall and its instrumentation reveal that a minimum space between WGTS end flange and RSCM of at least $320 \pm 20 \text{ mm}$ is required. In this range it is always possible to adjust the RSCM target magnetic field such that the full magnetic flux tube can be transported. In the final design of the Rear Wall chamber the distance between the WGTS end flange and the RSCM was fixed to 318 mm. Figure 5.2 shows a cut of the CAD model including the RSCM, the end cap of the DPS1-R, the Rear Wall and its instrumentation. It displays the technical

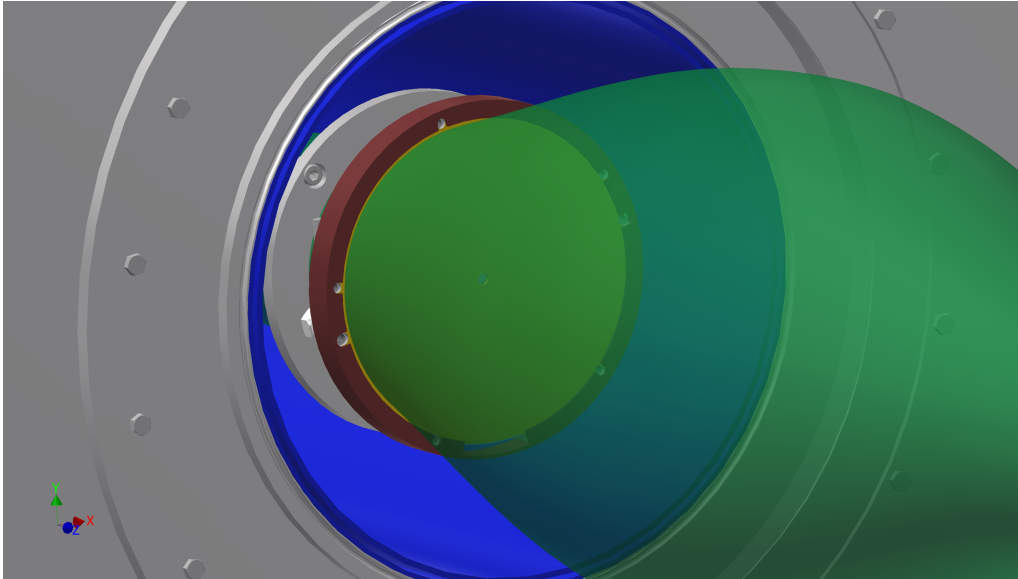


Figure 5.3.: Flux tube intersection with the Rear Wall - the technical flux tube (210 Tcm^2 in green) intersects only with the gold coated part of the Rear Wall. The remaining clearance is about 1.3 mm and can be further increased using the adjustable Z-positioning of the RW. The PEEK mounting ring can be turned on the back side of the Rear Wall mount if the risk of insulator charge-up must be avoided.

magnetic flux tube of 229 Tcm^2 with the final configuration of the RSCM operated at 4.7 T on the left (simulated by the Magfield3 code [67]). A current of 70 A in the 42721 windings of the RSCM is necessary to achieve the desired field. A specific challenge was to fit the flux tube into the vacuum vessel. This required to design a specifically shaped Rear Wall chamber, and to optimize the position and the strength of the RSCM. Figure 5.3 shows how the technical flux tube covers the gold-coated Rear Wall surface with a diameter of 134 mm. The target magnetic field strength of 4.7 T can be achieved with the RSCM since it is specified for field strengths up to 5.5 T. Hence, it would still be possible to increase the field strength and the compression of the flux tube if required. The resulting force between the superconducting magnet of the Rearsection and of the WGTS has been calculated with the Magforce package [115] to a value of 15.1 kN along the z-axis. This force is acceptable for the RSCM which is specified for a force up to 18 kN [88]. The forces on the DPS1-R superconducting magnets are reduced by the introduction of the RSCM in the case of normal operation because in this setup the forces towards the mid of the WGTS and the Rearsection compensate each other. In case of a quench in the WGTS central modules, the RSCM still applies an acceptable force on the DPS1-R modules which are specified for magnetic forces up to 18.5 kN [116]. After all design changes were implemented successfully, the RSCM module was ordered and included as important part of the Rearsection.

So far only issues related to the technical flux tube of $\Phi_{\text{tech}} = 210 \text{ Tcm}^2$ were discussed. In fact the WGTS can produce electrons and ions in the outer flux tube of $\Phi_{\text{tot}} = 229 \text{ Tcm}^2$. With the given magnet and vacuum design the outer flux tube can also be transported through the Rear Wall chamber up to the Rear Wall. This flux tube value is of minor importance because it can be expected that Φ_{tot} will not be fully transported through the whole KATRIN setup. Still, all charged particles should end up on the gold surface of the Rear Wall like all other particles of within Φ_{tech} . In the current design the outer flux tube intersects the Rear Wall at the very edge of the disc. To compensate for mechanical imperfections during construction, leading to a Rear Wall position where the technical and consequently also the outer flux tube does not fit on the surface, the Rear Wall has

to be adjustable along the Z-position. The requirement of a position flexibility which can be set manually by a margin of at least ± 5 mm has thus been added to the Rear Wall specifications.

The Rear Wall must be placed in a region with a smaller magnetic field strength compared to the WGTS field strength of 3.6 T. By this arrangement the polar angle of the impinging electrons is reduced according to the magnetic adiabatic collimation from a maximum angle of $< 90^\circ$ at the pinch field of 6 T to

$$\Theta_{RW,\max} = \arcsin \left(\sqrt{\frac{B_{RW}}{6 \text{ T}}} \right) \quad (5.3)$$

according to formula 2.6. The target field strength at the Rear Wall of 1 T [53] is not achievable because then the diameter of the corresponding flux tube would be too large for the given geometric restrictions by Rear Wall chamber and RSCM. The average magnetic field is rather 1.6 T at the Rear Wall with 134 mm diameter. The precise distribution of field strengths over the surface of the Rear Wall has been calculated and is shown in figure 5.4. The magnetic field strength varies in the range from 1.6 T at the center to 1.4 T at the border of the Rear Wall. This corresponds to maximum polar angles for electrons, which are adiabatically collimated from the 3.6 T field of the source, of 29° to 31° . Electron backscattering probabilities have been calculated based on the code package Penelope 2008 [117] which has the interactions of low energetic particles and matter correctly implemented [118]. The simulation setup consists of a gold cylinder representing the Rear Wall and a point like electron source emitting a conical beam. The cone angle towards the symmetry axis is set to 30° in order to match the maximum angle that can arrive at the Rear Wall. The energy spectrum is defined by the tritium β -spectrum (after inelastic scattering in the source) which has been discretized in 100 eV bins [119]. Totally 10^7 events have been generated for the Monte Carlo simulation. For each event the energy has been chosen randomly according to the probabilities in the spectrum and the direction isotropically within the cone. As a result a fraction of 57.5 % of the primary electrons is absorbed while the others are reflected. The rather high amount of backscattered electrons is caused by the high-Z material gold [120]. Reflected electrons may pass through the source and can thus contribute to the neutrino mass measurements. The probability for an electron to pass through the entire column density without inelastic scattering is 15.3 % [50]. Therefore, the total probability for an unscattered β -decay electron from the source to be reflected at the Rear Wall and pass through the whole source plasma is only 8.8 %. Still, this rather large contribution to the observed signal count rate has to be considered in the source analysis for the neutrino mass measurement.

5.1.3. Technical implementation of the Rear Wall

The final technical implementation of the Rear Wall assembly will include a mount for the gold coated Rear Wall disc itself. The main installations at the Rear Wall mounting are the electron beam tracker described in section 4.5 and the piezoelectric motor to cover the central Rear Wall hole described in section 4.4. The Rear Wall and its mounting system need to be electrically insulated against the surrounding vacuum vessel so that the Rear Wall potential can be shifted relative to the WGTS walls, as outlined in section 5.1.1. Access for assembly or maintenance is rather limited, due to the nearby large-scale components (WGTS and the Rearsection's superconducting magnet) and due to restrictions by tritium safety requirements. Therefore, the RW instrumentation should be installable and maintainable with minimized disassembly procedures of the vacuum system.

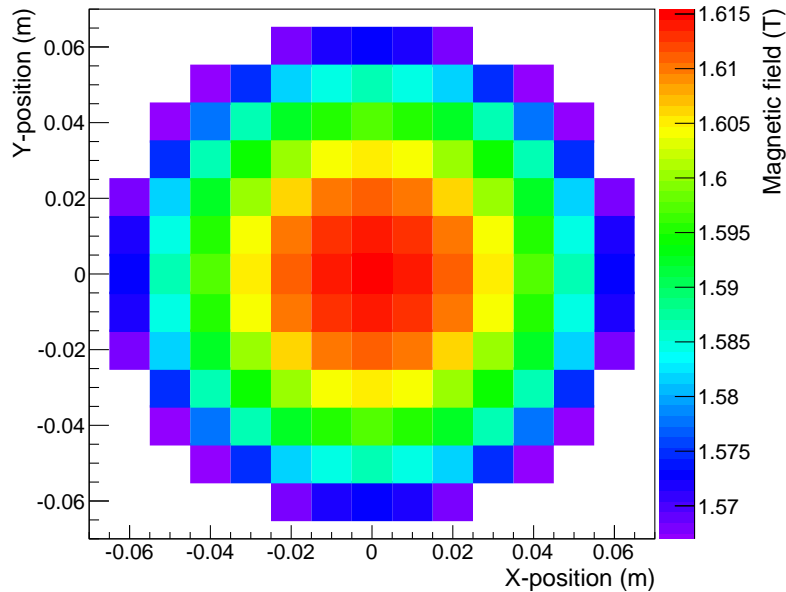


Figure 5.4.: Solenoid magnetic field at the Rear Wall - calculated absolute magnetic field on the Rear Wall surface. The RW had to be placed in a higher field than the original target value of 1 T because of mechanical constraints. The field strength drops by $\approx 3\%$ from the center to the Rear Wall edge.

The first decision for the Rear Wall implementation was to use a modular system which allows exchanging the gold coated disk (the “physical” Rear Wall). As a benefit, disks with the appropriate dimensions and shapes can be installed to the system. This is important because there are many candidates available that can potentially be used as physical Rear Wall. These prototypes differ by the disc substrate and by the utilization of different intermediate layers below the gold surface. The following list contains a description of possible substrates and layers:

- Top layer - surface of the Rear Wall. The very top layer of the Rear Wall is made of gold as this material excels most other elements by its chemical inertness, small degradation in many environments, the absence of catalytic effects on hydrogen molecules, small tritium adsorption (compare section 5.4.1) and a stable work function. The gold layer should be very pure and grown in a way that results in a homogeneous work function over the entire surface. Many different coating methods are available such as galvanization of dissolved gold, various chemical vapor deposition methods or physical vapor deposition methods (e.g. sputtering).
- Intermediate layer - modifications of the coating properties. The intermediate layer between gold and the underlying substrate depends on the Rear Wall substrate and application. Since gold does not stick equally well to every surface, sometimes an additional adhesion layer is required. The appropriate adhesion layer again depends on the two materials to be combined. Adhesion layers used during the Rear Wall prototyping were nickel-chromium or titanium-nitride. Furthermore, some material combinations require a diffusion barrier layer because otherwise the two materials can mix or the gold can completely dissolve in the substrate. When diffusion barriers were needed compounds like titanium nitride or titanium oxide are selected for the Rear Wall prototypes. For a Rear Wall with integrated current-based activity monitoring an insulation layer is required. With the insulation layer it is possible to separate the current of low energetic charges stopping in the gold layer from the current of the higher energetic beta-decay electrons penetrating into the substrate. This is

rather challenging as an insulation layer with this task must be very thin (order of 10 nm) but homogeneous. Also, it has to provide a large electric resistance ($> 10^6 \Omega$). During test experiments at UCSB insulation layers of aluminum oxide and silicon oxide have been tested [111].

- Substrate - the coating target. The intermediate layers and the gold layer are applied to a substrate which shall provide a flat homogeneous surface and the required mechanical stability. The first generation of Rear Wall prototypes used substrates of corundum, beryllium, silicon and copper. Pure α -aluminum oxide (“corundum”) has been tested thoroughly, as it is considered to be a substrate where a gold layer can be grown epitaxially and monocrystalline [121]. The choice of beryllium is caused purely historically: Before the introduction of the RSCM the Beta-Induced X-ray Spectroscopy worked with the X-rays that are transmitted instead of reflected at the Rear Wall. Therefore, an X-ray transparent thin beryllium sheet has been tested as substrate candidate. Silicon was the preferred substrate for all prototypes with integrated insulation layer for the direct current measurement. The most important advantages of silicon are the wide availability of high quality silicon wafers and the well understood growth processes. The final substrate on the list of the first generation substrates is copper because it shows very good work function properties after gold galvanization [122]. This was verified at the *a*SPECT experiment [123] where stable surface potentials are of comparable importance. The experiences gained from the first generation of RW prototypes led to the focus on a more simple and robust RW in the second generation prototyping. The investigations of the second generation RW prototypes were targeted on substrates using copper, aluminum or stainless steel. All of these are solid, easy machinable and non-magnetic materials that are widely available. If the diffusion barrier and adhesion layer are appropriately chosen it is possible to apply a stable gold coating on all off these second generation substrates.

Some of these combinations were produced and tested with small-scale samples in the framework of the qualification measurements described in the sections 5.2 and 5.3. With regard to the fragility of some substrates, the preferred holding mechanism for the disc is clamping. Accordingly, a clamping ring fixes the disc at the outer edge and is screwed to the Rear Wall holder. By this design the mechanical stress of the disc is minimized. The installation of the RW holder to the Rearsection again is done by a bayonet-like mount. This enables installation and maintenance from the front side even in case of limited accessibility. The most delicate part of the assembly procedure is having the Rear Wall mount (including the disc) held by two threaded rods, while it is installed by the push-and-turn movement of the bayonet mechanism. Since there should occur no torque during normal KATRIN operation, the installation method should be long-term reliable. The electric insulation against the wall fixture is implemented with vacuum compatible high-voltage ceramic insulators. The RW disc and mount are insulated to nearby surrounding walls by a generously dimensioned clamping ring made of PEEK. The custom shape of the PEEK ring allows clamping the Rear Wall disk to the holder and to provide a strong electrostatic insulation (at least 2 kV since PEEK has a dielectric strength of 17 kV/mm [124]) along the sides of the cylindrical disc and holder. The requirement of an adjustable Z-position is directly implemented at the holding mechanism: The Z-position of the bayonet feather tripod can be individually adjusted by their threaded rods. This allows a rotational alignment and a positional adjustment in z-direction by ± 10 mm. On the back side of the Rear Wall holder instruments like the piezoelectric motor for closure of the central hole or the electron beam tracker are installed. They have been implemented and aligned in the Rear Wall holder design. The Rear Wall cover must be moved closely behind the Rear Wall disc. Therefore, an appropriately sized milling groove and cover holder design

was necessary. Electric heaters and temperature sensors are also foreseen on the holder backside but not yet been implemented in the technical design. They will be used for temperature stabilization of the Rear Wall and temperature monitoring during bake-out of the Rear Wall chamber. Figure 5.5 shows a normal and an exploded view of all the described parts of the Rear Wall assembly.

5.2. Work function measurements using a Kelvin Probe

The work function distribution of several Rear Wall prototype samples has been measured with a Kelvin probe. This instrument provides one of the most commonly used methods to measure work functions [125]. The working principle of a Kelvin probe is described in the following section 5.2.1. The device used for the measurements reported here was a Kelvin probe, with a surface scan range of $200 \text{ mm} \times 200 \text{ mm}$, running at atmospheric pressure. This measurement device was available at the collaborating University of Mainz for the purpose of work function measurements for the KATRIN and *a*SPECT experiments [122]. The details of the setup including its advantages and limitations are described in section 5.2.2. The list of measured Rear Wall candidate samples and resulting work function distributions are given in the measurement section 5.2.3. The conclusions on the measurements in general and the qualification of the individual samples are given in section 5.2.4.

5.2.1. Kelvin probe working principle

A well established method to measure the work function in a non-invasive way is based on a “Kelvin probe” which makes use of the contact potential difference. The idea and the name of the Kelvin Probe goes back to the investigations of William Thomson [126]. In order to measure the work function of an arbitrary material, a probe tip close to this surface, made of a certain material with preferably stable work function, is required. Each surface (treated independently) has a material characteristic work function defining the potential step between vacuum potential and the Fermi sea (compare section 5.1.1). At the surface the potential increases like a $1/r$ function due to the image charge effect affecting free charges nearby the surface. When the two materials become electrically connected they are not completely independent anymore and their potentials are related. Conductive electrons move to compensate the potential gradient until the Fermi levels are equalized. Because the work functions do not change in this process, the heights of the vacuum potentials are now shifted relative to each other by the work function difference also called contact potential difference (CPD). Two materials can be approached close enough that a continuous potential gradient and a static electric field arise. Surface charges are induced at the facing surfaces to generate the potential gradient while shielding the field from the inside of the solid. This situation can also be described as a charged plate capacitor with a capacitance of

$$C = \epsilon_0 \frac{A}{d} \quad (5.4)$$

with the vacuum permittivity ϵ_0 , the area of the smaller surface (either the probe tip or sample) A and the probe to sample distance d . This formula uses the assumption that $\sqrt{A} \gg d$ and thus neglects stray fields and non-parallelism. The Kelvin probe now varies periodically the distance of probe tip and sample by applying a sine-like vibration on the probe tip. By this method the capacitance of the setup constantly changes while the voltage difference remains constant. As a consequence, charges must steadily move between the surfaces resulting in an alternating current I between probe tip and sample.

$$I = \frac{dQ}{dt} \propto \Delta U \frac{dC(t)}{dt} \propto \frac{d}{dt} \frac{1}{d + \Delta d \sin(\omega t)} \quad (5.5)$$

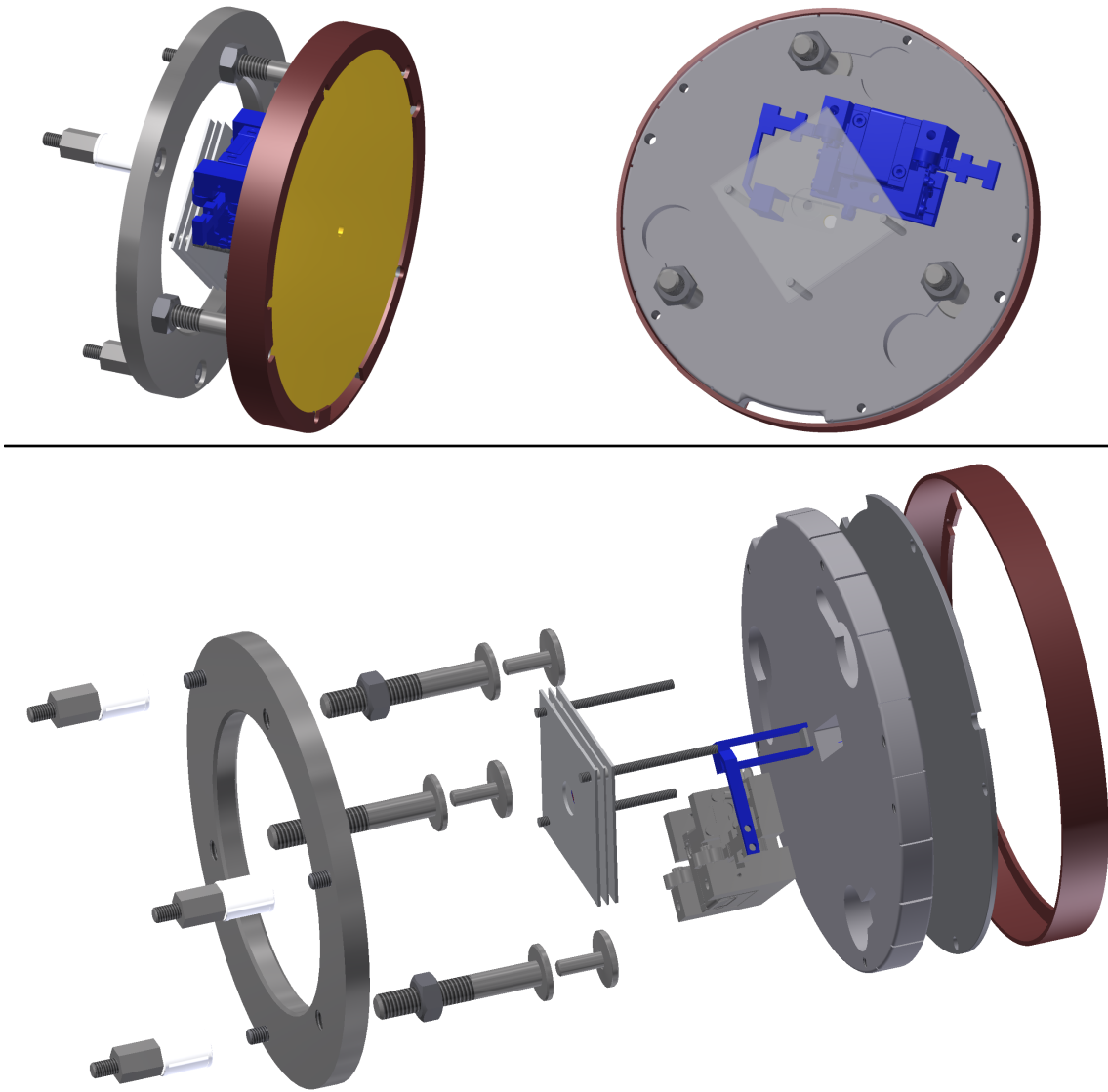


Figure 5.5.: Technical design of the Rear Wall mount - showing a front side (top left), a back side (top right) and an exploded view (bottom) of the Rear Wall mount. The piezoelectric motor to cover the Rear Wall hole and the electron gun beam tracker are both included in the design. Further details like temperature sensors or electric heaters are excluded. The mounting system features the installation of any Rear Wall disk of the right shape, insulation to the mount and the side wall. The bayonet mechanism shall enable the (dis)assembly of the system compliant with tritium safety and KATRIN operational requirements.

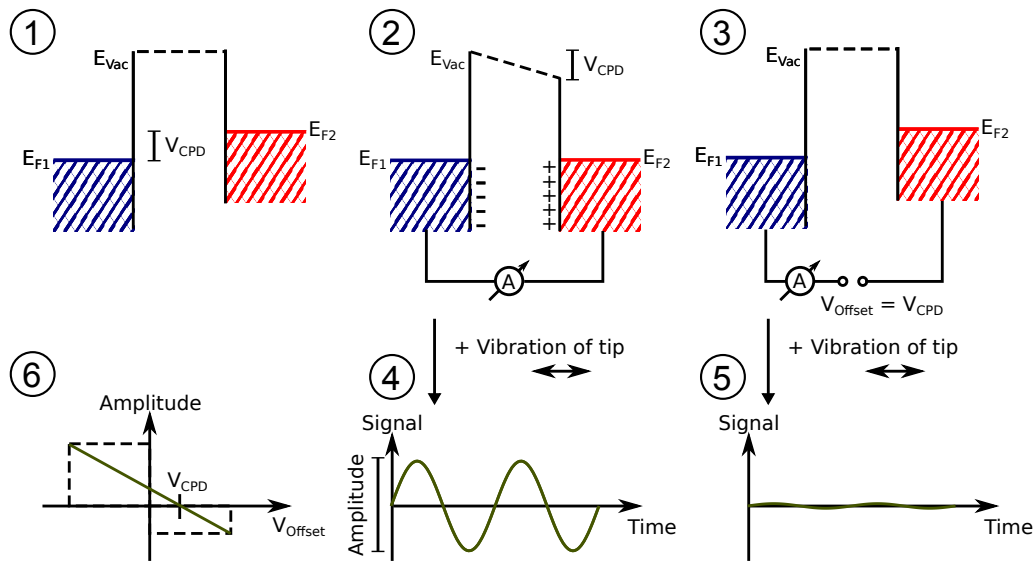


Figure 5.6.: Necessary steps for a Kelvin probe measurement - 1. Different metals have distinguished work functions meaning the distance of the Fermi level to the vacuum energy differs. 2. When these metals are connected electrically with low resistance, charges are transferred until the Fermi levels are equalized. As a consequence, the vacuum energy is bent which is caused by surface charges at the metal. 3. The effect can be reversed if a voltage is externally applied that equals the difference in work functions called the contact potential difference CPD. 4. If the surface charge exists, vibration applied on one of the metals result in an AC signal because the capacitance of the two metals changes constantly. 5. If V_{CPD} is applied the signal vanishes which is one way to measure the CPD value. 6. An improved way to measure the CPD is by a fit of two intentionally offset measurements and the subsequent determination of the X-axis intercept.

To finally measure the contact potential difference an external voltage is applied on the probe tip. Now the output signal can be increased, reduced or even inverted. The output signal disappears when the applied voltage is exactly the negated value of the CPD. This is also one of the operational methods for a Kelvin probe, by searching the zero crossing of the output signal amplitude. To improve this method, a lock-in amplifier can be used that is adjusted on the frequency of the Kelvin probe vibration. This method is very vulnerable to noise because when the signal vanishes noise becomes dominant and the exact voltage of the signal zero-crossing becomes difficult to find. The lock-in amplifier can not filter out all noise contributions because unlike the usual electrical or net noise, parts of the noise are caused by stray capacities and have exactly the same frequency like the main signal. The modern Kelvin probe used for the following measurements utilizes the off-null-technique [127]. In this technique, two or more voltages differing significantly from the CPD value but surround the CPD value are applied to the probe tip (e.g. +1 V and -1 V for CPDs in the range -0.5 V to +0.5 V). As a result a large output signal with a high signal-to-noise ratio can be retrieved. Now the linear dependence between signal strength and voltage difference can be used. With two or more value pairs, a linear fit can be applied to the data. If the linear fit is used to interpolate to a signal strength value of zero, the corresponding tip voltage is again the negated CPD value. Additionally, the gradient of the linear fit is an indicator for the tip-sample distance that can be used to maintain a constant distance during multiple measurements. Due to the measurement principle the retrieved work functions are not absolute values but relative to the probe tip. It is still possible to measure changes in the work function across a surface or during a certain time. Furthermore, it is possible to reconstruct the absolute work function if the measurement are reproducible with the same conditions and a sample with well known work function.

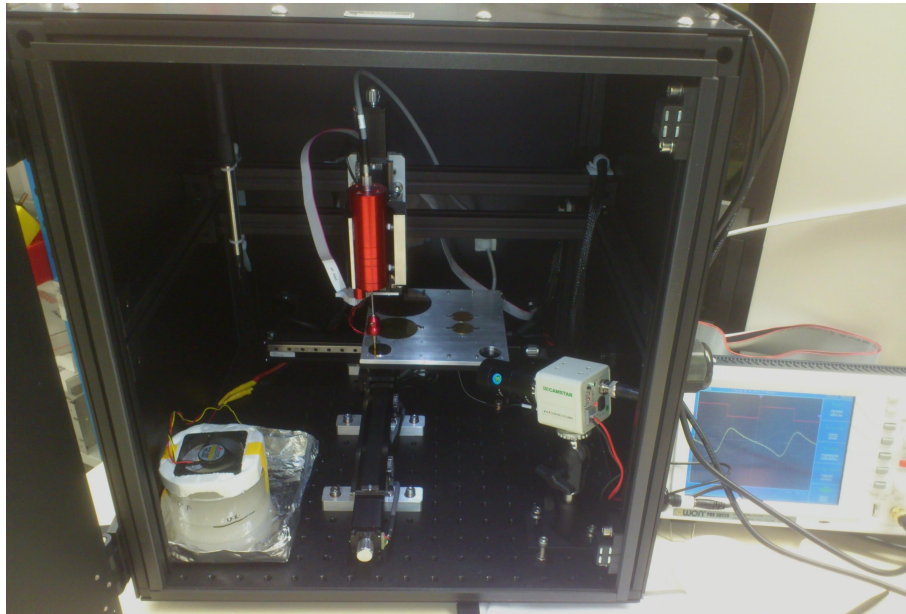


Figure 5.7.: Picture of the overall Kelvin Probe setup - It shows the black encasement and the experimental installations inside: The Kelvin probe head unit (red, central), the measurement platform with motorized stages (bottom center), the humidity stabilization system (bottom left) and the camera (bottom right).

5.2.2. Scanning Kelvin probe setup

The measurements of this theses were performed with a Kelvin probe available for KATRIN measurements at the physics department of the University of Mainz. The deployed Kelvin probe type ASKP150150 has been produced by KP Technologies Ltd.² and delivered in late 2011. The ASKP150150 works at ambient pressure and is able to scan a planar surface with a range of $150\text{ mm} \times 150\text{ mm}$ using stacked linear stages. The coarse approach of the probe tip to the sample is performed by a stepper-motor based linear stage. However, fine adjustment is also possible using the small coil which generates the tip vibration within the Kelvin probe head. This can be implemented by a static offset of the coil supply voltage to the usual sine like supply voltage. The Kelvin probe head is installed into an optical enclosure to stabilize the ambient conditions: Fluctuations in light, atmosphere and temperature become less dependent from the laboratory conditions. Picture 5.7 shows the Kelvin probe head and the motorized stages inside the opened optical enclosure.

Inside the enclosure a camera and an LED light source are installed in order to visually control the Kelvin probe operation. Both instruments can be enabled by the control software when the encasement is closed. By this procedure, a fail-safe navigation with the sensitive probe tip can be ensured while the scan platform is moving. The tip of the probe can be exchanged and different tip sizes are available. Since the capacity of the tip and the sample scales linearly with the tip area A , this can influence signal strength and sensitivity. During the measurements reported here a circular probe tip of 2 mm diameter is used. The tip is made of stainless steel but the probe surface is gold coated. The result of the measured samples is the contact potential difference to this specific gold surface. To monitor the behavior of the Kelvin probe and to quickly compare measured surfaces to known surfaces, a reference sample is installed permanently on the scan platform. The reference sample provides a gold and aluminum surface. The Kelvin probe tip, the scan platform and the reference sample are shown in the picture 5.8.

²KP Technology, Burn Street, Wick Caithness KW1 5EH, Scotland

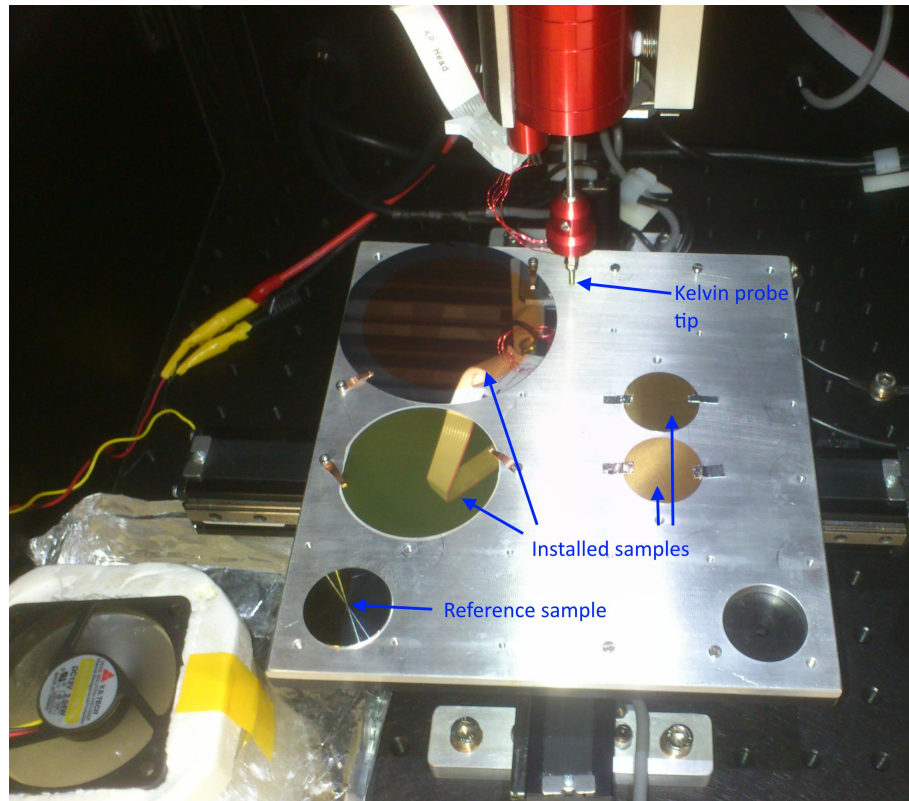


Figure 5.8.: Picture of the Kelvin probe measurement platform - Samples up to $150\text{ mm} \times 150\text{ mm}$ can be installed and scanned with the system. In this picture 4 test samples and the reference sample are placed on the platform. The aluminum tape ensures the mechanical fixation and the electric contact. At the Kelvin probe a 2 mm tip is installed.

The Kelvin probe calibration and early measurements for the *a*SPECT experiment revealed the atmosphere around sample and tip to be a source of systematic errors. To analyze the correlations occurring at ambient conditions, a temperature and a humidity sensor have been added to the setup. Especially the humidity of the air inside the enclosure can cause work function drifts of $> 20\text{ mV}$ [122]. Therefore, the humidity has been stabilized with a saturated salt solution: The used salt complex $\text{MgCl}_2 \cdot 6\text{H}_2\text{O}$ has a relative humidity of 32.7% at 25°C in equilibrium. Equilibrium to the surrounding atmosphere is reached after approximately 12 to 24 hours once the Kelvin probe encasement was closed. This equilibration time was always considered in the following measurements. Besides instrumentation and sensors in the enclosure, all other required electronics are placed outside of the box. The Kelvin probe needs a dedicated controller and amplifier while the motor stages also have a dedicated motor controller. The amplified signal is split into an oscilloscope for visual monitoring and into an ADC. The whole setup is controlled from a conventional PC. The interface between PC and the controllers is implemented with a National Instruments 6025E data acquisition system.

5.2.3. Measurements of prototypes

The measurements of different gold surfaces have been conducted within one week at the laboratory in Mainz. The most important measurements were scans across the maximum rectangular area available on the gold surface to check for inhomogeneities. The rectangular scan area is a limitation by the supplier-based KP control software. During these scans the stability of parameters such as temperature and humidity was ensured by constant monitoring. Before and after each scan the gold-coated reference sample has been checked to detect possible drifts during the measurements. The first step to each scan is to set up

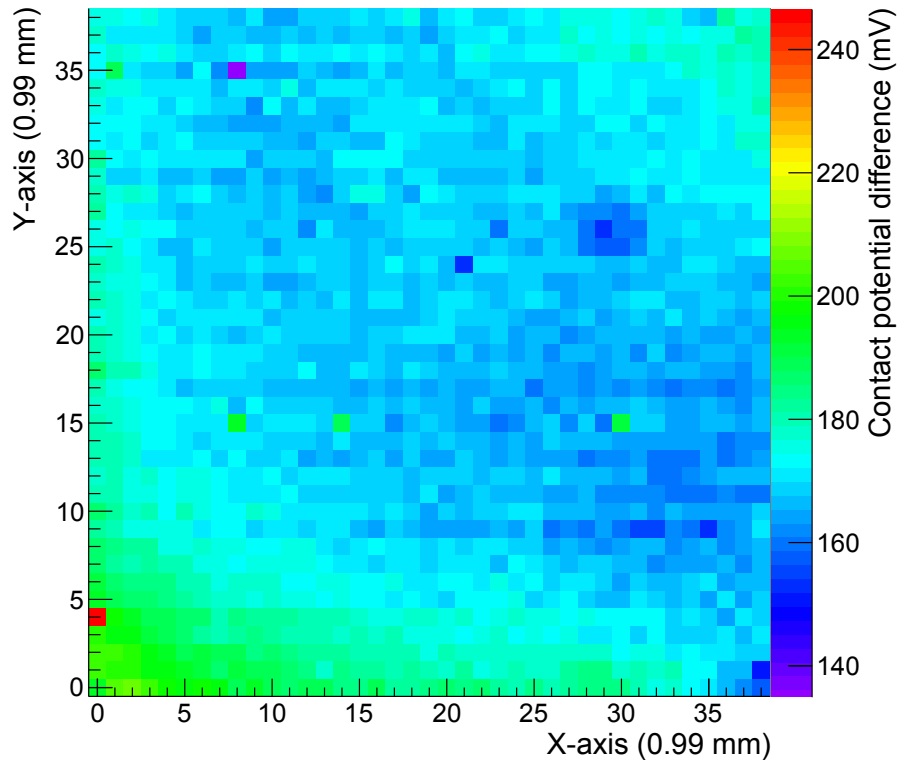


Figure 5.9.: Kelvin probe scan of the gold coated silicon wafer - Quadratic scan with 39×39 measurement points. The work function is homogeneously distributed over the surface with a lower CPD values in the center of the sample.

the Kelvin probe to the correct position. The starting surface position for the scan is navigated manually followed by a coarse approach of the tip height. The fine approach uses the Kelvin probe itself by approaching the sample surface in small steps parallel to fast measurements of the work function gradient. As described in section 5.2.2, the gradient of the linear work function fit provides information about the tip-to-sample distance. The gradients used for the measurements are either $G = 200$ or $G = 300$. In general a larger gradient means a shorter tip-to-sample distance and a stronger signal. The values are kept constantly to the configured values during the scan by an integrated tracking of the software. The values itself are device and amplifier dependent and are not calibrated to a certain tip-to-sample distance. The following list describes the samples that have been measured, the corresponding measurement configuration and the measurement results:

- **Gold-coated silicon wafer:** This 3-inch large prototype was produced by UCSB as a test sample for the Rear Wall intrinsic activity measurement. On the silicon substrate a layer (thickness ≈ 100 nm) of silicon dioxide was grown. The insulation layer is grown by thermal oxidation of the silicon and by atomic layer deposition. On top of the silicon dioxide layer an adhesion layer and diffusion barrier of titanium nitride is sputtered (< 10 nm). The top layer consists of ≈ 50 nm of sputtered gold. For the scan an area of about 39 mm \times 39 mm was chosen. The result of the scan is given in the chart 5.9. It shows a good homogeneity over the whole area with slight drifts towards the corners. There are several punctual outliers that are difficult to rate: It might be associated to an actual work function at this position, as intrinsic property of the gold. It might also point to an impurity on the surface such as dust or aerosol particle which is likely to happen with an ambient Kelvin probe in a non clean room laboratory. Since both cases can not be distinguished, all measurements points are considered for the data analysis. Accordingly, the average

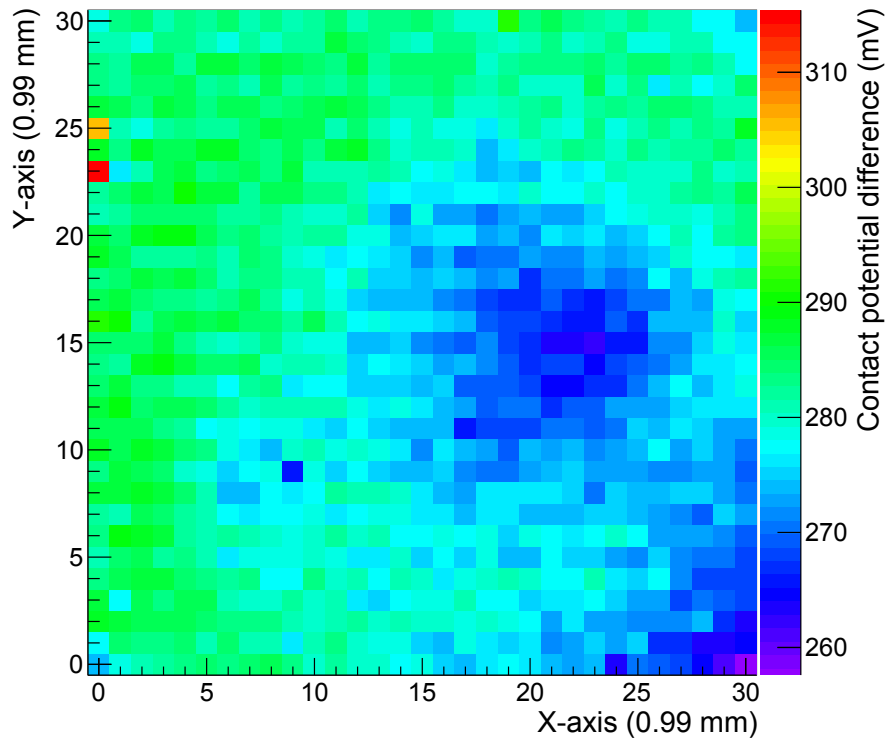


Figure 5.10.: Kelvin probe scan of the gold grown on corundum - Quadratic scan with 31×31 measurement points. The work function is homogeneously distributed over the surface with a lower CPD values in the center of the sample.

contact potential difference and the standard deviation in that area can be calculated to:

$$\Delta W(\text{SiI}) = 171 \pm 7 \text{ mV} \quad (5.6)$$

The given standard deviation is enough enough to qualify this prototype as a serious Rear Wall candidate. Of course full qualification as RW candidate requires all other qualification steps to be successful. Also, the technology of the sample production allows an upscaling to the final Rear Wall size. Before and after the measurements the measured CPD of the reference sample was shifted by 4 mV from $100.8 \pm 3.1 \text{ mV}$ to $104.6 \pm 1.9 \text{ mV}$. This shift is compatible within 2σ of the measured uncertainties.

- **Gold grown on corundum:** The substrate α -aluminum oxide³ was chosen as candidate because of reports in the literature [121] that it is possible to epitaxially grow monocrystalline gold on this substrate. This sample with a diameter of two inches was produced by CrysTec⁴. The specific method for epitaxial growth of the gold on the substrate was not defined by the company. To increase the likelihood of a perfect monocrystalline growth on the substrate no adhesion layer or diffusion barrier has been used. Still, the resulting gold surface was polycrystalline with approximate grain sizes of 1 mm^2 being dominantly ($> 90\%$) (111)-surface orientation. These properties have been measured at UCSB using low-energy electron diffraction (LEED) [111]. Nevertheless, the surface quality of the sample appeared to be appropriate to justify a measurement with the Kelvin probe. The results of the scan over an area of $31 \text{ mm} \times 31 \text{ mm}$ are given in figure 5.10. The homogeneity is mainly interrupted by two extended areas in the center and the lower right corner with a

³In crystallography it is well known as corundum. There exists a group of crystals based on aluminum oxide with different metal traces resulting in different coloring (e.g. sapphire and ruby).

⁴CrysTec GmbH, Köpenicker Str. 325, 12555 Berlin

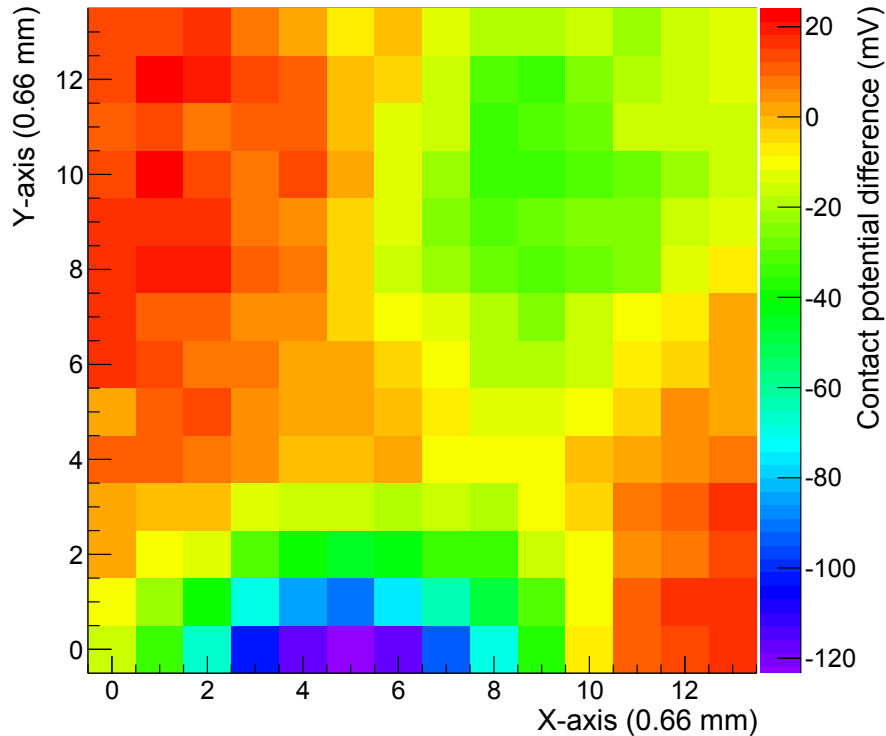


Figure 5.11.: Kelvin probe scan of the gold coated Beryllium window - Quadratic scan of 14×14 measurement points. Although the scan area is relatively small, there are huge variations in the contact potential difference. Concerning this surface quality the beryllium window can not compete with the previously measured samples. The shape of the CPD distribution seems not to be linked to the sample curvature.

slightly reduced CPD. Again there are a few punctual outliers that are included in the statistical evaluation. With an average CPD of

$$\Delta W(\text{Al}_2\text{O}_3) = 279 \pm 6 \text{ mV} \quad (5.7)$$

the sample takes the qualification step as well. Compared to the previously described sample the CPD of this gold surface is shifted by more than 100 mV. This is due to the fact that different gold surfaces are displaying non-identical absolute work functions depending on the character of the surface. However for KATRIN, the relative distribution and stability of the Rear Wall surface is of key importance, rather than the absolute value of the work function. During the scan the tip was very stable - the measurements with the reference sample before and after the scan only show a difference by 0.2 mV from $104.6 \pm 1.9 \text{ mV}$ to $104.8 \pm 2.3 \text{ mV}$.

- **X-ray transparent window for the TriADE test experiment:** The test experiment TriADE (Tritium Adsorption Desorption Experiment) [47] relies on an X-ray transparent window which is gold-coated in order to reduce the amount of tritium adsorption (compare section 5.4). For these reasons a Kelvin probe scan across the window inserted in a CF40 flange should qualify the gold coating of this product. Furthermore, it provides a reference for the work function homogeneity of a surface that has not been optimized for homogeneity. The Beryllium window sheet was joined to the CF40 flange with diffusion bonding by the company Materion⁵. The gold coating was applied by Siegert TFT⁶ in a separate step. The scanning condi-

⁵Materion Brush Beryllium & Composites, 14710 W. Portage River South Road, Elmore, OH

⁶SIEGERT TFT GmbH - THINFILM TECHNOLOGY, Robert-Friese-Straße 3, Hermsdorf

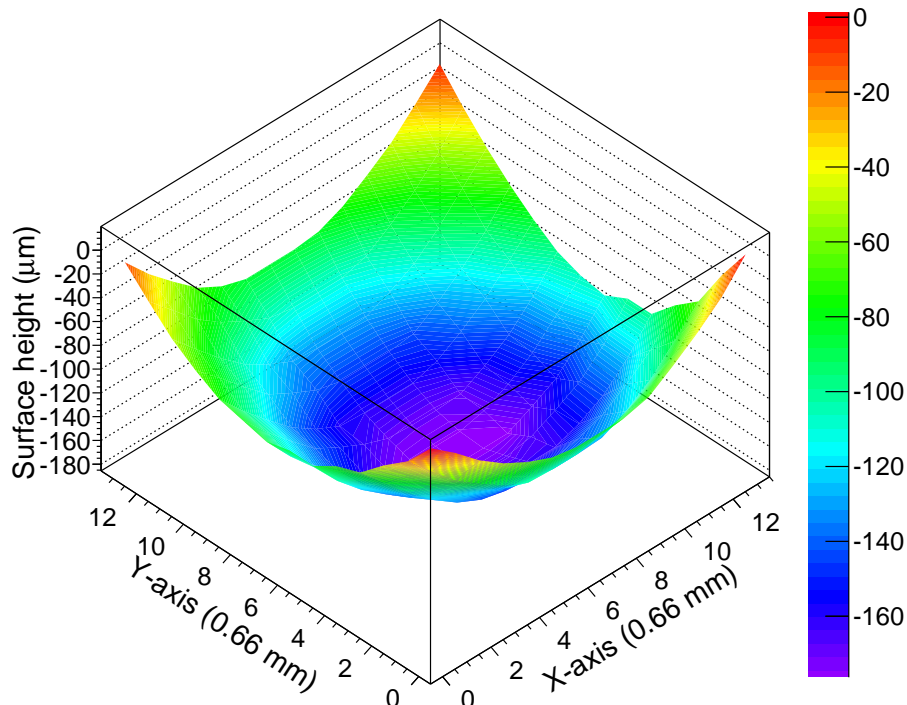


Figure 5.12.: Height profile of the beryllium window - The visible curvature of the window is also reflected in the tracking height data from the KP measurement. The experimental method is not only capable to measure the work function of a curved sample but also to recognize the contour down to the micrometer scale. Quantitatively the Kelvin probe might underestimate the depression because the 2 mm large tip limits the approach to a curved surface.

tions were more significantly more complex than at the other measurements: The available surface was rather small resulting in a scan area of only $9\text{ mm} \times 9\text{ mm}$. The surface also had a noticeable curvature because the beryllium window needs to be slightly bend to withstand the large forces resulting from the pressure difference from atmosphere to vacuum. The results of the CPD scan are displayed in the graph 5.11. The distribution of CPD values is rather broad especially when the small scanning area is considered. It is important to notice that the large spots of higher and smaller CPD values are not related to the curvature of the window. The height profile of the sample is also recorded by the Kelvin probe and shows the surface curvature in the graph 5.12. The average CPD value of all the scanned values can be calculated to

$$\Delta W(\text{Be}) = -12 \pm 26\text{ mV} \quad (5.8)$$

This sample was not actually a Rear Wall prototype. Therefore, it is uncritical that the error on the CPD scan exceeds the Rear Wall requirements limit of $\sigma < 20\text{ meV}$. However, this gold coated window shows that a homogeneous work function of a gold surface is not self-evident. To achieve an acceptable level of homogeneity a careful preparation of the sample surface and a careful coating procedure are required. Furthermore, this sample showed that CPD scans of curved surfaces are also possible with this Kelvin probe. Before and after the scan a nearly identical CPD value has been measured at the reference sample $\Delta U_{\text{CPD}} < 1\text{ meV}$.

- **Gold sputtered on beryllium:** Two small samples with gold coated beryllium (1 inch diameter) have also been tested. These were coated at UCSB using gold

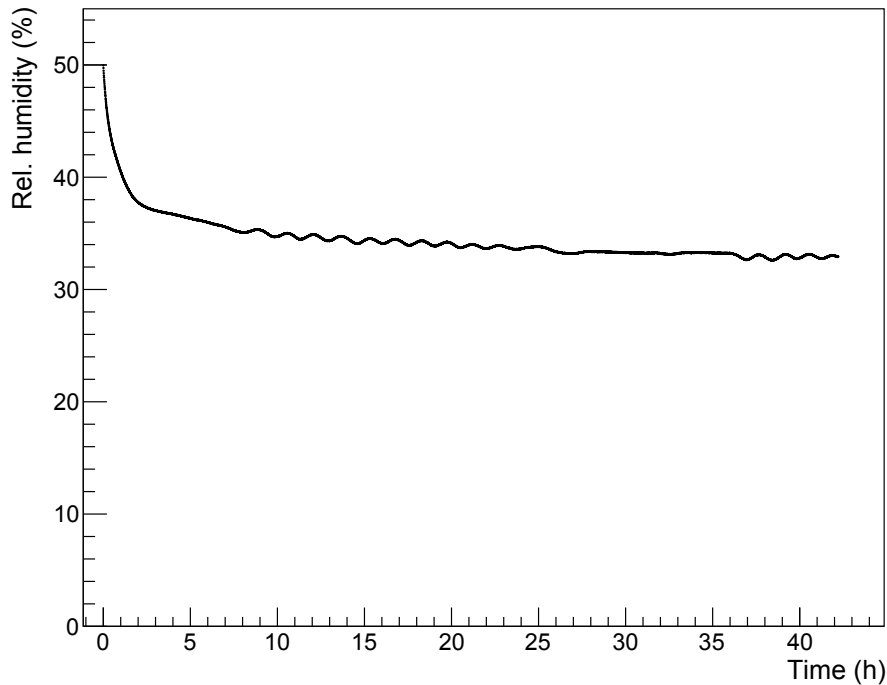


Figure 5.13.: Humidity in the Kelvin probe enclosure - Long term equilibration process of the humidity in the Kelvin probe enclosure. The data of the humidity sensor has been recorded for more than 40 hours after the enclosure has been opened and closed again. To consider the humidity in the enclosure as stable, at least 24 hours are recommended.[122]

sputtering [111]. The production of these samples has historical reasons: Before the introduction of the Rearsection superconducting magnet (RSCM) the Rear Wall had to be X-ray transparent to enable the BIXS activity monitoring system to work efficiently. After the introduction of the RSCM, the substrate option beryllium was discarded because of the complexity of beryllium handling and its high toxicity. Nevertheless, it is worth to mention that these samples also had encouraging results in scans with areas of $14 \text{ mm} \times 14 \text{ mm}$:

$$\Delta W(\text{Be} - 1) = 154 \pm 10 \text{ mV} \text{ and } \Delta W(\text{Be} - 2) = 181 \pm 8 \text{ mV} \quad (5.9)$$

Besides these measurements the stability of the CPD values derived was tested with the reference sample as a function of humidity and temperature. The monitoring measurement was carried out over a night after the samples have been exchanged. During this time period the atmosphere in the enclosure had to recover from laboratory atmosphere to its equilibrium leading to a large change of the humidity. The graph 5.13 shows the decrease of humidity towards equilibrium over a time range of 42 hours. During the equilibration time the value of the reference sample CPD value, given in 5.14, undergoes significant changes. Starting with 122 mV, the value first rises to 144 mV and then drops in an exponential shape to 68 mV. The standard deviation during this monitoring of $\sigma = 25 \text{ mV}$ would already exceed the Rearsection specification. Only after at least 48 hours the measurement becomes stable enough for precision measurements. However, the exact duration is correlated to the atmospheric conditions in the laboratory. Further analysis of the temperature and humidity effects is given in [122]. During all previously described measurements the equilibrium was always reached and the humidity was stable within 1% and the temperature within 1 °C. After all tested samples passed the Kelvin probe scans the conclusions on this qualification strategy are drawn in the following section and possible improvements are discussed.

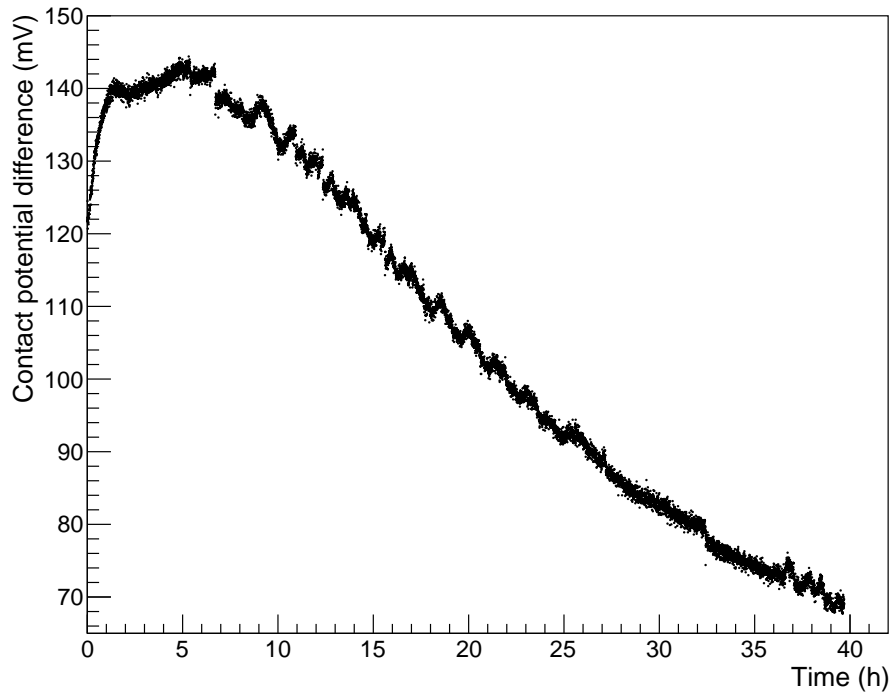


Figure 5.14.: Long-term stability of the reference sample - Kelvin probe measurements in a time range of 40 hours show significant drifts of the gold reference. The largest drift slope occurs after the enclosure has been locked. The variations on the CPD are reduced but not extinct with measurement time. Unlike the humidity the CPD measurements do not fully stabilize during the long-term measurement.

5.2.4. Conclusions for the qualification strategy

Measurements of the contact potential difference (CPD) with a Kelvin probe are an indispensable and efficient tool to test and qualify Rear Wall candidates. This technique can be used to measure the sample homogeneity by scanning over its surface or evaluate the CPD stability by continuous long-term measurements. However, a Kelvin probe has some intrinsic limitations: The work function can not be determined absolutely but only as a CPD value relative to the work function of the tip surface. Therefore, the measurement accuracy depends on any degradation or instability of the probe tip surface. To minimize this effect, the tip surface consists of a material with a rather high work function stability such as gold or stainless steel. Since the RW relies on a highly stable work function, the uncertainty introduced by the tip surface remains a risk. But variations during the work function measurements can be assigned to the sample when they appear only locally during a scan or the CPD to the reference sample remains constant during a long-term stability test.

Besides these intrinsic limitations of the method there are further setup-specific drawbacks. Most of them are caused by operating the Kelvin probe in ambient air. The work function measurements can vary considerably (> 50 mV) due to humidity or dust. In contrast, the final RW unit is placed in a vacuum system at a pressure of the order of 10^{-5} mbar. In vacuum systems water can remain stucked to surfaces but water vapor or humidity in the volume are not an issue. Dust can also occur at vacuum systems but the risk of dust deposits can be minimized by using cleaned parts only and by following ultra-clean working procedures. Once a vacuum system is closed and evacuated no additional dust is expected to end up during normal operation. Hence, the work function measurements should ideally be carried out in vacuum. With the Rear Wall placed in a vacuum system the results of the CPD measurements could also differ from the results obtained with

the atmospheric Kelvin probe in Mainz. After the measurements with the atmospheric Kelvin probe, the production of a gold surface that fulfills the work function homogeneity requirements appears to be achievable. Still, all Rear Wall candidates and backup RW solutions have to proof their intrinsic work function qualities in a vacuum environment. The effects of bake-out on the work function can also not be determined by the Kelvin probe at Mainz. For the final Rear Wall setup regular bake-out cycles at temperatures of 150 °C are foreseen. Once the prototyping has reduced the amount of candidates, the reproducibility is checked by the production of multiple samples by the same procedure. One part of the reproducibility checks is to find the appropriate cleaning procedure for the most promising candidate and a backup solution. After a surface cleaning process followed by an in-vacuum bake-out procedure has been established, the sample must again fulfill the work function requirements. The final candidates can then be upscaled to the final RW size and must still fulfill the limit on the work function homogeneity of $\sigma < 20$ meV. This requirement is relaxed somewhat as it applies to an area equivalent to a main detector pixel which corresponds to a RW area of ≈ 1 cm² after flux tube size transformation. In order to implement these further qualification steps, an in-vacuum Kelvin probe with bake-out capability has been built at KIT. With this instrument the final Rear Wall candidate and the established backup solution (stainless steel, an adhesion layer and gold, sputtered) will be thoroughly tested. The design of the vacuum Kelvin probe allows the measurement of the full-sized final Rear Wall, both with and without bake-out. The results of these measurements will be given in [86]. An alternative way to check the properties of the prototype surfaces is an absolute work function measurement by photo-emission. Such a measurement has been conducted with the prototype samples at the monitor spectrometer of KATRIN and will be described in the following section 5.3. Some of these measurements include already the previously proposed procedure such as bake-out and cleaning.

5.3. Work function measurements with the photoelectric effect

A direct and absolute measurement of the work function is possible via the effect of photoelectric emission. The measurement principle is based on the definition of the work function itself: The work function is the potential difference between the vacuum energy level and the Fermi sea within the metal. Photons with a higher energy than this potential gap can elevate electrons to the vacuum energy level and extract them from the metal surface. There are many effects that can reduce the total efficiency of this process, as described qualitatively in section 4.1.4. The accuracy of the work function itself is limited by the fact that, depending on the metal, the Fermi sea level will split into more complex surface states at the boundaries of the metal [128, 129]. Additionally, the sharpness of the Fermi-Dirac function gets smeared out by thermodynamic effects according to the statistical equation [130]:

$$f(\epsilon) = \frac{1}{e^{(\epsilon-\mu)/(k_B T)} + 1} \quad (5.10)$$

The formula describes the probability f for occupied states in as a function of the energy of the single particle state ϵ , the temperature T and the total chemical potential μ . The chemical potential μ is linked to the measurable photoelectric work function: In absence of an outer electric potential (compare figure 5.15) and without thermal broadening they are identical. The broadness of the smear effect can be estimated via $kT = 25$ meV at room temperature (20 °C). Furthermore, the emitted electrons have to be accelerated away from the originating surface in order to be detected and to inhibit electrons from returning to the metal. Therefore, a negative potential is applied to the metal. If this negative potential leads to a large electric field, the surface potential barrier can bent resulting in an effectively smaller work function (compare figure 5.15).

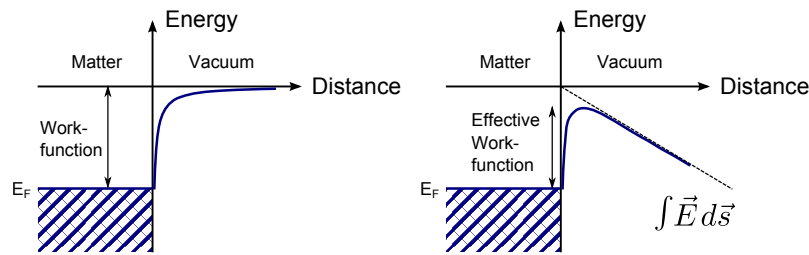


Figure 5.15.: Impact of electric fields on the effective surface work function - On the left the usual situation: To emit electrons from a metal the incoming photon needs at least the Fermi energy to lift an electron to the vacuum level. If a strong electric field is applied (on the right) the vacuum energy level and the surface potential can be modified. As a consequence, a new effective work function can be sufficient for electron emission. With increasingly stronger fields the shown potential barrier becomes narrower and the probability for electrons to tunnel through the barrier increases.

There are two possibilities to extract the work function by photo-emission when using a wavelength-selective ultraviolet (UV) light source: The wavelength of the light source can be scanned in the corresponding energy range of the expected work function. When the photon energy is sufficient, the emitted electron rate increases exponentially according to the Fowler function [82]. Fitting this function to a plot of measured electron rates over photon energy yields a value for the absolute work function. Another way to measure the work function is to measure at several wavelengths with energies well above the work function and to use electron spectroscopy to measure their kinetic energy. Since the kinetic energy of photoelectrons is linked to the photon surplus energy, it is possible to extrapolate the work function by equalizing to zero surplus energy. Both of these measurement methods are implemented for this Rear Wall qualification step. For the latter method the KATRIN monitor spectrometer⁷ was used as high-resolution electron spectrometer. Details of the measurement setup are given in the following section 5.3.1. This measurement is the only qualification step that can provide absolute values of the work function of a Rear Wall candidate sample. Unlike the Kelvin probe and its probe tip there exists no averaging involved, as the photoelectric emission can occur from any microscopic crystalline surface area with a sufficiently small work function. At the same moment the measurement is macroscopic because the emission can happen on the whole surface which is illuminated by the UV light spot. The analysis will try to extract maximum information about the WF distribution broadness in the illuminated area.

5.3.1. Measurement setup

The optical system to emit photoelectrons from different RW samples has been developed and implemented at the University of Mainz. On the one hand it consists of a sample holder which is also a high voltage cathode for electron acceleration and on the other hand of the UV light source. The Rear Wall prototype holder is installed in-vacuum and mounted on top of a flange using threaded rods. When mounting parts of the UHV-compatible plastic PEEK, the Rear Wall holder and cathode from the backside flange will be insulated by more than 10 kV. The connection to a HV source can be realized by connecting a KAPTON insulated wire to the cathode. The cathode features a two-part design where 2-inch or 3-inch samples can be installed and clamped in between. The clamping is done by the PEEK threaded rod and a PEEK nut. The front part of the cathode follows the shape for electro-optical focusing of the electron beam (“pierce electrode”). The pierce electrode idea has been developed and implemented at University of Mainz [131]. All cathode parts

⁷This MAC-E-Filter is the former spectrometer of the Mainz neutrino mass experiment which has been refurbished at KIT.



Figure 5.16.: Picture of the pierce electrode installed on a flange - The picture shows the special shape of the pierce electrode as well as an inserted and electrically contacted gold sample. The orange-brown sheet is a KAPTON-foil in order to protect the lower grounded parts of the construction from the high voltage cathode.

are made of stainless steel but parts of its surfaces are platinized. By this, systematic backgrounds in the work function measurement are minimized. This follows from the fact that stainless steel has a smaller work function than gold, which could lead to electrons being emitted from the steel surface instead from the RW sample, resulting in an incorrect work function measurement. On the other hand, platinum has a higher work function and thus should lead to a minor background during the measurements [132]. The pierce shaped cathode with an installed sample is shown in picture 5.16.

The light source for the photoelectric measurements is based on an UV deuterium lamp. The light of the lamp is focused into an optical prism spectrometer by a 5 cm focus lens. At the optical spectrometer the passing wavelength value and distribution broadness can be selected manually. Two further lenses re-focus the filtered light that has passed the spectrometer and apply a long distance focus. The light is then reflected back by a mirror with positional fine-adjustment into the vacuum chamber and onto the Rear Wall sample surface. The resulting optical power of this setup, including the UV-light compatible window to the vacuum system, has been calibrated at Mainz. Thereby the optical power was measured in dependence of the selected frequency. The results of the UV light source calibration are discussed in appendix B. The calibration is applied in all analyses described in the following sections. The optical setup of the fully assembled photoelectric emission system is visualized in schema 5.17.

All photo-emission measurements were conducted in the hall of the monitor spectrometer. Picture 5.18 shows the overall setup in the hall. The normally used calibration sources on

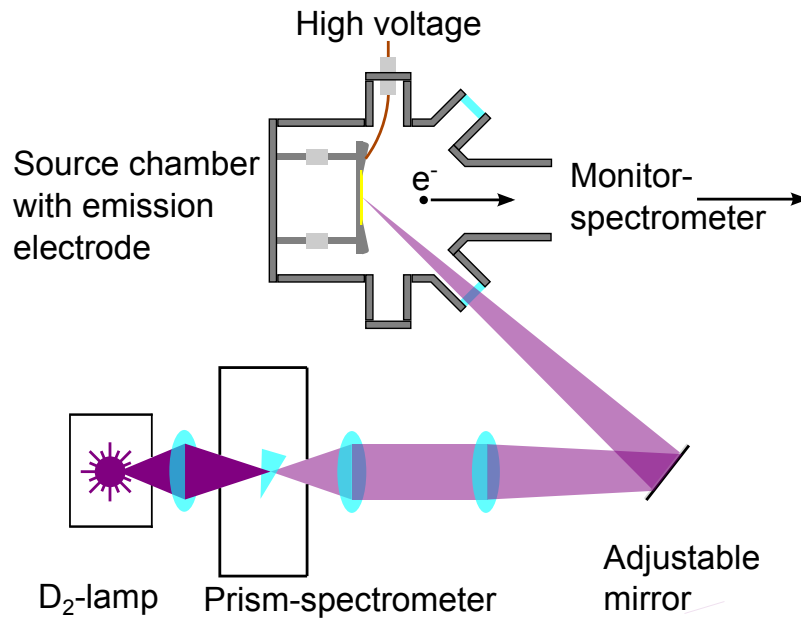


Figure 5.17.: Optical setup for the monitor spectrometer measurements - A part of the diffuse light from a deuterium lamp is focused into a prism spectrometer which filters to an adjustable wavelength. Two further lenses and a rotatable mirror steer the light beam on a long range focus through a side port window onto the electrode. In the chamber the pierce electrode is installed insulated to ground and connected to high voltage via feed-through.

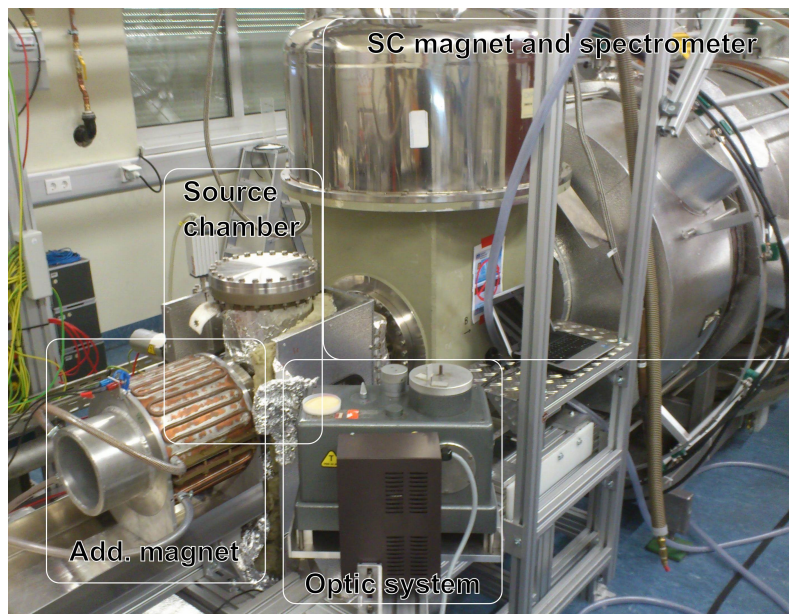


Figure 5.18.: Picture of the full measurement setup at the monitor spectrometer - The optic system is at the central front with the prism spectrometer and the deuterium lamp. On the left the source chamber, containing the gold sample and the cathode, is located. The magnet in front of the chamber was used to test if a stronger and more homogeneous magnetic field improves the electron transport. The spectrometer and one of the corresponding superconducting magnets can be seen in the center and in the back of the image.

the left are replaced by the photoelectric emission system. In the center the spectrometer is used as sharp electrostatic filter. It can also be set to a pass-through mode when its filter potential is set below the acceleration potential of the photo-emission cathode. At the downstream end a silicon detector measures and counts the transmitted electrons. As the detection efficiency drops significantly for small electron energies (< 8 keV) [133],

the applied cathode potential and the filter potential have been selected to approximately 10 kV. The flange with the Rear Wall sample holder is installed at the very end of the source vacuum chamber. The high voltage and the UV light are coupled into the vacuum system by a CF40 side flange available at the source chamber. Analogous to the other KATRIN MAC-E-filter superconducting magnets at the ends of the spectrometer generate high field regions while in the center of the spectrometer there is a fine-formed low magnetic field region. Combined with the large negative potentials on the spectrometer and the cathode, a Penning trap for electrons is created. To avoid continuous filling of the trap with electrons and subsequent discharges a wire sweeper is installed in the flux tube between cathode and spectrometer. This sweeper consists mainly of a grounded wire installed in a ring which is clamped into the vacuum tube. Due to the cyclotron motion and drifts of the trapped electrons their lifetime in the Penning trap is reduced significantly. By performing a dedicated magnetic field measurement at the sample holder position it was ensured that all samples are placed in a range of sufficiently strong and symmetric magnetic field. Another normally conducting magnet was placed upstream of the source chamber to increase the magnetic field parallelism at the cathode position. However first tests showed no significant difference in the measured emission rates depending on the magnet running state. The monitor spectrometer infrastructure allows baking out of the vacuum chambers. This feature will be used to perform test bake-out some of the samples. Another test is targeted to verify the β -radiation hardness of the Rear Wall samples: A high luminosity xenon lamp emits high currents from a stainless steel plate which again accelerates these electrons by 10 keV on to the sample. After irradiation of the sample, the absolute work function is measured again. It was not possible to include all tests for each available sample because the measurement time at an essential KATRIN component is limited. The tests were scheduled for 4 weeks of measurement time and were finally extended to 5 weeks.

The following samples were available for the measurements of this thesis:

- **Gold galvanized on copper:** This sample was provided by the university of Mainz, consisting of polished and electro-polished copper, which was galvanized with gold. The sample was tested as first type of backup solution after the good work function performance in measurements at Mainz and the *a*SPECT experiment [122].
- **Gold grown on corundum:** Two of the available samples of gold/corundum already described in section 5.2.3 were measured.
- **Gold evaporated on silicon:** One of the gold/silicon samples described in section 5.2.3 now including stress tests like illumination and bake out.
- **Platinum:** By removing the gold sample from its holder a surface of platinized steel is revealed. This surface is measured as cross-check to the gold surfaces.

5.3.2. Measurements using a photo-spectroscopic filter

For the work function measurements based only on the wavelength-dependent emission rate the filter spectrometer is “deactivated”. The MAC-E-filter is set to a pass-through mode by setting its electrostatic voltage to $U_{MS} \approx -9.98$ kV while the cathode acceleration potential is set to $U_C \approx -10$ kV $< U_{MS}$. The wavelength of the light incident onto the Rear Wall sample is modified in its wavelength by a prism-based monochromator. For each tested sample the filter wavelength was scanned in the range 210-320 nm or within a subrange of it. The scan steps were in most cases $\Delta\lambda = 5$ nm, but adaptively finer measurements were done using 2 nm or 2.5 nm scan steps. The broadness of the wavelength distribution is determined by the prism spectrometer’s slit size that can be manually adjusted in the value range 2-90. These arbitrary values are linked to the wavelength distribution broadness by

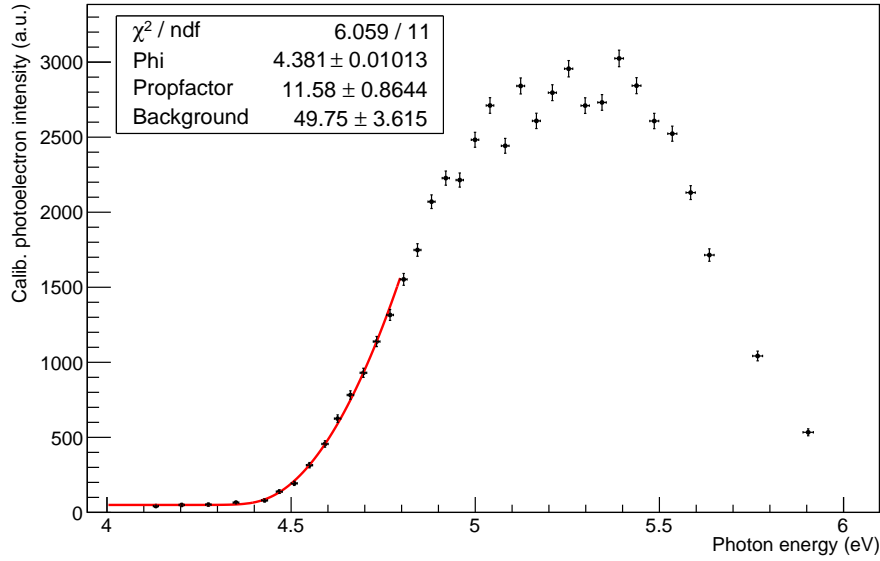


Figure 5.19.: Wavelength scan of the gold galvanized copper sample - The photon energy is varied between 4.1 eV and 5.9 eV. The measured electron rate is calibrated with the wavelength dependent UV-light measurements. The successful fit of the simplified Fowler function provides the parameters work function “Phi”, the “Background” at too small photon energies and a proportional factor “Propfactor”.

a formula defined in the manual of the monochromator. The first measurement searches for the start of electron emission at wavelengths of about 230 nm. This value was chosen because of literature-based values [132] stating a work function of 5.31 V for Au(111), 5.37 V for Au(110) and 5.47 V for Au(100) respectively. Other literature sources measured work functions for amorphous or polycrystalline gold in the range from 4.8 V to 5.5 V [134, 132]

The first measurements showed, already without detailed analysis, that the work function must be significantly lower. The emission rate already increases in relative long the wavelength range of 280 nm to 300 nm. This corresponds to a possible work function range of 4.43 V to 4.13 V. An example of such a wavelength scan is given in figure 5.19. The spectrum shows a Gaussian-like peak at about 250 nm with the emission rate dropping both towards larger and smaller wavelengths. The overall shape of the spectrum is discussed at the end of this section. For the evaluation of the work function only the increase of the rate at small photon energies is relevant. In this range the work function can be determined as the rate develops linearly with the quantum efficiency. The measurement data is therefore fitted to a derivative of the Fowler function as described in [82].

$$A \cdot (\pi^2/6 + 0.5\mu^2 - (e^{-\mu} - e^{-2\mu}/4 + e^{-3\mu}/9)) + C \text{ for } \mu > 0 \quad (5.11)$$

$$A \cdot (e^{\mu} - e^{2\mu}/4 + e^{3\mu}/9) + C \text{ for } \mu \leq 0 \quad (5.12)$$

with the proportional constant A , the background variable C and $\mu = e(E_{\gamma} - E_{\text{WF}})/(k_B T)$ given by the photon energy E_{γ} , the work function E_{WF} , the Boltzmann constant k_B and the temperature T . The fits have been conducted with a ROOT script using the Fowler function. A wavelength-dependent optical power calibration is included with interpolation in ranges where no calibration data are available. The measurement data is cut to the region-of-interest (ROI) at the long wavelength end of the spectrum. Before the start of the fitting routine, the wavelength is transformed to the corresponding photon energy.

The Fowler function has been fitted to all measurement runs with full wavelength scan. The result of the analysis of all samples including the measurement conditions, the work

Table 5.1.: Photo-spectroscopic work function evaluation - The table includes all measured samples with their treatment. Partially measurements have been repeated to check the reproducibility. In this case the measurement number is counted up. In most cases a fit of the Fowler function was successfully applied. The different samples show a wide spread of their work functions with an average at about 4.3 V. Obvious deviations are the baked silicon sample which dropped in work function compared to the unbaked measurement and the pure platinum measurements which reveals a slightly higher work function than gold.

Sample	Treatment	Slit size	Measurement no.	WF (V)	σ_{WF} (V)	Fit converged
Au galv on AgCu		5	0	4.3764	0.0139	1
Au galv on AgCu		5	1	4.3808	0.0101	1
Au on Al ₂ O ₃ II		5	0	4.4254	0.0091	1
Au on Al ₂ O ₃ II		5	1	4.3986	0.0074	1
Au on Al ₂ O ₃ II	baked	5	0	4.3766	0.0086	1
Au on Al ₂ O ₃ II	baked	5	1	4.4386	0.0110	1
Au on Al ₂ O ₃ IV		5	0	4.5138	0.0082	1
Au on Al ₂ O ₃ IV		5	1	4.2569	0.0062	1
Au on Al ₂ O ₃ IV		5	2	4.2390	0.0106	1
Au on Al ₂ O ₃ IV		5	3	4.3192	0.0222	1
Au on Al ₂ O ₃ IV		5	4	-	-	0
Au on Al ₂ O ₃ IV	illuminated	5	0	4.3363	0.0084	1
Au on SiO ₂ -Si	illuminated	5	0	4.3723	0.0061	1
Au on SiO ₂ -Si	baked	5	0	3.9287	0.0074	1
Au on SiO ₂ -Si	baked	5	1	-	-	0
Au on SiO ₂ -Si	baked	5	2	4.0089	0.0035	1
Au on SiO ₂ -Si	baked	3	3	4.0285	0.0089	1
Pure Pt		5	0	4.4380	0.0049	1
Pure Pt		5	1	4.4281	0.0005	0
Pure Pt		5	2	4.4245	0.0093	1

function and the corresponding error are listed in table 5.1. All samples reveal a work function which is well below previously published literature values. Most common are observed work function values in the range 4.3-4.4 V. Also the measured pure platinum sample with an average work function of 4.430 ± 0.006 V is, although slightly higher than the gold function, significantly below the literature values (5.64 V for polycrystalline platinum [132]). But there is an important difference between the literature values and the experimental results obtained here: Both are measured in UHV conditions but the reference values measure the work function directly after the gold is grown inside the vacuum system. Only when surfaces are grown and measured directly in this ultra-clean setup, these high work functions of the elementary metals can be measured. In our case all the samples have been transported and stored at ambient air which is the likely cause of the difference in work function. Yet, gold and platinum are noble elements and thus do not chemically react with ambient air at standard conditions. However, there is still the possibility of physisorption. A very likely candidate for degradation by physisorption are the water molecules condensed from the air humidity. Several sources ([135, 136]) confirm the work function degradation down to 4.2 V of gold at ambient air. Since this work function drop is nonrecurring and remains stable at this value the effect is not a show-stopper for the Rear Wall development. On the contrary the RW will always be exposed to ambient air before the installation, therefore the reliability of this “degradation” effect has to be ensured.

The measurement counts for each single sample is low due to the limited time available for each sample. In repeated measurements only pure platinum, the gold galvanized on copper and the unmodified gold on corundum II samples show a short-term reproducibility of $\sigma_{WF} < 20$ mV. The other gold on corundum sample and the gold on silicon sample exceed this minimum requirement. After these results, it is important to have a closer look at the effect of irradiation and bake out. The e-irradiation from the high intensity WGTS was emulated by a high luminosity xenon lamp emitting a beam of electrons from a stainless steel surface. By a drop of the electric potential of 10 kV towards the Rear Wall sample the electrons are accelerated above the average kinetic energy of tritium β -electrons. The total incident radiation is monitored with an ammeter to target for a total count of incident electrons that exceed a KATRIN run time of 5 years. The irradiated gold on corundum IV sample shows no significant degradation. Its work function of 4.336 ± 0.008 V is very similar to the average work function of all previous gold on corundum IV (4.332 ± 0.109 V). Also the irradiated gold on silicon sample with a work function of 4.372 ± 0.006 V, shows no significant change to previous measured values of gold surfaces. After these test results, radiation damage by low energy electrons on thin gold coatings is not expected to occur during the KATRIN run time. Still, this test needs to be repeated for the final Rear Wall.

Concerning bake-out effects, the measurements with gold on corundum II before and after bake-out show only a minor deviation of the mean work functions by 5 mV. On the other hand, the gold/silicon sample shows a remarkable shift in the work function by more than 300 mV down to an average of (3.99 ± 0.04) V. After the removal of the sample from the vacuum system, it also revealed a visible color change from gold to orange-gold. The compound on the surface is changed by bake out which clearly could be detected by the photo-emission analysis. The first suspicion was the multilayer front surface and that the gold was contaminated by silicon or titanium resulting in a compound. When discussing this issue with the manufacturer at UCSB, it was suspected the titanium adhesion layer of the sample has likely drifted into the gold at higher temperatures ([111, 137]). During the measurement operations one gold on corundum sample showed another undesirable effect: Slight mechanical friction could lead to abrasion of the gold from the surface. The fragile surface was not able to touch by a clean room tissue nor the force by a tape test. This makes the usability of this Rear Wall prototype at least questionable. The lack of an adhesion layer at these prototypes resulted in a very fragile surface.

The results of the wavelength scans will be summarized and compared to the measurements with the MAC-E-filter (section 5.3.3) in section 5.3.4. Concerning the shape of the emission rate as function of the photon energy, the peak and the subsequent drop was unexpected. The quantum efficiency of the photo-effect does not explain such a drop at higher energies within a metal. This effect is caused by a combination of multiple other effects: At first the optical reflection at the gold surface increases with shorter wavelengths [138]. Then the quantum efficiency can not continue to increase exponentially because the density of states and the surface density of states are limited and there are also gaps in certain energy ranges [128]. As a consequence the increase of excitable electrons in dependence of the photon energy is capped in some energy ranges. Finally, the excited electrons have a higher kinetic energy in the solid which results in significantly larger cross-sections for de-exciting reactions [81]. These effects and the resulting peak close to the metals work function are well understood and described in more detail in [139, 140] or [141, 142, 143]. Still, the full shape was not fitted by a regression function to find the work function because a full shape analysis would introduce more unknown parameters in the fit. As a result, the uncertainty on the work function fit parameter itself increases compared to a fit with the Fowler function.

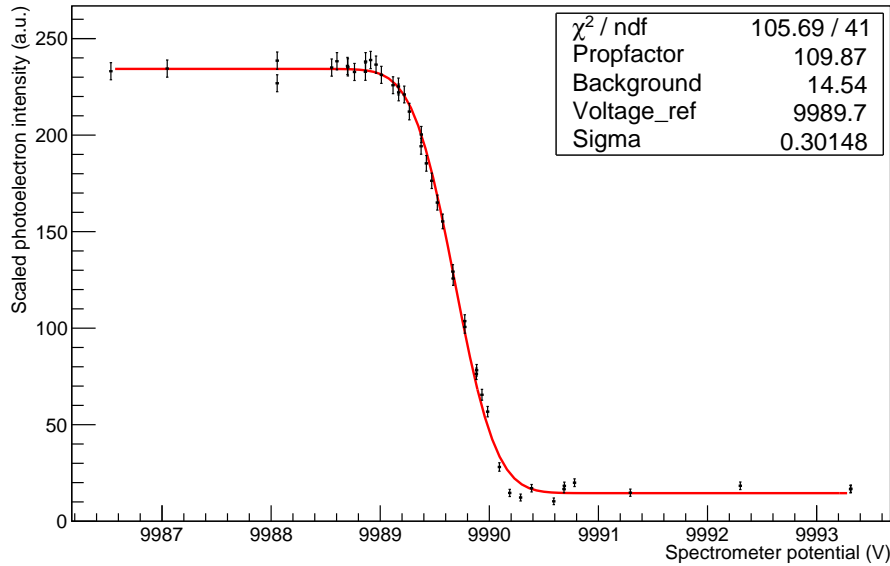


Figure 5.20.: Fit of a complementary error function to a monitor spectrometer voltage scan - The data has been generated with the illuminated gold on silicon sample and a light source wavelength at 220 nm. The only fit parameter that is further used in the evaluation is the step broadness “Sigma”. The parameters “Background”, the step turning point “Voltage_ref” and the proportional constant “Propfactor” do not provide further information.

5.3.3. Measurements with an electrostatic filter

A concurrent measurement of the work function has been tested using the monitor spectrometer. At several configured wavelengths of the UV light the energy spectrum of the emitted electrons was measured. The integrating MAC-E-filter has a transmission function analogous to the main spectrometer [42]. Since the photoelectric source provides mono-energetic electrons with a finite uncertainty in the energy distribution, a scan with the spectrometer potential delivers a simple response function: If the retarding potential is sufficiently small all electrons are transmitted, if the retarding potential is high enough all electrons become reflected. In the retarding potential area in between the electrons *can* be transmitted depending on the electron and spectrometer properties: It requires the electron’s kinetic energy projected on the magnetic field to always exceed the local spectrometer retarding potential. The broadness of this area is caused by the variance in the electron properties (e.g. kinetic energy, polar angle towards the magnetic field line) and the spectrometer properties (e.g. local potential variations). Depending on the UV-light energy compared to the work function the emitted electrons can gain surplus energy as initial kinetic energy. This broadness of the initial energy distribution is then reflected in the broadness of the partial transmission region of the response function. When the response function with the same Rear Wall sample is measured with different UV-light wavelengths, the transmission broadness can be used to determine the work function of the sample.

The electrostatic filter scans have been carried out alternating with the wavelength scan method. At least one scan was made for each sample, and after each special treatment of a sample, like bake out or irradiation. The filter scan method is more time-consuming than a scan of different wavelengths. For every configured wavelength the filter scans measure at up to 150 voltages. At each single voltage a detector integration time of 10-300s was configured to gain enough events to reduce the statistic error. The scan voltages including finer and coarser steps and detector integration times had to be adjusted and optimized for each voltage scan. As a result the filter scans were only conducted at a few wavelengths for

each sample rather than in 5 nm steps like at the wavelength scans. An example voltage scan showing the relative rate at the detector in dependence of the filter voltage is given in figure 5.20. In order to extract the electron surplus energy in dependence of the wavelength the broadness of the transmission area must be quantified. With the assumption that all error sources lead to a Gaussian error distribution with uncertainty σ the response function of an MAC-E-filter equals the error function. All the filter scans are therefore fitted in a custom ROOT program with the following complementary error function:

$$A \cdot \operatorname{Erfc} \left(\frac{x - \bar{U}}{\sqrt{2}\sigma} \right) + C \quad (5.13)$$

The complementary error function reaches its half height at the central transmission voltage \bar{U} and has a broadness caused by the error σ . The parameter A is a proportional constant for the fit of different emission rates and the parameter C takes varying backgrounds into account.

These fits deliver the change of the transmission broadness for each sample as a function of the incident light wavelength. As expected the transmission broadness is reduced with the emitting photon energy. But the initial electron energy by photo-emission is not the only cause for the transmission broadening. The first possible cause to mention is the inherent energy resolution of the monitor spectrometer of $\Delta E = 1.1$ eV [42]. The energy resolution of the MAC-E-filter is given by the limitations inherent to the magnetic collimation of the isotropically starting electrons. For this reason the spectrometer resolution should have a negligible influence on the transmission broadness because the electrons accelerated by the pierce shaped cathode are mainly parallel to the magnetic field lines. In this case there should be no broadening by remaining transversal energy. Another source of systematic error is the radial potential variation within the spectrometer which is known to be about 200 meV [42]. But also this error does not apply during the given measurements because the photoelectric electrons only use a very small flux tube of the spectrometer. With a flux tube disc diameter of approximately 10 cm the potential variation in the analysis plane is more than an order of magnitude smaller compared to normal operation. Finally, fluctuations from the high voltage power supplies will inevitably introduce a systematic error during the measurement. The HV was connected to the KATRIN high precision voltage divider [144] which enabled a precise measurement of the filter voltage and a detection of slow drifts. Also the precision of the cathode power supply is limited. An error of $\sigma_V = 10$ mV is assumed for the data analysis. These optimistic values were necessary for the fit algorithm to converge properly. The short measurement time for each single point of a few minutes maximum may justify the assumption of a small voltage variation.

Now the extracted error σ within the transmission broadness can be coupled to the varied UV light wavelength. In figure 5.21 the fit values for σ are visualized for different UV light wavelength settings at the prism spectrometer. At photon energies above 4.6 eV the contribution of the surplus energy dominates the total transmission broadness leading to a linear scaling between the two analysis parameters. To quantify this dependency a linear fit $\sigma = m \cdot E_\gamma + c$ is applied starting with photon energies of 4.6 eV. Still, the extraction of the work function is not straightforward because the other contributions to the transmission broadness are not known precisely. In case that all other contributions to the transmission broadness are neglected, the gold work function equals the x-intercept $E_{\text{WF}} = -c/m$. Certainly it can be used as an indicator for the smallest work function in the irradiated area - but this value can be shifted to lower values by other causes of the transmission broadness. Another interesting value that can be extracted of the linear fit is the broadness σ at the photon energy equal to the work function from the wavelength scans. The results from the fits and the described derived values including errors for all

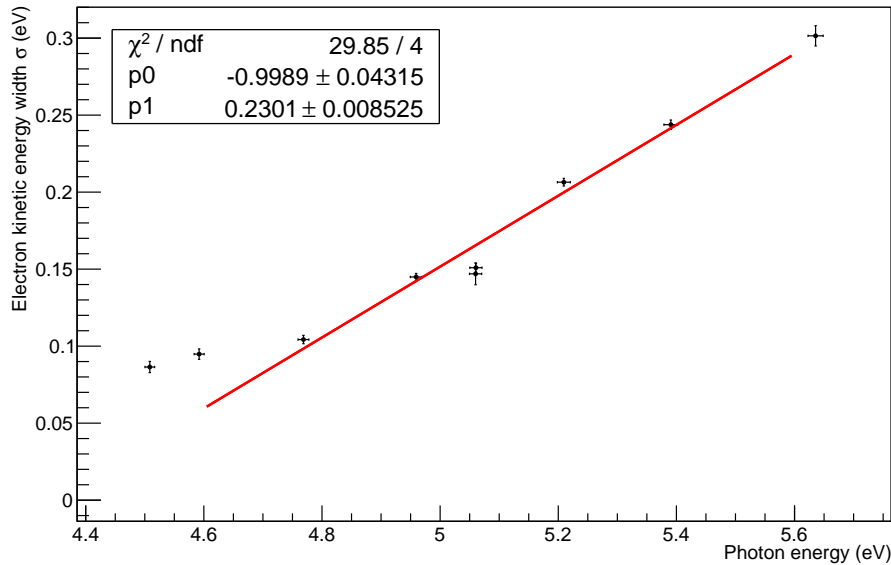


Figure 5.21.: Dependence of the photo-electron energy distribution broadness on the photon energy - Every point in the graph results from a filter scan at a certain light source wavelength with a silicon sample. The electron surplus energy after photo-emission can be measured precisely with the MAC-E-Filter. The dependence of the electron energy broadness on the photon energy shall be used to derive the materials work function.

measured samples are available in table 5.2. This analysis assumes that the photon surplus energy is the only cause for the broadening of the transmission function.

The gold galvanized on copper has a lowest work function of 4.1 ± 0.7 V according to the evaluation. This is 0.2 V below the result of the wavelength scan measurement and within the large error range. According to the linear fit the work function distribution broadness at the work function measured by wavelength scans could be up to $\sigma = 48$ mV in the irradiated area. The reliability of this result is doubtful considering the large error of $\sigma_\sigma = 170$ mV. The results of the gold on corundum sample No. II are similarly disappointing: The first measurement results in a work function of 4.02 ± 0.18 V with a difference of 400 mV to the wavelength scan measurements. As a consequence the projected transmission broadness (at the work function found by UV spectroscopy) is very large with 71 ± 34 mV. The other measurement fit is not successful at all, resulting in a negative slope of the linear fit and therefore a too large work function. Although they belong to the rare bake out measurements, the results must be discarded. With the gold on corundum sample No. IV exists a measurement before and after irradiation. Before irradiation, the measured work function of 4.4 ± 0.3 V differs by 0.12 V from the photo-spectrometric result. The transmission broadness at the work function measured with wavelength scans is $\sigma = 30 \pm 90$ mV. After radiation, the remaining work function difference between the two measurement strategies is only 40 mV. As a consequence, the projected transmission broadness is $\sigma = 9 \pm 46$ mV. The value itself therefore is within the Rear Wall specification for the work function distribution broadness. Still, the error is too large to rely on this result. For the gold on silicon sample the irradiated one fits also well to the photo-spectroscopic measurement: The work function difference to the photo-spectroscopic measurement is only 30 mV. The projected transmission function broadness is $\sigma = 7 \pm 52$ mV. Concerning this result the same findings as for the irradiated gold on corundum IV sample are valid. The other gold on silicon sample again had too blurred results for a reasonable linear fit and a negative slope leading to no reasonable data. It affected both baked out samples which can be explained by the fact that the overall signal quality after the bake out was significantly reduced. The two platinum measurements fit

Table 5.2.: MAC-E-filter measurements of photoelectrons - The table shows different samples with their treatment and the analysis results, but only when full filter scans have been made at different wavelengths and the following required analysis fits where successful. By the keys sample, treatment and measurement no. they are unique and can be compared with table 5.1. WF_{\min} is the axis intercept of the linear fit and should equal to the minimum work function of the surface. The value $\sigma@WF_{UV}$ compares with spectroscopic measurements and indicates the actual work function distribution broadness of the work function evaluated by photo-spectroscopy. Although the absolute values are realistic, the analysis reveals the large uncertainties that come with this method.

Sample	Treatment	Measurement no.	WF_{\min} (V)	Error on WF_{\min} (V)	$\sigma@WF_{UV}$	Error on $\sigma@WF_{UV}$
Au galv on AgCu		0	4.16	0.75	0.048	0.169
Au on Al ₂ O ₃ II		0	4.02	0.18	0.071	0.034
Au on Al ₂ O ₃ IV		0	4.39	0.34	0.034	0.094
Au on Al ₂ O ₃ IV	illuminated	0	4.30	0.21	0.009	0.046
Au on SiO ₂ -Si	illuminated	0	4.34	0.22	0.007	0.052
Pure Pt		0	4.26	0.21	0.034	0.040
Pure Pt		1	4.29	0.35	0.028	0.073

in the overall picture: The work function difference to the values in section 5.3.2 is 160 mV. The projected transmission function broadness is about $\sigma = 30$ mV again with errors that exceed the analyzed value itself.

The analysis reveals the mixed qualities of the filter spectrometer measurements. On the one hand this method is very good in finding the lowest work functions on the whole surface - even if the small work function only occurs locally on microscopic scales. This works because the method concentrates on the transmission function broadening instead of the emission rate. It provides an alternative way of measuring surface properties and even makes the electron surplus energy of the photo-effect seizable. On the other hand the measurement method and the required analysis are complex and time consuming. With large errors on the few measurement points and an analysis based on two consecutive fits the results have undesired large errors. A part of the deviations to the measurements described in section 5.3.2 can also be caused by unknown systematic errors during the filter spectroscopic measurements. For example the minimum work function difference between both methods is about 30 mV which could be partially or fully explained by systematic potential drifts during the filter scans. Still, this concurrent measurement method remains an interesting method when the final sample is measured. Such a measurement requires more time on each individual filter voltage, a finer voltage scan and measurements at more different wavelengths. Furthermore, the high voltage power supplies for the spectrometer and the cathode should both be highly stable and permanently monitored to a relative precision of 1 ppm. At these conditions the work function measurements with electrostatic filter can provide more quantitatively valuable information.

5.3.4. Conclusions for qualification

The Rear Wall qualification measurements at the monitor spectrometer using the photoelectric effect provided many important results and experiences for the Rearsection devel-

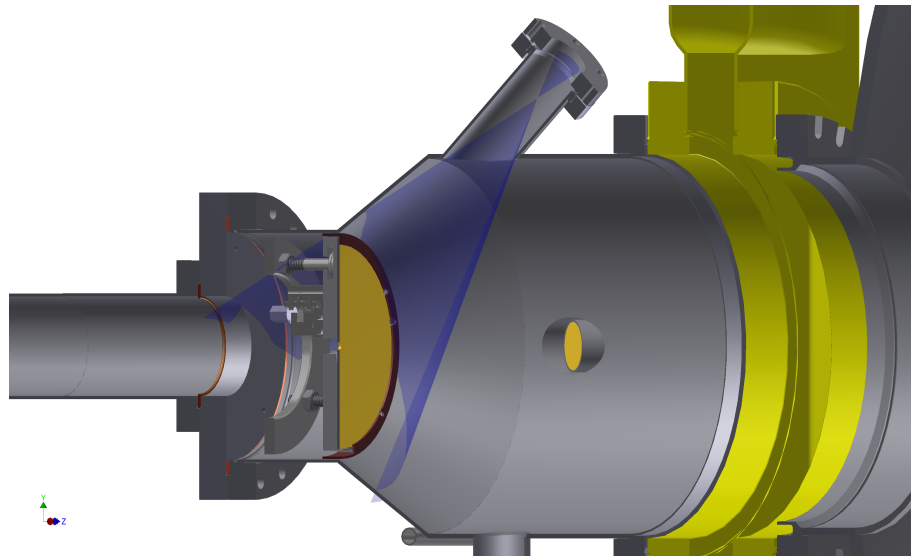


Figure 5.22.: UV light cone for Rear Wall illumination - The top port of the Rear Wall chamber has been aligned and positioned to allow a UV illumination of the full Rear Wall surface. An appropriate design has to be found with regard to several mechanical and constructive constraints. The current solution requires a UV light source starting with a diameter of 22.3 mm and a focus length of 35.5 mm at the optic flange position.

opment. Some of these results came rather by handling experiences and the stress tests instead of the quantitative results. In these measurements interesting candidates for the Rear Wall did actually fail the qualification in contrast to the Kelvin probe measurements described in section 5.2. For example the gold on corundum sample showed a weakness in the operability during the mounting/dismounting. The adhesion of the gold was too low to enable an easy handling as a later Rear Wall. This sample also failed in a consecutive tape test for the gold adhesion which was an unofficial requirement for the Rear Wall candidates. Combined with the proof that the epitaxial grown gold surface is not mono-crystalline and the work function properties are not superior to other samples the remaining arguments for corundum as substrate vanished. As a result, this substrate option was officially discarded. The gold on silicon sample made of a complex multilayer structure changed its work function measurable during the bake out. The color of the gold surface also changed in this process. Independently of the actual cause of the effect all further UCSB multilayer prototype samples will be carefully investigated on their reaction to bake out. The qualification of the silicon substrate sample with the given multilayer composition had to be rejected. The measurement results led to the design and test of “baseline” Rear Walls which use common metals as substrates and simplified coating techniques. The positive result of the measurements at the monitor spectrometer was the insensitivity of the work function to the electron irradiation tests. Both irradiated samples remained in the range of typical measured absolute work functions.

The results of the photoelectric measurements are also of importance for the electron gun design. Like at the Rear Wall a work function above 5 V has been expected for the E-gun gold cathode. The UV light source for the electron gun has been designed correspondingly with special band pass filters selecting a frequency spectrum that matches to the gold work function. The measured photoelectric emission spectrum is quite independent of the gold coating technique and the substrate therefore a similar emission rate to UV wavelength relation can be expected for the E-gun gold cathode as well. Therefore, additional ultraviolet band filters were ordered for the electron gun prototyping tests in the wavelength range 280-300 nm. For the Rear Wall prototyping photo-emission tests are a useful technique for qualification. Therefore, the measurements are repeated with the next generation of

Rear Wall samples and the baseline Rear Wall samples. The focus during this qualification step are the photo-spectroscopic measurements which are more efficient compared to the MAC-E-filter measurements. All samples must be checked with stress tests, for example their reaction on a bake out procedure. In order to check the homogeneity of the samples the emission light spot can be focused on different positions on the sample additional to the unfocused illumination of the whole surface. When the samples are manufactured with a hole, like the final Rear Wall, the work function behavior in the area close to the hole can be investigated. The results of the second generation of Rear Wall qualification via the photoelectric effect will be published in [86]. The precise measurement of the work function is not only important for the plasma potential at KATRIN but it can also be a good indicator for changes of the gold surface. This shall be used for repeated checks of the KATRIN Rear Wall. The possibility for in-situ photoelectric measurements of the whole Rear Wall surface has been added to the requirements. The right optical geometry for an illumination of the total gold surface is already designed (compare figure 5.22). The light source must also use a photo-spectroscopic filter. With a small negative potential combined with the post-acceleration at the KATRIN main detector, the main detector can be used to measure the emission rates. With the main spectrometer it is also possible to carry out electrostatic filter measurements of the photoelectrons. Alternatively to the work function measurement the light port can be used with high intensity UV light to emit low energetic electrons into the WGTS plasma. This might be necessary if the plasma can not maintain its quasi-neutrality and charges positively up because the electron mobility is so much higher than the ion mobility (compare section 5.1.1).

5.4. Tritium adsorption on the Rear Wall

An important issue excluded from the previous investigations is the interaction of tritium with the Rear Wall. Besides β -electrons and low energetic electrons, there will be tritium isotopologues impinging on the Rear Wall in form of ions and neutral molecules. Of course also the impurities in the source gas like helium or methanes can hit onto the Rear Wall either as molecules or ions. There are two undesired potential effects at the Rear Wall by the gas/plasma: On the one hand adsorbed molecules or ions can change the work function of the gold and on the other hand adsorbed or absorbed tritium can cause background in the neutrino mass measurement. For example at stainless steel the work function shifts by more than 100 mV by hydrogen adsorption [145]. Such a shift, especially if it is long-term drift, would be unacceptable for the required high stability of the plasma potential. For comparison, the electrostatic stability of the main spectrometer high voltage is $\sigma < 20$ mV. Concerning the contribution to the background the impact can be quantified using the estimated density of gold surface atoms of $15.2/\text{nm}^2$ ⁸. Further it is assumed that each of these surface sites can be occupied with one tritium atom. The total number of tritium gas molecules in the inner flux tube of the WGTS of $5.3 \cdot 10^{19}$ is a factor of 247 higher than one surface monolayer on the gold. Therefore, the background contribution of a Rear Wall covered with one monolayer of tritium equals up to 0.4% of the spectrum. The real impact of electrons emitted from the Rear Wall surface is reduced compared to an average WGTS electron because of the increased scattering probability. For example an electron starting in the center of the WGTS has a 33.8% chance to pass the source without inelastic scattering while for an electron starting at the rear side of the WGTS the chance is only 15.3% [50]. On the other hand the activity from the Rear Wall can further increase by absorption of multiple monolayer-equivalents in the bulk material. Still, the effect is limited: Only decays starting in a gold depth of the order of 10 nm have a chance to leave the gold without inelastic scattering. The following section 5.4.1

⁸This number was estimated with the gold density. The exact number of surface atoms depends on the crystal orientation and can hardly be given exactly for amorphous or polycrystalline gold.

summarizes the theory of tritium adsorption on gold and tries to quantify the effect for the Rear Wall. Section 5.4.2 describes an experiment with the goal to measure the tritium adsorption/absorption on gold.

5.4.1. Theory of tritium adsorption on gold

A good theoretical understanding of the adsorption processes at the Rear Wall can help to understand the severity of the problem by tritium adsorption. Since the specific adsorption process of tritium and gold lacks published data also sources reporting about similar effects like hydrogen/gold adsorption are used to understand the underlying processes. Whenever adsorption occurs there is also a finite chance for the reverse process namely the desorption of the adsorbate. Under stable conditions the two offsets will end up in an equilibrium where both processes occur at the same rate. A molecule of hydrogen isotopologues is non-polar and has no chemical interaction with pure gold. Therefore, in molecular form it can only bind to a gold surface via the physical van der Waals force (physisorption). Thermal desorption experiments showed that this kind of adsorption only works up to a temperature 15 K. Above this temperature molecular hydrogen desorbs completely from the gold surface [146].

Since the Rear Wall is operated at room temperature, the focus turns to chemisorption processes at the Rear Wall. Chemisorption requires some kind of chemical binding between adsorbate and the surface (adsorbent). Either covalent bonding, ionic bonding, metallic bonding or a mixture of these options can cause chemisorption. None of these chemical bindings arises by the interaction of molecules based on tritium isotopologues. But atomic hydrogen isotopologues can establish covalent bondings to a gold surface which are much more stable than physisorption. Thermal desorption experiments measured a peak of desorption rate at temperatures of 125 K [146]. Atomic hydrogen is a radical which can not exist in gaseous form for a long time. As most radicals it binds to nearly any other atom, molecule or surface it collides with. Experiments to measure the adsorption of radical atoms must dissociate them by radiation (e.g. photons with a kinetic energy that exceeds the molecular binding energy). In the KATRIN source plasma these radicals can be created in large numbers just like ions caused by β -decays and ionization [3]. Among these ions are Q^- , Q^+ and Q_3^+ (Q can be any of the isotopes H, D and T). Ions moving to the back side of the WGTS are automatically targeting for the Rear Wall surface because they are magnetically guided. At the grounded Rear Wall the ion can be neutralized by the metallic surface accepting or donating superfluous/missing electron charges. In the case of Q^-/Q^+ impinging on the Rear Wall the neutral ad-atom becomes automatically bonded to the surface since it can not desorb as radical. Molecules like Q_3^+ can not remain neutrally on the surface therefore a fragmentation into a bound ad-atom and a Q_2 molecule is expected. This oxidizing behavior makes tritium plasma acting similar to an acid besides the primary effects of the beta-decay. Overall a significant stream of radicals and similar-reacting ions will be impinging the Rear Wall surface. Therefore, the relevant processes of chemisorption will be described in detail. Very important for the quantification is the surface coverage Θ depending on the number of adsorbed ad-atoms N_{ad} and the total number of available surface sites N_{sites} :

$$\Theta = \frac{N_{ad}}{N_{sites}} \quad (5.14)$$

With the described adsorption properties of tritium and gold follows directly, that the surface coverage can not exceed one monolayer, $\Theta \leq 1$. For $\Theta > 1$ it is necessary that further layers of the adsorbing material can bind to the adsorbate itself. Otherwise, the incoming gas radical or ion would recombine with the ad-atom and desorb as Q_2 molecule.

Therefore, the resulting increase of adsorbed atoms scales with the number of free surface sites $(1 - \Theta)$, the incoming radical/ion stream j_Q and the sticking probability S as proportional factor [147]:

$$\frac{dN_{\text{ad}}}{dt} = S \cdot j_Q \cdot (1 - \Theta) \quad (5.15)$$

The surface occupation is the variable in the dynamic process. The incoming stream is estimated by rate of the generation of secondary electrons and ions in the source of $j_Q = 10^{12}$ 1/s and the sticking coefficient on the gold surface is assumed to be 100 %. Both estimates are chosen conservative or even pessimistic in order to find the theoretical maximum of tritium adsorption on the Rear Wall surface. To find the surface occupation in equilibrium it is also necessary to consider the desorption effects. One of these effects is the already mentioned recombination of surface adsorbed states with new incoming particles. This mechanism is also known as Eley-Ridael mechanism and it scales with the incoming stream j_Q and the current surface occupation Θ [147]:

$$\frac{dN_{\text{ER}}}{dt} = -\gamma \cdot j_Q \cdot \Theta \quad (5.16)$$

The Eley-Ridael recombination weighting factor used is $\gamma = 0.03$ as found in [148] for hydrogen recombination on metal surfaces. An alternative desorption mechanism is via the recombination and subsequent desorption of two adsorbed atoms. This mechanism is known as Langmuir-Hinshelwood desorption and scales with the temperature dependent mobility of the ad-atoms and the quadratic surface coverage as a 2 particle process [149]:

$$\frac{dN_{\text{LH}}}{dt} = -\nu \cdot \Theta^2 \cdot e^{-\frac{E_{\text{ad}}}{k_b T}} \quad (5.17)$$

Here again a scaling factor as indicator for the recombination speed is required and given by ν . In theoretic calculations the value is given by $\nu = kT/h = 6.1 \cdot 10^{13}$ /s while experiments measure the value with large errors due to dependencies to other measurement variables [150]. In the following the value $\nu = 10^{13}$ /s is used being aware that the error on this value might be one order of magnitude. The temperature dependence comes by the exponent $E_{\text{ad}}/k_b T$ which uses the relation of the adsorption energy (the energy amount created in the adsorption process and necessary for desorption) to the thermal energy on the surface. A value of $E_{\text{ad}}/k_b T = 0.57$ eV is used which was the result of thermal desorption measurements with atomic hydrogen and gold [151]. These three mechanisms describe the main adsorption and desorption reactions at the interface of the surface to the gas. Now it is possible to find the expected surface coverage when the system reaches its equilibrium.

$$\frac{dN_{\text{total}}}{dt} = \frac{dN_{\text{ad}}}{dt} + \frac{dN_{\text{ER}}}{dt} + \frac{dN_{\text{LH}}}{dt} \equiv 0 \quad (5.18)$$

This can be easily resolved to the equilibrium surface coverage

$$\Theta_{\text{eq}} = -\frac{\alpha}{2}(\gamma + S) + \sqrt{\left(-\frac{\alpha}{2}(\gamma + S)\right)^2 + \alpha S} \quad \text{with} \quad \alpha = \frac{j_Q}{\nu N_{\text{sites}}} e^{-\frac{E_{\text{ad}}}{k_b T}} \quad (5.19)$$

With the given values at the Rear Wall environment and a gold surface size of 141 cm² equal to $2.14 \cdot 10^{17}$ surface sites, the equilibrium surface coverage is $\Theta = 6.83 \cdot 10^{-5}$. This means the theoretically expected surface coverage is extremely low and equals only 0.05 % of a monolayer. At this low coverage the Eley-Ridael mechanism is only a minor contribution to the desorption. Mainly all desorption happens with the Langmuir-Hinshelwood mechanism due to the high recombination speed at room temperature. This result expresses the qualities of the noble metal gold allowing only a low coverage because of the small adsorption energy for atomic hydrogen and rejection of molecular hydrogen at room

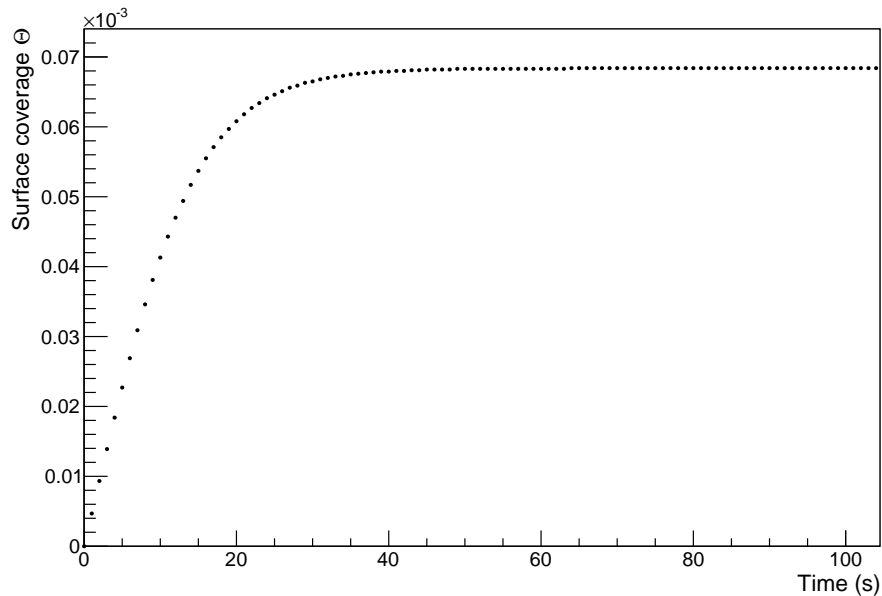


Figure 5.23.: Theoretical initial adsorption process - Time dependent adsorption from zero to equilibrium surface coverage. This result is received when the differential equations are numerically solved. On the time scale of one minute the equilibrium is reached with a very small surface coverage. But the used parameters have been determined for ultra-clean grown gold surfaces and might not apply to other gold surfaces.

temperature. The differential equations are also numerically expanded with different surface coverages as starting conditions. The chart 5.23 shows the adsorption progress on an uncovered gold surface - equivalent to the Rear Wall getting in contact with the tritium plasma for the first time. The result is a bounded function which steadily approaches the equilibrium value. The time to reach the equilibrium value is about 60s. Therefore, the adsorption is not a long term effect which causes a systematic error at KATRIN during the growth of the adsorbed layer. Similarly, the desorption process has been calculated starting from the equilibrium coverage with the incoming stream j_Q reduced to zero. The result is given in the plot 5.24. The time necessary for desorption to the stable, uncovered status is about 500s - nearly an order of magnitude higher than for the initial adsorption. Still, the time scale is negligible compared to normal KATRIN operation run times (measurement phases of 60 days are planned [3]).

After this theoretic quantitative analysis the Rear Wall seems to be a rather efficient recombination surface for ad-atoms than actually endangered by large amounts of adsorbed tritium. If the very small calculated equilibrium coverage would be true the impact on the KATRIN background or the work function can be neglected. The work function is unaffected because the small amount of randomly distributed ad-atoms can not lead to a consistent polarization layer. Plasma effects and cyclotron motion average across the surface making small amounts of ad-atoms irrelevant. The previous considerations excluded the subsequent absorption into the bulk material after the adsorption process. But tritium absorbing into the solid gold is very likely when considering the energy barriers for absorption. The energy levels for different processes concerning hydrogen and gold are visualized in figure 5.25. The necessary energy for an ad-atom to dissolve in the solid is < 0.21 eV which is significantly less than the associative desorption energy (0.59 eV). The absorbed atoms have a reduced influence on the work function of the surface because they are shielded by the overlaying gold layers [127]. But absorbed tritium can still contribute to the background. At least in the first few nanometers of the gold a β -decay electron may leave the gold without inelastic interactions. Absorption effects are not further analyzed

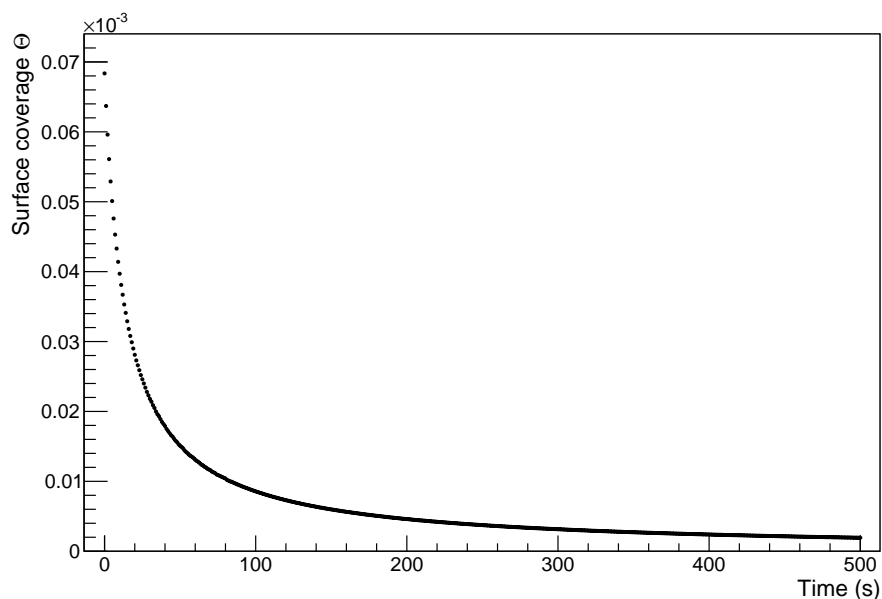


Figure 5.24.: Theoretical desorption process - This graph has also been calculated numerically with the differential equations. To simulate desorption the starting coverage is set to the equilibrium value and the incoming particle stream to zero. The desorption process only approaches the zero coverage value on the time scale of minutes.

quantitatively because the processes become extremely complex: Every atomic layer of the gold may occupy tritium atoms which have a temperature dependent probability to change into another layer. They might penetrate deeper into the gold or return to the surface. After returning to the surface the ad-atom can again either desorb by one of the recombination mechanisms or dissolve in the bulk again. Besides the neglect of absorption effects most of the theoretical analysis relies on hydrogen and gold reactions. They are missing all tritium specific features like the different nucleus mass and the radiochemistry. The environment conditions are different too: The gold in the adsorption measurement is carefully prepared and in-vacuum annealed which can not be ensured at the Rear Wall later on. Furthermore, radiochemical reactions of tritium can lead to hydrocarbons with a significantly increased sticking probability to surfaces even as neutral molecules. Overall the large number of uncertainties concerning the effects at the interface gold surface-low pressure tritium gas required a dedicated test experiment. The experiment conducted to find an estimate or an upper limit for adsorption and absorption effects with tritium and gold are described in the following section 5.4.2.

5.4.2. Test for tritium adsorption using a quartz crystal microbalance

Before the start of the so called “TriQuartz” experiment many methods to measure the amount of gas adsorption and absorption have been evaluated. The most important aspect is that the measurement method should be as model independent as possible and not be compromised by the tritium itself. Furthermore, the measurement method should be time efficient to provide fast results or estimates on the effect. With the result from this experiment the decision can be made if the process is sufficiently understood or a more precise experiment can be designed taking into account the received results. The preferred measurement method followed a recommendation [107] for a model and temperature independent working principle: A quartz crystal microbalance in the further abbreviated as QCMB. The QCMB method enables to measure changes at the crystal surface by the changes in the crystal resonance frequency. The method is a standard tool in modern coating technology to monitor the amount of atomic layers that have been deposited. In

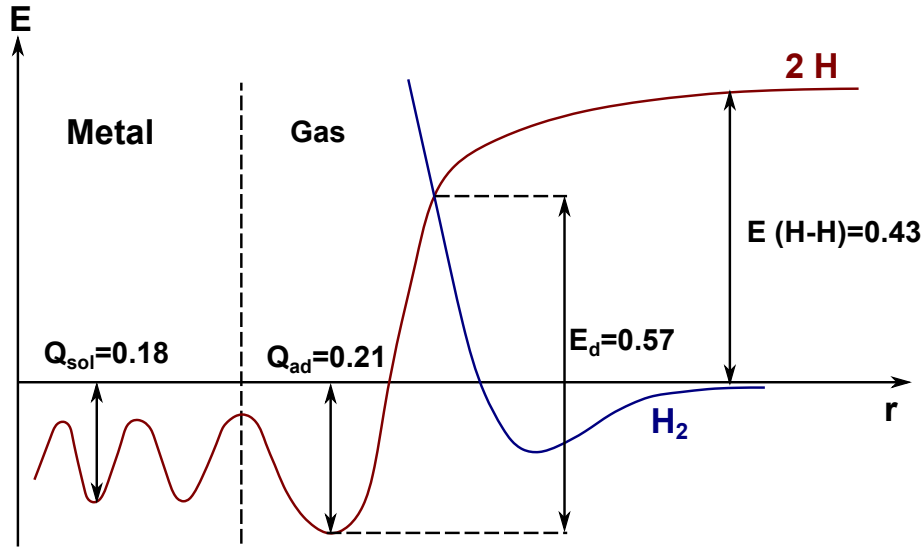


Figure 5.25.: Energy schema for adsorption/desorption of hydrogen on gold - The schema provides the relevant energies for either atomic or molecular hydrogen. For the process of associative desorption a value of 0.57 eV is given which was also used for the numerical calculations. Due to the small solubility heat there is a high probability for hydrogen/tritium absorption into the solid after the adsorption process. Schema adapted from [151].

detail a precisely cut resonance quartz crystal with large surface is driven at its resonance frequency by an RC-based resonator circuit. The sharp resonance of the quartz crystal forces the whole electric circuit on the resonance frequency. The crystal reacts on an adsorbed mass surface density $\Delta m/A$ with a frequency shift Δf according to the Sauerbrey equation

$$\Delta f = C_f \frac{\Delta m}{A} = \frac{-2f_0^2}{v_s \rho} \frac{\Delta m}{A} \quad (5.20)$$

as found by [152]. Thereby f_0 is the base frequency, $v_s = 3386$ m/s is the shear velocity and $\rho = 2.648$ g/cm³ is the density of the crystal [153]. The formula is only valid if the quartz sensor is opposed to a gaseous phase, the adsorption induced frequency change is small $\Delta f/f < 0.02$, the adsorbate is evenly distributed across the surface and the adsorbate connection to the quartz surface is rigid. In case of the tritium adsorption measurement all requirements are fulfilled: The adsorption occurs from the gaseous phase, the adsorption is randomly distributed, the expected amount is small and the chemical bonding to the surface is solid.

Depending on the crystal's base frequency results a prefactor describing the dependency between the adsorbed mass density and the frequency shift. The QCMB measurement system selected for the test experiment is the vacuum compatible 710-SH quartz crystal with the 710-OSC oscillator provided by Allectra⁹. The quartz crystal is already gold coated on the tritium exposed side. The quartz is located in a stainless steel holder and is connected to the corresponding RC oscillator. The 710-OSC runs at 6 Mhz therefore the frequency dependent constant can be calculated to

$$C_{f=6\text{ MHz}} = -8.03 \text{ Hz/g}\cdot\text{cm}^2 \quad (5.21)$$

The estimated¹⁰ surface site density of flat gold $\frac{dN_{\text{sites}}}{dA} = 1.5 \cdot 10^{15} \text{ cm}^2$ can be used to

⁹Allectra GmbH, Traubeneichenstr. 62-66, D-16567 Schönfließ b. Berlin

¹⁰The estimate bases on the gold density and molar mass. The accuracy of the "sites" count is limited anyway by a non-perfect surface with kinks and steps.

calculate the mass of a tritium monolayer to

$$\frac{\Delta m_{\text{T,ML}}}{A} = \frac{dN_{\text{sites}}}{dA} \cdot 3 \text{ u} = 7.55 \text{ ng/cm}^2 \quad (5.22)$$

with the mass of a single tritium ad-atom as three times the unified atomic mass unit. With these figures the frequency shift by the adsorption of one monolayer of tritium on the 710-SH results to

$$\Delta f = -0.6 \text{ Hz} \Rightarrow \frac{\Delta f}{f} = 0.1 \text{ ppm} \quad (5.23)$$

Because of the small mass of tritium and the limitation of the surface coverage to one monolayer the expected frequency shift is very small. The reliable measurement of a 0.1 ppm relative frequency change is close to the limit of the QCMB technology [154]. At least the measurement of a frequency of a periodic signal is one of the physical properties that can be measured with the highest precision [155]. To maximize the sensitivity of the measurement all instruments used at the setup must be very stable. The overall systematic errors introduced by the instrumentation must not exceed the 0.6 Hz/0.1 ppm level. The following parts of the setup had to be selected and optimized for the task: The power supply for the quartz oscillator, the frequency counter, the installation or electromagnetic protection of the quartz crystal and the temperature stabilization.

As voltage source for the QCMB electronics a conventional high precision linear power supply has been used at first. In order to further increase the frequency stability the power supply has been replaced by a lead-acid accumulator (6 V). The voltage was down-converted by a low dropout linear voltage regulator to 5 V in a custom minimized circuit. The resulting voltage was very stable with a hardly measurable remaining ripple of $U_{\text{p-p}} < 5 \text{ mV}_{\text{pp}}$. The accumulator had to be exchanged and re-charged every second day to avoid voltage deviations. For the frequency measurement a high precision frequency counter, namely a Tektronix FCA3000, is used. The device includes the long-term high stability option using a temperature stabilized OCXO-timebase. With this option the aging effect is guaranteed to be smaller than 0.01 ppm per month [127]. The quartz crystal itself must be operated in an ultra high vacuum vessel to ensure a sufficient leak tightness according to the TLA [4] for operation with tritium. The vessel is a Conflat CF100-63 4-way reduction cross. One of the CF100 flanges is used to install the quartz crystal on top of two stacked Peltier elements. The purpose of the Peltier elements is described later in the discussion about thermal stabilization. The other CF100 flange is reduced to CF40 flange by a zero length adapter and completed by the electric feed-through for the quartz crystal signal. The RC-oscillator is installed directly to the coaxial connector on the atmosphere side to minimize the signal cable length. One of the CF63 flanges is used to install the vacuum handling system consisting of gas type independent pressure sensors (measurement range 10^{-5} mbar to 1 bar) and connections for gas inlet/evacuation. The other CF63 flange was needed for electric feed-throughs of the thermo-stabilization system. The UHV encasement ensured the necessary stable environment conditions at the crystal, vacuum/gas control and the tritium safety. Furthermore, it consists only of metal and is therefore a good protection from electromagnetic interference impacting the QCMB measurements. The full setup is visualized in the schema 5.26.

As already mentioned the setup includes a temperature control system. This is required to increase stability and accuracy of the measurement system because the crystal frequency does strongly depend on the crystal temperature. An example of a crystal temperature dependence is given in figure 5.27. The temperature sensitivity depends on specific properties of the crystal with a maximum steepness shown in the graph of 6 ppm/°C. Therefore, a temperature stability of better than $\sigma_T < 10 \text{ mK}$ is required to reduce the systematic error contribution to the relative frequency shift to $\sigma_{\Delta f/f} < 0.06 \text{ ppm}$. To achieve this thermal

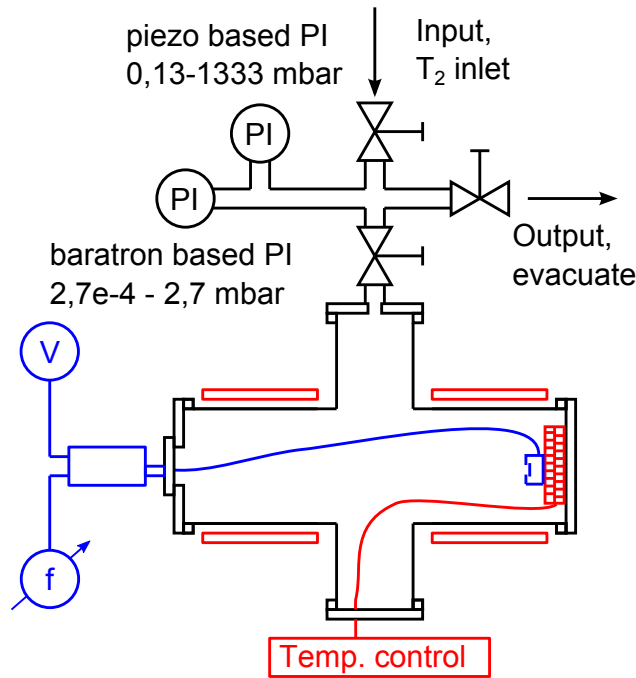


Figure 5.26.: Schema of the QCM experimental setup - The quartz crystal holder is placed on the stacked TECs and they are glued to the aluminum flange. The quartz crystal is connected via feed-through to its oscillator. Pressure sensors allow a quantitatively controlled evacuation, venting and filling of the vacuum system.

stability a dedicated temperature regulation system is located as close as possible to the quartz crystal. An active heating/cooling system has been selected using thermoelectric heaters/coolers (TEC). They are based on the Peltier effect [156] and built as a solid-state heat pump between the two sides of the device when a current is applied to the device. The hot and cold side is typically a flat quadratic surface of ceramic. The semiconductor material causing the Peltier effect is positioned between the two ceramic plates. For a fast response and to reduce the thermal mass the TECs have to be installed in the vacuum directly to the quartz crystal holder. There were no TECs available specifically optimized for vacuum application, but TECs are typically characterized in vacuum to find measure their performance [157]. For this application standard commercial TECs have been selected which have no imprinting on the ceramic which could potentially cause outgassing. As further preparation for vacuum operation the original cable has been removed and replaced with KAPTON insulated, ultra high vacuum (UHV) cables [158]. The cables were installed to the TEC with UHV compatible solder [158]. Totally two $40\text{ mm} \times 40\text{ mm}$ TECs with each 65 W electrical power have been stacked and installed to the flange. These components were glued together using an UHV compatible compound and the quartz crystal holder was glued on top of it. With the stacked elements it is planned to do the temperature stabilization as well as measuring the temperature dependent effects of the quartz crystal and the tritium adsorption. To complete the temperature control the heat delivered by the stacked TECs (up to 130 W) must be removed by a thermal sink. The main problem is the stainless steel CF100 flange with its small thermal conductivity of $16\text{ W}/(\text{mK})$ [159] preventing the heat transport out of the vacuum system. Therefore, a CF100 aluminum flange is used instead - the conductivity of aluminum is about $230\text{ W}/(\text{mK})$ [159]. With the aluminum flange it can be calculated that only a temperature difference of $\approx 7\text{ K}$ occurs through the 2 cm thick flange if the full heating power of 130 W is applied on one side. To dissipate the heat on the atmospheric side a conventional active computer processor cooler (designed for 180 W CPUs) is used.

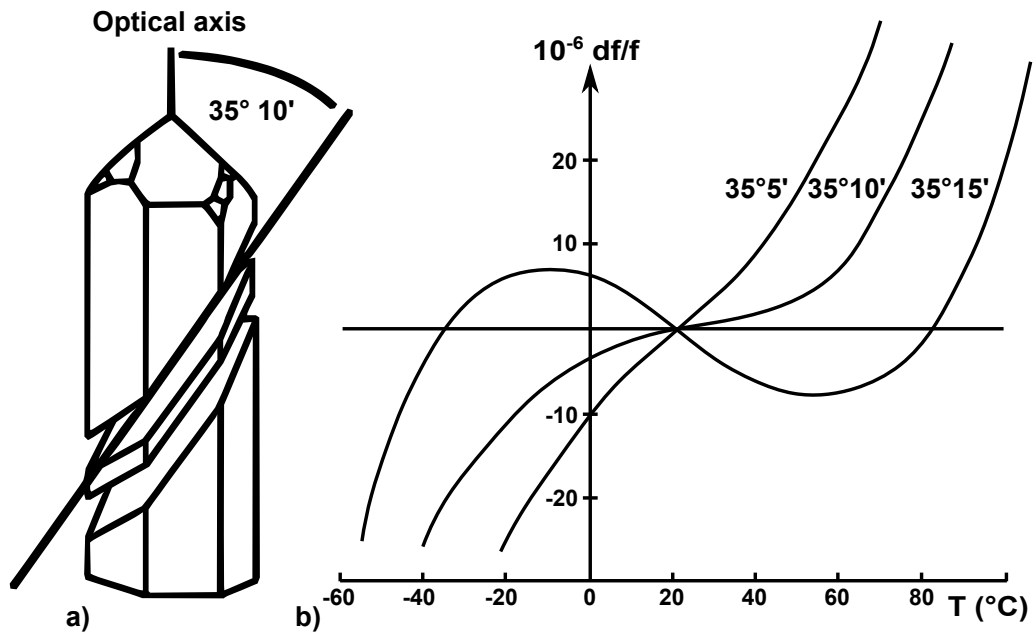


Figure 5.27.: Temperature dependence of AT-cut quartz crystals - a. Definition of the cutting orientation and angle for the AT-cut. b. Temperature dependence of quartz crystal with different cutting angles. This dependence is a potential cause of a large systematic error for a QCM system and must be minimized by a temperature stabilization system. Adapted from [153]

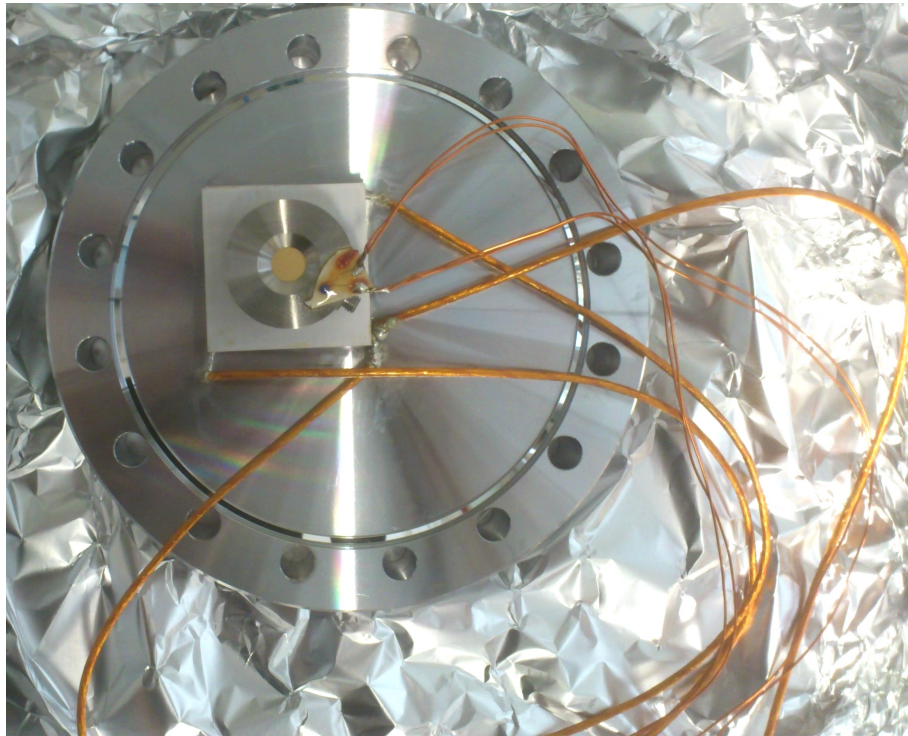


Figure 5.28.: Picture of the quartz crystal installed to the CF flange - The quartz crystal in its holder is glued on to the stacked TECs. The TECs are again glued to the aluminum CF flange. A temperature sensor is mounted on top of the crystal holder to measure the temperature close to the quartz crystal. All used cables and glues are qualified for ultrahigh vacuum systems.

The setup of quartz crystal and holder, TECs and temperature sensor mounted on the aluminum flange is shown in picture 5.28. To enable an active temperature stabilization

a Pt100 resistance temperature sensor has been glued to the quartz crystal holder. The temperature sensor is measured with the four-wire technique to maximize the accuracy. All required electric connection for the Pt100 sensor and the TECs use a single Sub-D 25 feed-through. The main desired advantage of the active Peltier heating/cooling system is the temperature stabilization in a large temperature range. In this concern the solution supersedes the temperature stabilization by water-cooling as it is usually implemented in QCM systems.

The system was first built, tested and commissioned without tritium in one of the cold laboratories¹¹ of the TLK. After construction, the QCM system was fully controlled by a custom LabVIEW software. The temperature regulation system used a PID controller¹² to adjust the voltage at the power supplies for the TECs in dependence of the difference of target temperature and the actual measured temperature. After multiple, iterative configuration steps of the PID controller parameters the temperature stabilization worked as required. During the first QCM measurements with an evacuated vacuum chamber ($p < 10^{-5}$ mbar) the thermal controller achieves to maintain a stability of $\sigma_T < 5$ mK. The thermal controller is used to measure the temperature dependence of the crystal frequency in vacuum. The result is given in the chart 5.29. In this measurement the frequency-temperature dependency is linear in the full range of 25 °C to 70 °C. The linear calibration is given by [160]

$$f(T) = (-10.4 \pm 0.3) \frac{\text{Hz}}{\text{K}} \cdot T \quad (5.24)$$

This result is not in full agreement with the standard curves for AT-cut crystals: Instead of the measured linear drop the frequency should follow a higher order polynomial function in dependence of the temperature (compare figure 5.27).

Another dependency investigated is the frequency change by different gas pressures. This investigation used pure nitrogen gas in the pressure range 2 mbar to 150 mbar. The measurements reveal a clear dependency of a dropping frequency with an increase of pressure (compare figure 5.30). The steepness of the curve reduces with the increasing pressure. The sign and the overall shape of the frequency-pressure dependence agree with other findings on the behavior of quartz crystals [161]. In this reference the negative shift is explained by adsorption while the reduction of steepness with increasing pressure shall be caused by the friction of the rough surface to the gas. While the qualitative shape of the measured pressure dependence is compatible with [161], the quantitative frequency shifts are too large by a factor of 10.

Already starting at the vacuum measurements the first problems with the system occurred. Both TECs have defects resulting in the loss of the temperature control system while only temperature monitoring remains possible. The TECs become faulty separately with a few days of measurement in between. The vacuum system is opened but the malfunction of the TECs can not be explained. Due to the installation with UHV compatible epoxy glue the TECs can not be exchanged either. As a result further measurements rely on the temperature monitoring and use the already measured dependency to unfold thermal effects from other changes in the frequency. Further difficulties are caused by the appearance of long-term drifts where the frequency-temperature dependency is broken even during vacuum measurements (compare figure 5.31). To quantify this behavior the data is not only fitted for its thermal behavior (compare equation 5.24) but also gets a frequency drift linear in

¹¹Cold laboratories distinguish themselves by the absence of radioactive materials available for research.

In case of the tritium laboratory it means no tritium is used or processed in the experiments.

¹²A PID controller uses a closed loop feedback mechanism and is widely used in industrial applications.

The full name is proportional-integral-derivative controller and describes the operations applied to the difference of actual value to target value.

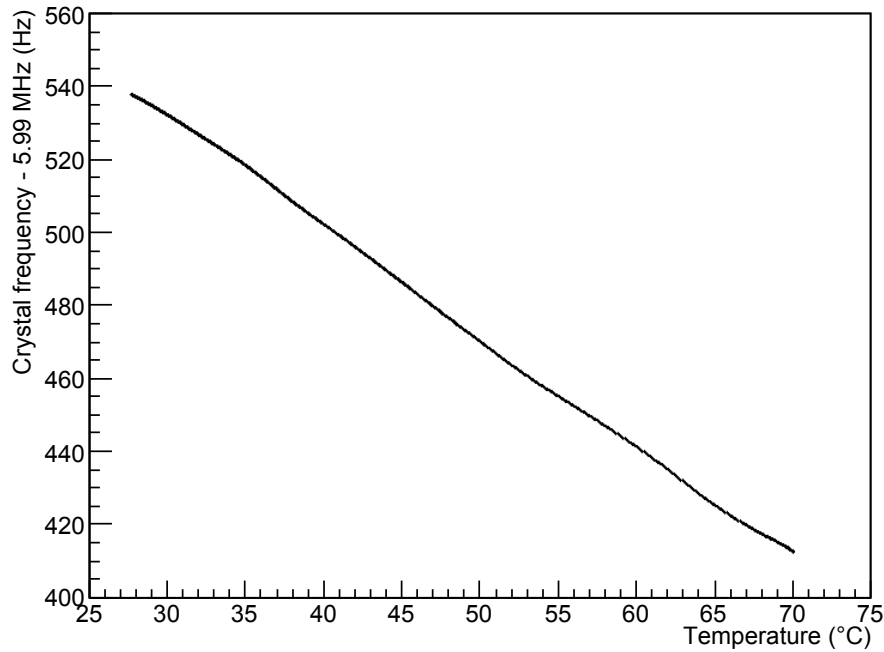


Figure 5.29.: Temperature dependence of the QCMB - The temperature of the system is changed in a wide range with the TECs, while temperature and frequency are recorded. By a temperature change of 40° the QCMB frequency changes over 100 Hz. While a strong dependency has been expected, the linear shape does not match to the usual curves. [160]

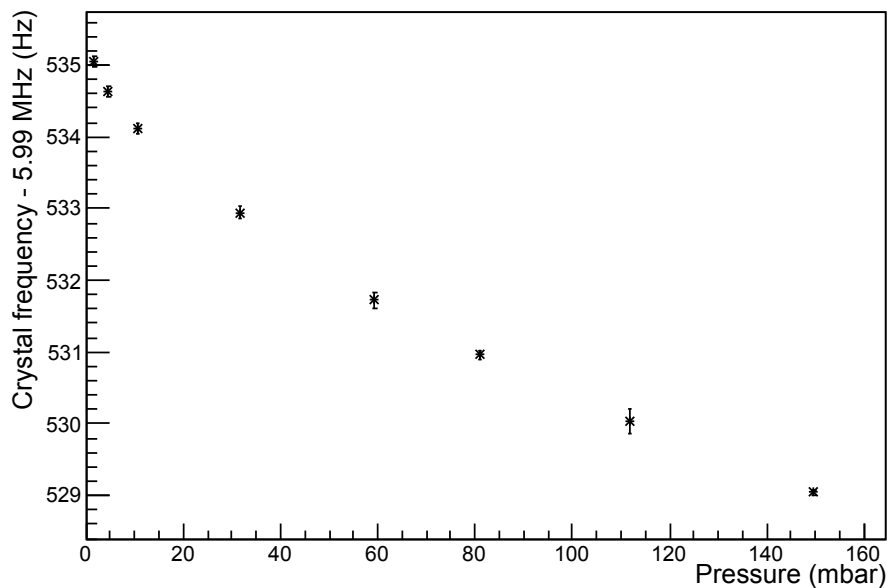


Figure 5.30.: Pressure dependence of the QCMB - Changes in the QCMB frequency have been measured at different nitrogen pressures up to 150 mbar. The frequency change is small enough that the effect could be disregarded in the further measurements. The shape of the dependency matches to a published source [161] but the absolute values differ. [160]

time. This shift behaves similar to an adsorption effect but the seemingly random drift is rather considered as electric instability. The last measurements in the cold laboratory compares different non-radioactive gases: Besides vacuum and nitrogen also hydrogen and helium atmospheres are tested. The parameter results are comparable within the large errors they have due to the drifts and signal instabilities.

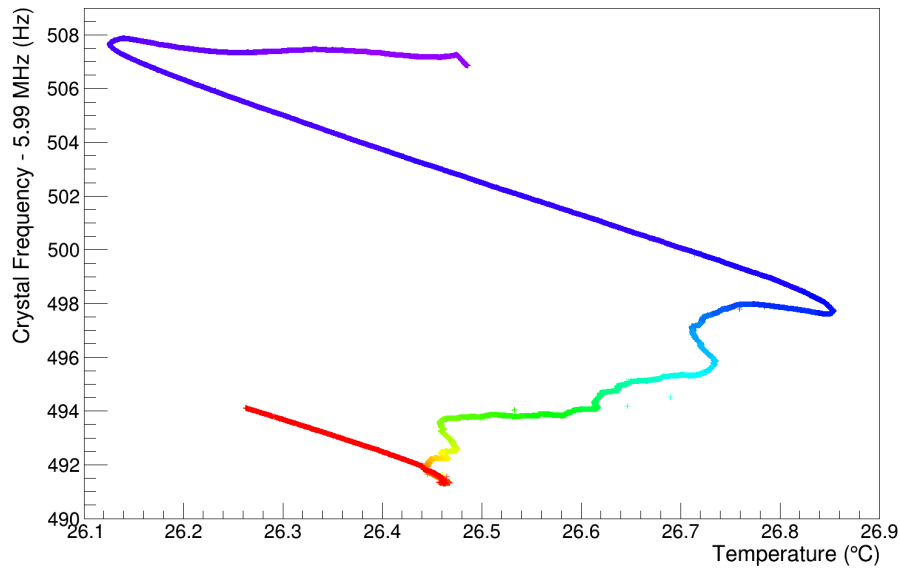


Figure 5.31.: Long term drifts of the QCMB in vacuum - In long term runs, after the failure of the TECs, the frequency values undergo large drifts. The coloring equals to the measurement time from purple to red. Very common in the temperature-frequency graphs are parts where the frequency drops linearly with temperature increase or vice versa. This effect has been considered in the data evaluation to reduce the systematic effects. [160]

Although the first measurement problems occurred, the QCMB system was installed in the TRAP chamber in the warm laboratory. The goal remained to search for indications of adsorption or changes at the gold coated quartz crystal. The measurements comprised 3 runs with initial tritium pressures of $1.6 \cdot 10^{-3}$ mbar, $3.1 \cdot 10^{-2}$ mbar and $4.6 \cdot 10^{-2}$ mbar. The tritium measurements were long-term runs of 25 hours, 11 days and 32 days respectively. The long measurement durations revealed the destructive effects of the signal instabilities on the systematic precision. The graph 5.32 shows a variation in the frequency close to 10 Hz while the temperature remains within a 1 K range. Efforts have been made to increase the temperature stability again with external heating tapes on the vacuum vessel combined with a heating controller. By this the temperature stability did improve but the drifts of the frequency were still too large. With the given systematic errors due to instabilities, the detection of a 0.6 Hz shift (one adsorbed monolayer of tritium) has not been feasible. Nevertheless, the fits previously described have been applied to all measured data. The fits deliver a time-dependent constant which was compared for the tritium measurements with the vacuum measurements under consideration of the errors on this parameter. As a result an upper limit on the adsorption could be found: During the measurement time of 32 days an upper limit of 1120 adsorbed monolayer-equivalents can be given with 1σ confidence. This corresponds to an upper limit on the adsorption rate of 36.1/day adsorbed monolayer-equivalents with 1σ confidence. The fully detailed analysis about the QCMB measurements are available in [160].

Despite the fact that the experimental design was more effortful than originally planned the achieved results are overall dissatisfactory. Therefore, the description of measurements and the hardly meaningful results is intentionally kept briefly. The cause of the drifts could not definitely be found. The thermal instabilities might have contributed or instabilities injected in the circuit by the oscillator. The required sensitivity might have been beyond the capabilities of the used QCMB system. The reason for the failure of the Peltier coolers can be the non-UHV compatibility of all parts resulting in vaporization of an essential part at low pressures. An alternative explanation might be overheating due to bad thermal conductance of the special epoxy glue. When the system was disassembled for disposal a

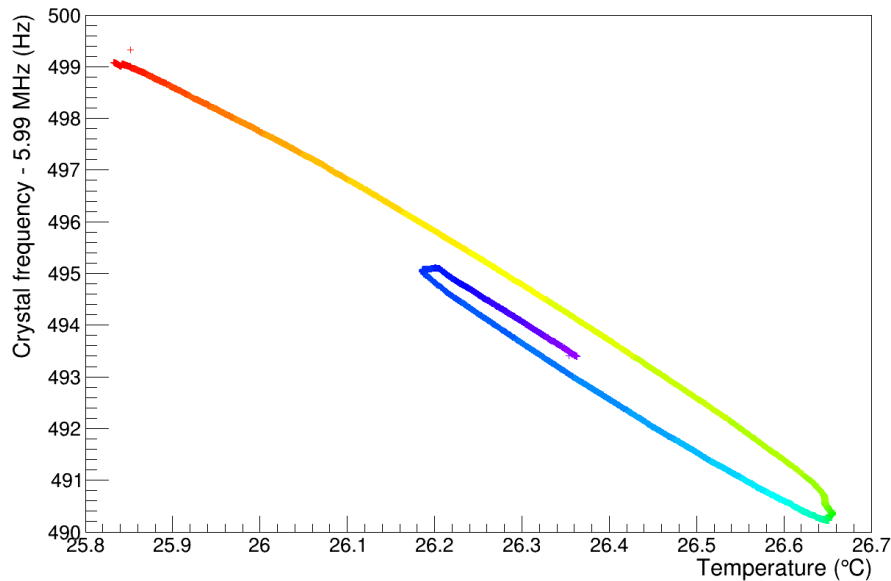


Figure 5.32.: Long term drifts of the QCMB in tritium - The drifting behavior of the QCMB did not change significantly in the experimental runs with tritium. Different trials to increase the temperature stability could not remove the mixture of linear and random frequency drifts. The final data analysis investigated the linear drift parts for differences in the vacuum and the tritium measurements. [160]

visual check of the quartz gold coating revealed no damage or distortion - the gold layer was still intact and unchanged in color or reflectiveness. Since the QCMB experiment was not able to clarify which amounts of tritium can adsorb on and absorb in gold, another experiment was designed and built: The TriADE (Tritium Adsorption/Desorption Experiment) experiment. This experiment uses the beta-induced X-ray spectroscopy of tritium similar to the Rearsection activity monitoring system (described in section 5.5). The details of the setup and the proof-of-principle are described in [162]. The measurement results with Rear Wall prototypes will be published in [47].

5.5. Implementation of the beta-induced X-ray spectroscopy system

The design and development for the beta-induced X-ray spectroscopy (BIXS) system to monitor the WGTS activity has not been covered in the scope of this thesis. Still, the concrete implementation of the BIXS system at the Rearsection was a part of the design accomplishments within the thesis. Therefore, this section describes briefly the working principle of the BIXS system and its current status. Then it shows the final design how the X-ray radiation detectors are installed at the Rear Wall chamber. The normal operation modes are defined just like different maintenance options that might become necessary.

Free electrons entering a solid material interact with the charged particles in the matter via the electromagnetic force. By inelastic scattering processes photons can be created which are essential for the BIXS method. The photons can either result of interactions with shell electrons or the nuclei in the solid. When the unbound electron scatters at a shell electron, the shell electron is excited to a higher energy level or to an unbound state. In the latter case the related atom is ionized. In both cases a shell vacancy is created which can be filled by de-excitation of electrons from higher energy levels. The process can either occur combined with the emittance of a photon (radiative recombination) or by the excitation of another shell electron (non-radiative recombination, Auger recombination). Only the

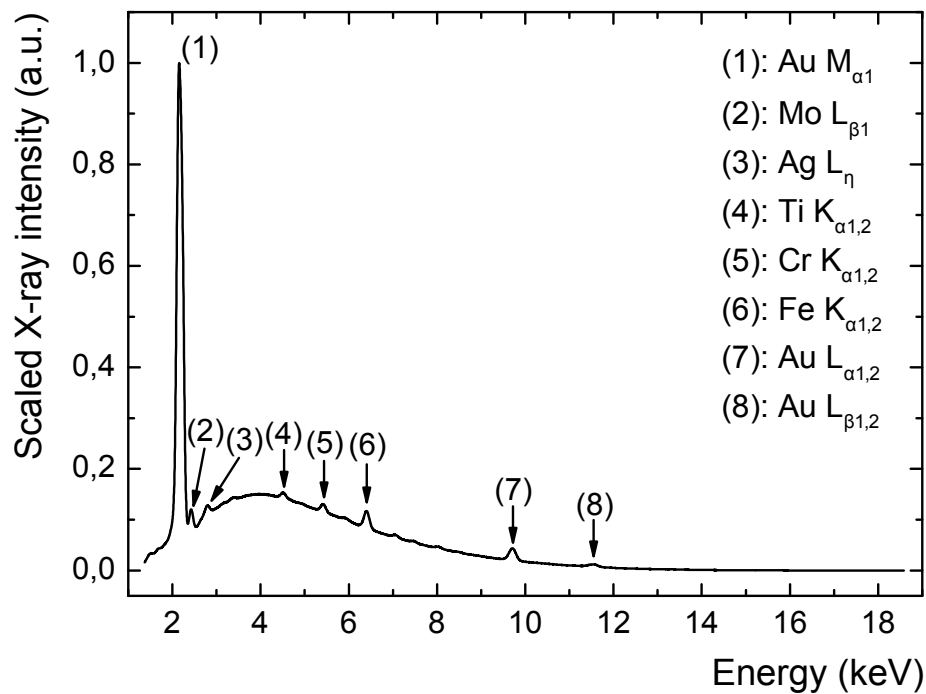


Figure 5.33.: Exemplary BIXS spectrum - Calibrated spectrum of X-rays induced by tritium β -decay electrons recorded at the TRACE experiment. It shows the overlay of the continuous bremsstrahlung and multiple identified characteristic X-ray peaks. A similar spectrum can be expected from the BIXS measurement at the Rearsection. [164]

radiative processes are relevant for the BIXS measurements. The energies of the photons are defined by the energy that becomes available by the electron de-excitation. As a result of the quantized shell energies and the transition selection rules the possible photon energies for every element is limited and characteristic. Therefore, this radiation caused by ionization is called characteristic X-ray radiation. Despite the interaction with the shell electrons the incident electron can also scatter off the nuclei by the Coulomb force. By this the process energy and momentum of the electrons change and a photon is emitted. The photons created in the interaction are called “bremsstrahlung” because the process is based on the retardation of the unbound electron. In contrast to the characteristic X-rays the energy spectrum of the bremsstrahlung is continuous. The possible energy of the photons ranges from greater than zero up to nearly the primary electron’s kinetic energy (limited by the requirement for the energy-momentum conservation of the 3-particle process). A typical BIXS spectrum is an overlay of characteristic radiation and bremsstrahlung (compare figure 5.33). Overall the electron energy losses in solid materials can accurately be calculated by the empiric Berger-Seltzer formula given in [163]. The produced X-rays can then be detected and analyzed by semiconductor detectors. The first inelastic interaction of soft X-rays in matter is either the photoelectric effect or Compton scattering. Both processes and the previously described electron interactions in solid materials result in a large cascade of electrons and photons. Finally, the shower in the semiconductor ends up in numerous low-energetic quasi-particles in the form of phonons and electron-hole pairs. When all energy of the primary X-ray is deposited in the semiconductor detector and noise sources are disregarded the resulting amount of electron-hole pairs scales directly with the primary particle energy. The electron-hole pairs can be separated in a detector by the appropriate shaping of the conduction and valence bands. Finally, the number of created electron-hole pairs can be measured as detector signal. Therefore, the semiconductor detectors can not just notice incident particles but also measure their energy spectrum.

Using the soft X-rays, created by the β -electrons in solid materials, for tritium activity

monitoring is a well evaluated concept at the TLK [165]. The essential component is the detector which must combine a good energy resolution with a large active area. The energy resolution is needed to detect also low energetic X-rays, reduce systematic errors caused by noise and for an in-situ calibration with the characteristic X-ray peaks in the spectrum. A silicon drift detector (SDD) [166] is an excellent option because it combines a good energy resolution with a large sensitive area (< 200 eV FWHM at 6 keV and ≥ 100 mm² commercially available). The working principle has first been tested with an Axas M SDD from KETEK¹³ and electrons from a photoelectric electron gun [119]. The target for X-ray production was a gold coated KAPTON foil. In these measurements the resulting rates and spectra were in agreement with the expectations and simulations for X-ray production by a mono-energetic electron source. Following up these investigations the same detector has been used in the proof-of-principle experiment “TriReX” with tritium. The experimental setup and the measurements results are given in [63]. At TriReX for the first time a gold coated beryllium window was used to protect the detector but in this case it was at the same time the target for the X-ray production. In contrast, the Rearsection will also use gold coated beryllium windows for the protection of the detectors while the X-ray protection target for the β -electrons is the Rear Wall. During the TriReX operational time the measured spectra and the conversion rate of the process could be reproduced in simulations. Finally the TriReX experiment has proven that a very small relative change in the source activity (tested was a 0.2% increase of the tritium amount) can be detected. The success of the TriReX experiment lead to several tritium analysis systems based on the BIXS principle.

The detectors for the final BIXS implementation at the Rearsection have been selected and ordered already in the year 2012: Two Axas M silicon drift detectors from KETEK with 100 mm² sensitive area will be used. The kit comprises not only the SDD itself but also the Axas M2 power supply unit. The detector head unit (Axas M1) was ordered in a customized version with a CF25 flange welded on the detector finger. The flange is used for mounting of the detector and to enclose and evacuate the volume around the SDD detector head which is needed for a proper operation. The customizable length of the detector finger was specified to be 260 mm. This length is a remnant of the Rearsection design before the superconducting re-condenser has been added. In the current design a rather compact detector would have been possible and actually simplified the design of the Rear Wall chamber. For the data acquisition system (DAQ) the signal from the detector head’s preamplifier is passed to the digital pulse processor DP5 from the company Amptek¹⁴. For the final data integration of the BIXS system to the KATRIN databases the Amptek DP5 shall be controlled by ORCA [167] which is the same system that controls the main detector. The ORCA software is therefore currently extended by the Institute of Data Processing and Electronics (IPE) at KIT to support the new signal processor.

On the hardware side all assembly steps are defined: Both detectors are installed to the Rear Wall chamber via symmetric ports. A cut of the assembly design is available in drawing 5.34. The detector housing is a result of safety regulations by the TLK and the experiences collected at the TriReX experiment. The detector head is in an enclosed volume that is closed by the gold coated beryllium window on the front side and the detector’s own CF25 flange on the back side. The X-ray transparent beryllium window is connected to a pipe with CF40 flange by diffusion bonding. This part is connected to a CF40-CF40 extension pipe with a VCR gas connection for evacuation of the detector chip chamber. The extension pipe is followed up by a special zero length adapter with CF40 connection on the one side and CF25 & CF100 connector on the other side. The detector flange is connected to the smaller CF25 terminal. Finally, the housing of the

¹³KETEK GmbH, Hofer Str. 3, 81737 München

¹⁴Amptek, Inc., 14 DeAngelo Drive, Bedford, MA 01730, USA

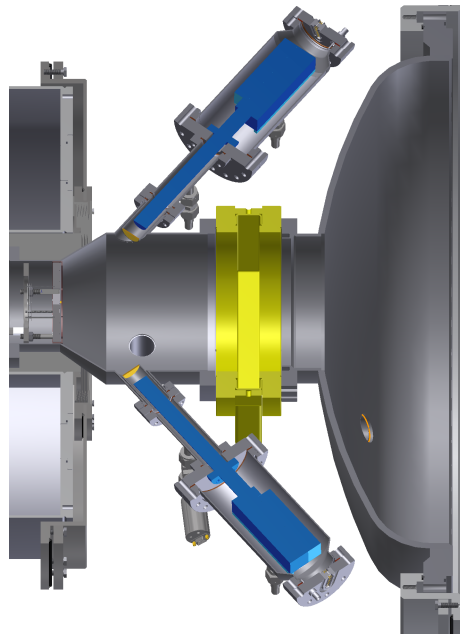


Figure 5.34.: Design of the BIXS detector systems at the Rearsection - The CAD drawing shows the 2 silicon drift detectors with pre-amplifier electronics (blue) as they will be installed at the Rear Wall chamber. They are both aligned with their silicon sensor towards the Rear Wall where the X-rays are produced. Gold coated beryllium windows protect the detectors and separate them from the KATRIN vacuum system. Both detectors are identically encapsulated in small ultrahigh vacuum chambers.

detector electronics is enclosed by a CF100 pipe with a VCR gas connection included. The CF100 pipe is reduced in its diameter towards the end to be finally closed by a CF75 flange. With the diameter reduction conduces to the space-saving around the Rear Wall chamber. The CF75 flange includes all electric feed-throughs which are required to supply and read out the SDD detector. This complex encasement ensures that the whole system is always contained by a full metal enclosure with metallic sealings according to the Conflat standard. Neither the beryllium window nor the flange at the silicon drift detector are officially certified as tritium safe enclosure. In fact helium leakage rates measured with a beryllium window proofed that the window can seal very well [63]. In contrast, the detector is constantly leaking through the electronics and the detector head unit. Therefore, the volume at the detector head must be constantly evacuated to protect the SDD chip from ambient air. This is done in a closed loop, pumping the gas back to the detector electronic volume where it originally leaked from. Because of that, each of these chambers has a gas connection line for the pump inlet/outlet. Two identical of these sealed detector constructs are installed to the ports of the Rear Wall chamber. The ports are welded to the Rear Wall chamber that the rotation axis of the detector finger targets for the center of the Rear Wall with an angle of 52° to the Rear Wall normal. The goal of the geometry is to ensure that X-rays originating from a large area of the Rear Wall can directly hit the sensitive area of the SDD. At the same time the steel surface in the Rear Wall chamber that have a direct line of sight to the detector shall be small. By this the signal from the Rear Wall shall be maximized compared to background caused by adsorbed/absorbed tritium at the steel surfaces. Further geometric restrictions were caused by the requirement of a technical feasible construction. Figure 5.35 shows the front side of the chamber where a “sight cone” of the detector is indicated. All surface points that intersect with the cone have a direct line of sight to the full active area of the SDD. The surface area from which X-rays can reach at least a part of the SDD sensitive area is significantly larger.

During normal operation at KATRIN, both detectors will be running permanently, pow-

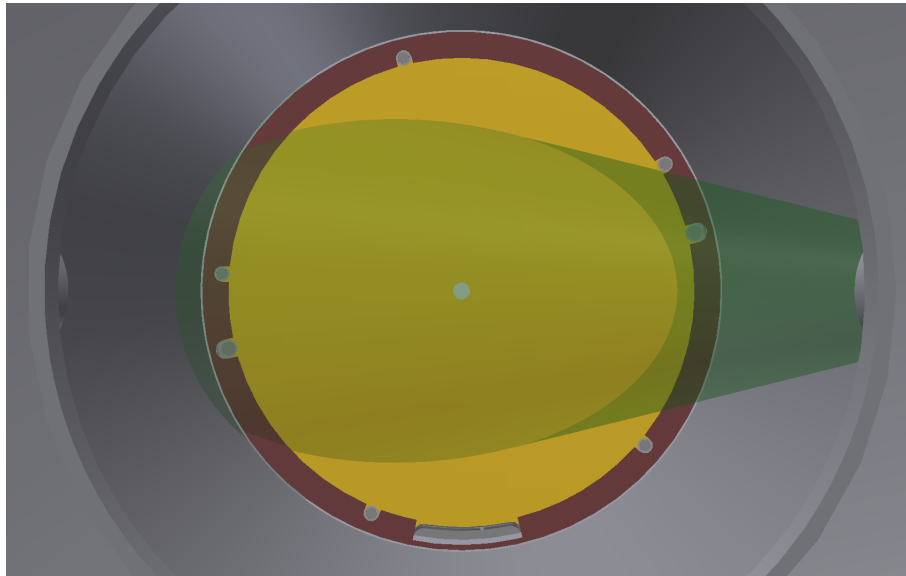


Figure 5.35.: Monitoring cone of one BIXS detector - The green cone indicates the alignment of the BIXS detectors to the Rear Wall. The intersection covers mainly the Rear Wall and only a small part of the stainless steel surface. The intersection with the surface comprises all points that have a direct line of sight to the full detector chip surface. The area of points that can reach chip surface at least partially is significantly larger.

ered by the Axas M2 and the signal processed by the Amptek DP5. The power supply and the signal processor will be both placed within the second containment of the Rear Wall chamber. This improves the signal quality and avoids the usage of complicated or proprietary electric feed-throughs at the glove box. The detectors are cooled indirectly by a water-cooling of the steel pipes around the detector electronics. This will be sufficient because the heat dissipation from SDD and electronics is small compared to other heat sources in the second containment. The data processing is controlled by a custom software, preferably within the ORCA toolchain, based on the Amptek development kit. Measured and analyzed data will be written to the KATRIN database. The scope of the data has yet to be defined but possible are the raw spectrum, total counts/count rate, analysis of the characteristic X-ray peaks and flags to validate the data quality. Definitely needed is also an indicator for relative shifts of the source activity - the original purpose of the BIXS system at the Rearsection. The measurement frequency might be adjusted to the time scale necessary to measure a 0.1 % relative shift of the source activity with $1-\sigma$ precision. This dependence of measurement duration to precision comes by the statistical error on the measured X-ray count according to Poisson statistics. The TriReX experiment revealed this statistical error as the largest contribution to the source activity uncertainty. This is because of the small X-ray conversion factor at the given electron energy scale. After simulations of the Rearsection setup, an X-ray rate of the order of 10^4 cps [48] is expected for each of the Rearsection BIXS detectors. The usage of two detectors ensures a redundant system if one of them should fail. The system would continue to run with a reduced sensitivity until the defect is repaired. If the detector power supply or the DAQ has a defect the component must be repaired in the glove box or exchanged. The exchange is possible in a safe manner because the primary tritium system stays closed during the operation. A defect at the SDD itself is more complex. The detector can be disassembled from the Rear Wall chamber while the beryllium window keeps the vacuum system sealed. For a tritium safe enclosure of the primary system a CF25 blind flange must be installed in place of the detector's flange. Afterwards the detector can be repaired or exchanged eventually even outside of the second containment if the detector is evidently

uncontaminated. The most severe problem is a defect (crack, breakage) of the gold coated beryllium window. The design as dedicated part allows exchanging the window without disassembling of the Rear Wall chamber. Still, the primary vacuum system of KATRIN must be opened. During this operation the valves to the WGTS and the E-gun part of the Rearsection (compare vacuum schema 3.3) must be shut. The KATRIN measurement must be interrupted till the port is closed by a blind flange again. Such a delicate part can not be repaired but it would be replaced by an available spare part. In the worst case of a breakage of the beryllium window further cleaning steps are necessary because beryllium dust is highly toxic [168]. The risks of a faulty beryllium window have been analyzed during the Rearsection hazard and operability analysis (HAZOP). To minimize the risk, safety requirements were added for the window. For example the thickness was defined to be 0.25 mm thick (normally a thickness of 0.1 mm should be sufficient for such a window). The window is also required and tested from the manufacturer to withstand a pressure difference of 1 bar in either direction. In conclusion the BIXS system at the Rearsection should be a safe and deliberate system which fulfills all demands to a KATRIN source monitoring instrument.

Conclusion

Within the scope of this thesis several essential development milestones for the Rearsection of the KATRIN experiment have been accomplished. This important part of the control and monitoring sections has completed the concept & design phase and its parts find themselves now in the status of assembly or already commissioning. All investigations were conducted with the goal to provide a high precision measurement device for the source and transport sections of the KATRIN experiment. The Rearsection complements the high source stability with regular calibration or monitoring for the goal of a precise neutrino mass measurement: Recognized long-term variations of source parameters can be corrected in the data analysis and therefore do not increase the systematic error. Besides the computer aided design and simulations several dedicated test experiments have been conducted to clarify specific questions - often the purpose was a feasibility study. The results of the test experiments were used as guidelines for further design and development of the Rearsection.

The developed mechanical design is more than just a framework for the physics instrumentation. On the one hand a good vacuum system with small leaking rates is required for the tritium safety. On the other hand the impact on the electron gun beam by electron scattering with rest gas molecules is minimized. To achieve a minimal pressure at the most delicate parts of the electron gun the vacuum system is designed as differential, cascaded pumping stage. Two apertures (at the Rear Wall and in the center of the Rearsection) and two turbomolecular pumps are used to implement this pumping scheme. The vacuum layout uses enough valves to decouple parts of the Rearsection from the KATRIN vacuum system for maintenance or to control the flow of purge gas. Pressure sensors are installed with measurement ranges matched to the pre-calculated operating pressure. The primary encasement itself is mainly constructed of standard CONFLAT¹⁵ tubes & chambers and VCR¹⁶ parts and pipes. According to the tritium safety requirements the vacuum system is installed inside of another encasement realized as two glove boxes. First and second containments require a certain set of interfaces to experiment and infrastructure, which have been planned and defined. This double contained system will be constructed on a rigid support that lifts the Rearsection on to the KATRIN beam line height. The support planning did not only include the forces by the weight of the load but also the attracting magnetic forces of the superconducting magnet (RSCM) to the magnets of the tritium source. To ensure the proper operation of sensors and pumps close to the RSCM the most critical instrumentation has been operated in a magnetic field test stand. The results are used to define and design necessary magnetic shieldings. One of the major milestones was the acceptance of the mechanical design within a technical design review (TDR). With the completion of the TDR all required parts could be ordered and the construction could be started.

One of the two essential calibration instruments included in the Rearsection is the electron gun (E-gun). The specifications require a highly customizable electron beam with config-

¹⁵Registered trademark of Varian, Inc.

¹⁶Registered trademark of Swagelok Company

urable and well defined electron kinetic energies and polar angles to the magnetic field. Building and commissioning of the E-gun is the major task assigned to a KATRIN collaborating member institute at the University of California Santa Barbara (UCSB). Still, most of the electromagnetic design (EMD) has been accomplished at KIT using KATRIN simulation code which was partially extended for the Rearsection EMD. At the electron gun the photoelectric effect is utilized to emit electrons from the gold coated cathode surface. The particle acceleration starts between two parallel, turnable plates (cathode and anode), followed up a short distance of non-accelerated cyclotron motion. At a stronger magnetic field the post-acceleration stage increases the kinetic energy of the electrons to its maximum. After this the electron beam passes through the complex electromagnetic transport stage of the Rearsection which steers and conditions the beam by magnetic and electric dipole fields. The magnetic dipole fields are necessary to steer the electron beam through the two gas-flow reducing apertures. The electric dipoles are used to separate reflected electrons from the primary beam and to remove incoming ions from the tritium source. Each of the mentioned components and their interplay have been optimized to ensure all specified configurations, with the corresponding required beam properties, can be accomplished. Any modification to the electromagnetic design has also been tracked in the mechanical design. This synchronization was an essential improvement over the very first electromagnetic and technical designs resulting in collisions and unfeasible design concepts. A very important step for both models was the addition of a superconducting magnet at the Rearsection. All necessary parameters could be defined in a short time frame and both models have been updated and optimized after the design change. Experimental investigations were focused on the E-gun beam transport as the electron gun construction is carried out at UCSB. The E-gun construction has been recently completed precisely following the design that has been developed with simulations. Currently all components of electron gun and transport section are commissioned in order to transport it to KIT for the full Rearsection assembly in the near future. An electron gun beam tracker consisting of a quadrant detector with a central inner hole shall monitor and detect collisions of the beam at the two apertures. This detector has been designed, built and successfully tested within the scope of this thesis. Another test experiment checked the capabilities of a piezoelectric motor in a stress test in vacuum and tritium environment. Such an in-vacuum motor is necessary to either open or close the central Rear Wall aperture depending on whether the KATRIN experiment runs in a measurement mode using the E-gun or in normal operation.

The other important feature of the Rearsection is the Rear Wall (RW) with its related monitoring tools. By virtue of the magnetic confinement of the tritium plasma in the source most of the charged particles (primary β -electrons, secondary ionization electrons, ions) will be either adsorbed or neutralized at the Rear Wall. Considering the directional dependent plasma conductivities it is expected that the Rear Wall has an important impact on the electric potential in the tritium source components. Therefore, the Rear Wall must have a high surface quality, a stable work function and must be non-degrading in the tritium environment during the KATRIN measurement runs. The noble metal gold is known to remain stable in reactive environments and was adapted as the preferred Rear Wall surface material. Gold as Rear Wall surface material also has another advantage due to its high atomic number: The conversion factor for X-ray production by the inverse photoelectric effect is relatively large. This is useful for the beta-induced X-ray spectroscopy (BIXS) system which is used to monitor the tritium source activity. Two detectors can be installed at the Rear Wall chamber which are directed towards the gold surface measuring the rate of induced X-rays. Another port of this chamber will be instrumented with an ultraviolet (UV) light source for a full-surface illumination of the Rear Wall. The UV light source serves for multiple purposes at once - it can be used for cleaning procedures or photo-electron emission to check the Rear Wall surface. With photo-electron emission it is possible to measure the work function of a surface directly. With regard to the impor-

tance of the Rear Wall surface potential for the tritium plasma several RW prototyping samples have been tested. These measurements took place at the KATRIN monitor spectrometer which enabled two different methods to determine the work function: Either by dependence of the emission rate on the photon energy or by precise energy spectroscopy of the emitted electrons. Furthermore, a complementary measurement method, the “Kelvin Probe microscopy”, has been used to determine the spatial work function distribution of the prototype samples. With this method the work function can be measured locally and with high precision but only relative to the surface of a probe tip. For most of the tested samples limitations have been revealed in the measurements which lead to the development of a simplified "baseline" solution. Finally, the effect of tritium adsorption on gold surfaces needed to be investigated because it can result in work function changes and a background signal for the neutrino mass measurement. Therefore, the tritium adsorption on gold has been estimated theoretically and an upper limit was found with a dedicated experiment. The Rear Wall will be installed within the superconducting magnet and limited possibilities for maintenance access. A special Rear Wall mount has been designed which allows the usage of different Rear Walls and feasible installation/dismount procedures.

Most of the Rearsection parts are ready for assembly and already partially assembled. The Rearsection is scheduled to be commissioned in the year 2015 and to be fully operative at the start of KATRIN.

Bibliography

- [1] F. Reines and C. Cowan: *Detection of the free neutrino*. Physical Review, 92:830–831, 1953.
- [2] V. Aseev, A. Belev, A. Berlev, E. Geraskin, A. Golubev, N. Likhovid, V. Lobashev, A. Nozik, V. Pantuev, V. Parfenov, A. Skasyrskaya, F. Tkachov, and S. Zadorozhny: *Upper limit on the electron antineutrino mass from the Troitsk experiment*. Physical Review D, 84:112003, 2011.
- [3] KATRIN collaboration: *KATRIN design report*. FZKA scientific report, 7090, 2005. <http://bibliothek.fzk.de/zb/berichte/FZKA7090.pdf>.
- [4] TLK Betriebsbüro: *Technische Liefer- und Abnahmebedingungen des Tritiumlabor Karlsruhe (TLA)*. internal document, 2013.
- [5] P. Pal: *An Introductory Course of Particle Physics*. Taylor & Francis, 2014, ISBN 9781482216981.
- [6] W. Pauli, R. Kronig, and V. Weisskopf: *Collected scientific papers*. Interscience, New York, NY, 1964. Offener Brief an die Gruppe der Radioaktiven bei der Gauvereinastagung zu Tübingen (datiert 4. Dez. 1930).
- [7] C. L. Cowan, F. Reines, F. B. Harrison, H. W. Kruse, and A. D. McGuire: *Detection of the free neutrino: a confirmation*. Science, 124(3212):103–104, 1956. <http://www.sciencemag.org/content/124/3212/103.short>.
- [8] C. Grupen: *Astroparticle Physics*. SpringerLink: Springer e-Books. Springer, 2005, ISBN 9783540253129. <http://books.google.de/books?id=ueqGAKjt0-MC>.
- [9] J. Lesgourgues and S. Pastor: *Neutrino mass from cosmology*. Advances in High Energy Physics, 2012, 2012. <http://dx.doi.org/10.1155/2012/608515>.
- [10] D. J. Fixsen and J. C. Mather: *The spectral results of the far-infrared absolute spectrophotometer instrument on coBE*. The Astrophysical Journal, 581(2):817, 2002. <http://stacks.iop.org/0004-637X/581/i=2/a=817>.
- [11] The Borexino Collaboration: *Neutrinos from the primary proton–proton fusion process in the sun*. Nature, 512:383–386, 2014.
- [12] B. Cleveland, T. Daily, J. R. Davis, J. Distel, K. Lande, C. Lee, P. Wildenhain, and J. Ullman: *Measurement of the solar electron neutrino flux with the homestake chlorine detector*. The Astrophysical Journal, 496(1):505, 1998.
- [13] W. Hampel, J. Handt, and G. Heusser: *GALLEX solar neutrino observations: results for GALLEX IV*. Physics Letters B, 447(1–2):127 – 133, 1999, ISSN 0370-2693. <http://www.sciencedirect.com/science/article/pii/S0370269398015792>.
- [14] J. N. Abdurashitov, V. N. Gavrin, and V. V. Gorbachev: *Measurement of the solar neutrino capture rate with gallium metal. iii. results for the 2002–2007 data-taking period*. Phys. Rev. C, 80:015807, Jul 2009. <http://link.aps.org/doi/10.1103/PhysRevC.80.015807>.

- [15] Wendell, R. et al. (Super-Kamiokande Collaboration): *Atmospheric neutrino oscillation analysis with subleading effects in super-kamiokande I, II, and III*. Physical Review D, 81:092004, 2010.
- [16] Aharmim, B. et al. (SNO Collaboration): *Combined analysis of all three phases of solar neutrino data from the sudbury neutrino observatory*. Physical Review C, 88:025501, 2013.
- [17] U. Schmitt: *Entwicklung eines Monitordetektors für das KATRIN-Experiment*. PhD thesis, Universität Karlsruhe (TH), 2008. <http://digbib.ubka.uni-karlsruhe.de/volltexte/1000010172>.
- [18] Abe, S. et al. (KamLAND Collaboration): *Precision measurement of neutrino oscillation parameters with KamLAND*. Physical Review Letters, 100:221803, 2008.
- [19] Adamson, P. et al. (MINOS Collaboration): *Measurement of neutrino and antineutrino oscillations using beam and atmospheric data in MINOS*. Physical Review Letters, 110:251801, 2013.
- [20] K.A.Olive et al. (Particle Data Group): *Review of particle physics*. Chin. Phys. C, 38:090001, 2014. <http://pdg.lbl.gov>.
- [21] Abe, Y. et al. (Double Chooz Collaboration): *Reactor $\bar{\nu}_e$ disappearance in the Double Chooz experiment*. Physical Review D, 86:052008, 2012.
- [22] R. N. Mohapatra, S. Antusch, and K. S. Babu: *Theory of neutrinos: a white paper*. Reports on Progress in Physics, 70(11):1757, 2007. <http://stacks.iop.org/0034-4885/70/i=11/a=R02>.
- [23] G. Lazarides, Q. Shafi, and C. Wetterich: *Proton Lifetime and Fermion Masses in an $SO(10)$ Model*. Nucl.Phys., B181:287–300, 1981.
- [24] N. Arkani-Hamed, S. Dimopoulos, G. Dvali, and J. March-Russell: *Neutrino masses from large extra dimensions*. Phys. Rev. D, 65:024032, Dec 2001. <http://link.aps.org/doi/10.1103/PhysRevD.65.024032>.
- [25] R. Mohapatra, S. Nasri, and H.-B. Yu: *Grand unification of symmetry*. Physics Letters B, 636(2):114 – 118, 2006, ISSN 0370-2693. <http://www.sciencedirect.com/science/article/pii/S0370269306003820>.
- [26] S. M. Bilenky and A. Faessler: *Majorana neutrino masses, neutrinoless double beta decay, and nuclear matrix elements*. Phys. Rev. D, 70:033003, Aug 2004. <http://link.aps.org/doi/10.1103/PhysRevD.70.033003>.
- [27] Agostini, M. et al. (GERDA Collaboration): *Results on neutrinoless Double- β decay of ^{76}Ge from phase i of the GERDA experiment*. Physical Review Letters, 111:122503, 2013.
- [28] The EXO-200 Collaboration: *Search for majorana neutrinos with the first two years of EXO-200 data*. Nature, 510:229–234, 2014.
- [29] Arnold, R. et al. (NEMO-3 Collaboration): *Search for neutrinoless double-beta decay of ^{100}Mo with the NEMO-3 detector*. Physical Review D, 89:111101, 2014.
- [30] Andreotti, E. et al. (CUORICINO collaboration): *^{130}Te neutrinoless double-beta decay with CUORICINO*. Astroparticle Physics, 34(11):822–831, 2011.
- [31] C. L. Bennett, A. J. Banday, and K. M. Gorski: *Four-year cobe dmr cosmic microwave background observations: Maps and basic results*. The Astrophysical Journal Letters, 464(1):L1, 1996. <http://stacks.iop.org/1538-4357/464/i=1/a=L1>.

- [32] C. L. Bennett: *Nine-year Wilkinson Microwave Anisotropy Probe (WMAP) Observations: Final Maps and Results*. 2012.
- [33] Planck Collaboration: *Planck 2013 results. xxvi. background geometry and topology of the universe*. 2014. <http://dx.doi.org/10.1051/0004-6361/201321546>.
- [34] J. E. Sansonetti and W. C. Martin: *Handbook of basic atomic spectroscopic data*. Journal of Physical and Chemical Reference Data, 34(4):1559–2259, 2005. <http://scitation.aip.org/content/aip/journal/jpcrd/34/4/10.1063/1.1800011>.
- [35] U. Seljak, A. Slosar, and P. McDonald: *Cosmological parameters from combining the lyman- α forest with cmb, galaxy clustering and sn constraints*. Journal of Cosmology and Astroparticle Physics, 2006(10):014, 2006. <http://stacks.iop.org/1475-7516/2006/i=10/a=014>.
- [36] M. Cirelli and A. Strumia: *Cosmology of neutrinos and extra-light particles after wmap3*. Journal of Cosmology and Astroparticle Physics, 2006(12):013, 2006. <http://stacks.iop.org/1475-7516/2006/i=12/a=013>.
- [37] M. Sisti, C. Arnaboldi, and C. Brofferio: *New limits from the milano neutrino mass experiment with thermal microcalorimeters*. Nuclear Instruments and Methods in Physics Research Section A: Accelerators, Spectrometers, Detectors and Associated Equipment, 520(1–3):125 – 131, 2004, ISSN 0168-9002. <http://www.sciencedirect.com/science/article/pii/S0168900203031814>, Proceedings of the 10th International Workshop on Low Temperature Detectors.
- [38] T. Thümmeler: *Präzisionsüberwachung und Kalibration der Hochspannung für das KATRIN-Experiment*. PhD thesis, Westfälische Wilhelms-Universität Münster, 2007. <http://nbn-resolving.de/urn:nbn:de:hbz:6-16539562785>.
- [39] J. Kristiansen, G. L. Vacca, and L. Colombo: *Coupling between cold dark matter and dark energy from neutrino mass experiments*. New Astronomy, 15(7):609 – 613, 2010, ISSN 1384-1076. <http://www.sciencedirect.com/science/article/pii/S1384107610000138>.
- [40] J. Wolf: *Size matters: The vacuum system of the katrin neutrino experiment*. Journal of the Vacuum Society of Japan, 52(5):278–284, 2009.
- [41] S. Bauer, R. Berendes, F. Hochschulz, H. Ortjohann, S. Rosendahl, T. Thümmeler, M. Schmidt, and C. Weinheimer: *Next generation KATRIN high precision voltage divider for voltages up to 65kv*. Journal of Instrumentation, 8(10):P10026, 2013.
- [42] M. Erhard, S. Bauer, A. Beglarian, T. Bergmann, J. Bonn, G. Drexlin, J. Goulon, S. Groh, F. Glück, M. Kleesiek, N. Haußmann, T. Höhn, K. Johnston, M. Kraus, J. Reich, O. Rest, K. Schlösser, M. Schupp, M. Slezák, T. Thümmeler, D. Vénos, C. Weinheimer, S. Wüstling, and M. Zbořil: *High-voltage monitoring with a solenoid retarding spectrometer at the KATRIN experiment*. Journal of Instrumentation, 9(6):P06022, 2014.
- [43] J. S. Schwarz: *The Detector System of the KATRIN Experiment - Implementation and First Measurements with the Spectrometer*. PhD thesis, Karlsruher Institut für Technologie (KIT), 2014. <http://nbn-resolving.org/urn:nbn:de:swb:90-427724>.
- [44] M. Babutzka, M. Bahr, J. Bonn, B. Bornschein, A. Dieter, G. Drexlin, K. Eitel, S. Fischer, F. Glück, S. Grohmann, M. Hötzel, T. James, W. Käfer, M. Leber, B. Monreal, F. Priester, M. Röllig, M. Schlösser, U. Schmitt, F. Sharipov, M. Steidl, M. Sturm, H. Telle, and N. Titov: *Monitoring of the operating parameters of the*

- KATRIN windowless gaseous tritium source*. New Journal of Physics, 14(10):103046, 2012.
- [45] M. Sturm, M. Schlösser, R. Lewis, B. Bornschein, G. Drexlin, and H. Telle: *Monitoring of all hydrogen isotopologues at tritium laboratory karlsruhe using raman spectroscopy*. Laser Physics, 20(2):493–507, 2010.
- [46] M. Röllig, F. Priester, M. Babutzka, J. Bonn, B. Bornschein, G. Drexlin, S. Ebenhöch, E. Otten, M. Steidl, and M. Sturm: *Activity monitoring of a gaseous tritium source by beta induced x-ray spectrometry*. Fusion Engineering and Design, 88(6-8):1263–1266, 2013.
- [47] M. Röllig: *Tritium analytics by beta induced x-ray spectrometry*. PhD thesis, KIT, TLK, 2015. Forthcoming.
- [48] M. Röllig: *Activity monitoring of the katrin tritium source - monte-carlo simulation results for activity monitoring by bixs/faraday-cup*. Talk at Collaboration Meeting 03/2013, 2013.
- [49] M. Babutzka: *Untersuchung eines verfahrenbaren Monitordetektors zur Überwachung der Aktivität des β -Zerfalls in der kryogenen Pumpstrecke des KATRIN-Experiments*. Diploma Thesis, Karlsruher Institut für Technologie (KIT), 2010. <http://www.katrin.kit.edu/publikationen/dth-babutzka.pdf>.
- [50] M. Hötzel: *Simulation and analysis of source-related effects for KATRIN*. PhD thesis, Karlsruher Institut für Technologie (KIT), 2012. <http://digbib.ubka.uni-karlsruhe.de/volltexte/1000031259>.
- [51] F. Glück. Personal correspondance, 2013.
- [52] N. D. Lang and W. Kohn: *Theory of metal surfaces: Work function*. Phys. Rev. B, 3:1215–1223, Feb 1971. <http://link.aps.org/doi/10.1103/PhysRevB.3.1215>.
- [53] M. Babutzka, M. Bahr, M. Beck, M. Ghilea, M. Leber, B. Monreal, and K. Schoenung: *Katrin rearsection system specification document*, 2013.
- [54] H. A. Kramers: *On the theory of x-ray absorption and of the continuous x-ray spectrum*. Philosophical Magazine Series 6, 46(275):836–871, 1923.
- [55] G. Zschornack: *Handbook of X-Ray Data*. Springer, 2007, ISBN 9783540286189.
- [56] M. Sturm: *Aufbau und Test des Inner-Loop-Systems der Tritiumquelle von KATRIN*. PhD thesis, Karlsruher Institut für Technologie (KIT), 2010. <http://digbib.ubka.uni-karlsruhe.de/volltexte/1000019355>.
- [57] E. Rathakrishnan: *Gas Dynamics*. Prentice Hall India Pvt., Limited, 2004, ISBN 9788120309524.
- [58] D. W. Umrath: *Grundlagen der Vakuumtechnik*. Oerlikon Leybold Vacuum, 2007. <http://www.oerlikon.com/leyboldvacuum/de/dokumentation/downloads/>, besucht: 2014.
- [59] A. Roth: *Vacuum Technology*. Elsevier Science, 2012, ISBN 9780444598745.
- [60] N. Yoshimura: *Vacuum Technology: Practice for Scientific Instruments*. Springer-Link: Springer e-Books. Springer, 2007, ISBN 9783540744337.
- [61] R. Dobrozemsky and G. Moraw: *Comparison of outgassing rates from stainless steel, aluminium and copper after badeout under high vacuum and atmospheric pressure*. 1973. https://inis.iaea.org/search/search.aspx?orig_q=RN:5133063#.

- [62] Oerlikon Leybold: *Technical data sheet of the TURBOVAC MAG W 600 P*. https://leyboldproducts.oerlikon.com/products/pics/FileResources/Orig/TD_Technische%20Daten/TD_410600V0005_EN.pdf.
- [63] F. Priester: *Tritiumtechnologie für die fensterlose Quelle WGTS von KATRIN*. PhD thesis, Karlsruher Institut für Technologie (KIT), 2013. <http://digbib.ubka.uni-karlsruhe.de/volltexte/1000035699>.
- [64] J. Wolf, B. Bornschein, G. Drexlin, R. Gehring, R. Größle, S. Horn, N. Kernert, S. Riegel, R. Neeb, and A. Wagner: *Investigation of turbo-molecular pumps in strong magnetic fields*. *Vacuum*, 86(4):361–369, 2011.
- [65] A. Jansen. Personal correspondence, 2014.
- [66] A. Jansen: *Modellierung der Rotortemperatur von Turbomolekularpumpen in Magnetfeldern mit unterschiedlichen Gasflüssen*. Diploma Thesis, Karlsruher Institut für Technologie (KIT), 2011.
- [67] B. Leiber: *Non-axially symmetric field and trajectory calculations for the KATRIN-experiment*. Diploma thesis, Karlsruher Institut für Technologie (KIT), 2010. <http://www.katrin.kit.edu/publikationen/dth-leiber.pdf>.
- [68] D. Meeker: *Finite element method magnetics*, 2014. <http://www.femm.info>.
- [69] N. Wandkowsky: *Study of background and transmission properties of the KATRIN spectrometers*. PhD thesis, Karlsruher Institut für Technologie (KIT), 2013. <http://digbib.ubka.uni-karlsruhe.de/volltexte/1000036631>.
- [70] A. Hervé: *Magnetic shielding calculations and design for the rearsection*. internal document, 2013.
- [71] V. Klyukhin, N. Amapane, and A. Ball: *Validation of the cms magnetic field map*. *Journal of Superconductivity and Novel Magnetism*, 2014, ISSN 1557-1939. <http://dx.doi.org/10.1007/s10948-014-2809-4>.
- [72] P. Souers: *Hydrogen Properties for Fusion Energy*. University of California Press, 1986, ISBN 9780520055001.
- [73] KATRIN Rear Section Group: *Rear section technical design report for the primary vacuum system, 2nd containment and support structures*, 2013.
- [74] M. Meloni: *Installation planning building 452*, 2014.
- [75] A. Einstein: *Über einen die Erzeugung und Verwandlung des Lichtes betreffenden heuristischen Gesichtspunkt*. *Annalen der Physik*, 1905. <http://dx.doi.org/10.1002/andp.200590004>.
- [76] B. Klaus: *Abschlussbericht zum Projekt KATRIN Feldberechnungen*, 2013.
- [77] F. Paschen: *Über die zum Funkenübergang in Luft, Wasserstoff und Kohlensäure bei verschiedenen Drucken erforderliche Potentialdifferenz*. *Annalen der Physik*, 1889. <http://dx.doi.org/10.1002/andp.18892730505>.
- [78] R. Arora and W. Mosch: *High voltage insulation engineering: behaviour of dielectrics, their properties and applications*. New Age International Publishers, 1995, ISBN 9788122406191.
- [79] CeramTec GmbH: *Custom feedthrough assemblies*. http://www.ceramtec.com/files/us_ceramaseal_feedthroughs.pdf.

- [80] A. Beer: *Bestimmung der Absorption des rothen Lichts in farbigen Flüssigkeiten*. Annalen der Physik, 1852. <http://gallica.bnf.fr/ark:/12148/bpt6k151715.image.f90.langDE>.
- [81] M. P. Seah and W. A. Dench: *Quantitative electron spectroscopy of surfaces: A standard data base for electron inelastic mean free paths in solids*. Surface and Interface Analysis, 1(1):2–11, 1979, ISSN 1096-9918. <http://dx.doi.org/10.1002/sia.740010103>.
- [82] R. H. Fowler: *The analysis of photoelectric sensitivity curves for clean metals at various temperatures*. Phys. Rev., 38:45–56, Jul 1931. <http://link.aps.org/doi/10.1103/PhysRev.38.45>.
- [83] L. A. DuBridge: *Theory of the energy distribution of photoelectrons*. Phys. Rev., 43:727–741, May 1933. <http://link.aps.org/doi/10.1103/PhysRev.43.727>.
- [84] Energetiq Technology, Inc.: *Official product image of an energetic eq-99x*, 2014. <http://www.energetiq.com/high-resolution-images/ldls-eq99x-with-psu-energetiq.jpg>.
- [85] Energetiq Technology, Inc.: *Technical data sheet of the EQ-99X LDLS*. <http://www.energetiq.com/DataSheets/EQ99X-Data-Sheet.pdf>.
- [86] K. Schönung: *Investigation of tritium compatibility of Rear Section related components and development of a Rear Wall for the Rear Section*. PhD thesis, KIT, TLK, 2015. Forthcoming.
- [87] T. Northrop: *The adiabatic motion of charged particles*. Interscience tracts on physics and astronomy. Interscience Publishers, 1963.
- [88] Cryomagnetics Inc.: *Technical proposal for the katrin project - 5 superconducting magnet systems*, 2012.
- [89] J. Jackson, C. Witte, and K. Müller: *Klassische Elektrodynamik*. Überarbeitete Auflage. Bod Third Party Titles, 2006, ISBN 9783110189704.
- [90] M. Leber: *Internal reports on optimizations of the rearsection electron gun*. internal document, 2011.
- [91] R. Poole, R. Leckey, J. Jenkin, and J. Liesegang: *Photoelectron angular distributions from gold*. Journal of Electron Spectroscopy and Related Phenomena, 1(4):371 – 376, 1972–1973, ISSN 0368-2048. <http://www.sciencedirect.com/science/article/pii/0368204872800380>.
- [92] F. Glück: *Preliminary electromagnetic design for the rearsection*. internal document, 2010.
- [93] F. Heizmann: *Optimization of a katrin source analysis tool and investigations of the relic neutrino discovery potential*. Master’s thesis, KIT, IEKP, January 2015. Forthcoming.
- [94] G. Courville: *Mechanical design of the rearsection electron gun*. internal CAD model, 2013.
- [95] PI Ceramic GmbH: *Piezoelectric actuators - components, technology, operation*, 2014.
- [96] A. Malkmus. Personal e-mail correspondance, 2010.
- [97] Robert Bosch GmbH: *Technical data sheet of the Bosch GLM150*. <http://www.bosch-professional.com/de/de/glm-150-23315-ocs-p/>.

- [98] O. Kazachenko, B. Bornschein, L. Bornschein, F. Eichelhardt, N. Kernert, and H. Neumann: *Trap — a cryo-pump for pumping tritium on pre-condensed argon*. Nuclear Instruments and Methods in Physics Research Section A: Accelerators, Spectrometers, Detectors and Associated Equipment, 587(1):136 – 144, 2008, ISSN 0168-9002. <http://www.sciencedirect.com/science/article/pii/S0168900207024941>.
- [99] S. Sarvestani. Personal e-mail correspondance, 2012.
- [100] H. Spieler: *Radiation detectors and signal processing*. Lecture Notes - VII. Heidelberg Graduate Lectures in Physics, 2001. http://www-physics.lbl.gov/~spieler/Heidelberg_Notes/.
- [101] T. Eggert: *Die spektrale Antwort von Silizium-Röntgendetektoren*. 2004.
- [102] Micron Semiconductor Ltd.: *Data sheet of the LL14 in the catalogue*. <http://www.micronsemiconductor.co.uk/pdf/cat.pdf>.
- [103] Analog Devices, Inc.: *Technical data sheet of the AD8669*. http://www.analog.com/static/imported-files/data_sheets/AD8663_8667_8669.pdf.
- [104] mindshape GmbH: *Dämmerungszeiten in Karlsruhe: Februar*, 2013. <http://www.sonnenuntergang-zeit.de/daemmerungszeiten:karlsruhe:februar.html>.
- [105] O.-L. Huianu: *Aufbau und inbetriebnahme eines elektronenemitters für tests von teilchendetektoren*. Master's thesis, Institut für Kernphysik Forschungszentrum Karlsruhe, 2003.
- [106] S. Reimer: *Ein elektrostatisches dipolsystem zur eliminierung von ionen in der DPS2-F des KATRIN experimentes*. Diploma thesis, Karlsruher Institut für Technologie (KIT), 2009. <http://www.katrin.kit.edu/publikationen/dth-reimer.pdf>.
- [107] I. Baikie. Personal e-mail correspondance, 2011.
- [108] E. Otten: *Wgts plasma potential under influence of patch effect potentials at rear plate*. internal document, 2012.
- [109] U. Inan and M. Golkowski: *Principles of Plasma Physics for Engineers and Scientists*. Cambridge University Press, 2010, ISBN 9781139492249.
- [110] H. Alfven: *Cosmic Plasma*. Springer, 1981, ISBN 9789027711519.
- [111] M. Bahr: *Gold coating on diverse substrates for rear wall prototyping*. internal document, 2011.
- [112] R. Park and M. Lagally: *Solid State Physics: Surfaces*. Methods in Experimental Physics. Elsevier Science, 1985, ISBN 9780080860077.
- [113] L. Neumann: *Simulation of the KATRIN tritium source and first measurements with the windowless gaseous tritium source*. PhD thesis, KIT, TLK, 2016. Forthcoming.
- [114] A. Hobl: *Superconducting magnet system wgts for katrin*, 2006.
- [115] F. Glück: *Software code to calculate forces between magnetic solenoids*. internal document, 2012.
- [116] A. Kosmider. Personal correspondance, 2013.
- [117] F. Salvat, J. Fernandez-Varea, and J. Sempau: *Penelope-2008: a code system for monte carlo simulation of electron and photon transport (issy-les-moulineaux: Oecd nuclear energy agency)*, 2006.

- [118] P. Renschler: *KESS - A new Monte Carlo simulation code for low-energy electron interactions in silicon detectors*. PhD thesis, Karlsruher Institut für Technologie (KIT), 2011. <http://digbib.ubka.uni-karlsruhe.de/volltexte/1000024959>.
- [119] D. Maurel: *Designstudien zur Messung der Aktivität der Tritiumquelle im KATRIN-Experiment mit Röntgenstrahlung*. Diplomarbeit, Institut für experimentelle Kernphysik Universität Karlsruhe, 2009.
- [120] D. A. Muller: *Structure and bonding at the atomic scale by scanning transmission electron microscopy*. *Nature materials*, 8(4):263–270, 2009.
- [121] G. Kästle, H.-G. Boyen, B. Koslowski, A. Plettl, F. Weigl, and P. Ziemann: *Growth of thin, flat, epitaxial (111) oriented gold films on c-cut sapphire*. *Surface science*, 498(1):168–174, 2002.
- [122] C. Schmidt: *Investigation of the work function fluctuations for the precision experiments aspect and katrin*. Master’s thesis, Institut für Physik an der Johannes Gutenberg-Universität Mainz, 2003.
- [123] O. Zimmer, J. Byrne, M. van der Grinten, W. Heil, and F. Glück: *“aspect” – a new spectrometer for the measurement of the angular correlation coefficient a in neutron beta decay*. *Nuclear Instruments and Methods in Physics Research Section A: Accelerators, Spectrometers, Detectors and Associated Equipment*, 440(3):548–556, 2000.
- [124] M. Biron: *Thermoplastics and Thermoplastic Composites*. *Plastics Design Library*. Elsevier Science, 2012, ISBN 9781455730353.
- [125] D. Woodruff and T. Delchar: *Modern Techniques of Surface Science*. *Cambridge Solid State Science Series*. Cambridge University Press, 1994, ISBN 9780521424981.
- [126] L. Kelvin: *Contact electricity of metals*. *Philosophical Magazine Series 5*, 46:278, 82–120, pages 37–41, 1898. <http://www.tandfonline.com/doi/pdf/10.1080/14786449808621172>.
- [127] Tektronix, Inc.: *Technical data sheet of the FCA3000*. http://de.tek.com/sites/tek.com/files/media/media/resources/FCA3000_Series_Timer-Counter-Analyzers_Datasheet_3CW-25556-4_1.pdf?zct=US.
- [128] B. Feuerbacher and R. Willis: *Photoemission and electron states at clean surfaces*. *Journal of Physics C: Solid State Physics*, 9(2):169, 1976.
- [129] J. Güdde and U. Höfer: *Femtosecond time-resolved studies of image-potential states at surfaces and interfaces of rare-gas adlayers*. *Progress in surface science*, 80(3):49–91, 2005.
- [130] S. Roy: *Thermal Physics And Statistical Mechanics*. New Age International (P) Limited, 2001, ISBN 9788122413021.
- [131] E. Otten: *Pierce electrode for generating a focused and parallelized electron beam from rear wall prototype samples*. internal document, 2012.
- [132] D. Lide: *CRC handbook of chemistry and physics*. CRC Press, Boca Raton, 2005, ISBN 0-8493-0486-5.
- [133] K. Schlösser. Personal correspondance, 2012.
- [134] P. A. Anderson: *Work function of gold*. *Physical Review*, 115(3):553, 1959.
- [135] G. F. Saville, P. Platzman, G. Brandes, R. Ruel, and R. L. Willett: *Feasibility study of photocathode electron projection lithography*. *Journal of Vacuum Science & Technology B*, 13(6):2184–2188, 1995.

- [136] X. Jiang, C. Berglund, A. E. Bell, and W. A. Mackie: *Os₃: Photoemission from gold thin films for application in multiphotocathode arrays for electron beam lithography*. Journal of Vacuum Science & Technology B, 16(6):3374–3379, 1998.
- [137] W. E. Martinez, G. Gregori, and T. Mates: *Titanium diffusion in gold thin films*. Thin Solid Films, 518(10):2585–2591, 2010.
- [138] M. N. Polyanskiy: *Refractive index database*, 2014. <http://refractiveindex.info>.
- [139] K. Mitchell: *The theory of the surface photoelectric effect in metals. i*. Proceedings of the Royal Society of London. Series A, 146(857):442–464, 1934.
- [140] K. Mitchell: *The theory of the surface photoelectric effect in metals. ii*. Proceedings of the Royal Society of London. Series A-Mathematical and Physical Sciences, 153(880):513–533, 1936.
- [141] H. Thomas: *Zum äußeren lichtelektrischen effekt der alkalimetalle*. Zeitschrift für Physik, 147(4):395–418, 1957.
- [142] H. Mayer and H. Thomas: *Zum äußeren lichtelektrischen effekt der alkalimetalle*. Zeitschrift für Physik, 147(4):419–441, 1957.
- [143] S. Methfessel: *Zum äußeren lichtelektrischen effekt der alkalimetalle*. Zeitschrift für Physik, 147(4):442–464, 1957.
- [144] T. Thümmeler, R. Marx, and C. Weinheimer: *Precision high voltage divider for the KATRIN experiment*. New Journal of Physics, 11(10):103007, 2009.
- [145] R. D’arcy and N. Surplice: *Electric charges on stainless steel surfaces: The effects of hydrogen, charged particles, illumination, and electric fields on the work function*. Surface Science, 34(2):193–211, 1973.
- [146] L. Stobiński, L. Zommer, and R. Duś: *Molecular hydrogen interactions with discontinuous and continuous thin gold films*. Applied surface science, pages 319–325, 1999. <http://www.sciencedirect.com/science/article/pii/S0169433298005170>.
- [147] L. Stobiński and R. Duś: *Atomic hydrogen adsorption on thin gold films*. Surface science, 269:383–388, 1992.
- [148] G. A. Melin and R. Madix: *Energy accommodation during hydrogen atom recombination on metal surfaces*. Transactions of the Faraday Society, 67:2711–2719, 1971.
- [149] B. Mildner, E. Hasselbrink, and D. Diesing: *Electronic excitations induced by surface reactions of h and d on gold*. Chemical physics letters, 432(1):133–138, 2006.
- [150] Z. Wang and E. Seebauer: *Estimating pre-exponential factors for desorption from semiconductors: consequences for a priori process modeling*. Applied surface science, 181(1):111–120, 2001.
- [151] L. Stobinski and R. Dus: *Model of atomic hydrogen adsorption on thin gold film surface*. Vacuum, 45(2–3):299 – 301, 1994.
- [152] G. Sauerbrey: *Verwendung von Schwingquarzen zur Wägung dünner Schichten und zur Mikrowägung*. Zeitschrift für Physik, 155(2):206–222, 1959, ISSN 0044-3328. <http://dx.doi.org/10.1007/BF01337937>.
- [153] J. Janata: *Principles of chemical sensors*. Springer, Dordrecht, 2009, ISBN 978-0387699301.
- [154] C. O’sullivan and G. Guilbault: *Commercial quartz crystal microbalances—theory and applications*. Biosensors and bioelectronics, 14(8):663–670, 1999.

- [155] T. Hänsch: *Passion for precision*. Nobel Lecture, 2005. http://www.nobelprize.org/nobel_prizes/physics/laureates/2005/hansch-lecture.pdf.
- [156] R. Huebener: *Conductors, Semiconductors, Superconductors*. ISBN 9783319091419.
- [157] B. Huang, C. Chin, and C. Duang: *A design method of thermoelectric cooler*. International Journal of Refrigeration, 23(3):208–218, 2000.
- [158] Allectra GmbH: *High vacuum and uhv components*, 2014. <http://www.allectra.com/images/Downloads/english/ALLECTRA-2012-EE.pdf>.
- [159] S. Kakani: *Material Science*. New Age International (P) Limited, Publishers, 2006, ISBN 9788122415285.
- [160] J. Weis: *Bestimmung der Dicke einer Tritiumschicht auf einer Goldoberfläche mit TriQuarz*, 2012.
- [161] V. Tsionsky, L. Daikhin, M. Urbakh, and E. Gileadi: *Behavior of quartz crystal microbalance in nonadsorbed gases at high pressures*. Langmuir, 11(2):674–678, 1995.
- [162] M. Babutzka, B. Bornschein, F. Priester, M. Röllig, and F. Schneck: *Triade: A new instrument for adsorption and desorption measurements using beta-induced x-ray spectroscopy*. 2015. Forthcoming.
- [163] S. M. Seltzer and M. J. Berger: *Improved procedure for calculating the collision stopping power of elements and compounds for electrons and positrons*. The International Journal of Applied Radiation and Isotopes, 35(7):665 – 676, 1984, ISSN 0020-708X.
- [164] D. Walter: *Charakterisierung eines BIXS-Systems zur Bestimmung der Tritiumkonzentration in Prozessgasen mittels statischen und dynamischen Messungen*, 2014.
- [165] M. Röllig, F. Priester, M. Babutzka, J. Bonn, B. Bornschein, G. Drexlin, S. Ebenhöch, E. W. Otten, M. Steidl, and M. Sturm: *Activity monitoring of a gaseous tritium source by beta induced x-ray spectrometry*. Fusion Engineering and Design, 88(6–8):1263 – 1266, 2013.
- [166] E. Gatti and P. Rehak: *Semiconductor drift chamber — an application of a novel charge transport scheme*. Nuclear Instruments and Methods in Physics Research, 225(3):608 – 614, 1984, ISSN 0167-5087.
- [167] M. Howe, G. Cox, P. Harvey, F. McGirt, K. Rielage, J. Wilkerson, and J. Wouters: *Sudbury neutrino observatory neutral current detector acquisition software overview*. IEEE Transactions on Nuclear Science, 51(3):878–883, 2004.
- [168] T. P. Taylor, M. Ding, D. S. Ehler, T. M. Foreman, J. P. Kaszuba, and N. N. Sauer: *Beryllium in the environment: a review*. Journal of Environmental Science and Health, Part A, 38(2):439–469, 2003.

Appendix A

E-gun beam tracker - circuitry documentation

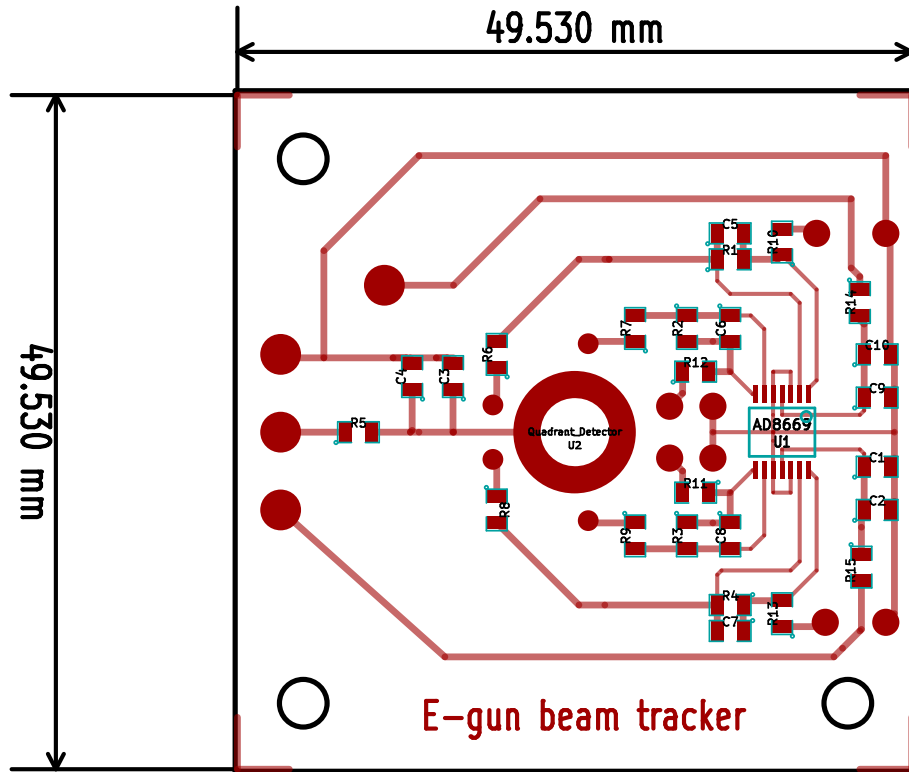


Figure A.1.: Board layout of the E-gun beam tracker - It shows the ceramic outer shape and boreholes (black) and the as print conductor paths. The one-sided board layout required some compromises and some wire bridges have been avoided by the soldered signal cables. The detector connector pads have been positioned to minimize the bond wire length. Except for detector and amplifier all parts are SMD0805.

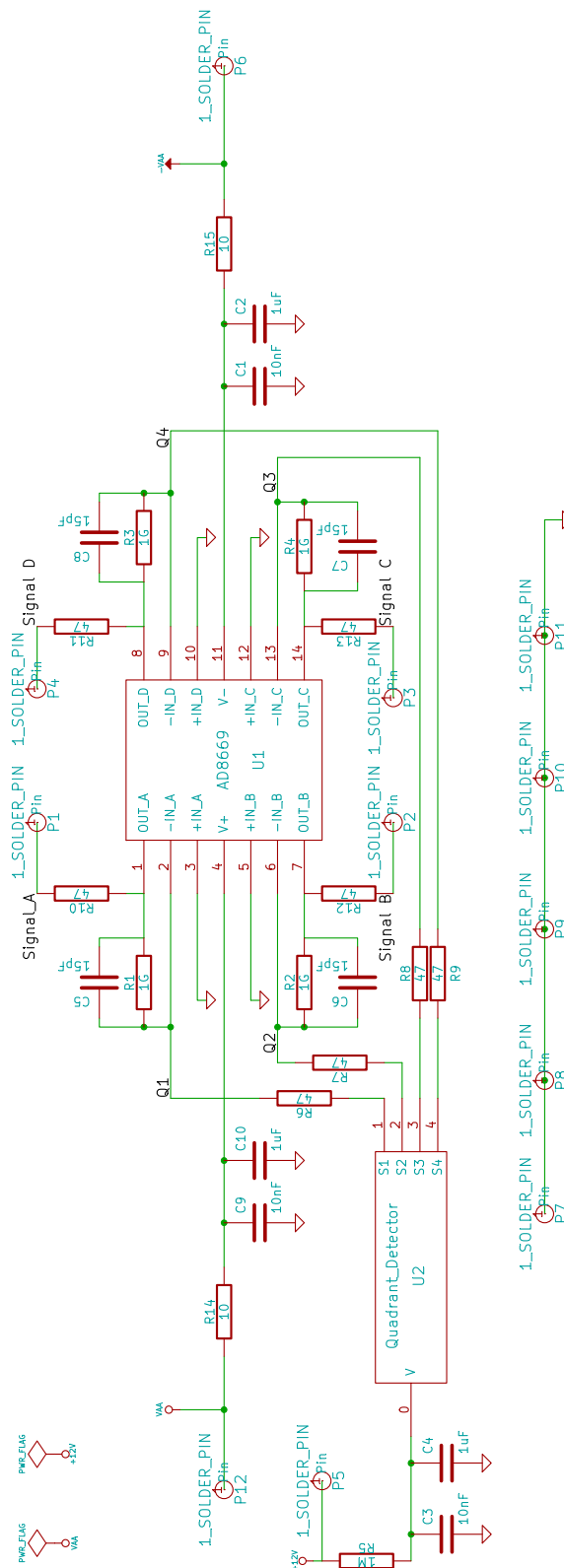


Figure A.2.: Circuit layout of the E-gun beam tracker - Circuit schema of all 4 channels with amplifier, detector and power flags. Voltage supplies of detector and operational amplifier are always protected by an RC-low pass filter. All channels are identical transimpedance converters with 10^9 V/A amplification.

Appendix B

UV light source calibration

Table B.1.: Calibration of the filtered UV light source - in a setup as used at the monitor spectrometer measurements. Relative efficiencies normalized on a wavelength of 300 nm. Only the slit size 5 data is used for the analysis because all measurements have been carried out with slit sizes 3 to 5. For the analysis the values have been interpolated.

Wave-length (nm)	Efficiency - slit size 5	Efficiency - slit size 10	Wave-length (nm)	Efficiency - slit size 5	Efficiency - slit size 10
210	0.119	0.335	260	0.586	0.747
212	0.117	0.330	262	0.619	0.776
214	0.119	0.330	264	0.646	0.795
216	0.120	0.330	266	0.676	0.818
218	0.122	0.330	268	0.693	0.838
220	0.127	0.330	270	0.711	0.849
222	0.131	0.332	272	0.727	0.858
224	0.137	0.338	274	0.743	0.866
226	0.144	0.344	276	0.756	0.872
228	0.154	0.352	278	0.773	0.878
230	0.166	0.366	280	0.784	0.878
232	0.180	0.372	282	0.805	0.881
234	0.198	0.392	284	0.827	0.895
236	0.219	0.409	286	0.841	0.903
238	0.241	0.426	288	0.856	0.920
240	0.265	0.452	290	0.872	0.923
242	0.296	0.477	292	0.908	0.929
244	0.325	0.503	294	0.934	0.949
246	0.354	0.531	296	0.956	0.963
248	0.386	0.563	298	0.980	0.986
250	0.416	0.591	300	1.000	1.000
252	0.451	0.625	305	1.071	1.050
254	0.485	0.653	310	1.134	1.095
256	0.518	0.685	315	1.181	1.140
258	0.554	0.719	320	1.221	1.170

Acknowledgements

Finally I want to thank all people that contributed to this thesis in any way and/or increased the enjoyment during its realization.

Special regards are for all the persons of the following (but surely not fully complete) list:

Thank you,

- ❑ Prof. Guido Drexlin for the interesting and challenging scope of the thesis and the freedom to test and implement many different ideas on the Rearsection component.
- ❑ Prof. Thomas Müller for taking over the task of the co-supervisor of this thesis.
- ❑ all members of the examination committee who invest their time for my examination.
- ❑ Dr. Florian Priester, Kerstin Schönung and Marco Roellig for the collective efforts on making the Rearsection work and of course for the awesome working atmosphere.
- ❑ Dr. Beate Bornschein, Dr. Michael Sturm and the whole ITeP-TLK team for their support during a major part of my thesis and a the pleasant discussions beyond the daily work.
- ❑ Dr. Ferenc Glück and the numerous code developers which enabled the detailed EMD simulations ...
- ❑ ... and the whole IKP team with its wonderful pizza day, goodies store and memorable joint activities.
- ❑ our collaborating Rearsection team at the University of California Santa Barbara: Prof. Ben Monreal, Greg Courville, Dr. Michelle Leber, Matt Bahr, Dean White, Luiz de Viveiros and Marian Ghilea. Especially for their hospitality during my stay at UCSB. Special thanks to Greg for adding a large boost of ideas and enthusiasm speeding up the E-gun prototyping.
- ❑ our collaborating colleagues from the University of Mainz: Prof. Ernst Otten, Dr. Marcus Beck and Christian Schmidt for various contributions to the Rear Wall design and test measurements.
- ❑ Dr. Kathrin Valerius, our decent young scientist investigator group and in particular
- ❑ ... Florian Heizmann for his hard work on re-implementing the Rearsection in the most recent KATRIN simulation code and Laura Neumann for her efforts on the source plasma potential. Not forgetting the enjoyable working atmosphere.
- ❑ Alexander Jansen for his great help during the magnetic field compatibility measurements.
- ❑ Dr. Sascha Wüstling and the IPE team for electrotechnical advice, printing and mounting the E-gun beam tracker.
- ❑ Dr. Klaus Schlösser and the monitor spectrometer team that allowed and supported us during the photo-emission measurements.
- ❑ Dr. Jochen Bonn, Dr. Nikita Titov and Dr. Markus Steidl for many ideas and constructive criticism during the Rearsection design phase.

- ❑ Rainer Gumbsheimer and his team - in particular the engineers Daniel König and Valery Popov - for adding some engineering realism to my CAD model.
- ❑ Dr. Johannes Schwarz and Dr. Sebastian Fischer for the enjoyment of their company and friendship from the first term of studying physics till the finalization of each thesis at the KATRIN project.
- ❑ all readers and correctors of this thesis.
- ❑ ... and all who have been forgotten in this list.

Special thanks also to my parents and my family general, my girlfriend and all my friends for giving me support and confidence anytime and in particular during the completion of this thesis.